Studies in Optical Resonator Gyroscopes

by

Farhad Zarinetchi

B.S., M.S. Massachusetts Institute of Technology
(1986)

Submitted to the Department of Electrical Engineering and
Computer Science
In partial fulfillment of the requirements for the degree of

Doctor of Philosophy

at the
MASSACHUSETTS INSTITUTE OF TECHNOLOGY
MAY 1992

Author .....
Department of Electrical Engineering and Computer Science
May 15, 1992

Certified by .....
Shaoul Ezekiel,
Thesis Supervisor

Accepted by .....
Campbell L. Searle
Chairman, Departmental Committee on Graduate Students

Studies in Optical Resonator Gyroscopes
by
Farhad Zarinetchi

Submitted to the Department of
Electrical Engineering and Computer Sciences
on May 15, 1992 in partial fulfillment of the
requirements for the degree of Doctor of Philosophy in
Electrical Engineering

ABSTRACT

The behavior and error sources of three different optical resonator gyroscopes were studied. All of these gyroscopes determine the inertial rotation rate by measuring the Sagnac effect in an optical ring cavity.

First, the behavior and error sources of a passive resonator gyroscope made of discrete mirrors were studied. Important sources of noise and drift for this gyroscope were evaluated, and compared with the theoretical shot noise limit. These sources include the effects of backscattering, as well as the variations in both the state of polarization and spatial alignment of the input beams. Short term rms noise was very close to that predicted by shot noise limit, i.e. 0.17 deg/hr for τ =10 ms. For τ = 100 sec, we observed an rms noise of 0.01 deg/hr, which is several times larger than the shot noise. This difference is attributed to several effects that need to be studied. These effects include incomplete carrier suppression and residual gas flow effects inside the sealed resonator. Additionally, the existence of lockin at low rotation rates was demonstrated and a nonmechanical method of eliminating this effect was presented.

Next, the behavior of a passive resonator gyroscope using a fiberoptic ring resonator was studied. Several sources of drift and offset were evaluated. These included backscattering, variations in the state of polarization of light, and the optical Kerr effect.

Finally, we studied the feasibility of a fiberoptic ring laser gyroscope based on the use of stimulated Brillouin scattering as the laser gain medium. The measurement of rotation rate by this device was demonstrated, and a nonmechanical approach to eliminate the lockin problem was presented. Several sources of bias were also identified.

Thesis Supervisor: Dr. S. Ezekiel

Title: Professor of Aeronautics and Astronautics
and Electrical Engineering and Computer Sciences

I would like to thank all the people who made this thesis possible. First and foremost, I would like to thank my advisor Prof. S. Ezekiel, to whom this thesis is dedicated, for his invaluable support and guidance of this research. Through him, I was exposed to many valuable research techniques, for which I am deeply grateful. I would especially like to thank him for teaching me the value of organization.

I would like to thank Prof. M. Prentiss, Prof. R. Weiss and Prof J. Roberge for reading this thesis and making helpful suggestions. Additionally, I would like to express my deep appreciation to Steve Smith for his invaluable technical and emotional support. I would also like to thank my friends and fellow graduate students, A. Kazeroonian, K. Smith, J. Kierstead, B. Barat, J. Villasenor, G. Wornell, J. Shapiro, S. Shahriar, P. Hemmer, B. Tench, C. O'Connor, L. Hergenroeder, R. Meyer, J. Mar, J. Brauer.

I would also like to thank all my friends at the MIT Tae Kwon Do club and SIA Technologies for their kind thoughts and moral support. Last but not least I would like to thank my family, who stand by me through thick and thin.

This thesis was supported in part by the Joint Services Electronics Program at the MIT Research Laboratory of Electronics, U.S. Air Force Office of Scientific Research and C.S.Draper Laboratories

Table of Contents

CHAPTER 1

Introduction

The advent of lasers has promoted a variety of optical sensors which measure inertial rotation rate, temperature, pressure, magnetic field, concentration of gas species, distance, time, and so on. All optical rotation sensors, so far, are based on the Sagnac effect[1], and are called optical gyroscopes inspite of their lack of a spinning mass.

Gyroscopes in general are useful in fields such as navigation and geophysics where precise measurement of angular velocity is required. A navigation grade gyroscope must have a precision better than 10^{-3} deg/hr[2,3]. In addition, gyroscopes with precision better than 10^{-6} deg/hr[4] can be used in geophysics experiments to measure variations in the rotation of earth.

1.1. The Sagnac Effect

As mentioned previously, the physical principle behind the operation of an optical gyroscope is the Sagnac effect, which is a nonreciprocal optical propagation effect due to rotation. In this section we will present a simplified derivation of the Sagnac effect. In a closed optical path such as the continuous ring illustrated in figure 1.1.1, the Sagnac effect will cause a clockwise-traveling beam, E^-, to experience a different perimeter than that observed by a counterclockwise-traveling beam, E^+. This difference, labeled ΔP_Ω, is illustrated in figure 1.1.1, where during the time, τ_r, when light goes once around the loop, the point S on the loop has moved to a new position S', so that the effective perimeter for E^- has been shortened by approximately $\Omega R \tau_r$ and similarly the effective perimeter for E^+ has been elongated by approximately $\Omega R \tau_r$. The round trip travel time τ_r is approximately given by $2\pi R/c$, where c is the speed of light, and thus ΔP_Ω becomes:

$$\begin{aligned} \Delta P_\Omega &= 2\tau_r(\Omega R) \\ &= \frac{4A}{c}\Omega \end{aligned} \tag{1.1.1}$$

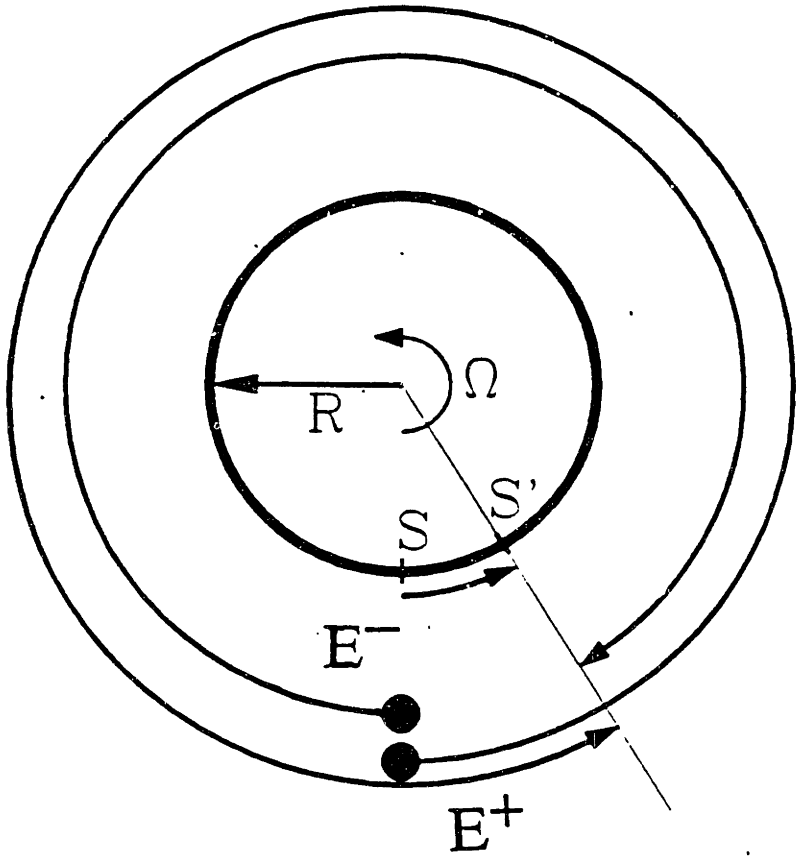

Figure 1.1.1. Illustration of the Sagnac effect in a rotating circular ring.

where A is the area of the loop. As shown above, ΔP_Ω is directly proportional to the angular rotation rate. It should be noted that ΔP_Ω is only sensitive to the component of the angular velocity vector that is perpendicular to the plane of the loop.

ΔP_Ω is typically very small. For example, the 10^{-3} deg/hr accuracy, required for a navigational gyroscope, corresponds to a ΔP_Ω of only 10^{-19} m, for a circular loop with a diameter of 0.1 m. This is approximately 3×10^{-19} of the perimeter of the loop. By comparison, reciprocal or common mode perturbations, such as thermal variations of the optical path, can be orders of magnitude larger than the Sagnac effect, but these reciprocal perturbations can only change the Sagnac scale factor $(4A/c)$ and do not contribute to ΔP_Ω directly.

1.2. The Optical Interferometer Gyroscope

One way of measuring the Sagnac effect, manifested in ΔP_Ω, is to use a so called Sagnac interferometer[5]. Figure 1.2.1 shows an example of a Sagnac interferometer setup made from bulkoptic components. The interferometer is composed of a 50/50 beamsplitter BS and 3 maximum reflectivity mirrors M_1 through M_3.

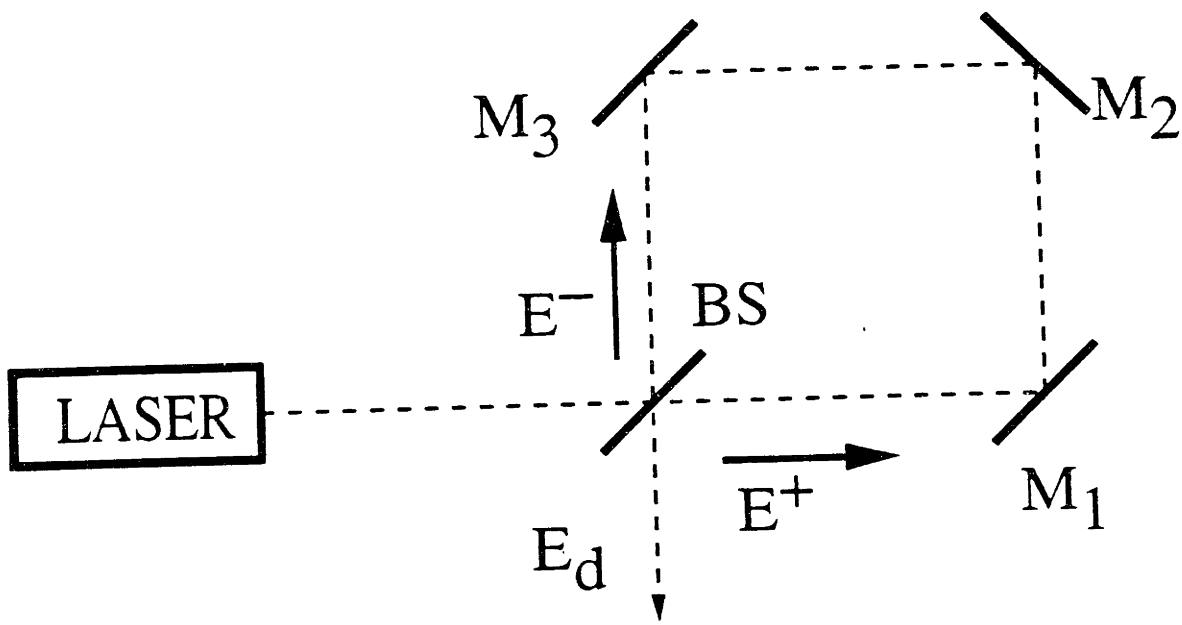

Figure 1.2.1. Example of a bulkoptic Sagnac interferometer.

Light from a laser is split into two beams E^+ and E^- by BS. E^+ travels in the counterclockwise direction in the interferometer and E^- travels in the clockwise direction. E^+ and E^- are combined into a single beam, E_d, by BS. It is obvious from figure 1.2.1 that E^+ and E^- both travel through physically identical paths through the interferometer. However, in the presence of rotation, because of ΔP_Ω, there is a phase difference, $\Delta\phi_\Omega$,

between E^+ and E^- as they exit the interferometer, which is given by:

$$\begin{aligned} \Delta\phi_\Omega &= \frac{2\pi}{\lambda_\circ}\Delta P_\Omega \\ &= \frac{2\pi}{\lambda_\circ}\frac{4A}{c}\Omega \end{aligned} \tag{1.2.1}$$

where $\lambda_\circ$ is the free space wavelength of the laser source. $\Delta\phi_\Omega$, which is directly proportional to the rotation rate, Ω, causes a measurable variation in the intensity of E_d as a function of Ω as illustrated in figure 1.2.2. It should be noted that the choice of E_d as the output of the interferometer is presented here for illustration purposes. In practice, reciprocity issues associated with the beamsplitter require us not to choose E_d but to choose the output along the other arm of the interferometer, which goes back towards the light source.

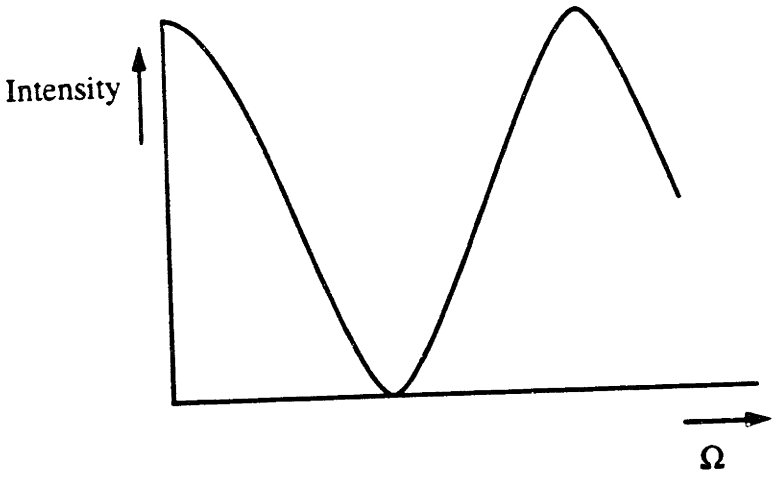

Figure 1.2.2. Variations in the intensity of E_d in the Sagnac interferometer vs. rotation rate, Ω.

The interferometer of figure 1.2.1 can be replaced by a multiturn fiber interferometer[6] as shown in figure 1.2.3. The beamsplitter BS is replaced by a fiberoptic evanescent wave coupler C, and the body of the interferometer is a continuous strand of single mode fiber wrapped N times around a cylinder of area A. The Sagnac phase shift for the multiturn fiber interferometer is proportional to the total area covered by the interferometer, i.e. $N \times A$, and is given by:

$$\Delta\phi_\Omega = \frac{2\pi}{\lambda_o}\frac{4AN}{c}\Omega \tag{1.2.2}$$

Thus, the rotation sensitivity of the gyroscope increases both with the loop area A and the number of turns N.

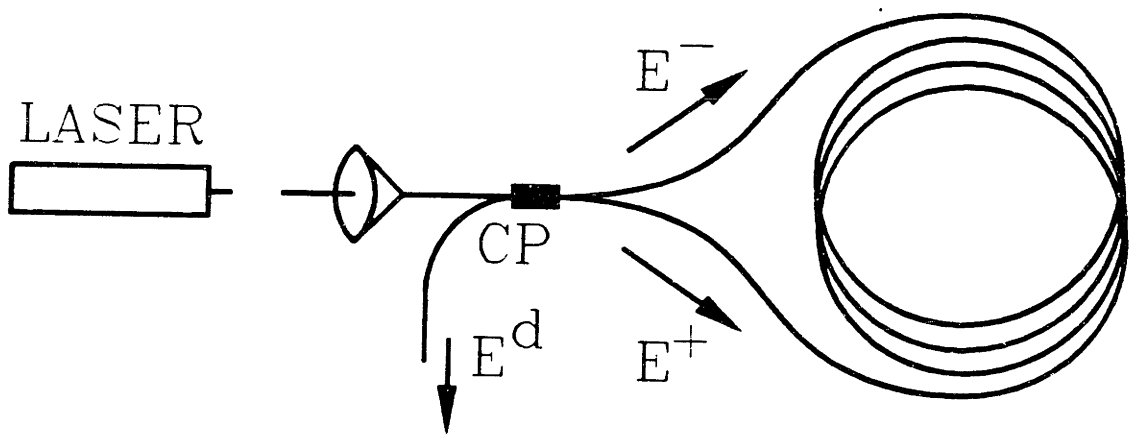

Figure 1.2.3. Example of a fiberoptic Sagnac interferometer.

1.3. The Optical Resonator Gyroscope

Another way of measuring the Sagnac effect is by the use of an optical ring resonator[7,8]. Figure 1.3.1 shows an example of such a resonator consisting of four mirrors, M_1 through M_4, which form a closed square cavity. Light can be coupled into and out of the resonator via the partially transmitting mirrors M_1 and M_2.

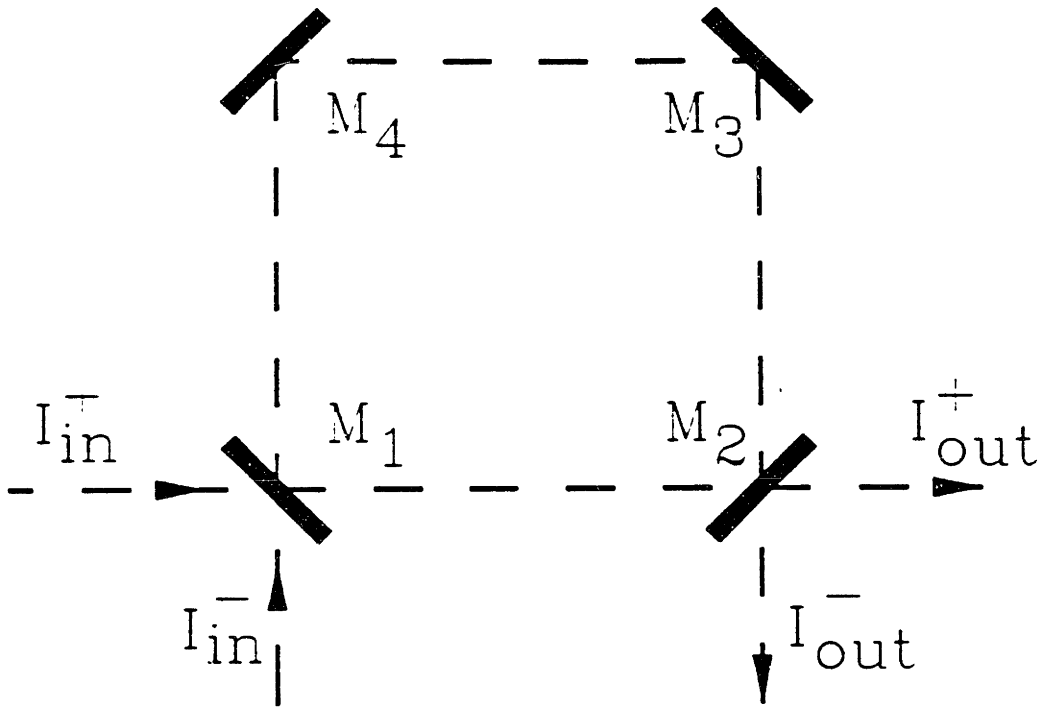

Figure 1.3.1. Example of a bulkoptic ring resonator.

Figure 1.3.2a shows the output along the clockwise and counterclockwise directions of the cavity, as a function of the frequency of the input light, when $\Omega = 0$. The resonance frequencies of the cavity, labeled f_c, are exact multiples of the free spectral range of the cavity, c/P, where P is the perimeter of the cavity, i.e.:

$$f_c = q\frac{c}{P} \tag{1.3.1}$$

where q is the longitudinal mode number associated with a particular cavity resonance. Also indicated in figure 1.3.2a, the clockwise direction of the ring cavity has identical resonance frequencies as the counterclockwise direction, when $\Omega = 0$.

In the presence of rotation, because of ΔP_Ω, there is a separation of Δf_Ω between a counterclockwise resonance frequency f_c^-, and a clockwise resonance frequency f_c^+, as indicated in figure 1.3.2b. Δf_Ω is thus given by:

$$\begin{aligned} \Delta f_\Omega = f_c^- - f_c^+ &= q\frac{c}{P^-} - q\frac{c}{P^+} \\ &= qc\frac{\Delta P_\Omega}{P^+P^-} \\ &= \frac{qc}{P^+P^-}\frac{4A}{c}\Omega \end{aligned} \tag{1.3.2}$$

where P^+ and P^- are the effective perimeters of the ring resonator along the counterclockwise and clockwise directions, respectively. Using the simplification $P^+ \approx P^- = P$, Δf_Ω is given by:

$$\begin{aligned} \Delta f_\Omega &\approx \frac{qc}{P^2}\frac{4A}{c}\Omega \\ &= \frac{f_c}{P}\frac{4A}{c}\Omega \\ &= \frac{4A}{\lambda_\circ P}\Omega \end{aligned} \tag{1.3.3}$$

where $\lambda_\circ$ is the free space wavelength of light with frequency f_c, which is on resonance with the q^{th} longitudinal mode of the cavity.

An optical resonator gyroscope can also be implemented using fiberoptics[9] as shown in figure 1.3.3. It is a straight forward matter to show that Δf_Ω for a fiber ring resonator is given by:

$$\Delta f_\Omega = \frac{4A}{\lambda_\circ nP}\Omega \tag{1.3.4}$$

where n is the index of refraction of the fiber. It should be noted that for a resonator, consisting of N turns wrapped around a cylinder with area A and perimeter P, the total enclosed area is NA and the effective resonator perimeter is NP so that Δf_Ω is given by:

$$\begin{aligned} \Delta f_\Omega &= \frac{4AN}{\lambda_\circ nNP}\Omega \\ &= \frac{4A}{\lambda_\circ nP}\Omega \end{aligned} \tag{1.3.5}$$

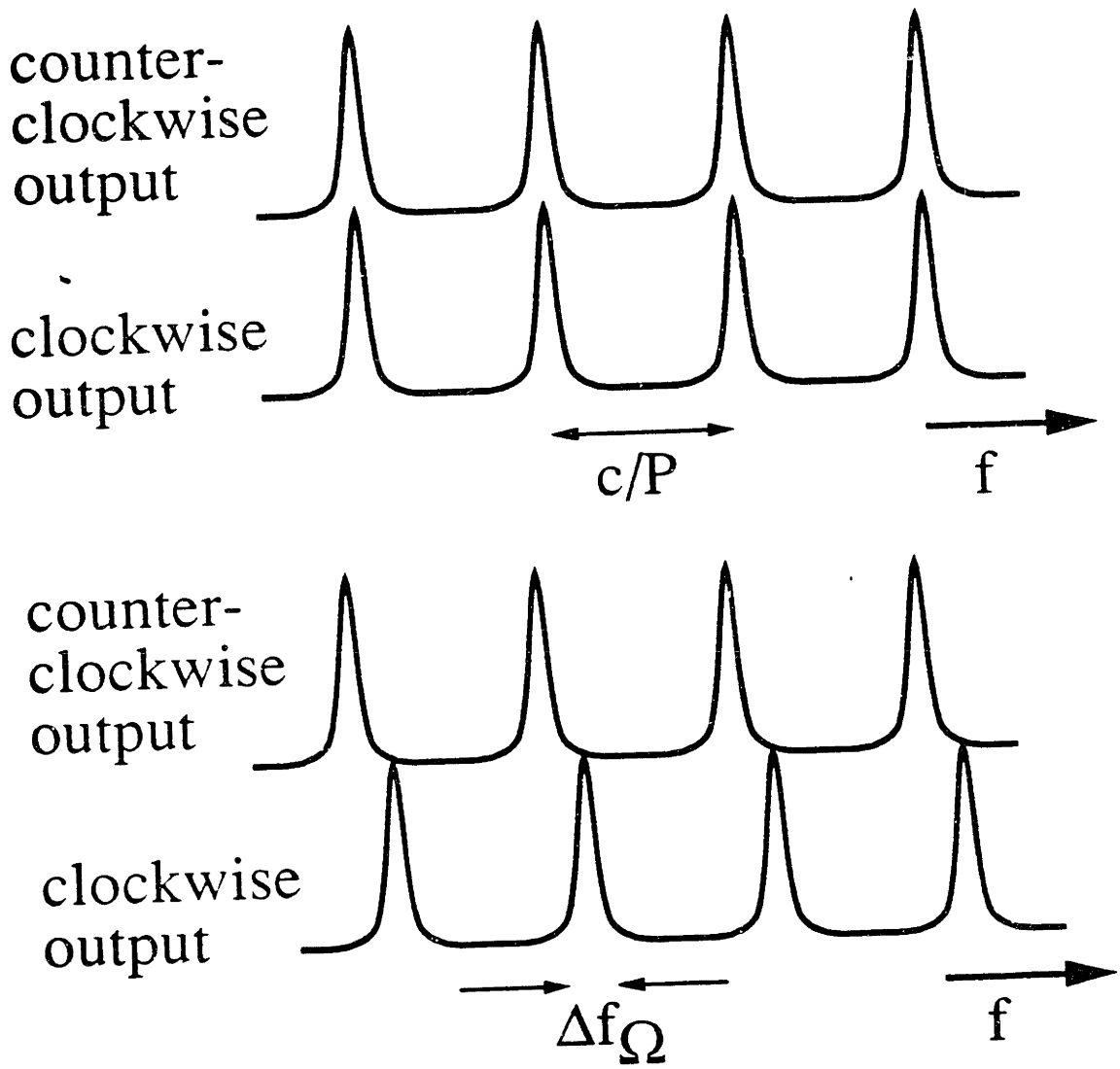

Figure 1.3.2. Clockwise and counterclockwise cavity resonances (a) in the absence of rotation (b) in the presence of rotation indicating a resonance separation of Δf_Ω, due to the Sagnac effect.

which is identical to Δf_Ω for a single-turn resonator in equation 1.3.4. Thus, unlike the

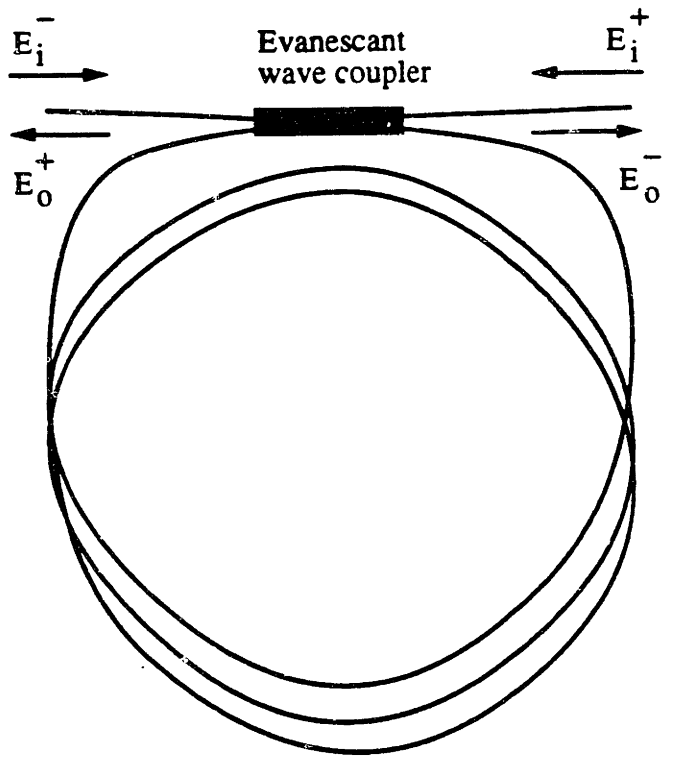

Figure 1.3.3. Example of a fiberoptic ring resonator.

interferometer gyroscope, the scale factor of a resonator gyroscope is independent of N.

There are two ways of measuring Δf_Ω. The first is the active approach, which is based on a ring laser technique[7,10,11] as illustrated in figure 1.3.4. Here, an appropriate optical gain medium is placed inside the ring resonator to produce laser oscillations along the clockwise and counterclockwise directions. Outside of the ring resonator, the outputs of the two lasers are combined to generate a beatnote at Δf_Ω, which is proportional to Ω as indicated in equation 1.3.3. The commercially available Ring Laser Gyroscope (RLG) uses the active approach with a He-Ne gain medium as the optical amplifier.

The second way of measuring Δf_Ω is the passive approach[12,13], which is illustrated in figure 1.3.5. In this approach, there is no lasing action inside the ring resonator, and Δf_Ω is determined by two probing externally generated light beams, E^+ and E^-. The

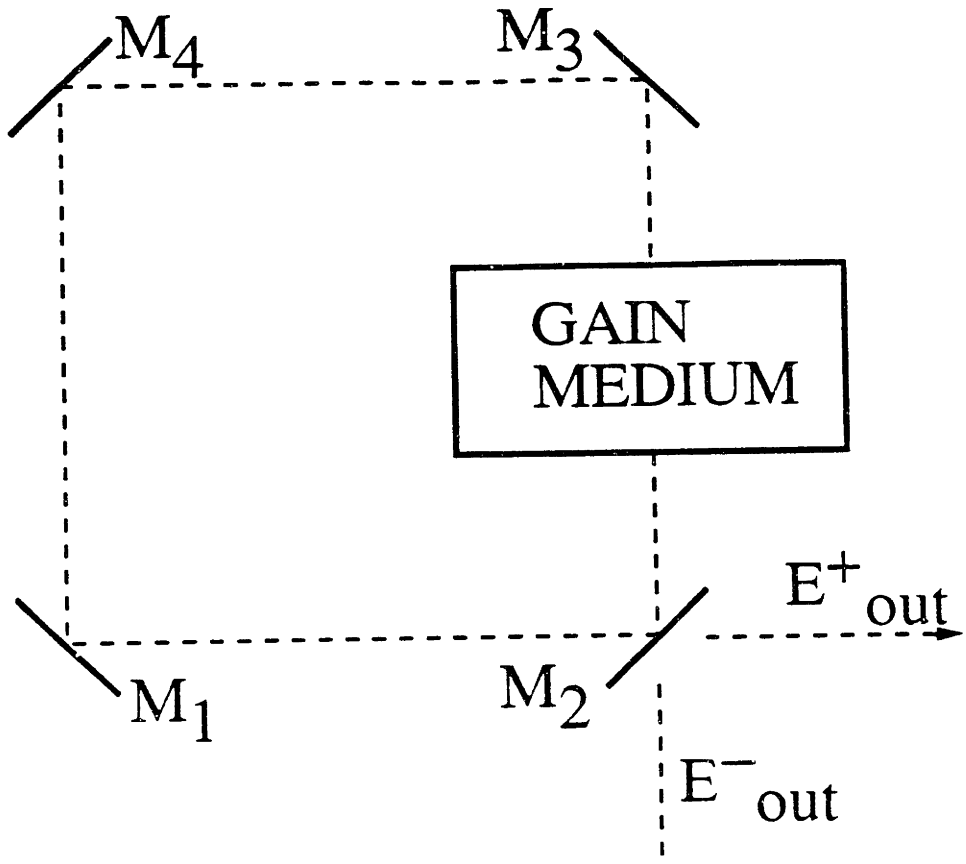

Figure 1.3.4. Illustration of a ring laser gyroscope (RLG)

actual implementation of a passive resonator gyroscope (PRG) is described in detail in chapter 3.

1.4. Thesis Synopsis

In this thesis we will study the behavior of optical ring resonator gyroscopes and the error sources associated with them.

In chapter 2, some of the important considerations in a PRG are described, including the generation of a discriminant and the fundamental noise limit in a PRG.

In chapter 3, we present data on the operation of a bulkoptic PRG. We demonstrate the measurement of rotation in the open loop and closed loop modes of operation, and discuss the gyroscope error sources, which are due to backscattering, state of polarization of the input light, and misalignment of the input beams.

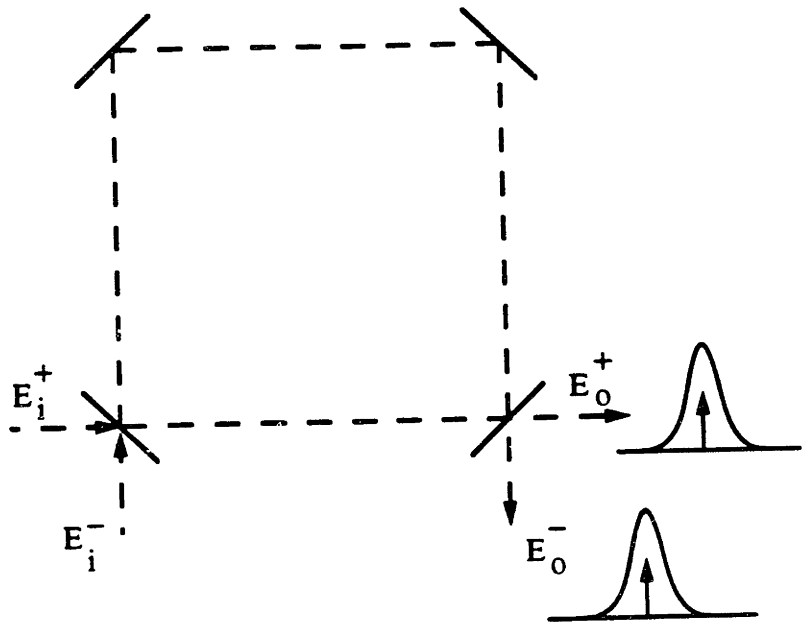

Figure 1.3.5. Illustration of a passive resonator gyroscope (PRG)

In chapter 4, the behavior of a fiberoptic PRG is analyzed. We demonstrate measurement of rotation with this gyroscope, and describe important error sources due to backscattering, state of polarization of light, and the so called optical Kerr effect.

In chapter 5, the first implementation of a fiberoptic ring laser gyroscope (RLG) is demonstrated, which uses the Stimulated Brillouin Scattering as the laser gain medium. We demonstrate the measurement of rotation by this fiberoptic RLG, and discuss some of the error sources associated with it.

Finally, in chapter 6, we present an overall summary and suggestions for future work.

CHAPTER 2

Principles of a Passive Resonator Gyroscope (PRG)

As mentioned in section 1.3, all optical resonator gyroscopes detect rotation rate by measuring the separation between the clockwise and counterclockwise resonance frequencies of the cavity, Δf_Ω, represented either by equation 1.3.3 for a bulkoptic resonator or by equation 1.3.4 for a fiberoptic resonator. In a passive resonator gyroscope (PRG), Δf_Ω is determined by using light generated by a laser source outside of the ring cavity. In this chapter, we describe the generation of the discriminant in a PRG which is used to determine the resonance frequency of the cavity. We also present the fundamental noise limit in a PRG, due to shot noise.

2.1. The Discriminant

The discriminant in a PRG is a signal approximately proportional to the derivative of the cavity output intensity with respect to the frequency of the input light. Thus, when this signal is zero, the frequency of the input light is equal to the effective cavity resonance frequency.

We will now describe the process of generating a discriminant in our PRG. Figure 2.1.1 shows the cavity output, I, along one of the directions of the cavity, as a function of the frequency of the input light, f illustrating the resonance lineshape of the cavity with a center-frequency at f_c. If we set the frequency of light at f_1 and add a small sinusoidal frequency modulation at a rate f_m, we observe a sinusoidal modulation on the cavity output intensity, I with an amplitude approximately proportional to the slope of the resonance lineshape, $\partial I/\partial f$, as indicated in figure 2.1.1. If we now set the frequency of light at f_2, on the other side of the resonance linecenter, we observe a 180° phase shift

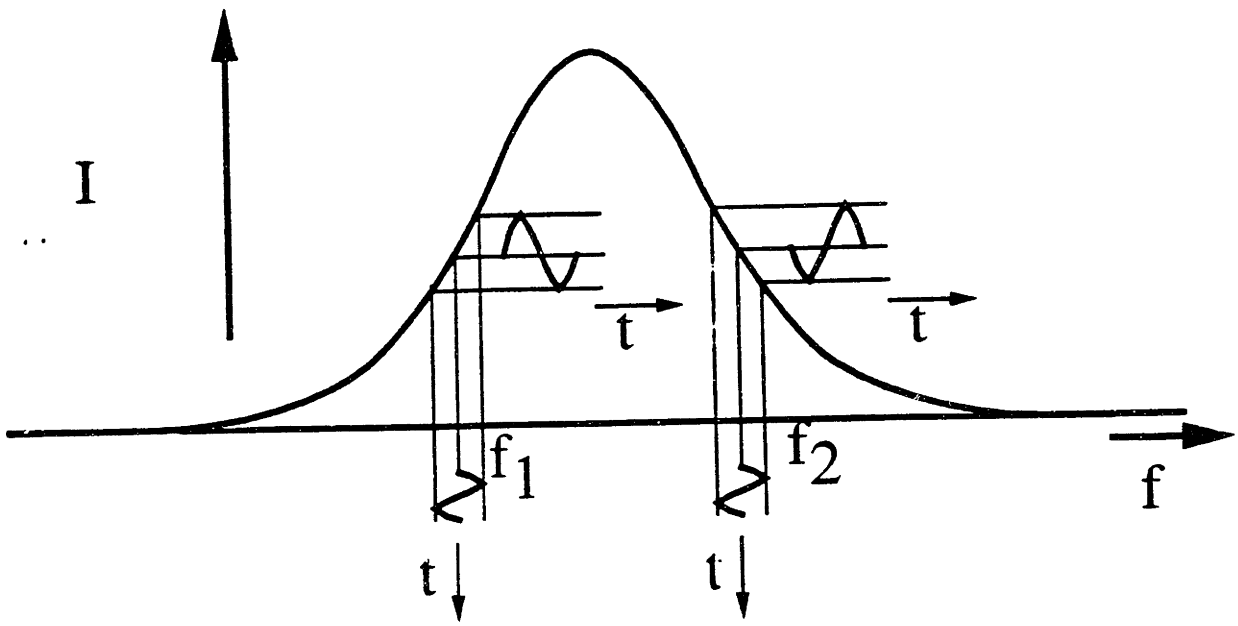

Figure 2.1.1. Illustration of the discriminant modulation technique

in the intensity modulation on I, which is consistent with the change in the sign of the resonance slope, as indicated in figure 2.1.1.

The f_m component in the output intensity is the discriminant. The amplitude of this component is approximately proportional to $|\partial I/\partial f|$, and its phase indicates the sign of $\partial I/\partial f$. Figure 2.1.2a illustrates this discriminant, displayed simultaneously with the unmodulated cavity output (figure 2.1.2b) both as a function of f. As can be seen in figure 2.1.2a, when the laser frequency is at the cavity linecenter the discriminant is zero, and away from the linecenter it is approximately proportional to $\partial I/\partial f$.

2.2. The Fundamental Noise Source in PRG

The fundamental frequency noise in the passive gyroscope is due to the shot noise on the light, which gives rise to a fluctuation of the discriminant voltage.

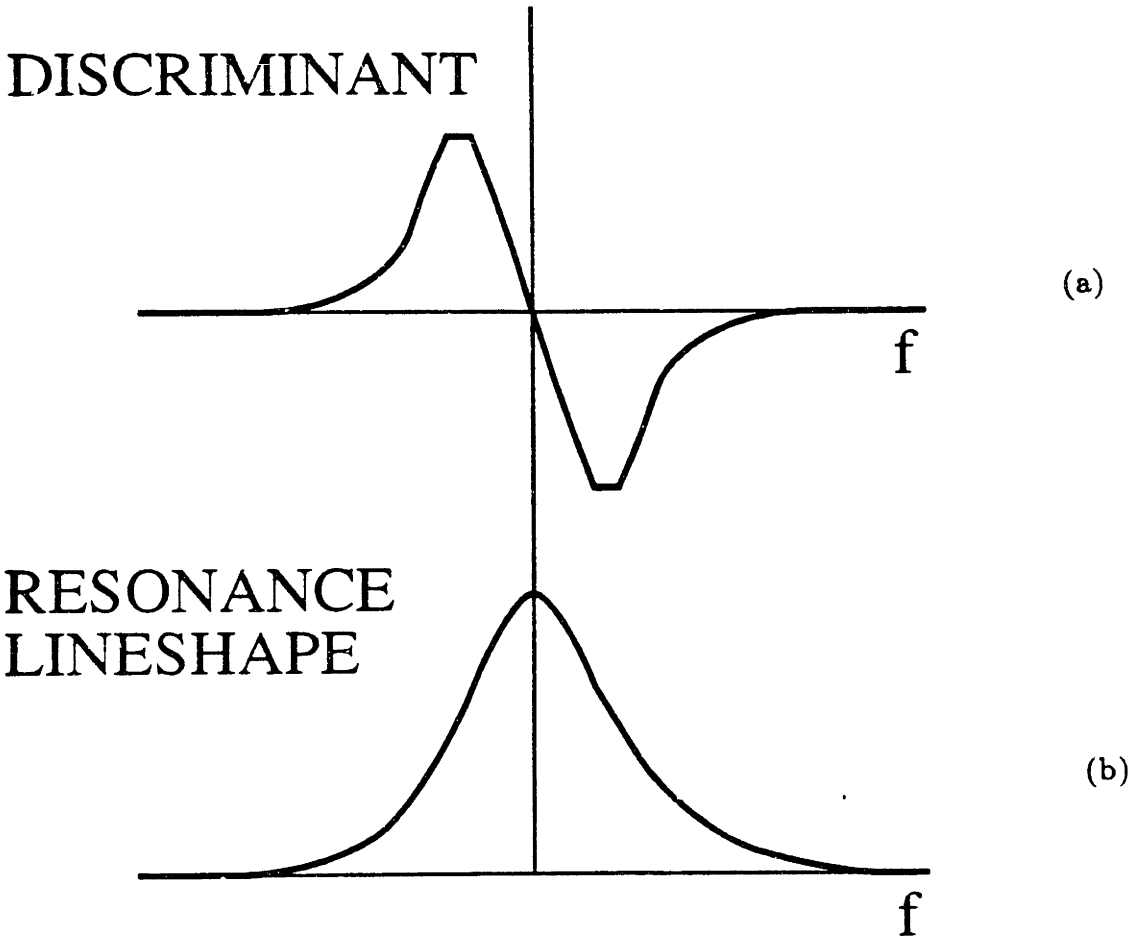

Figure 2.1.2. (a) The discriminant voltage as a function of laser frequency (b) the corresponding cavity output

The shot noise associated with the detection of a light beam by a photodetector can be calculated using a simplified treatment[14]. If the light beam is represented as a stream of photons with an average arrival rate of $\bar{N}_{ph}$, then over a period of time τ, the total number of photoelectrons N_{ph} generated by the photodetector is given by:

$$N_{ph} = \bar{N}_{ph}\eta\tau \tag{2.2.1}$$

where η is the quantum efficiency of the photodetector. If both the time interval between the successive photons and the photon-electron conversion inside the photodetector, follow

a Poisson distribution, then the rms fluctuation in N_{ph}, labeled as δN_{ph}, for an ensemble of samples each taken over a measurement period τ, is given by:

$$\delta N_{ph} = \sqrt{\bar{N}_{ph}\eta\tau} \tag{2.2.2}$$

Thus the inherent signal to noise ratio, SNR, due to shot noise, is given by:

$$\text{SNR} = \frac{N_{ph}}{\delta N_{ph}} = \sqrt{\bar{N}_{ph}\eta\tau} \tag{2.2.3}$$

which indicates that the signal to noise ratio increases with $\sqrt{\tau}$.

The voltage output of the photodetector, labeled V_o, is given by:

$$\begin{aligned} V_o &= Ri_p \\ &= R(\bar{N}\eta e) \end{aligned} \tag{2.2.4}$$

where R is the equivalent resistance of the photodetector, i_p is the photocurrent generated by the photodetector, and e is the electronic charge. The corresponding rms voltage noise of the output of the photodetector is labeled δV_o and is given by:

$$\begin{aligned} \delta V_o = \frac{V_o}{\text{SNR}} &= \frac{Ri_p}{\sqrt{\bar{N}\eta\tau}} \\ &= R\sqrt{\frac{i_p e}{\tau}} \end{aligned} \tag{2.2.5}$$

The shot noise expression in equation 2.2.5, indicates the rms noise voltage of the photodetector around DC, but in a passive gyroscope we are interested in the rms intensity noise obtained from demodulating the detector output at f_m. However, because shot noise is a white noise source, the rms noise obtained from demodulating the detector output at f_m is numerically identical to the rms noise at DC.

The equivalent frequency noise of the gyroscope, δf, is obtained by converting the discriminant voltage noise into frequency using the discriminant slope, κ, as indicated in figure 2.2.1., so that:

$$\delta f = \frac{\sqrt{2}}{\kappa}\delta V_o = \frac{R}{\kappa}\sqrt{\frac{2i_p e}{\tau}} \tag{2.2.6}$$

The factor of $\sqrt{2}$ in equation 2.2.6 is due to the addition of the uncorrelated shot noise of the clockwise and counterclockwise beams. The slope, κ, depends on the modulation parameters and has a maximum of approximately V_o/Γ_c where Γ_c is the full width half maximum linewidth of the cavity. Therefore the frequency error due to shot noise can be given as:

$$\begin{aligned} \delta f &\approx \sqrt{2}\Gamma_c \frac{\delta V_o}{V_o} \\ &\approx \Gamma_c \sqrt{\frac{2e}{i_p \tau}} \end{aligned} \tag{2.2.7}$$

The corresponding rms noise in the measurement of rotation rate, labeled $\delta\Omega$, for a bulkoptic resonator is obtained by dividing δf by the rotation scale factor of the resonator, indicated in equation 1.3.3, i.e.:

$$\begin{aligned} \delta\Omega &= \frac{\lambda_o P}{4A}\delta f \\ &\approx \frac{\lambda_o P \Gamma_c}{4A}\sqrt{\frac{2e}{i_p \tau}} \end{aligned} \tag{2.2.8}$$

and for a fiber optic resonator using equation 1.3.4, $\delta\Omega$ is given by:

$$\delta\Omega \approx \frac{\lambda_o n P \Gamma_c}{4A}\sqrt{\frac{2e}{i_p \tau}} \tag{2.2.9}$$

Thus, $\delta\Omega$ can be reduced by increasing the light intensity i_p, increasing the measurement time τ, and reducing the cavity linewidth Γ_c. In a bulkoptic resonator, Γ_c is given by:

$$\Gamma_c = \frac{FSR}{F} = \frac{c}{PF} \tag{2.2.10}$$

where FSR is the free spectral range of the ring cavity, P is the perimeter of the cavity, and F is the cavity finesse, which is determined by the round-trip cavity loss. Thus in order to reduce Γ_c in a bulkoptic resonator, one must either reduce the round trip cavity loss, which leads to an increase in F, or increase the perimeter of the ring resonator. By contrast, in a fiberoptic ring resonator, Γ_c is given by:

$$\Gamma_c = \frac{FSR}{F} = \frac{c}{n\mathcal{N}PF} \tag{2.2.11}$$

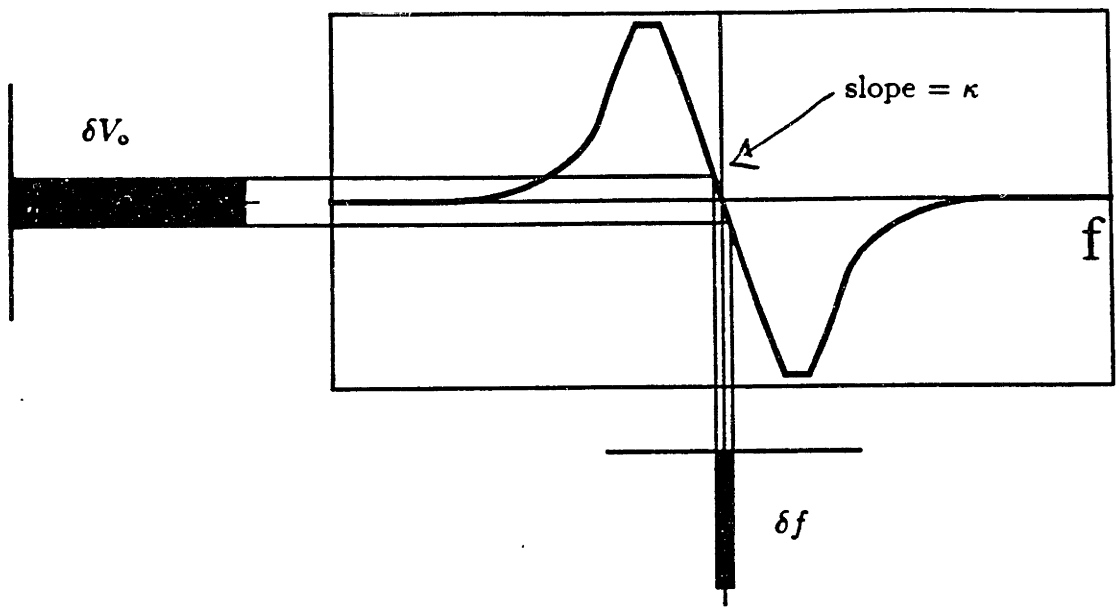

Figure 2.2.1. Conversion of the discriminant voltage noise, δV_o, into an equivalent frequency noise, δf

where n is the index of refraction of the fiber, N is the number of fiber turns in the resonator, and P is the perimeter of a single fiber loop. Thus in a fiber ring resonator with low loss fiber, Γ_c and consequently $\delta\Omega$ can both be reduced by increasing N. This reduction in Γ_c due to N does not affect the rotation scale factor of the resonator, $4A/\lambda_o nP$, which is independent of N.

CHAPTER 3

The Bulkoptic PRG

In this chapter the performance and error sources of a bulkoptic passive resonator gyroscope are presented. First the experimental setup of the gyroscope is described, which includes both the optical and the electronic components. Then, the open loop and closed loop modes of operation of the gyroscope are presented, as well as an analysis of the sources of noise and offset.

3.1. The Experimental Setup

In this section, we present the implementation of a bulkoptic resonator gyroscope[8]. Figure 3.1.1 shows the schematic diagram for the open loop mode of operation. The laser light source in the setup is a Melles Griot 2 mW single transverse mode He-Ne laser with a wavelength of 632.8 nm. The laser oscillates in a single longitudinal mode when the frequency of that mode is near the center of the Ne gain curve. A piezoelectric transducer PZT_L is glued to the side of the laser tube so that by applying a 0-1000 volt to this transducer, the length of the laser cavity can be changed to vary the laser frequency by approximately 80 MHz. To extend the 80 MHz tuning range provided by PZT_L, a 75 Ω resistor, R_L, is also glued to the side of the laser. By driving this resistor the laser cavity can be heated and stretched, thus extending the tuning range of the laser.

As shown in figure 3.1.1, the laser light is split into two beams by the beamsplitter BS. Each beam is passed through an acousto-optic modulator (AO), where it is frequency shifted by an amount equal to the AO drive frequency supplied by an RF oscillator (OSC).

The AO modulators shown in figure 3.1.1 are Coherent model 305A which have a peak efficiency of 80% when driven by a 2 W signal at 40 MHz. The AOs can be tuned from 30 MHz to 53 MHz, which gives a tuning range of 23 MHz.

OSC^-, which provides the drive frequency for AO^-, is a frequency synthesizer (PTS model 160) with 0.1 Hz resolution. The frequency reference of the synthesizer is generated

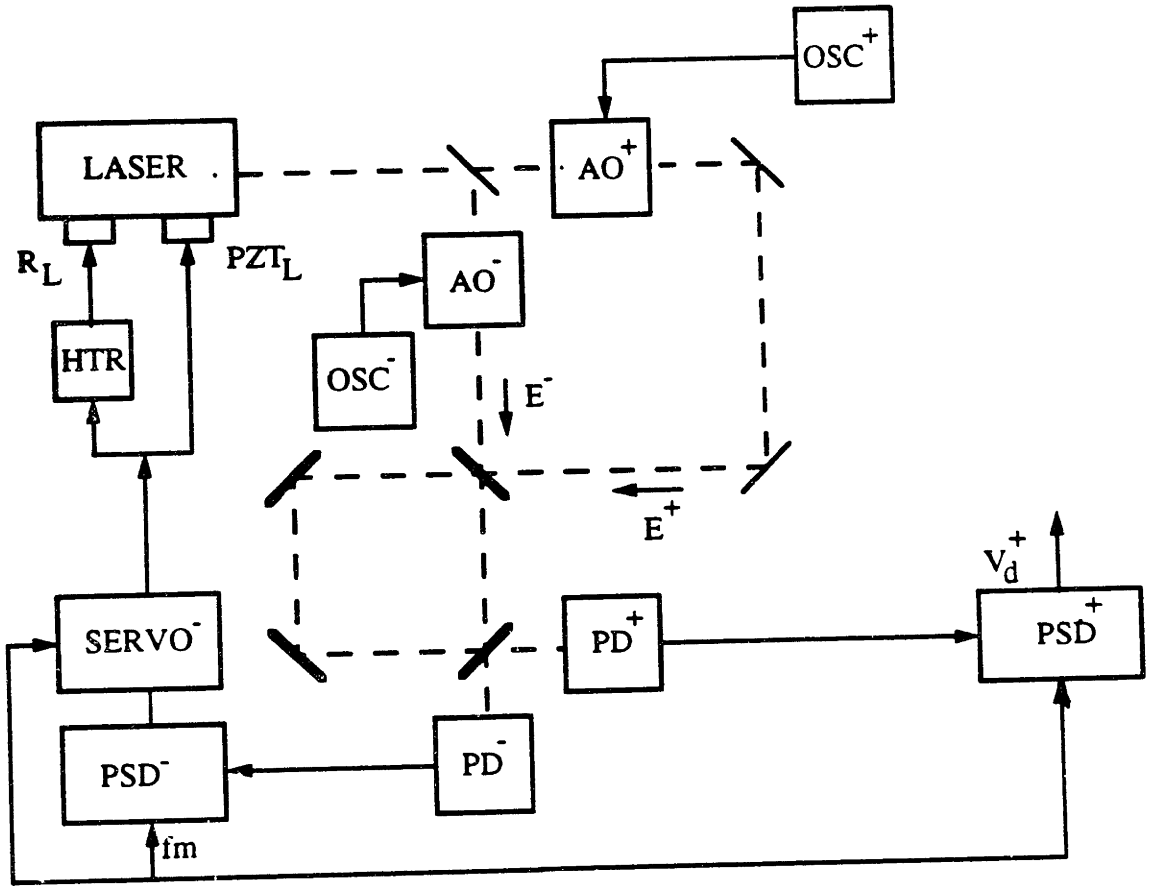

Figure 3.1.1. The experimental setup for the bulkoptic PRG in open loop mode

by an oven stabilized crystal oscillator. OSC^+, which provides the drive frequency for AO^+, is also a frequency synthesizer (General Radio model 1061), using the same reference frequency as OSC^-. The relative drift between the two oscillators is less than 10^{-3} Hz measured during a 20 minute interval. * After being frequency shifted by the AOs, the two beams, which are now labeled E^+ and E^-, are coupled into the cavity, as shown in figure 3.1.1. E^+ is coupled along the counterclockwise direction and E^- is coupled along the clockwise direction. The intensity outputs of the cavity along the clockwise and counterclockwise directions are monitored by photodetectors PD^- and PD^+, respectively.

PD^- and PD^+, which are shown schematically in figure 3.1.2, use EG&G SGD-100A photodiodes, which operate under a 15 volt reverse bias to reduce the diode junction capacitance. The photocurrent from each diode is converted to a voltage by a transconductance amplifier with an equivalent resistance of 500 kΩ and a 3db bandwidth of 400 kHz, as shown in figure 3.1.2.

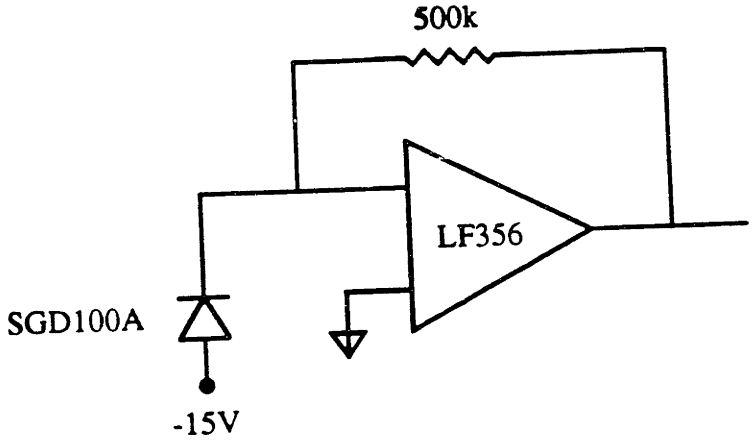

Figure 3.1.2. Schematic diagram for the photodetectors.

A primary feedback loop holds the frequency of E^- at the center of a clockwise cavity resonance by controlling the laser frequency using PZT_L. The operation of the primary feedback loop is based on a discriminant voltage, V_d^-, which is described in section 2.1, and in our case is obtained by FM modulating the laser at a rate f_m and demodulating the output of PD^- by a phase sensitive detector PSD^-, as shown in figure 3.1.1.

PSD^- is a Princeton Applied Research model 124A lockin amplifier, which consists of an input bandpass filter with a manually adjustable center frequency and a variable Q of 1 to 100, followed by a mixer stage with input frequency range of 0.1 Hz to 100 kHz, followed by an output lowpass filter with an adjustable bandwidth, from a maximum of 700 Hz down to a minimum of approximately 5×10^{-4} Hz. The reference modulation frequency, f_m, is generated within PSD^-.

The output of PSD^- drives the electronic circuit, labeled $SERVO^-$, which as shown in figure 3.1.3, contains an integrator stage to boost the low frequency gain of the feedback loop, and a high voltage stage (0-1000 volts) to drive PZT_L. As shown in the integrator stage of $SERVO^-$, 356A type operational amplifiers are used to implement the integrators, where each op amp with feedforward resistors r_f and feedback capacitor c_b acts as a single integrator. By selecting different capacitors from the capacitor bank, the gain of the integrator can be varied. The series addition of a variable potentiometer to the capacitor provides a tunable zero for the integrator. As seen in the high voltage stage of $SERVO^-$, the high voltage amplifier is a single op amp in conjunction with a high voltage transistor SK3115 ($h_{fe} \approx 5$). The modulation frequency, f_m, is added to the signal in this stage as shown in figure 3.1.3. The output of $SERVO^-$ also drives the resistor R_L after an isolation/attenuation stage labeled HTR in figure 3.1.1.

Normally, in the open loop operation of the gyroscope, the frequency of E^+ is set equal to that of E^-. The AO arrangement in our setup is used for diagnostic purposes to introduce a very small but nonzero frequency difference between E^+ and E^-, when required. This means that, in the open loop operation, the frequency of E^+, as well as that of E^-, is held at the center of a clockwise resonance frequency.

The difference between the clockwise and counterclockwise resonance frequencies, Δf_Ω, can now be obtained from the counterclockwise discriminant, V_d^+, which measures the detuning of the frequency of E^+ with respect a counterclockwise cavity resonance frequency. i.e:

$$V_d^+ = \kappa \, \Delta f_\Omega \tag{3.1.1}$$

where κ, as illustrated in figure 2.2.1, is the slope of the discriminant voltage with respect to the frequency of E^+. Thus V_d^+ is proportional to Δf_Ω, which, as indicated by equation 1.3.3, is proportional to the applied rotation Ω. As seen in equation 3.1.1, the open loop operation requires stability of the discriminant slope κ which is influenced by many factors such as the intensity of E^+. In this thesis, we have used open loop operation

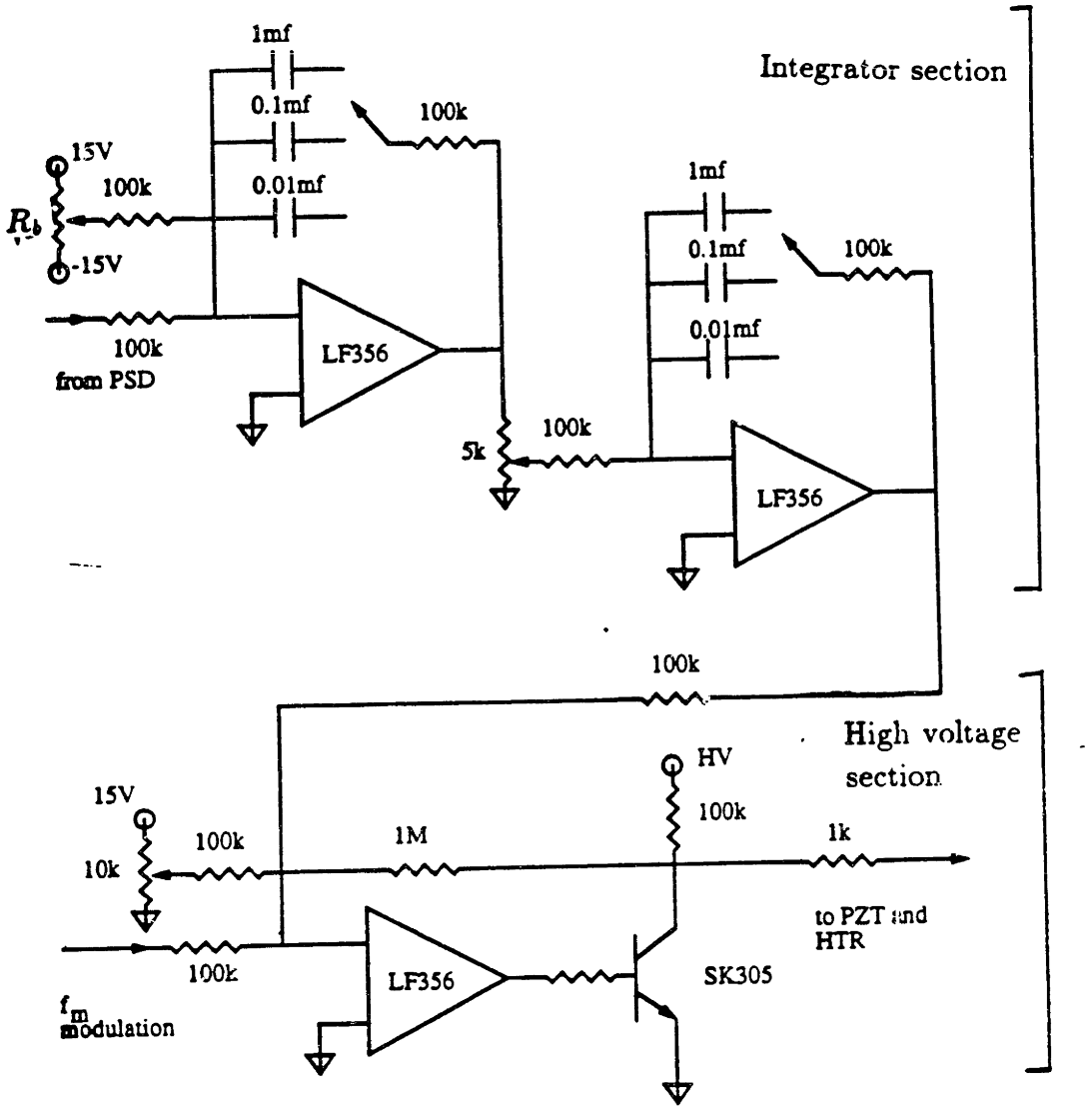

Figure 3.1.3. Schematic diagram for the servo electronics.

as a diagnostic tool to demonstrate error sources, and to determine the performance of the gyroscope under controlled conditions described in section 3.2.5. However, it is clear that open loop operation has limited applications in the precision measurement of angular velocity, and in general we need to use the so-called closed loop mode of operation.

In the closed loop mode of operation, in addition to the primary loop, we have a sec-

ondary feedback loop, which holds the frequency of E^+ at the center of a counterclockwise cavity resonance. Δf_Ω is therefore equal to the frequency difference between the clockwise and counterclockwise beams, and is independent of the slopes of clockwise or counterclockwise discriminants. The schematic of the closed loop setup is shown in figure 3.1.4, where the secondary loop controls the frequency of E^+ by driving the voltage controlled oscillator VCO^+.

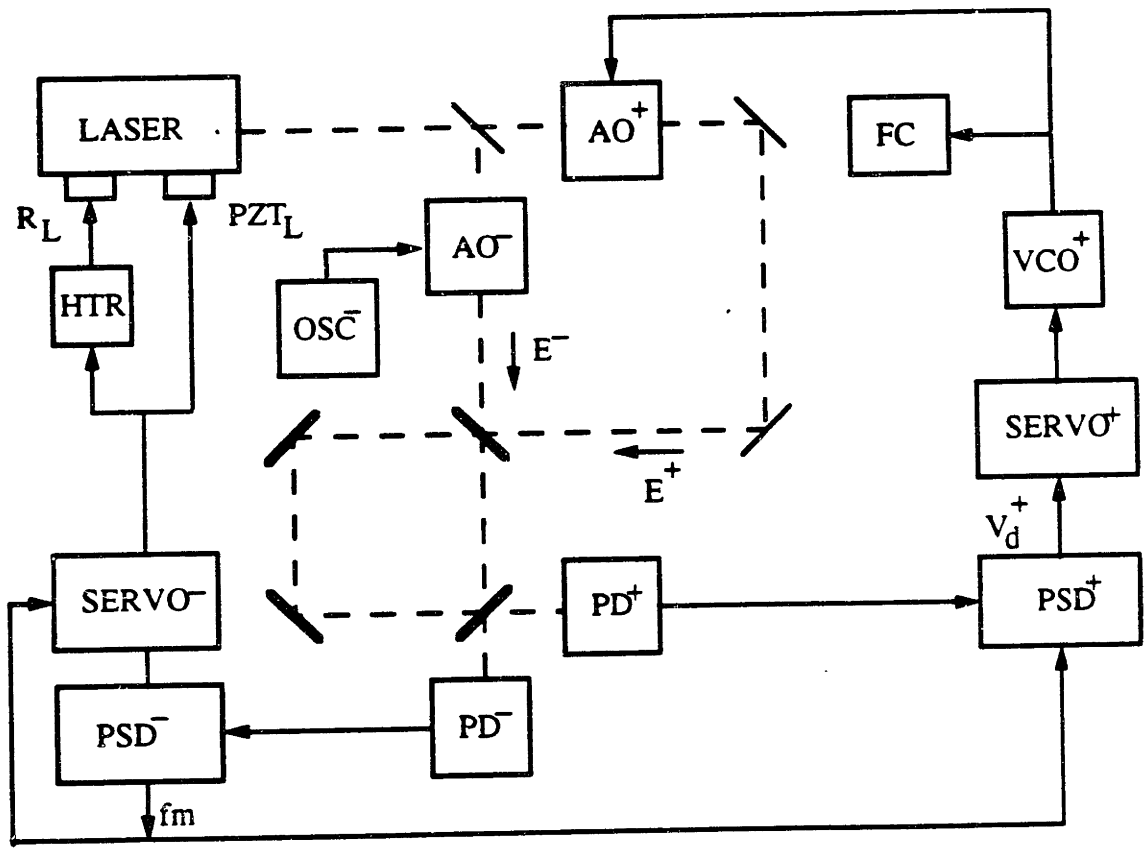

Figure 3.1.4. The experimental setup for the bulkoptic PRG in closed loop mode

3.1.1. The Optical Cavity

Figure 3.1.5 shows the optical cavity used in our experiments. The cavity is made of four highly reflective mirrors mounted on a quartz block (provided by Litton Guidance and Control). Two of the cavity mirrors, M_1 and M_2, are flat, while the other two mirrors, M_3 and M_4, have a radius of curvature of 50 cm. M_1 and M_2 are partially transmitting and are used as input/output ports for the two directions of the cavity. The perimeter of the cavity is 52 cm, corresponding to a FSR of 600 MHz. The cavity resonance frequencies can be tuned approximately 300 MHz by two independent PZTs which translate the curved mirrors of the cavity.

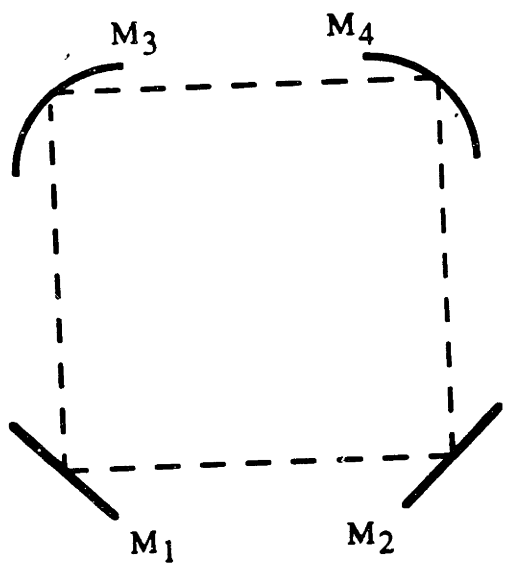

Figure 3.1.5. Illustration of the bulkoptic cavity in the setup.

Figure 3.1.6a shows the resonance lineshape of the cavity as a function of the laser frequency when p polarized (or TM) light, is coupled into the cavity at mirror M_1. The full width at half maximum (FWHM) of the resonance for p polarization is measured to

be 500 kHz corresponding to a finesse of 1200. The peak transmission for p polarization is 10%.

Figure 3.1.6b shows the cavity resonance lineshape for s polarized (or TE) light. This resonance has a FWHM of 35 kHz, corresponding to a cavity finesse of 17000. The peak transmission for s polarization is 2%, which is a factor of 5 smaller than for p polarization.

Figure 3.1.6c shows the output of the cavity when the polarization of the input beam is misaligned with respect to a cavity eigen polarization s or p. As shown in the figure, the narrower s resonance is separated from the wider p resonance by approximately 10 MHz because of the difference in the reflection phase of the cavity mirrors for s and p polarized light.

3.1.2. Performance of the Primary Feedback Loop

As described in the previous section, the primary loop holds the frequency of the beam E^- at the center of a clockwise cavity resonance. The discriminant, V_d^-, used by the primary loop, is generated by modulating the laser frequency at 10 kHz with a modulation excursion of ± 15 kHz. Figure 3.1.7a shows the output of PD^- as a function of the laser frequency, showing the cavity resonance in the presence of this laser modulation. The output of PD^- is then demodulated by PSD^- at 10 kHz, as described in section 3.1. Figure 3.1.7b shows the output of PSD^-, which is the discriminant voltage for clockwise propagation. As indicated previously in section 2.1, the discriminant has a central linear region with zero voltage corresponding to the center of the resonance lineshape.

The primary loop holds the discriminant voltage at zero volts, by appropriately driving the laser frequency. The loop has a phase crossover frequency of approximately 1.5 kHz, and a gain crossover set at 750 Hz, which results in a loop phase margin of 60°. As mentioned in section 3.1, the dynamic range of PZT_L is 80 MHz and the loop will compensate for laser frequency fluctuations within 80 MHz. However, any sudden jumps

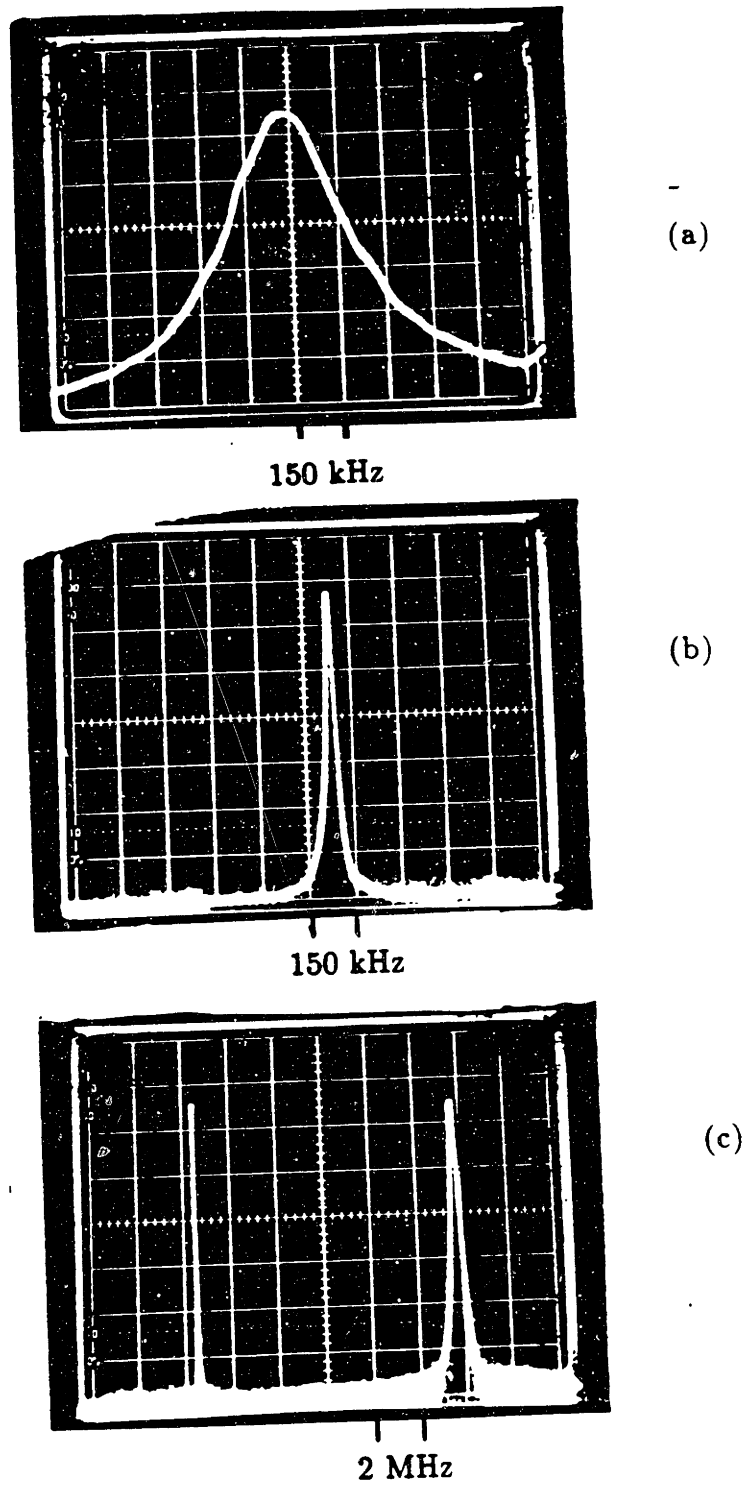

Figure 3.1.6. The resonance lineshapes of the cavity for (a) *p* polarized input (b) *s* polarized input (c) mixed state of polarization.

in the laser frequency of more than the width of the discriminant, or approximately 40

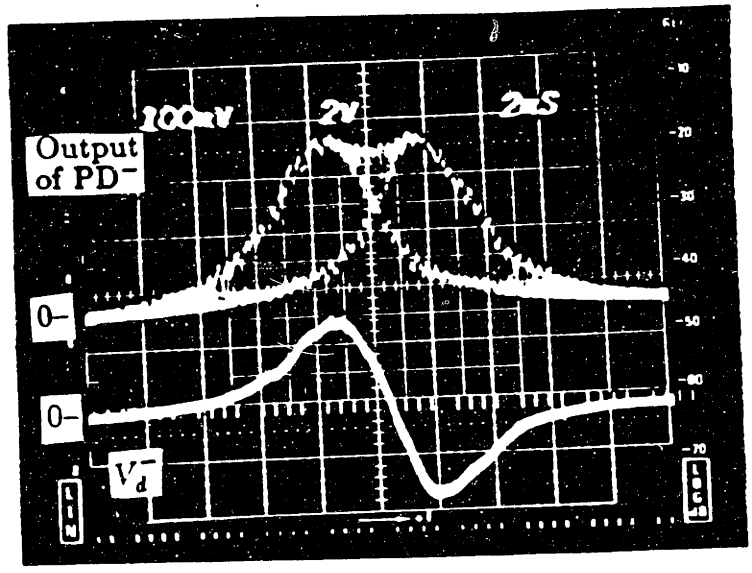

Figure 3.1.7. Generation of the discriminants in the bulkoptic PRG showing the modulated resonance lineshape as a function of the laser frequency (top) the discriminant voltage as a function of the laser frequency (bottom).

kHz, will unlock the loop. No relock circuitry is implemented in this setup.

The residual relative jitter between the laser frequency and the cavity resonance, which is not removed by the primary loop, can be directly observed on V_d^-. Figure 3.1.8a shows V_d^- simultaneously with the output of PD$^-$ as a function of time when the primary loop has only one integrator. PSD$^-$ has a single pole lowpass output filter with a time constant of 160 μs. The residual jitter shown by V_d^- in figure 3.1.8a has a peak to peak value of approximately 14 kHz.

The large peak to peak fluctuation of V_d^- can be reduced by adding a second integrator with a zero at 200 Hz. Figure 3.1.8b shows the output of PD$^-$ and the corresponding V_d^- for the case with two integrators. As can be seen, the peak to peak fluctuations in V_d^- has been reduced to approximately 5 kHz which corresponds to a factor of 3 improvement over the single integrator case. The small improvement in the fluctuation is consistent with the small (order of unity) loop gain contribution of the second integrator at high frequencies.

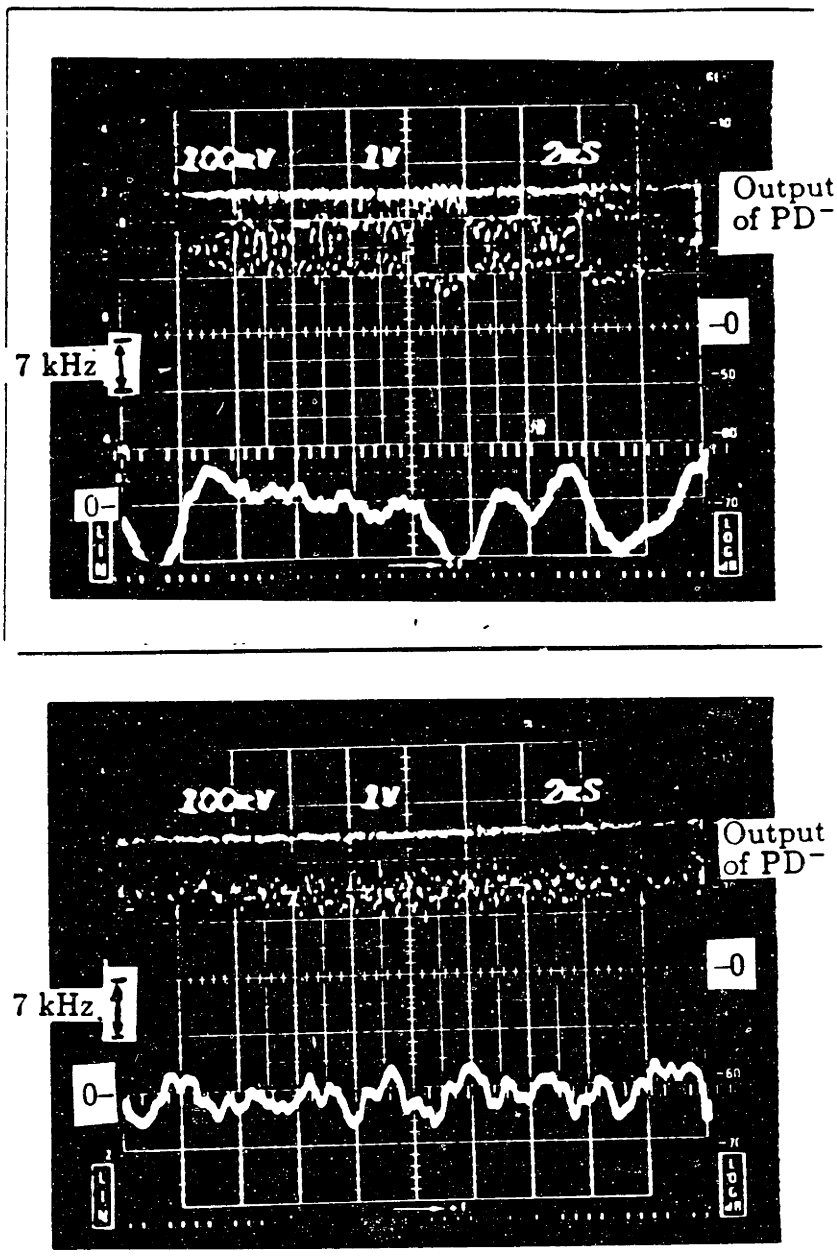

Figure 3.1.8. The behavior of the primary loop with (a) one integrator in the feedback loop (b) with two integrators in the feedback loop. The top trace in each is the output of the photodetector PD^-, and the bottom trace is the residual discriminant voltage V_d^-.

The reduction in the fluctuation of V_d^- is more dramatic at low frequencies. Figure 3.1.9a shows the residual low frequency perturbations of V_d^- for a single integrator feedback loop observed on a separate PSD with a single pole lowpass output filter (time constant=1 sec), demonstrating a peak to peak fluctuation of approximately 1 kHz. Figure 3.1.9b shows the residual low frequency perturbations of V_d^- in the presence of the second integrator, demonstrating a further reduction to 0.4 Hz peak to peak, which is approximately 2000 times lower than in the single integrator case. This reduction is also in agreement with the large increase in the loop gain at low frequencies due to the addition of the second integrator.

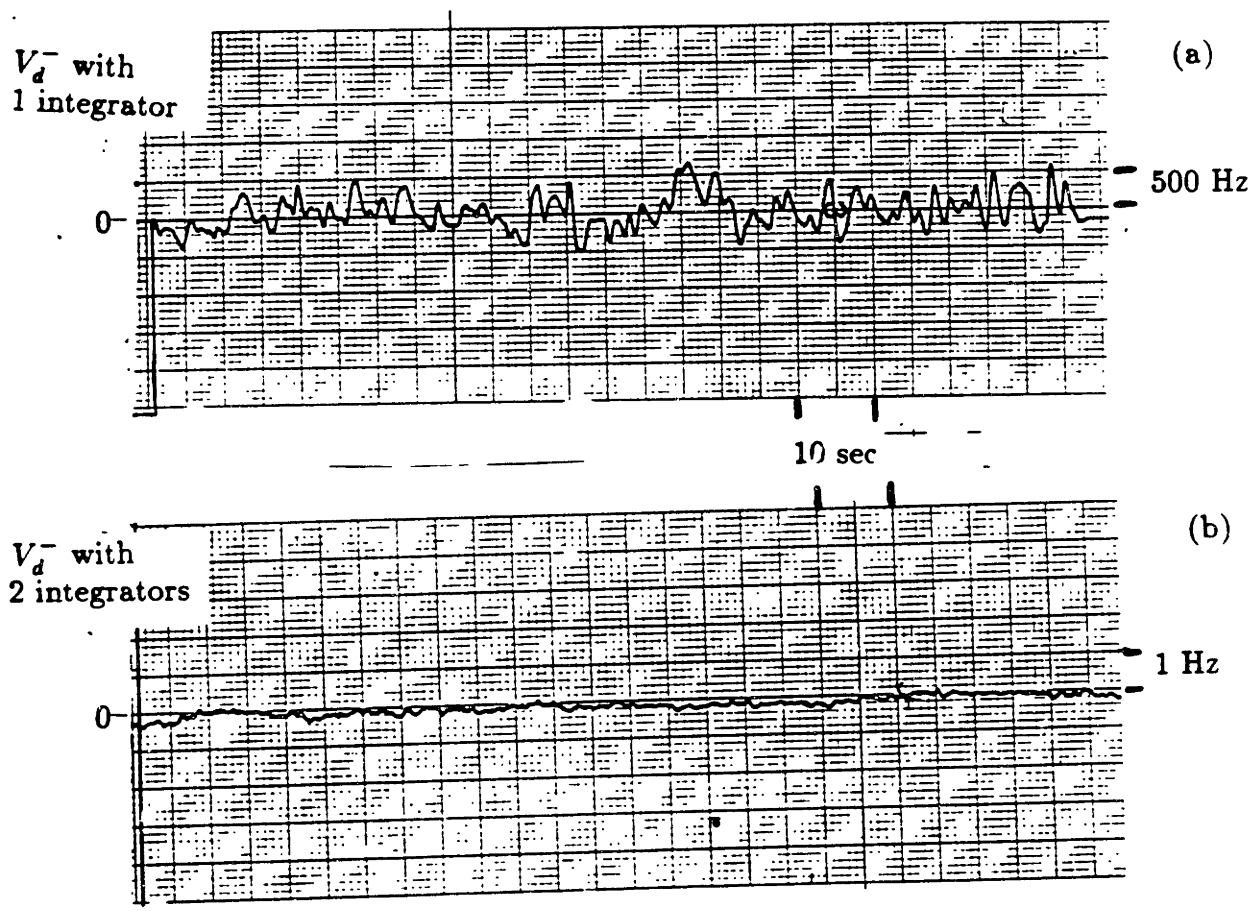

Figure 3.1.9. Low frequency perturbations of V_d^- (a) with one integrator in the loop (b) with two integrators in the loop.

The residual peak to peak noise observed on V_d^- in figure 3.1.9b is the common mode loop tracking error, which can be removed by subtracting V_d^- from V_d^+. This subtraction is

analogous to common mode rejection used in many electronic circuits. Figure 3.1.10 shows the revised schematic of the open loop gyroscope with subtraction, where the outputs of PD^+ and PD^- are subtracted from each other prior to demodulation by PSD^+. This subtraction is done inside PSD^+ and the element A_1 adjusts both the amplitude and the phase of the PD^- output, so that the best subtraction ratio can be achieved. Using subtraction, the 0.4 Hz loop tracking error on the output of the gyroscope can be reduced to 4×10^{-5} Hz by our common mode rejection ratio of approximately 10^4.

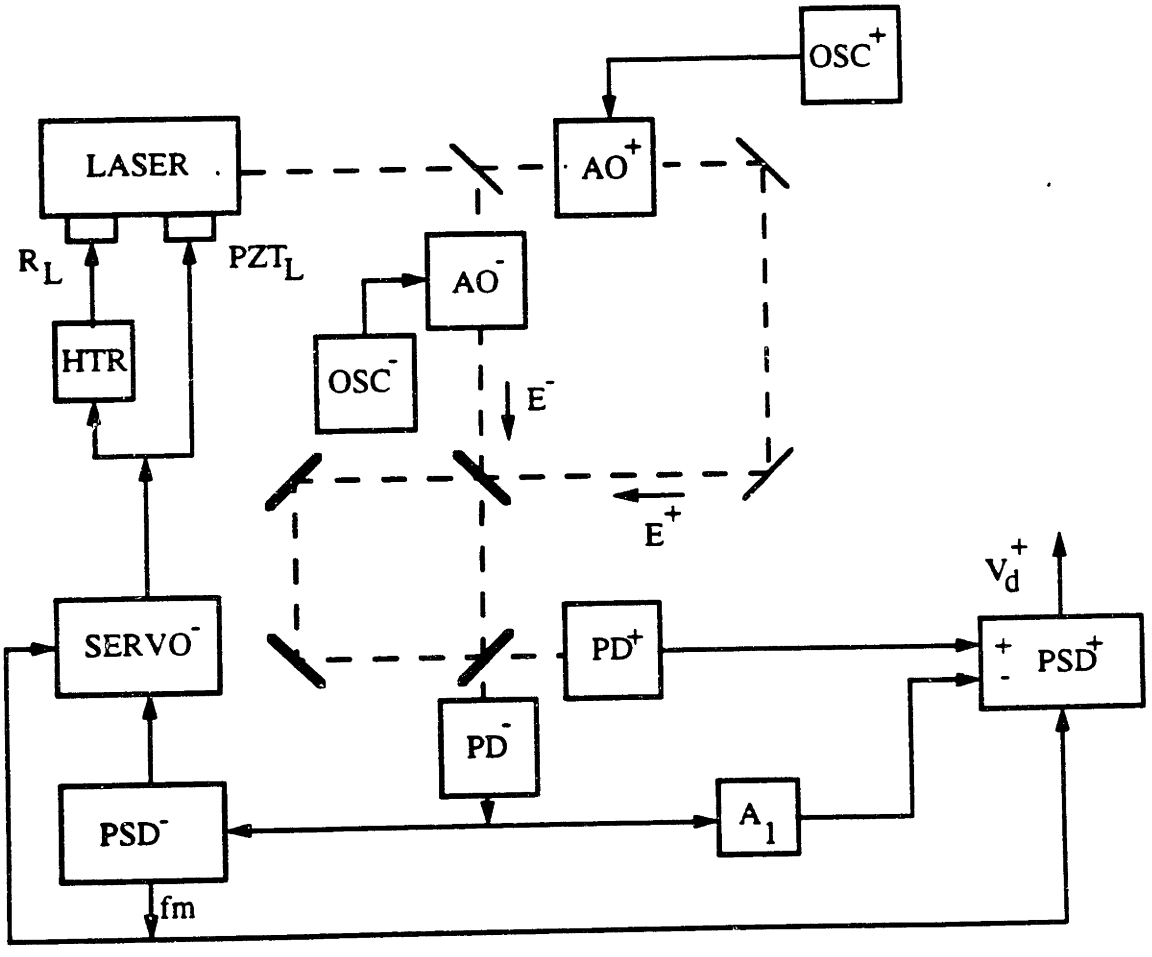

Figure 3.1.10 Revised schematic of the PRG with subtraction

The secondary loop, used in closed loop operation, is similar to the primary loop. The secondary loop has only one integrator because the primary loop compensates for most of the drift between the laser frequency and the cavity resonance. Such drift is common to both clockwise and counterclockwise directions.

3.2. The Open Loop Operation of the PRG

In this section, we will discuss the open loop operation and performance of the bulkoptic PRG. This includes an analysis of the effects of backscattering inside the resonator, and an analysis of the noise and offset of the gyroscope.

3.2.1. Observation of drifts due to Backscattering

We now present the initial gyroscope drift data for the open loop operation, when the clockwise and the counterclockwise beams, E^- and E^+, have the same frequency. Figure 3.2.1a shows V_d^+ as a function of time observed with a 30 ms 6 db/octave output filter, indicating a bounded fluctuation with an equivalent peak to peak amplitude of approximately ± 120 Hz. We now set a 1 Hz frequency difference between E^+ and E^-. Figure 3.2.1b shows V_d^+ as a function of time for the same output filter as that in figure 3.2.1a, demonstrating the transformation of the bounded drifts in figure 3.2.1a, into a 1 Hz oscillation of V_d^+ with an equivalent peak to peak amplitude of ± 120 Hz. Both the drifts of figure 3.2.1a and the oscillation of figure 3.2.1b can be caused by backscattering from scattering centers inside and outside of the cavity, which will be individually discussed in the next two subsections.

a. Internal Scatterers

In order to illustrate the effects due to a scatterer inside the ring cavity, let us consider a ring cavity with a clockwise intracavity beam E_r^-, a counterclockwise beam E_r^+, and a single scatterer located at point S on the mirror M_1, as shown in figure 3.2.2. At S, a

The secondary loop, used in closed loop operation, is similar to the primary loop. The secondary loop has only one integrator because the primary loop compensates for most of the drift between the laser frequency and the cavity resonance. Such drift is common to both clockwise and counterclockwise directions.

3.2. The Open Loop Operation of the PRG

In this section, we will discuss the open loop operation and performance of the bulkoptic PRG. This includes an analysis of the effects of backscattering inside the resonator, and an analysis of the noise and offset of the gyroscope.

3.2.1. Observation of drifts due to Backscattering

We now present the initial gyroscope drift data for the open loop operation, when the clockwise and the counterclockwise beams, E^- and E^+, have the same frequency. Figure 3.2.1a shows V_d^+ as a function of time observed with a 30 ms 6 db/octave output filter, indicating a bounded fluctuation with an equivalent peak to peak amplitude of approximately ± 120 Hz. We now set a 1 Hz frequency difference between E^+ and E^-. Figure 3.2.1b shows V_d^+ as a function of time for the same output filter as that in figure 3.2.1a, demonstrating the transformation of the bounded drifts in figure 3.2.1a, into a 1 Hz oscillation of V_d^+ with an equivalent peak to peak amplitude of ± 120 Hz. Both the drifts of figure 3.2.1a and the oscillation of figure 3.2.1b can be caused by backscattering from scattering centers inside and outside of the cavity, which will be individually discussed in the next two subsections.

a. Internal Scatterers

In order to illustrate the effects due to a scatterer inside the ring cavity, let us consider a ring cavity with a clockwise intracavity beam E_r^-, a counterclockwise beam E_r^+, and a single scatterer located at point S on the mirror M_1, as shown in figure 3.2.2. At S, a

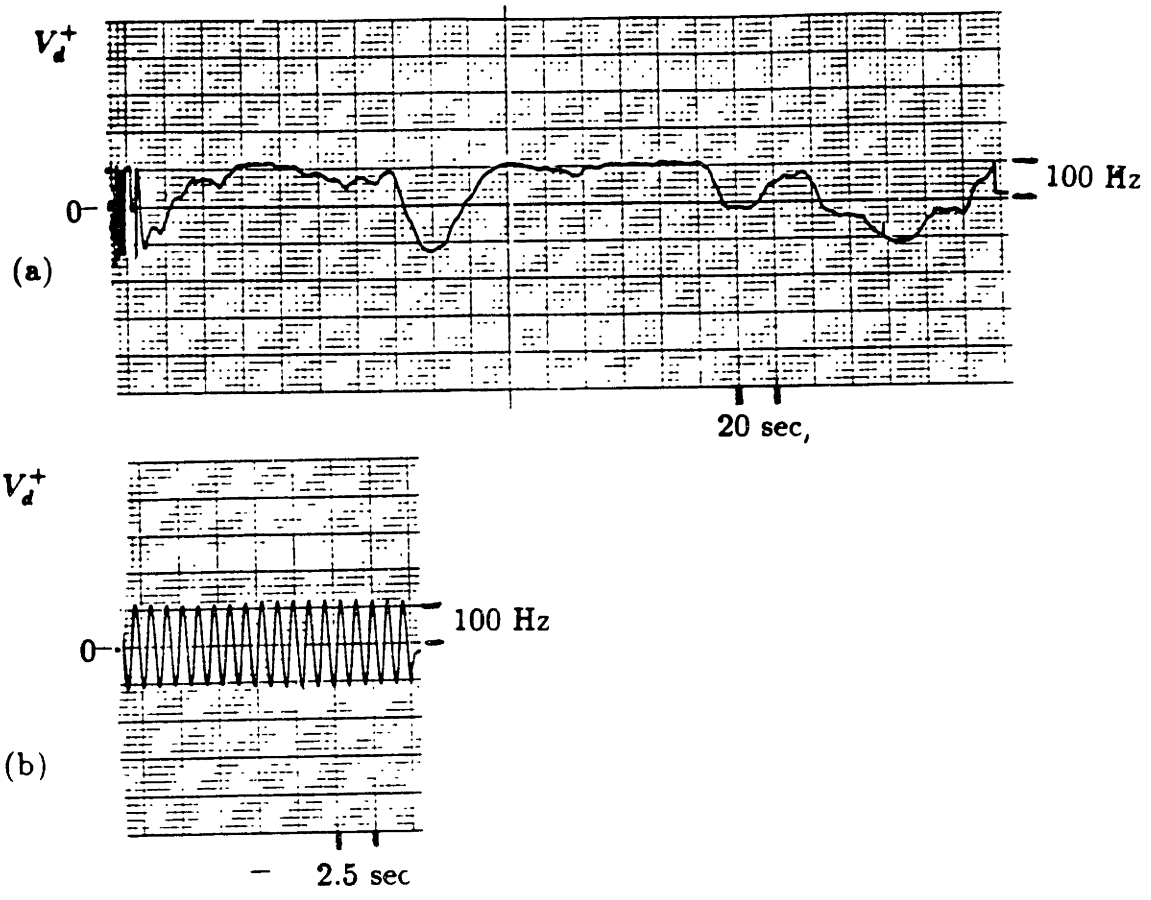

Figure 3.2.1. Bounded variations of V_d^+ due Observed backscattering when (a) E^+ and E^- have the same frequency (b) E^+ and E^- have a 1 Hz frequency difference

fraction of E_r^+, $\alpha^- E_r^+$, is scattered along E_r^-, and similarly a fraction of E_r^-, $\alpha^+ E_r^-$ is scattered along E_r^+. The injection of $\alpha^+ E_r^-$ along E_r^+ will generate an effective scattered field, E_s^+, propagating along the same direction as that of E_r^+, which is given by:

$$E_s^+ = \alpha^+ E_r^- \tag{3.2.1}$$

Figure 3.2.3 shows the vector addition of E_s^+ and E_r^+, which perturbs the phase of E_r^+ by $\Delta\phi_s^+$, given by:

$$\begin{aligned} \Delta\phi_s^+ &= \frac{E_s^+}{E_r^+} \sin(\Delta\phi) \\ &= \frac{\alpha^+ E_r^-}{E_r^+} \sin(\Delta\phi) \end{aligned} \tag{3.2.2}$$

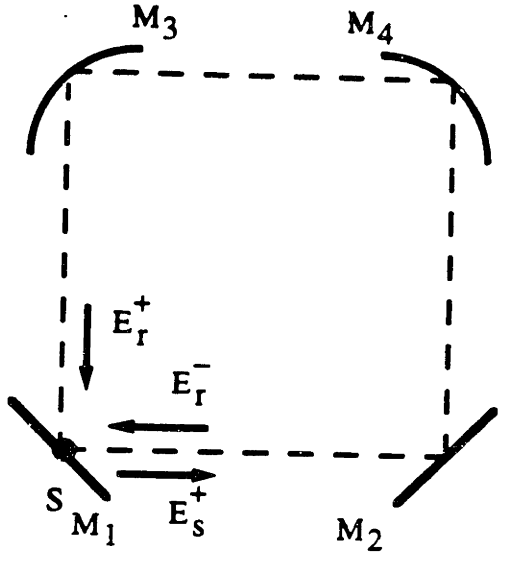

Figure 3.2.2. Illustration of the backscattering due to a single scatterer, S, inside the ring cavity

where $\Delta\phi$ is the difference between the optical phase of E_r^- and E_r^+ at point S.

The phase $\Delta\phi_s^+$ is added to the round trip phase of E_r^+, and results in a change in the counterclockwise resonance frequency of the cavity by an amount Δf_s^+, given by the expression:

$$\begin{aligned}\Delta f_s^+ &= -\frac{FSR}{2\pi}\Delta\phi_s^+ \\ &= -\frac{FSR}{2\pi}\frac{\alpha^+ E_r^-}{E_r^+}\sin(\Delta\phi)\end{aligned} \tag{3.2.3}$$

Similarly, we can obtain an expression for the perturbation in the phase of E_r^-, labeled $\Delta\phi_s^-$, which is given by:

$$\Delta\phi_s^- = \frac{\alpha^- E_r^+}{E_r^-}\sin(-\Delta\phi) \tag{3.2.4}$$

where $-\Delta\phi$ is the difference between the optical phase of E_r^+ and E_r^-. The phase shift $\Delta\phi_s^-$ causes a shift in the clockwise resonance frequency by an amount Δf_s^- given by:

$$\begin{aligned}\Delta f_s^- &= -\frac{FSR}{2\pi}\Delta\phi_s^- \\ &= \frac{FSR}{2\pi}\frac{\alpha^+ E_r^-}{E_r^+}\sin(-\Delta\phi)\end{aligned} \tag{3.2.5}$$

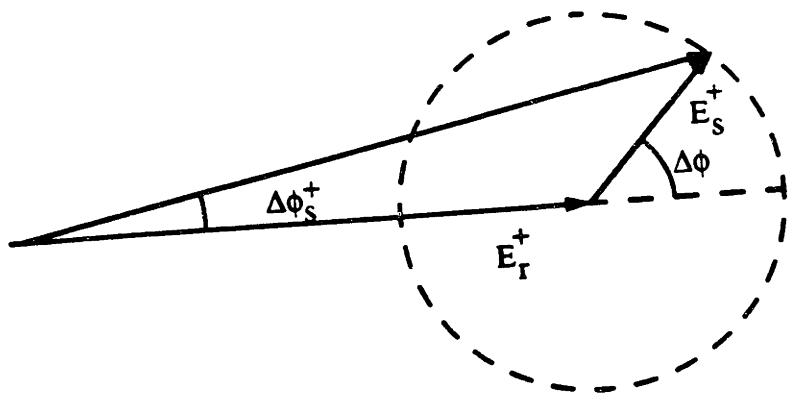

Figure 3.2.3. Illustration of the phase perturbation $\Delta\phi_s^+$ on E_r^+ due to backscattering

Thus, the overall separation between the clockwise and counterclockwise resonance frequencies due to backscattering, labeled as Δf_s, is given by the difference between Δf_s^- and Δf_s^+, i.e.:

$$\begin{aligned}\Delta f_s &= \Delta f_s^- - \Delta f_s^+ \\ &= \frac{FSR}{2\pi}\left(\frac{\alpha^+ E_r^-}{E_r^+} + \frac{\alpha^- E_r^+}{E_r^-}\right)\sin(\Delta\phi) \\ &= \gamma_s \sin(\Delta\phi)\end{aligned} \tag{3.2.6}$$

where:

$$\gamma_s = \frac{FSR}{2\pi}\left(\frac{\alpha^+ E_r^-}{E_r^+} + \frac{\alpha^- E_r^+}{E_r^-}\right)\sin(\Delta\phi) \tag{3.2.7}$$

which shows that Δf_s is proportional to $\sin(\Delta\phi)$ and thus proportional to the interference beatnote between E_r^+ and E_r^-. Therefore, this backscattering error is referred to as the coherent backscattering effect.

b. External scatterers

We now consider the effect of a single external scatterer S_e with a field reflection coefficient of α_e^+ as shown in figure 3.2.4. Following the treatment presented in section 3.2.1, we can determine the perturbations in the resonance frequencies along the clockwise and counterclockwise directions due to this scatterer, i.e. Δf_{se}^- and Δf_{se}^+. In order to determine Δf_{se}^+, we must first determine the scattered field E_{se}^+. This field is calculated by first coupling E_r^- out of the resonator via mirror M_1. The corresponding output field is given by tE_r^-, where t is the transmission coefficient of the mirror M_1. The field tE_r^- subsequently scatters from S_e so as to yield $\alpha_e^+ tE_r^-$. This field is then coupled back into the resonator, resulting in an intracavity scattering field E_{se}^+, which is given by:

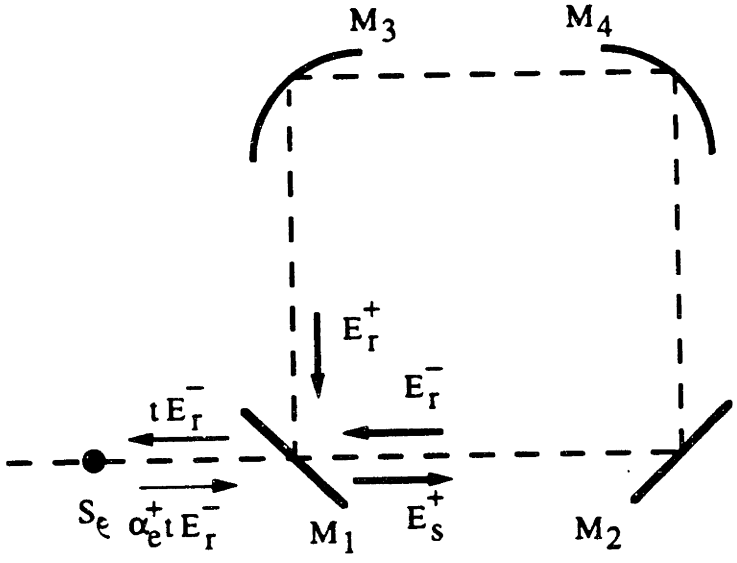

Figure 3.2.4. Illustration of the backscattering due to a single scatterer, S_e, outside of the ring cavity

$$\begin{aligned} E_{se}^+ &= \alpha_e^+ t^2 E_r^- \\ &= \frac{\pi}{F} \alpha_e^+ E_r^- \end{aligned} \tag{3.2.8}$$

where $t^2 \approx \pi/F$, and F is the finesse of the resonator. Similar to the case in equation 3.2.2, the counterclockwise scattering phase perturbation $\Delta\phi^+_{se}$ is given by:

$$\begin{aligned}\Delta\phi^+_{se} &= \frac{E^+_{se}}{E^+_r}\sin(\Delta\phi + \phi^+_e) \\ &= \frac{\pi}{F}\frac{\alpha^+_e E^-_r}{E^+_r}\sin(\Delta\phi + \phi^+_e)\end{aligned} \tag{3.2.9}$$

where ϕ^+_e is twice the propagation phase delay from the mirror M_1 to the scatterer S_e, a^+_e is the amplitude of the phase perturbation due to external backscattering along counterclockwise direction, and $\Delta\phi$ is the phase difference between the clockwise beam and the counterclockwise beams at the mirror M_1. By comparing equation 3.2.1 and 3.2.8 we observe that if an internal and an external scatterer have the same scattering coefficient α, the backscattering phase perturbation due to the internal scatterer is a factor of F/π larger than that due to the external scatterer. The perturbation in the counterclockwise resonance frequency is thus given by:

$$\Delta f^+_{se} = -\frac{FSR}{2\pi}\frac{\pi}{F}\frac{\alpha^+_e E^-}{E^+}\sin(\Delta\phi + \phi^+_e) \tag{3.2.10}$$

The backreflection from S_e does not perturb the clockwise resonance frequency, so that $\Delta f^-_{se} = 0$.

A similar argument can be constructed for an external scatterer along the clockwise direction, which yields:

$$\Delta f^-_{se} = -\frac{FSR}{2\pi}\frac{\pi}{F}\frac{\alpha^-_e E^+}{E^-}\sin(-\Delta\phi + \phi^-_e) \tag{3.2.11}$$

and in this case $\Delta f^+_s = 0$.

Thus, we have demonstrated that for external scatterers, both Δf^+_{se} and Δf^-_{se} vary sinusoidally with $\Delta\phi$, however, they do not have the same amplitude, and in general have a phase difference determined by the location of the external scatterers.

In figure 3.2.1b we measured the amplitude of the coherent backscattering, i.e. γ_s, to be 120 Hz. As mentioned before, internal scatterers are more effective than external

scatterers by a factor of F/π. This factor is $17000/\pi = 6000$ [for s polarization in our case]. Thus, the observed coherent backscattering in figure 3.2.1b is most probably due to internal scatterers. By using equation 3.2.7, we estimate an internal backscattering coefficient to be approximately 6×10^{-7}.

Also, in addition to coherent backscattering errors, we can have intensity backscattering errors, which are due to the intensity of the backscattered light. In our case, we have not been able to observe such intensity effects for a bulkoptic PRG; however, they are a very important error source in a fiberoptic PRG, as described later in section 4.2.3.

3.2.2. Elimination of the Drifts due to Backscattering

In the previous section, we observed the coherent backscattering error in the open loop operation of the PRG. Here, we will demonstrate the suppression of the coherent backscattering error by a sinusoidal phase modulation of E^+, using an electrooptic phase modulator, EO (coherent model 28), as shown in the revised schematic of the setup in figure 3.2.5.

We now demonstrate the suppression of coherent backscattering in our setup. We apply a sinusoidal phase modulation to E^+ with a modulation frequency, f_j, of 50 Hz and a variable phase amplitude of $\delta\phi_j$. The bottom trace of figure 3.2.6 shows the peak to peak amplitude of this applied phase modulation, indicating a stepwise increase in $\delta\phi_j$ from 0 to 3.6 rad. The top trace of the figure is V_d^+ as a function of time with a 30 ms 6db/octave filter, showing the coherent backscattering error for a 2 Hz frequency difference between E^+ and E^-. Sections A through F present the gradual suppression of the coherent backscattering as $\delta\phi_j$ is increased from 0 (section A) to 2.4 rad (section E). Section E demonstrates the complete removal of coherent backscattering. In section F, $\delta\phi_j$ is increased to 3.6 rad, and the coherent backscattering reappears.

We now use a simple model to explain the removal of the coherent backscattering using phase jitter. Figure 3.2.7a shows the spectra of E^+ and E^-, which in the absence of phase jitter, indicate delta functions at optical frequencies, f_o^+ and f_o^-, respectively.

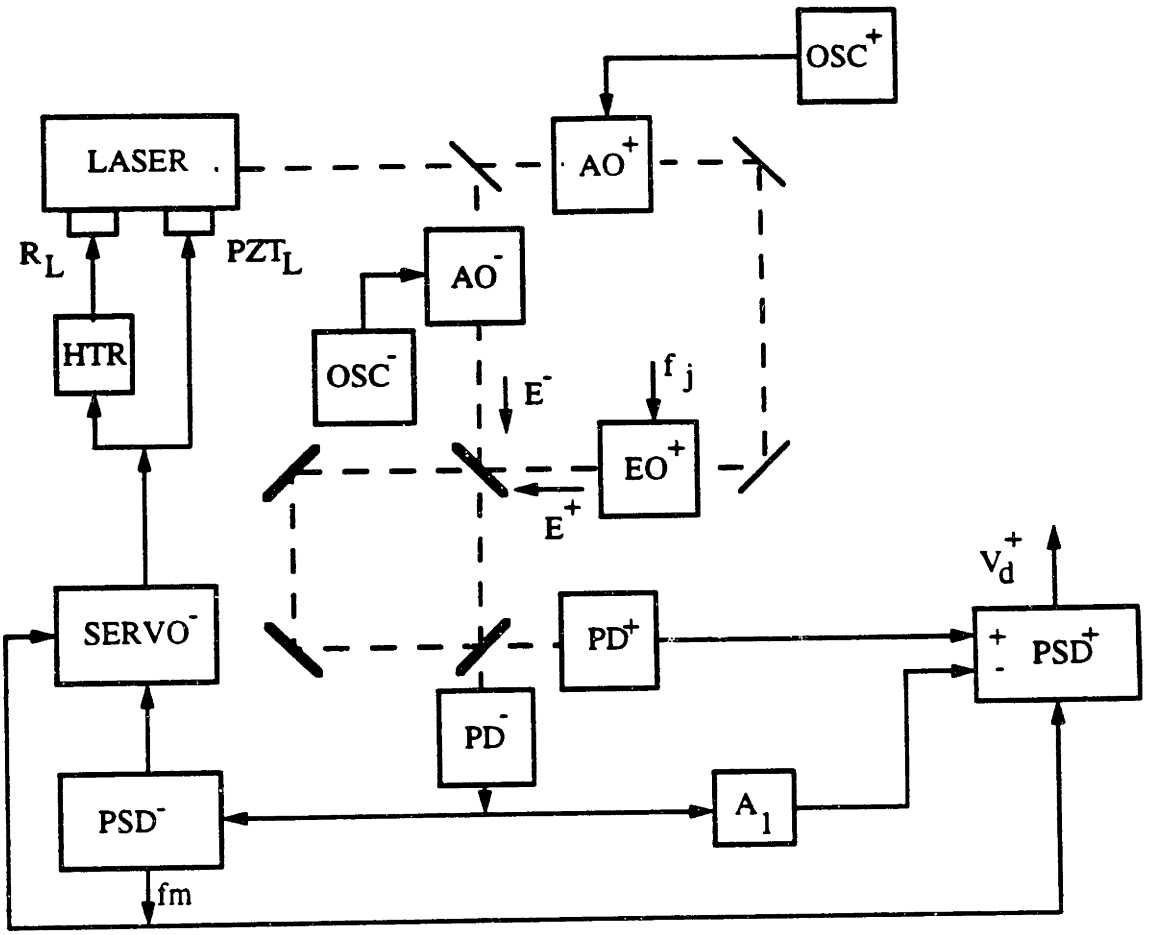

Figure 3.2.5. The schematic setup for open loop operation with an EO phase modulator

As indicated in equation 3.2.7, the coherent backscattering is proportional to $\sin(\Delta\phi)$, which in this case is a sinusoidal variation representing the beatnote between the two delta functions in figure 3.2.7a. Figure 3.2.7b shows the spectra of E^+ and E^- in the presence of a phase jitter, clearly indicating sidebands of E^+ at $f_o^+ + mf_j$. The amplitude of the m^{th} sideband of E^+ is given by $J_m(\delta\phi_j)$, where J_m is the m^{th} order Bessel function of the first kind. The coherent backscattering is now represented by the sum of the beatnotes between E^- and each of the sidebands of E^+. All of these beatnotes are at harmonics of f_j and are removed by lowpass filtering, except for the original beatnote between E^- and the carrier

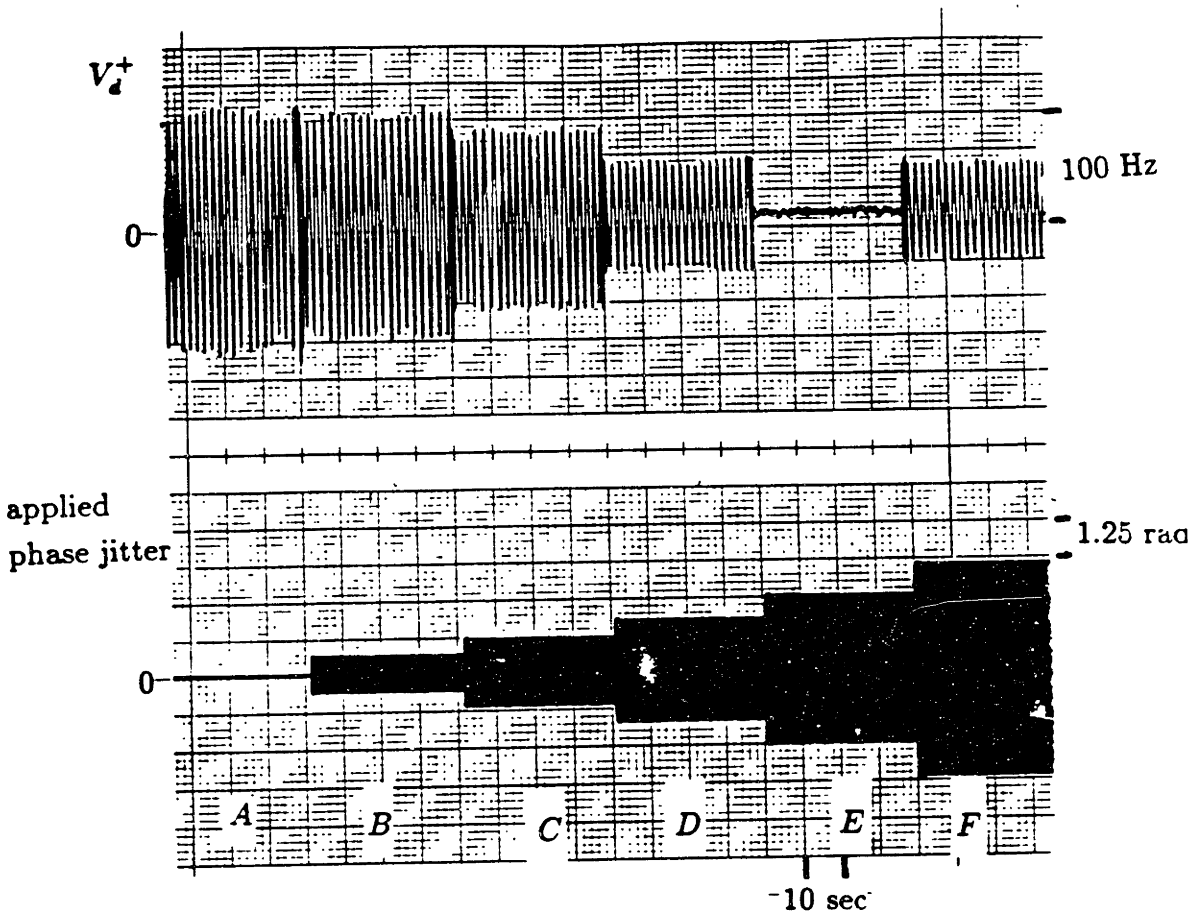

Figure 3.2.6. Elimination of the coherent backscattering on (a) V_d^+ as a function of (b) the amplitude of the applied phase modulation. The carrier suppressed case is indicated in E.

component of E^+. This component is now attenuated by $J_0(\delta\phi_j)$ due to the application of phase jitter, and its corresponding beatnote completely disappears when $J_0(\delta\phi_j) = 0$, i.e. $\delta\phi_j = 2.4$ rad. This result is in excellent agreement with our observation in section E of figure 3.2.6. Furthermore, as $\delta\phi_j$ is increased beyond 2.4 rad, $J_0(\delta\phi_j)$ is no longer zero which will result in the reappearance of the coherent backscattering as observed in section F of figure 3.2.6.

In our setup, we obtained a carrier suppression ratio of approximately 5×10^{-3}, which

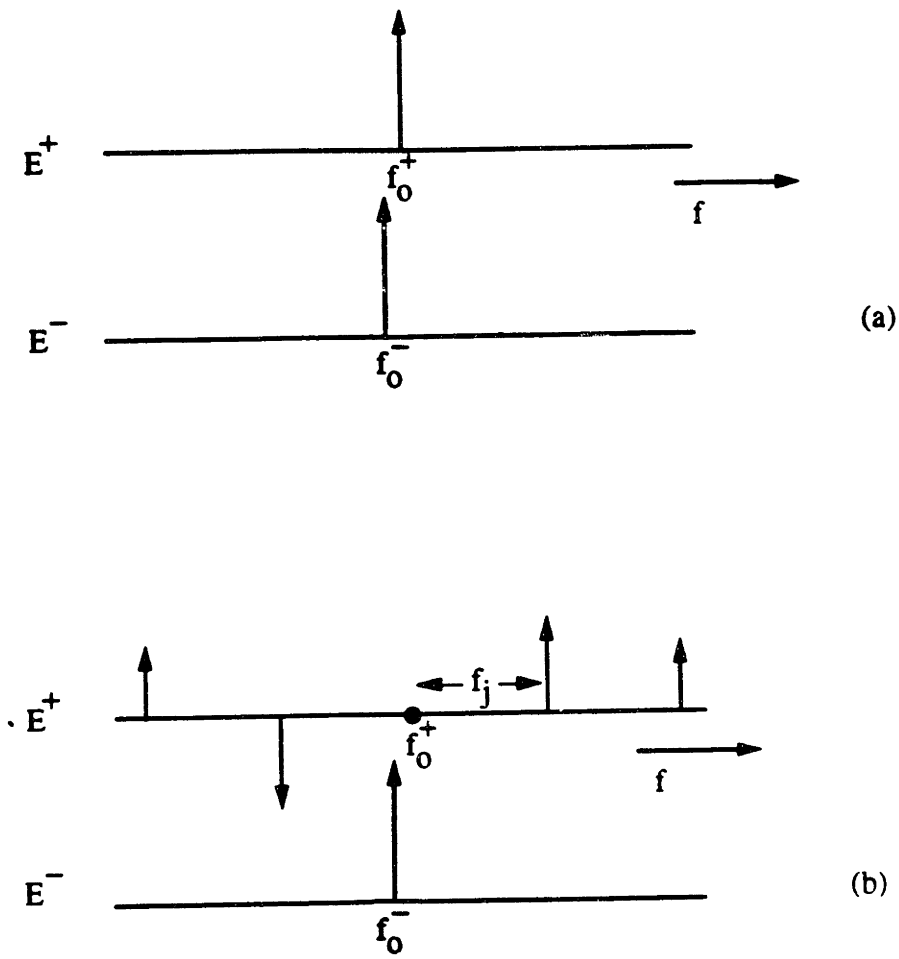

Figure 3.2.7. The spectrum of E^+ and E^- when (a) there is no phase modulation (b) the carrier component at f_o^+ has been completely suppressed by the phase modulation

is limited by the purity of the phase jitter. Thus in our case, for $\gamma_s = 120$ Hz, the coherent backscattering error after carrier suppression results in a ± 0.6 Hz of bounded drift, which is not tolerable. Therefore, better suppression is needed for a precision rotation sensor.

3.2.3. Observation of an Anomolous Discriminant Jump

In the absence of carrier suppression, as described in the previous section, an anomolous discontinuity in V_d^+ was observed in the open loop operation of the gyroscope when the frequency difference between E^+ and E^-, labeled Δf_o, was slowly changed from a positive value to a negative value. Figure 3.2.8a shows V_d^+ as a function of time, with a 100 ms 12 db/octave lowpass filter, when Δf_o is swept from 100 Hz to -100 Hz, indicating the equivalent of a a 20 Hz jump in V_d^+ as Δf_o goes through zero. It should be noted that this jump is not the same as the open loop oscillation on V_d^+, described in section 3.3.2. This oscillation is shown for a $\Delta f_o = 1$ Hz in figure 3.2.8b, indicating a γ_s of 120 Hz.

In order to determine the dependence of this jump on γ_s, we increased γ_s by attenuating E_r^+, as predicted by equation 3.2.7. Figure 3.2.8d shows V_d^+ as a function of time for $\Delta f_o = 1$ Hz, after attenuating E_r^+, indicating an increase in γ_s to 800 Hz. Figure 3.2.8c shows V_d^+ as a function time observed with a 100 ms 12db/octave lowpass filter, when Δf_o was swept from 100 Hz to -100 Hz. Although the noise on V_d^+ has increased dramatically as compared with figure 3.2.8a, the jump at Δf_o is still 20 Hz. Thus the magnitude of this jump is independent of γ_s.

In our setup, it was observed that the application of the carrier suppressed phase jitter os section 3.2.2 also eliminates this jump. However, the exact origin of this jump may be worth investigating further, and is left for future studies.

3.2.4. Measurement of the Sagnac Scale Factor

The Sagnac scale factor for the bulkoptic ring resonator can be easily measured by rotating the optical cavity and measuring the variation in Δf_Ω as indicated by V_d^+. To apply rotation, the setup was mounted on an aluminum slab and bolted to a rotating platform, which was then rotated back and forth sinusoidally around the axis perpendicular to the plane of the cavity by an electric motor as shown in figure 3.2.9. Figure 3.2.10a shows the rotation angle of the platform, θ_p, as a function of time, which is a sinewave with a period

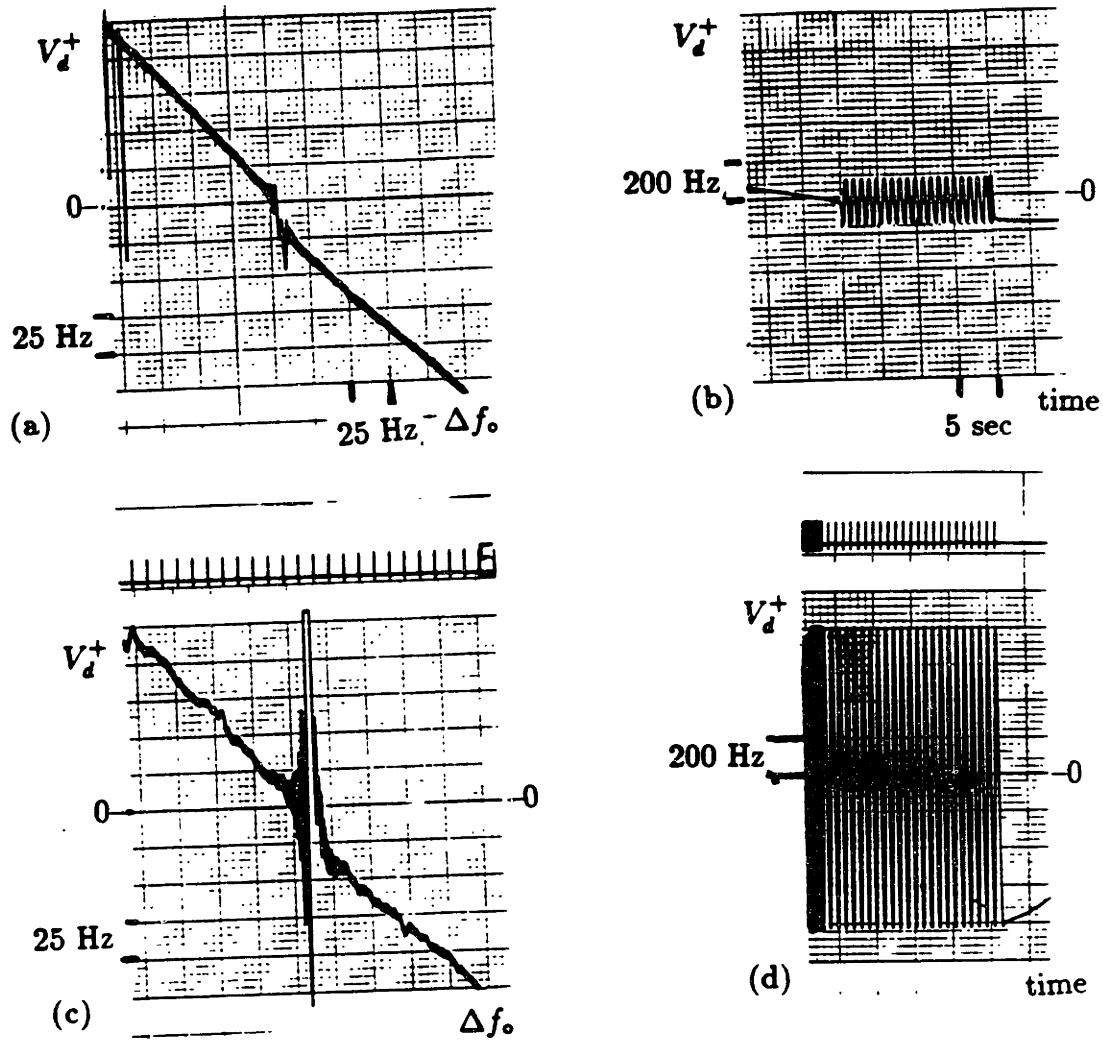

Figure 3.2.8. (a) The anomolous jump in V_d^+ as a function of frequency and (b) the corresponding coherent backscattering amplitude for $\gamma_s = 120$ Hz. (c) and (d) show the case for $\gamma_s = 800$ Hz

of 130 sec and an amplitude of ±2.5°. This motion corresponds to a sinusoidal variation in angular velocity with a peak amplitude of ±430 deg/hr.

Figure 3.2.10b shows V_d^+ as a function of time, with a 1 sec 6db/octave filter, when the rotation of figure 3.2.10a was applied to the setup, demonstrating a sinusoidal variation in V_d^+, 90° out of phase with respect to θ_p. The peak amplitude of the variation in V_d^+ corresponds to 430 Hz and it occurs at the maximum rate of change of the rotation angle (i.e. 430 deg/hr). This corresponds to a Sagnac scale factor of 1 Hz per deg/hr which is

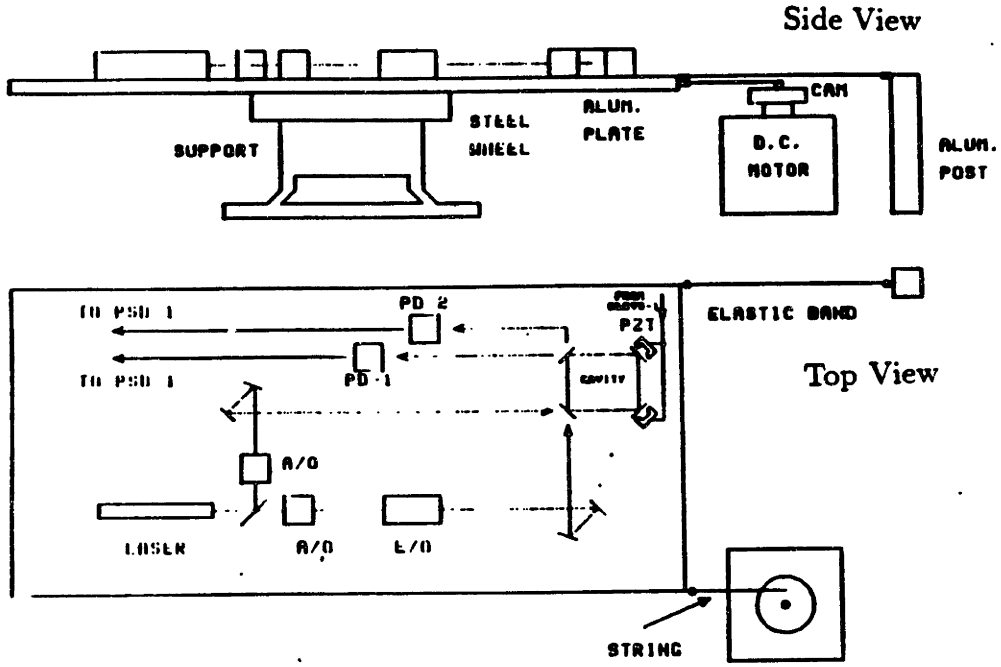

Figure 3.2.9. Schematic diagram for the rotation platform

in agreement with the value predicted by $4A/\lambda_o P$ for our setup when:

$$\begin{cases} A = 1.7 \times 10^{-2}\text{m}^2 \\ P = 0.52\text{m} \\ \lambda_o = 632.8\text{nm} \end{cases}$$

3.2.5. Random Noise of the Gyroscope

In this section we present the noise performance of the bulkoptic PRG. We used s polarized light, for which the cavity linewidth, Γ_c, is 35 kHz, as presented in section 3.1.1. The peak output intensity along either the clockwise or the counterclockwise direction of the cavity is

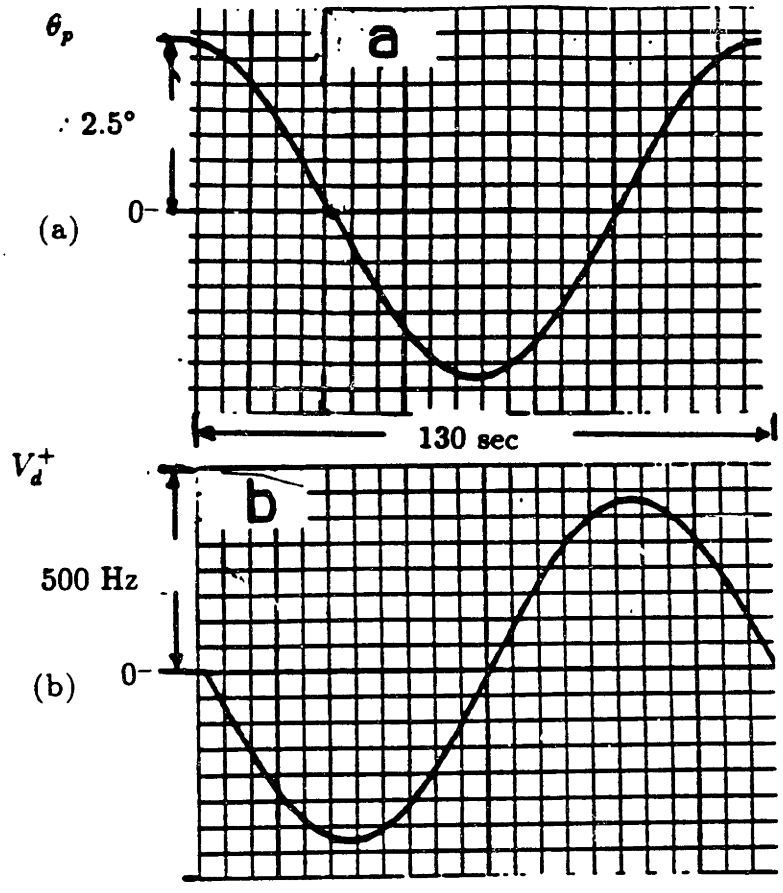

Figure 3.2.10. Simultaneous recording of (a) the rotation angle θ_p as a function of time and (b) the variation of V_d^+

approximately 2 μW, corresponding to a photocurrent, i_p, of 1.4 μA, and a photodetector output of 0.7 V. The discriminant slope κ in our case is approximately 20 μV/Hz.

As described in section 2.2, the fundamental noise of the gyroscope, δf, is due to shot noise of the light, given by equation 2.2.6. In our case for:

$$\begin{cases} R = 500\ \text{k}\Omega \\ i_p = 1.4\ \mu\text{A} \\ \kappa = 20\ \mu\text{V/Hz} \end{cases}$$

we have:

$$\begin{aligned} \delta V_d = \sqrt{2}\delta V_o &= \frac{360\ \text{nV}}{\sqrt{\tau}} \\ \delta f &= \frac{1.7 \times 10^{-2}\ \text{Hz}}{\sqrt{\tau}} \end{aligned} \qquad (3.2.12)$$

where δV_d is the noise voltage on the discriminant, and τ is given in units of seconds. We have neglected the attenuation in the average intensity of the light due to the f_m modulation.

We start by measuring the short term noise of the gyroscope for $\tau = 10$ ms. In this measurement, the frequencies of E^+ and E^- are set equal to each other. The drifts due to coherent backscattering , presented in section 3.2.2, are ignored since they are very slow (order of 10 sec and longer). We then sample V_d^+ at a rate of 1 kHz for 500 ms, average these 500 samples to obtain 50 new samples each 10 ms in duration, and calculate the rms fluctuation for these 50 samples. This experiment was repeated several times, and each time we obtained an rms noise voltage of approximately 3.5 μV, corresponding to 0.17 Hz. This result is plotted in figure 3.2.11, which indicates the rms noise of V_d^+ as a function of τ. The solid line in this figure indicates the shot noise limit predicted by equation 3.2.12. As shown in the figure for $\tau = 10$ ms the measured noise of V_d^+ is equal to the shot noise limit. We will now describe the procedure for obtaining other points of this plot for larger values of τ.

In order to measure δf for larger values of τ, we can no longer ignore drifts due to coherent backscattering, so we remove the coherent backscattering by the application of a phase jitter to E^+, as described in section 3.2.2. As mentioned in section 3.2.2, the residual coherent backscattering due to incomplete carrier suppression is 0.6 Hz. This residual coherent backscattering is removed by having a 10 Hz frequency difference between E^+ and E^- and filtering the resulting oscillation of V_d^+ by a 100 ms 12db/octave filter. We then sample V_d^+ at a rate of 10 Hz for 50 sec, and average these 500 samples to obtain 50 new samples each 1 sec in duration, and calculate the rms fluctuation for these 50 samples. We thus obtain an rms noise voltage of 740 nV, corresponding to 3.7×10^{-2} Hz. By comparison, equation 3.2.12 predicts a noise of 1.7×10^{-2} Hz, which is a factor of 2 smaller than the measured noise.

We now demonstrate possible contributions to this factor of 2 deviation of δf from the shot noise limit for $\tau = 1$ sec. Figure 3.2.12a shows the fluctuations of V_d^+ as a function of

time, observed with a 300 ms 12db/octave output filter, in the presence of a phase jitter with $f_j = 40$ Hz and $\delta\phi_j = 2.4$ rad. This figure indicates a 0.2 Hz peak to peak noise. We now increase $\delta\phi_j$ to 5.5 rad so that it corresponds to the second zero of J_0. It should be noted that we are still suppressing the carrier of E^+. Figure 3.2.12b shows the fluctuations of V_d^+ as a function of time with a 300 ms 12 db/octave filter, for this case, indicating an increase of the peak to peak noise to 0.5 Hz. Thus we have demonstrated an increase in noise as $\delta\phi_j$ is increased.

To further illustrate the dependence of the residual frequency noise on the amplitude of the phase jitter, we turn off the phase jitter, and set a 30 Hz frequency difference between E^+ and E^-. The coherent backscattering effect at 30 Hz is then removed by our 300 ms 12db/octave low pass filter. Figure 3.2.12c shows the fluctuations of V_d^+ as a function of time, indicating a reduction of the peak to peak noise to 0.1 Hz. We then made a similar measurement of the rms noise of V_d^+ for $\tau = 1$ sec in the absence of phase jitter. We obtained an rms noise voltage of 450 nV, corresponding to 2.3×10^{-2} Hz. This noise is smaller than the noise measured for the phase jittered case, and is now a factor of 1.5 larger than the shot noise limit predicted by equation 3.2.12. Thus we have shown that δf increases with an increase in the amplitude of the phase jitter, and decreases when the phase jitter is turned off.

To understand the dependence of δf on the phase jitter, let us consider figure 3.2.13a, which shows V_d^+ as a function of time, for a 10 Hz frequency difference between E^+ and E^-. The phase jitter for this case has been turned off, so that we can observe a 10 Hz oscillation due to coherent backscattering. As can be seen in the figure, the segment of the oscillation cycle labeled A has very low noise because in this segment the slope of V_d^+, i.e. κ^+, is equal to that of V_d^-, i.e. κ^-, so that any high frequency common mode noise on the discriminants is subtracted. By contrast, the segment of the figure labeled B is noisy, indicating incomplete noise subtraction, which means that κ^+ and κ^- are no longer equal to each other. In figure 3.2.13b we eliminated the noise shown in segment B of figure 3.2.13a

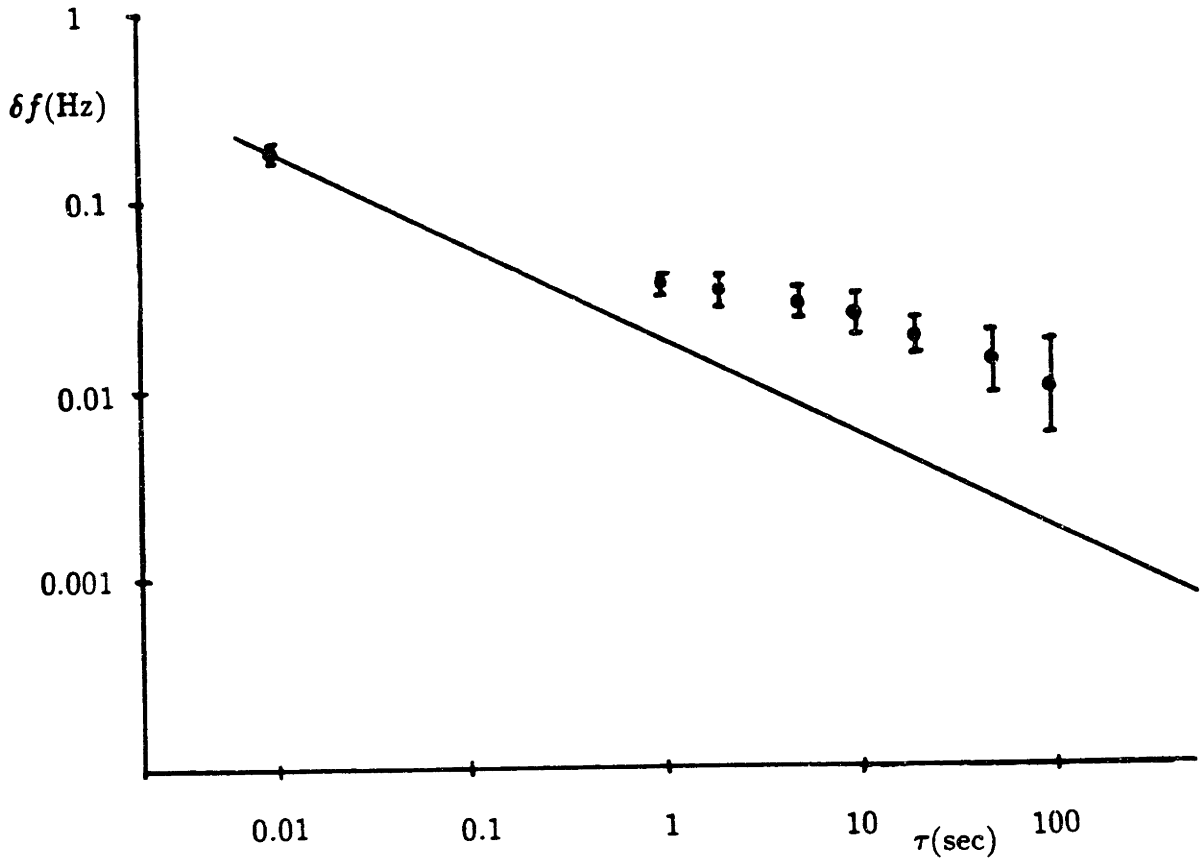

Figure 3.2.11 rms frequency noise of the gyroscope δf as a function of the averaging time τ

by adjusting κ^- via the gain adjustment element A_1, shown in figure 3.1.12. However, by doing so, we now have excess noise in segment A, indicating incomplete subtraction there. Thus, figures 3.2.13a and b conclusively demonstrate a fluctuation in the slope of the discriminant, tied to $\Delta\phi$, i.e. the phase difference between E^+ and E^-. In the presence of phase jitter, $\Delta\phi$ is modulated sinusoidally, which also corresponds to a modulation of κ^+. This modulation of κ multiplies the high frequency noise of the discriminant thus mapping certain components of this noise to around DC. This additional noise is thus

directly related to phase jittering. We can eliminate this additional noise by increasing the jitter frequency to above the bandwidth of the laser frequency fluctuations.

We now measure the rms noise of V_d^+ as a function of τ for values larger than 1 sec. These results are plotted in figure 3.2.11 next to the noise measurement at $\tau = 10$ ms. As mentioned previously, the solid line in the figure is the shot noise limited performance predicted by equation 3.2.12. For these noise measurements, we used phase jittering with $f_j = 40$ Hz and $\delta\phi_j = 2.4$ rad. The rms noise for $\tau = 1$ sec, as previously measured, is 3.7×10^{-2} Hz, which is a factor of 2 above the value predicted by shot noise. Although the rms noise generally decreases with τ within our measurement range (1 sec$< \tau <$100 sec) it deviates further from the shot noise for larger values of τ. For example, for $\tau = 100$ sec, the rms noise frequency is 1.2×10^{-2} Hz which is 7 times the value predicted by shot noise limit. This gradual deviation from the predicted noise is due to very low frequency offset drifts. In the next sections, we will consider some of these additional drift sources.

3.2.6. Additional Sources of Drift in Bulkoptic PRG

Earth's rotation results in approximately 9.5 Hz of offset in our setup due to the Sagnac effect. In addition to this constant offset, we also have drifts which cause the increase in the rms noise observed at large values of τ in figure 3.2.11.

We observe a 0.5 Hz change in offset when the plane of polarization of one of the input beams is rotated by approximately 40° with respect to s polarization. In our setup we can maintain the plane of polarization of the input beams to better than 0.1°, which approximately corresponds to an offset of 0.0013 Hz. This offset is within the shot noise limit of light at $\tau = 100$ sec. Thus, polarization misalignments do not explain the enhanced noise of figure 3.2.11

We also measured the sensitivity of the offset to perturbations in the input alignment. In our setup, for 2 arc minutes of misalignment, the offset varies by less than 0.05 Hz. By using very stable mirror mounts, we can hold our input alignment to within 2 arc seconds,

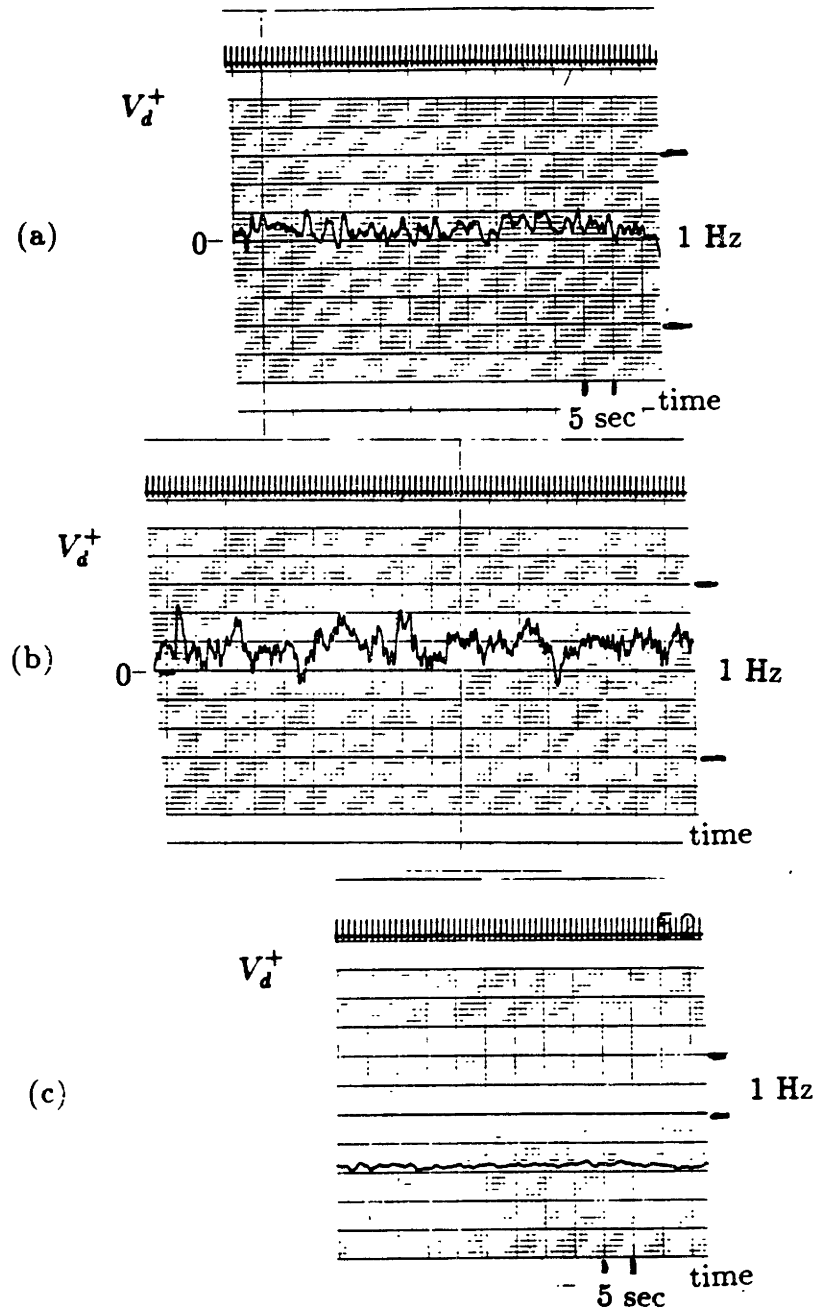

Figure 3.2.12 Variations in V_d^+ as a function of time when the amplitude of the phase jitter is (a) 2.4 rad corresponding to the first zero of J_0 (b) 5.5 rad corresponding to the second zero of J_0 (c) zero and there is a 30 Hz frequency difference between E^+ and E^-

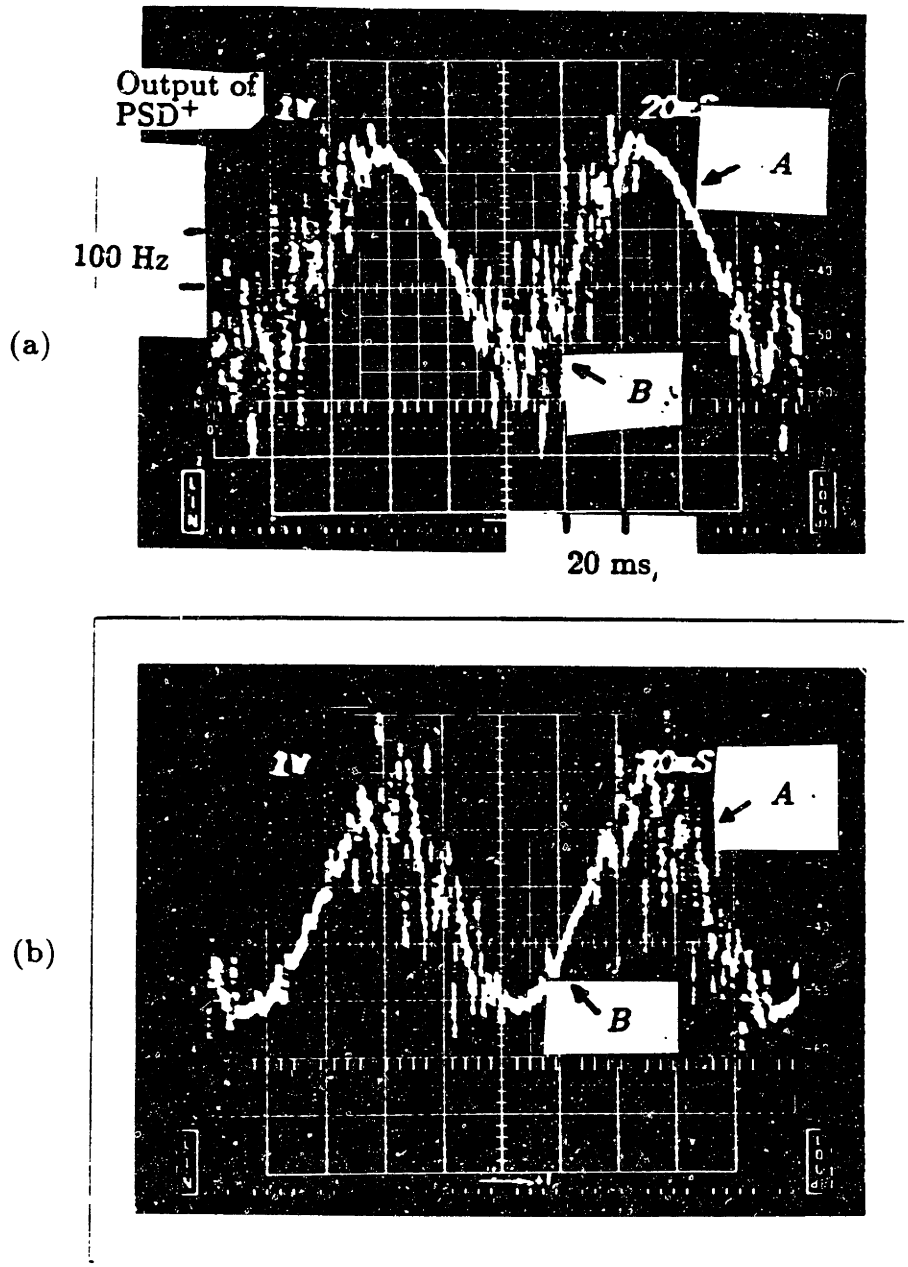

Figure 3.2.13 (a) Oscillations of V_d^+ due to coherent backscattering indicating a fluctuation in the slope of V_d^+ synchronous with the oscillation cycle (b) after increasing the subtraction gain of V_d^+ by 2%

which corresponds to approximately 0.001 Hz of fluctuation. This is also approximately equal to the shot noise limit at $\tau = 100$ sec. Thus misalignment does not contribute significantly to the drifts observed in figure 3.2.11 either.

Another source of error in the gyroscope is due to the drift between the optical phases of E^+ and E^- before they are coupled into the cavity. These drifts are caused by air currents, thus we must seal all of the optical paths in our setup. We have independently checked for the contribution of this error source in our setup by removing the optical resonator, and recombining E^+ and E^- into a single beam, E_d, by a 50/50 beamsplitter, as shown in figure 3.2.14a. A photodetector PD now monitors E_d as a function of time. Figure 3.2.14b shows the output of PD as a function of time when we have a 1 Hz frequency difference between E^+ and E^-, showing the intensity variation due to the interference between E^+ and E^-. Figure 3.2.14c shows the variation in the output of PD as a function of time, when the same drive frequency is used for both AO^+ and AO^-. Thus, here we see the relative phase drift between E^+ and E^-. The maximum rate of drift is in the section indicated by arrow C, and corresponds to approximately 0.25 cycles over 300 sec, or 0.0008 Hz. Therefore, the phase drifts between E^+ and E^- in our case do not contribute to the added noise in figure 3.2.11. Thus, we now propose several additional sources of drift to be explored in future studies.

One possible source of drift in our setup is due to the fluctuation of the discriminant slope, observed in figure 3.2.13. As seen in this figure, the discriminant slope fluctuates periodically as a function of $\Delta\phi$. Since the coherent backscattering error also fluctuates periodically with $\Delta\phi$, we may have a direct demodulation of the coherent backscattering due to this discriminant slope variation. We measured a $\pm 1\%$ fluctuation in the slope and a coherent backscattering amplitude of ± 120 Hz. This corresponds to a worst case drift contribution of approximately 0.6 Hz, which is very significant. It should be noted that although the application of the phase jitter removes the low frequency components of the coherent backscattering errors, it does not eliminate this demodulation behavior. The contribution of this potential error source, must be studied further.

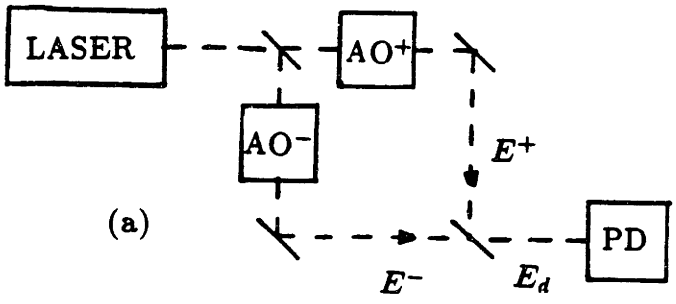

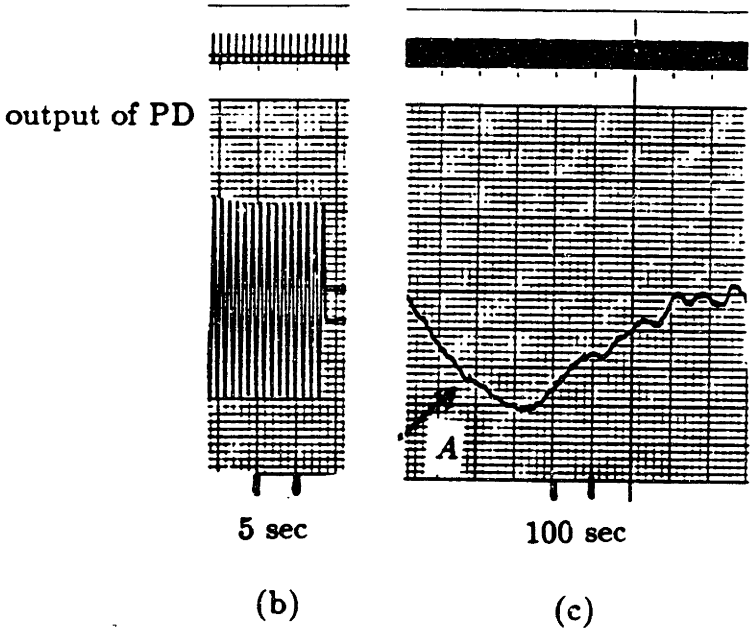

Figure 3.2.14 (a) Setup to measure the phase drift between E^+ and E^- (b) the beatnote between E^+ and E^- when there is a 1 Hz frequency difference between them (c)the relative phase drift between E^+ and E^-.

An additional source of drift is due to the discriminant jump, observed in section 3.2.3,

which in our case corresponds to ± 10 Hz. This jump is suppressed by the sinusoidal phase jitter described in section 3.2.2, however, a variation in the amplitude of the phase jitter, labeled $\delta\phi_j$ in section 3.2.2, can result in the incomplete removal of this jump. Thus, a 0.1% fluctuation in $\delta\phi_j$ will result in an offset fluctuation of approximately ± 0.01 Hz. This offset is now approximately equal to the long term fluctuations we observe (for $\tau = 100$ sec) in figure 3.2.11. The errors due to this source should be also studied further.

Finally, we must also consider the effect of Fresnel drag in our cavity. Fresnel drag is the change in the index of refraction of a medium to to its motion. This change in the index of refraction, Δn, is s approximately given by $\Delta n = (n-1)v_m/c$ where v_m is the velocity of the medium. In our case, the cavity is filled with a mixture of He at approximately 1 Torr and Ne at approximately 0.1 Torr. Therefore for a gas velocity of 2 mm/sec, we get the equivalent of 0.001 deg/hr of offset error. This contribution is significant, and can be easily removed by evacuating the cavity completely.

3.3. The Closed Loop Operation of the PRG

As described in section 3.1, in closed loop operation, both primary and secondary loops are active. The closed loop output of the gyroscope is the frequency difference between E^- and E^+. This frequency difference can be measured by optically interfering E^+ and E^-, or by electronically mixing the drive frequencies of A/O^+ and A/O^-. In our case the drive to A/O^- is generated by an oven stabilized frequency synthesizer which drifts less than 0.01 Hz per hour. Thus we need only measure the drive frequency of A/O^+, i.e. f_a^+, to infer the frequency difference between E^+ and E^-. We measure f_a^+ by a digital frequency counter.

The closed loop operation of the gyroscope can be demonstrated by applying a sinusoidal rotation to the setup via a rotation platform as described in section 3.2.5. Figure 3.3.1a shows the rotation angle of the platform, labeled θ_p, as a function of time. θ_p has an amplitude of 2.5° and a period of 130 sec, corresponding to a sinusoidal variation in

angular velocity with a peak of 430 deg/hr. Figure 3.3.1b shows the variation in f_a^+ as a function of time corresponding to this applied rotation. In this figure, zero frequency indicates E^+ and E^- having the same frequency. Region A in figure 3.3.1b corresponds to the case where the frequencies of E^+ and E^- are locked together, inspite of a rotation rate. The lockin threshold, Ω_T, is the maximum angular velocity for which the frequencies of E^+ and E^- are still locked together, and can be measured from figure 3.3.1b. In our case, the applied angular velocity near lockin varies approximately linearly with time, with a slope of approximately 21 deg/hr per second. As show in figure 3.3.1b, the dead zone, that is associated with the lockin behavior, extends ±6 sec from its center, which corresponds to a lockin threshold of approximately 125 deg/hr.

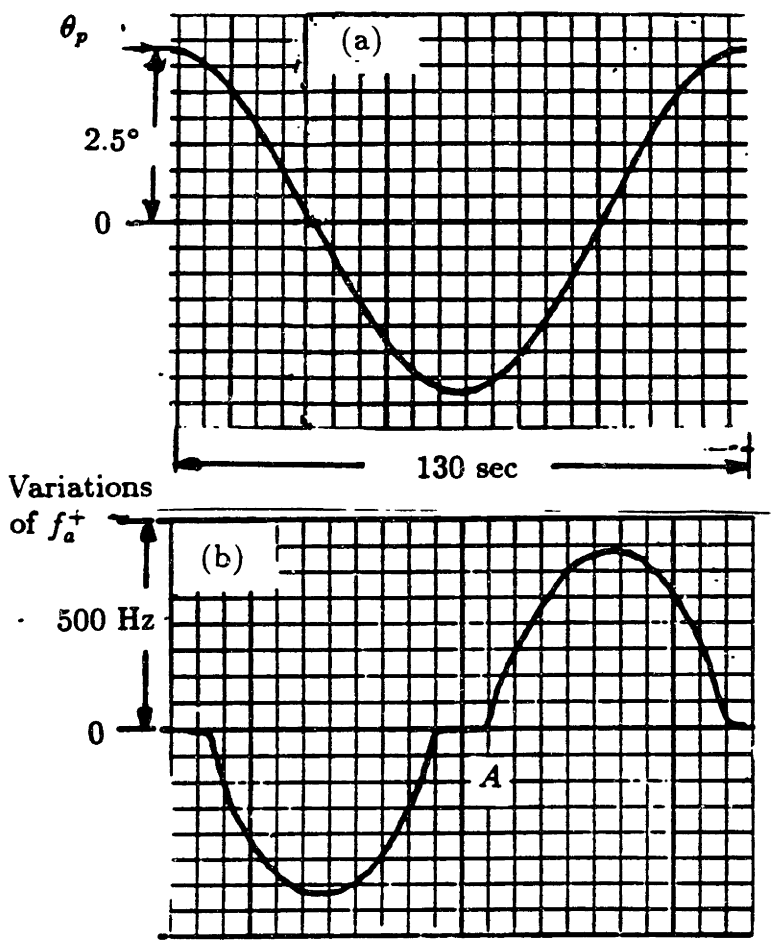

Figure 3.3.1. Demonstration of the closed loop behavior of the setup showing (a) rotation angle applied to the ring resonator (b) corresponding variation in the drive frequency of VCO^+ indicating the lockin zone in the region marked A

3.3.1. The Lockin Behavior

The lockin behavior is the manifestation of the coherent backscattering in the closed loop operation. In order to derive the lockin behavior, let us consider the overall separation between the clockwise and the counterclockwise resonance frequencies. This is represented by the sum of Δf_Ω, which is due to the Sagnac effect, and Δf_s, which is due to the coherent backscattering. As described in section 3.1, during the closed loop operation, the difference between the frequencies of E^+ and E^-, i.e. Δf_o, is set equal to the separation between the clockwise and counterclockwise resonance frequencies. Thus Δf_o is given by:

$$\begin{aligned} \Delta f_o &= \Delta f_\Omega + \Delta f_s \\ &= \Delta f_\Omega + \gamma_s \sin(\Delta\phi) \end{aligned} \tag{3.3.1}$$

where $\Delta\phi$ is the phase difference between E^+ and E^-, and is related to Δf_o by the simple relationship:

$$\Delta f_o = \frac{1}{2\pi}\frac{\partial}{\partial t}(\Delta\phi) \tag{3.3.2}$$

Δf_o can be eliminated between equations (3.3.1) and (3.3.2), to give a differential equation describing the closed loop behavior of the gyroscope[15,16], i.e.:

$$\frac{\partial}{\partial t}(\Delta\phi) = 2\pi(\Delta f_\Omega + \gamma_s \sin(\Delta\phi)) \tag{3.3.3}$$

For a given Δf_Ω and γ_s, this equation can be solved analytically for $\Delta\phi$ as a function of time to give:

$$\Delta\phi = \frac{\pi}{2} + 2\tan^{-1}\left(\tan\left(\pi\sqrt{\Delta f_\Omega^2 - \gamma_s^2}\, t - \frac{\pi}{4}\right)\sqrt{\frac{\Delta f_\Omega + \gamma_s}{\Delta f_\Omega - \gamma_s}}\right) \tag{3.3.4}$$

The beat note between E^+ and E^-, given by $\sin(\Delta\phi)$, can be expressed as:

$$\sin(\Delta\phi) = \frac{\gamma_s + \Delta f_\Omega \sin\left(2\pi\sqrt{\Delta f_\Omega^2 - \gamma_s^2}\, t\right)}{\Delta f_\Omega - \gamma_s \sin\left(2\pi\sqrt{\Delta f_\Omega^2 - \gamma_s^2}\, t\right)} \tag{3.3.5}$$

We show the variation of $\sin(\Delta\phi)$ as a function of time for several values of Δf_Ω in figure 3.3.2. When Δf_Ω is much larger than γ_s, $\sin(\Delta\phi)$ is a pure tone with frequency $\Delta f_\circ = \sqrt{\Delta f_\Omega^2 - \gamma_s^2}$. As Δf_Ω approaches γ_s, $\sin(\Delta\phi)$ becomes non sinusoidal, but remains periodic with a period $t_\circ = 1/\sqrt{\Delta f_\Omega^2 - \gamma^2}$. The average frequency of $\sin(\Delta\phi)$, labeled $\widetilde{\Delta f_\circ}$, is equal to $1/t_\circ$, and is given by:

$$\begin{aligned}\widetilde{\Delta f_\circ} = \frac{1}{t_\circ} &= \sqrt{\Delta f_\Omega^2 - \gamma_s^2} \\ &= \sqrt{(\frac{4A}{\lambda_\circ P}\Omega)^2 - \gamma_s^2} \\ &= \frac{4A}{\lambda_\circ P}\sqrt{\Omega^2 - \frac{\lambda_\circ P}{4A}\gamma_s}\end{aligned} \tag{3.3.6}$$

Figure 3.3.3 shows a plot of $\widetilde{\Delta f}$ as a function Ω in equation (3.3.6), clearly indicating the lockin zone, where the lockin threshold Ω_T is given by:

$$\Omega_T = \frac{\lambda_\circ P}{4A}\gamma_s \tag{3.3.7}$$

As determined previously, the lockin behavior in figure 3.3.1b represents $\Omega_T = 125$ deg/hr, which corresponds to $\gamma_s \approx 125$ Hz. However, as illustrated in section 3.2.1, γ_s can also be measured from the open loop behavior of the gyroscope. This measurement is carried out by switching to open loop operation immediately after the closed loop measurements, and determining γ_s. Figure 3.3.4 shows the oscillation of V_d^+ in the open loop operation, indicating $\gamma_s = 120$ Hz. This is in good agreement with the closed loop measurement of γ_s.

3.3.2. Elimination of the Lockin Behavior

The lockin behavior can be eliminated by mechanically dithering the cavity, such as the case in a commercial Ring Laser Gyroscope (RLG). However in our case the lockin can also be removed by a non-mechanical jitter. Figure 3.3.5 shows the revised schematic for the closed loop operation with jitter, where a sinusoidal phase jitter with frequency f_j

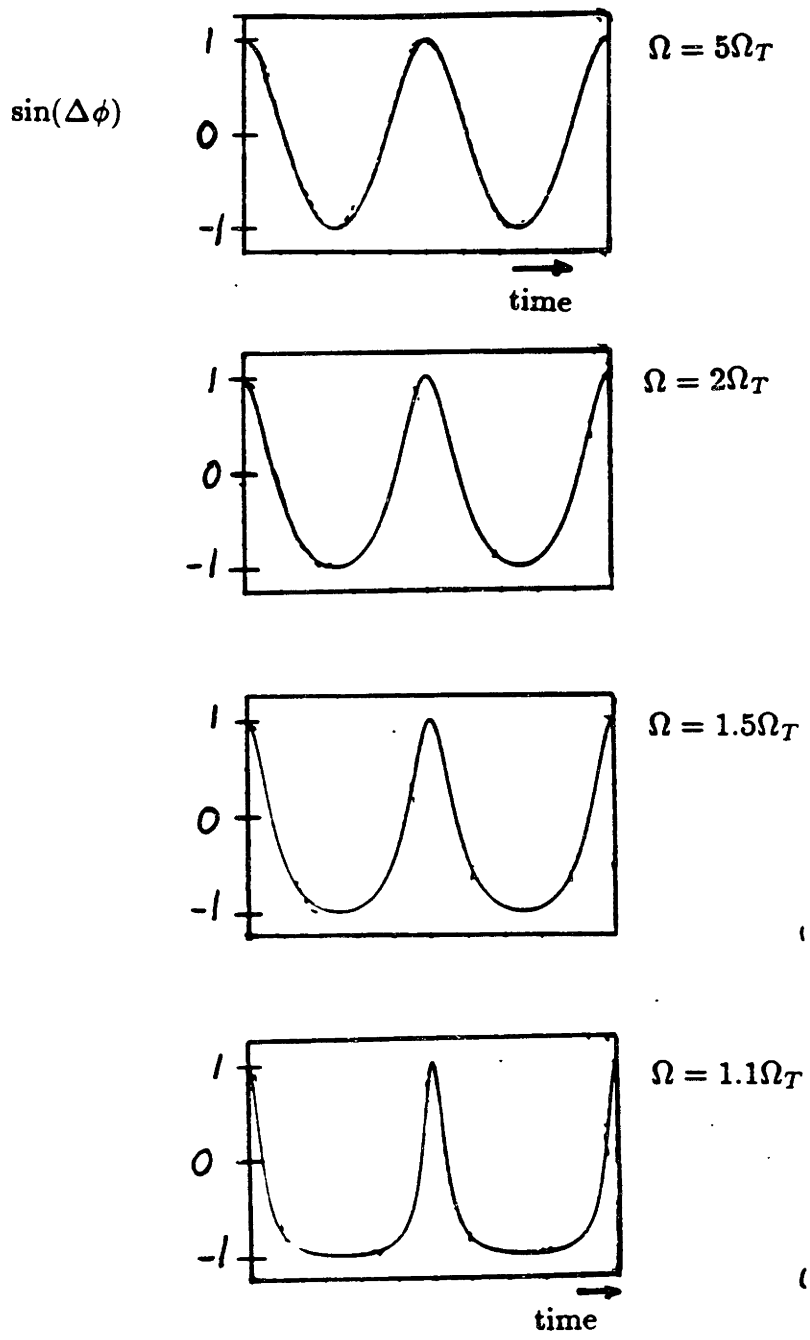

Figure 3.3.2. $\sin(\Delta\phi)$ as a function of time for $1.1\Omega_T < \Omega < 5\Omega_T$ for two cycles of $\sin(\Delta\phi)$

and phase amplitude $\delta\phi_j$, is applied to E^+ by the electrooptic EO to wash out the lockin

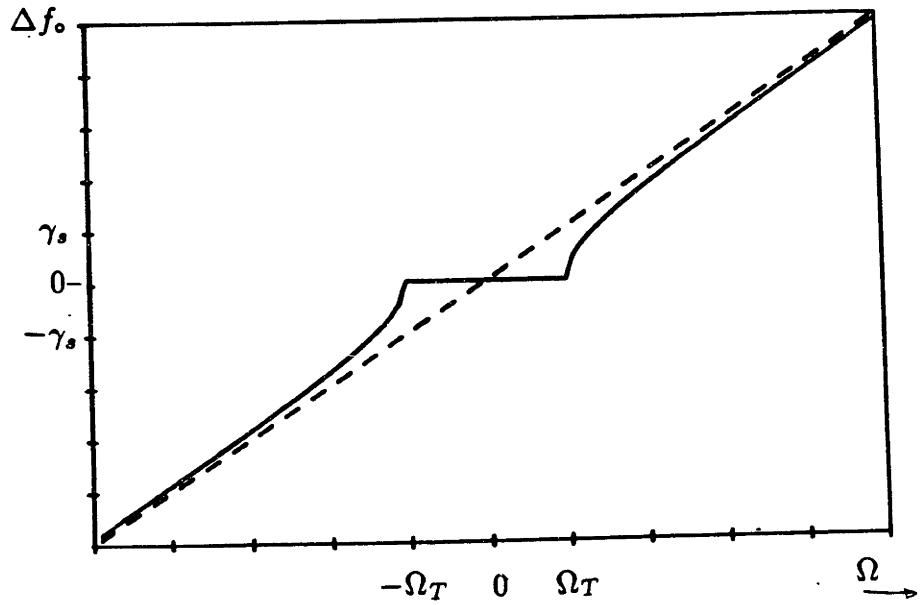

Figure 3.3.3. $\widetilde{\Delta f_o}$ as a function of Ω demonstrating the lockin behavior with a threshold $\Omega_T = (\lambda_o P/4A)\gamma_s$

behavior. f_j must be set larger than the bandwidth of the secondary loop, which is 900 Hz in our case. This is to insure that the secondary loop will not compensate for the applied jitter.

Figures 3.3.6 a through f show the frequency of VCO$^+$, f_a^+, as a function of time, for the applied rotation illustrated in figure 3.1.1a, when $f_j = 3$ kHz and $\delta\phi_j$ is increased from 0 (in figure 3.3.6a) to 2.88 rad (in figure 2.3.6f). In figure 3.3.6 a through e, the width of the lockin zone gradually decreases until in figure 3.3.6e the lockin behavior disappears completely. In this case $\delta\phi_j = 2.4rad$, which corresponds to $J_0(\delta\phi_j) = 0$. This is the closed loop equivalent of the carrier suppression technique of section 3.2.2. A further increase in $\delta\phi_j$ results in the reappearance of the lockin behavior as indicated in figure 3.3.6f

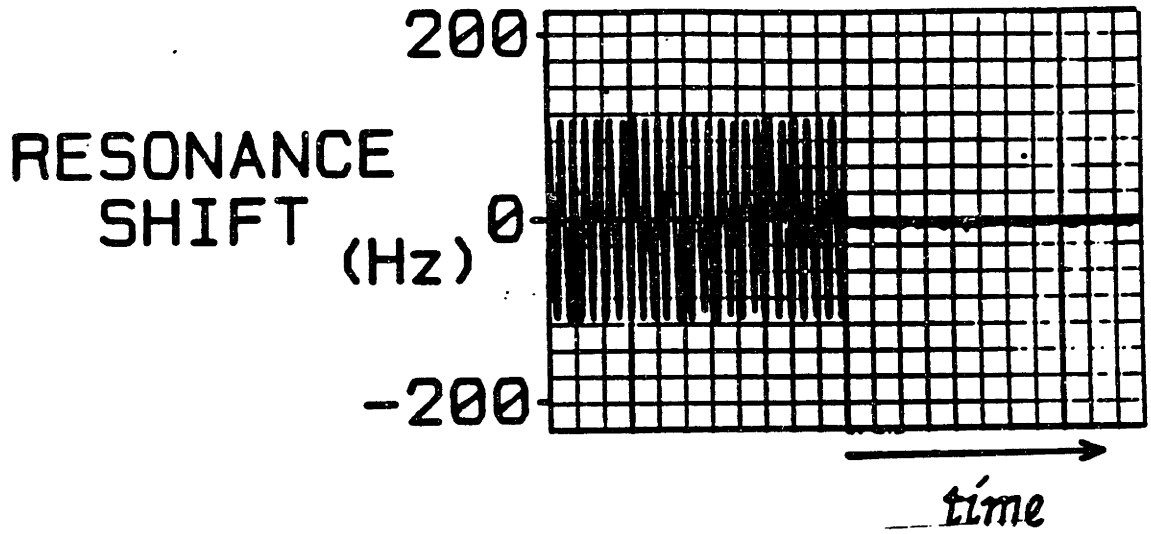

Figure 3.3.4. Coherent backscattering oscillation of V_d^+ as a function of time in the open loop operation indicating $\gamma_s = 120$ Hz

Thus, we have demonstrated the lockin behavior in the closed loop operation of the PRG, and presented a nonmechanical approach to eliminate it. We have also explored several other nonmechanical methods to eliminate the lockin behavior in our PRG, which are variations of the method described above. These are presented previously in another work[17].

3.4. Investigation of Errors due to Birefringence within a Ring Resonator

In this section, we calculate the effects of an intracavity birefringent element on the resonance frequencies of a ring resonator. We demonstrate the validity of these calculations by placing a birefringent element inside a bulkoptic ring resonator, and observing the resulting changes in the cavity eigen polarizations and resonance frequencies. This treatment is of interest to the fiber optic PRG described in chapter 4.

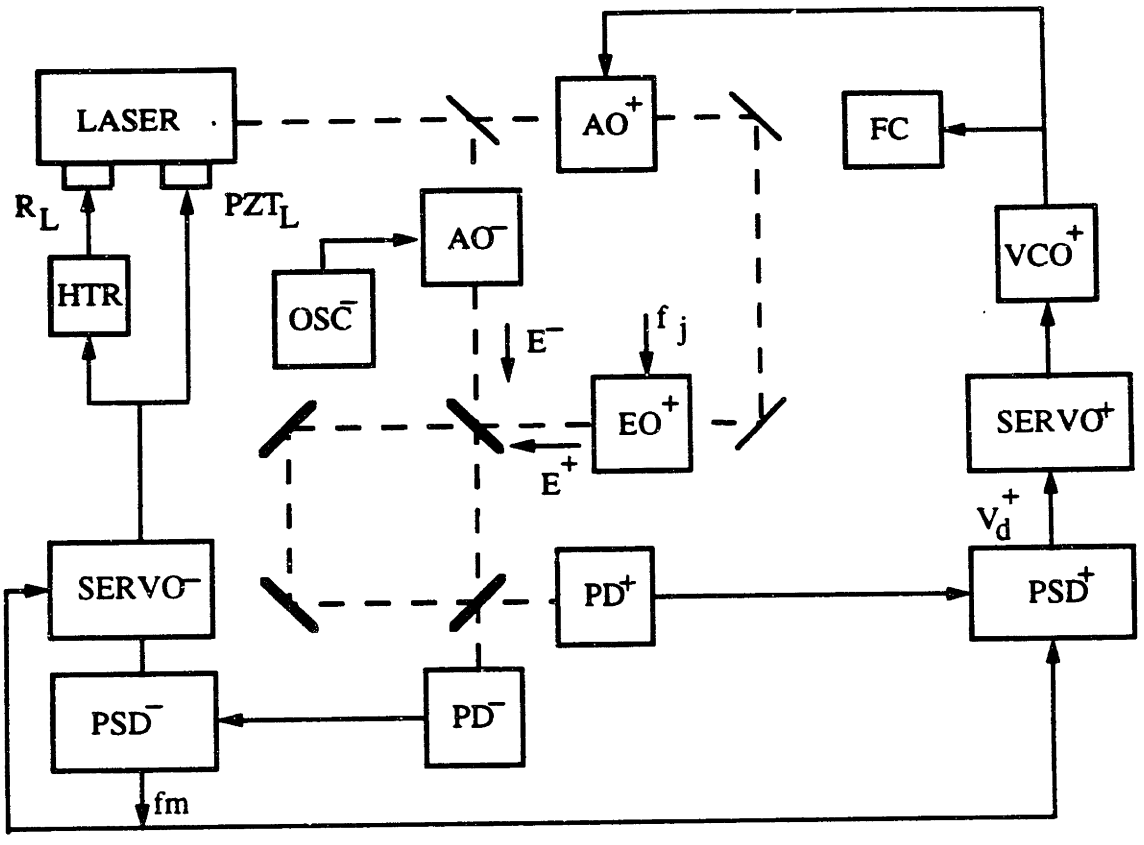

Figure 3.3.5. Revised closed loop schematic diagram with an electrooptic phase modulator EO

3.4.1. Reciprocity Considerations for an Intracavity Birefringent Element

Figure 3.4.1a shows a simple ring cavity composed of 3 mirrors. The partially transmitting mirror, M_1 is the input port for this resonator, and the mirror M_2 is the output port. In order to analyze the behavior of the cavity for different states of polarization, we choose a coordinate system (s,p,z). At every point inside the ring cavity, the z axis is along the direction of a counterclockwise propagating beam, the p axis parallel to the plane of the

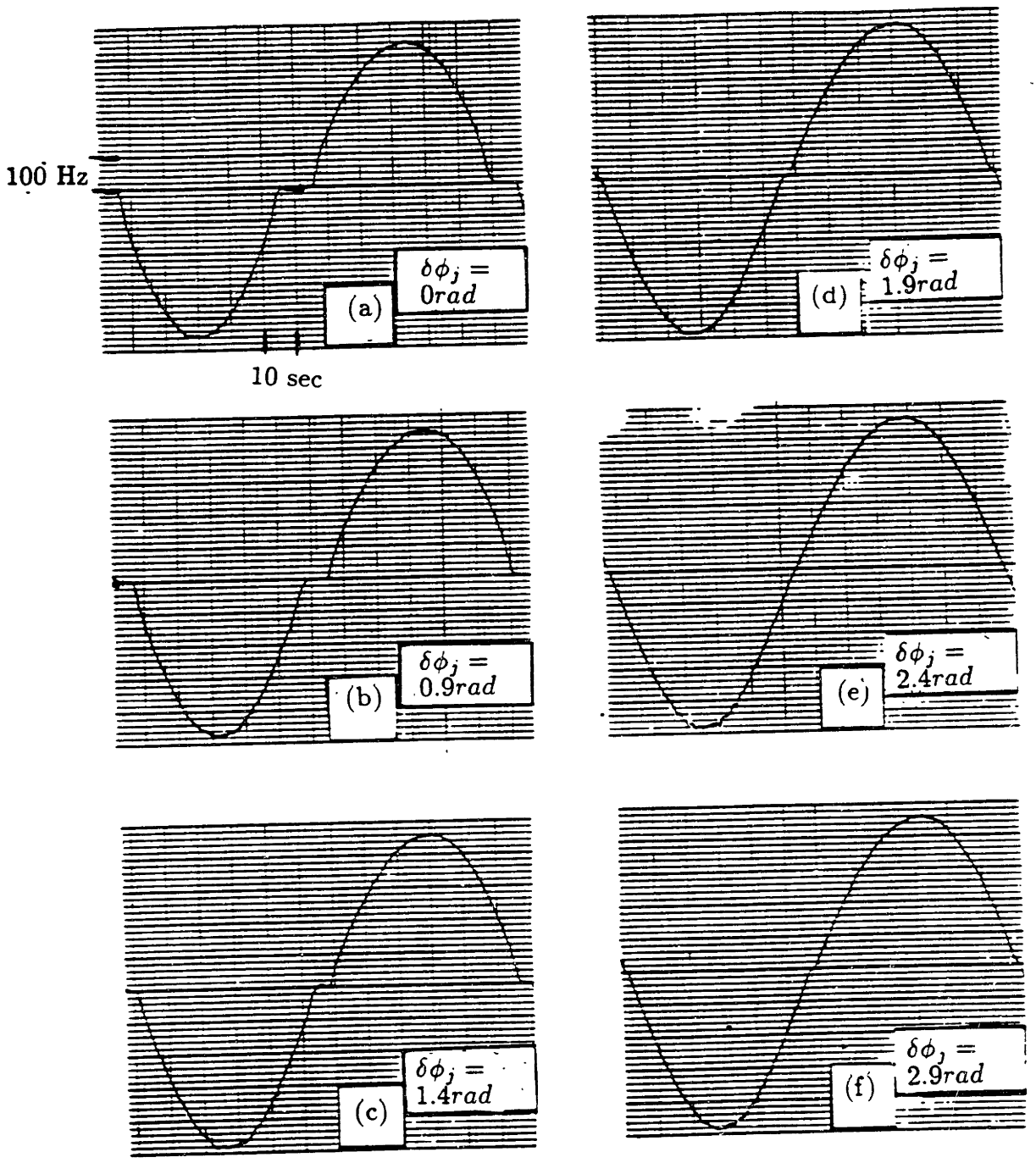

Figure 3.3.6. f_a^+ as a function of time for the applied rotation of figure 3.3.1a, in the presence of a sinusoidal phase jitter with f_j = 3 kHz, and $\delta\phi_j$ varying from 0 to 2.9 rad indicating the elimination of the lockin behavior in (e)

ring cavity, and the s axis is perpendicular to the plane of the ring cavity, as for example

shown for point A in figure 3.4.1a. The electric field vector, E, of any beam with an arbitrary state of polarization can now be represented by its two components along the p6 and s axes. E is represented by:

$$E = \begin{pmatrix} E_p \\ E_s \end{pmatrix} \tag{3.4.1}$$

The propagation of E around the counterclockwise direction of the resonator, is represented by the multiplication of E with a counterclockwise propagation matrix, M^+. In our simple simple ring resonator M^+ is given as:

$$M^+ = M_\circ = \begin{pmatrix} R_p e^{j\xi_p} & 0 \\ 0 & R_s e^{j\xi_s} \end{pmatrix} \tag{3.4.2}$$

where R_p and R_s are the round trip field attenuation coefficients for p and s polarizations respectively, and ξ_p and ξ_s are the normalized frequencies given by:

$$\begin{aligned} \xi_p &= \frac{P}{c}\omega + \phi_p \\ \xi_s &= \frac{P}{c}\omega + \phi_s \end{aligned} \tag{3.4.5}$$

where ω is the optical frequency of light, P is the perimeter of the cavity, c is the speed of light in the cavity, ϕ_p is the phase due to reflection from the three mirrors for p polarization, and ϕ_s is the phase due to reflection from the three mirrors for s polarization. These two phase delays, ϕ_p and ϕ_s, can be slightly different because the reflection phase of the mirrors can be different for s and p polarized light.

The eigen vectors of M^+ are the eigen polarizations of the cavity, and represent the electric field vectors, which repeat their particular state of polarization after traveling once around the resonator. In our case, these two vectors are $\binom{1}{0}$ corresponding to p polarized light, and $\binom{0}{1}$ corresponding to s polarized light . The propagation matrix for an electric field along an eigen polarization, E_n, simply becomes λ_n^+, which corresponds to the eigen value of the propagation matrix for E_n.

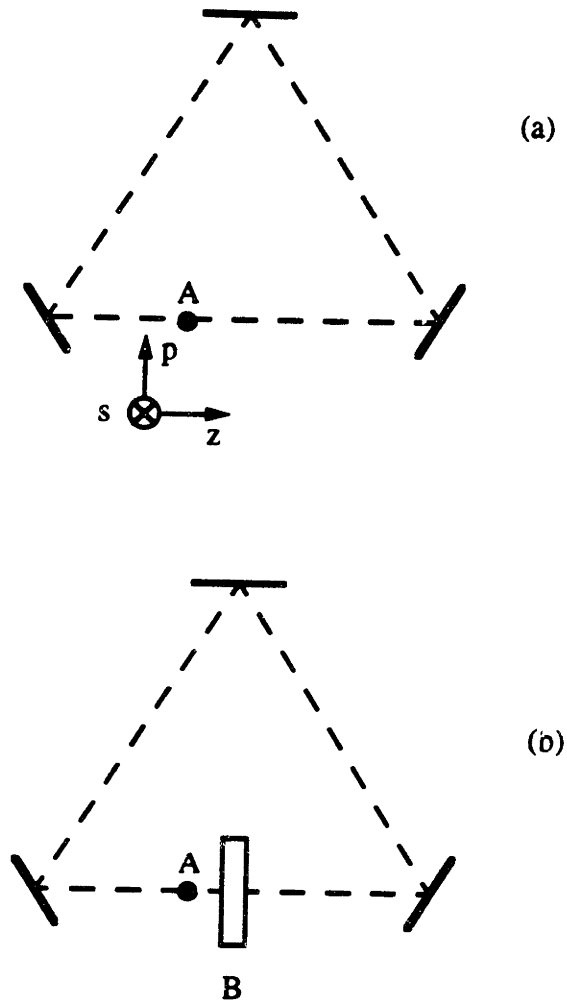

Figure 3.4.1. Illustration of a triangular ring cavity (a) without any intracavity elements and (b) with an intracavity birefringent element B

Let us now consider the case where an electric field along one of the eigen polarizations, E_n, is launched into the cavity. The output field of the resonator, E_o, is given by an infinite sum of the round trip reflections inside the resonator, which becomes:

$$E_o = \frac{t^2}{1 - \lambda_n^+} E_i \tag{3.4.4}$$

where t is the transmission coefficient of the input/output mirrors, M_1 and M_2. Thus, the resonance frequency of the cavity for the eigen polarization E_n, depends only on the eigen value of M^+ for E_n.

In the absence of rotation, we can extend these arguments to a beam traveling in the opposite direction, such that the clockwise propagation matrix M^- is given by:

$$M^- = \begin{pmatrix} R_p^* e^{-j\xi_p} & 0 \\ 0 & R_s^* e^{-j\xi_s} \end{pmatrix} = (M_o)^* \tag{3.4.5}$$

The complex conjugate of R_p and R_s simply accounts for the fact that the direction of propagation has now been changed. As can be seen, the eigen values for M^-, i.e. λ^-, are given by:

$$\lambda_n^- = (\lambda_n^+)^* \tag{3.4.6}$$

Once we consider the difference in the direction of propagation, these eigenvalues represent the same resonance frequencies along the clockwise and counterclockwise directions.

The addition of an intracavity optical element, B, inside the ring resonator, as shown in figure 3.4.1b, can be represented by the inclusion of the transfer matrix of this element, B^+, in M^+, i.e.:

$$M^+ = B^+ M_o \tag{3.4.7}$$

It should be noted that this changes both the eigen vectors and the eigen values of M^+.

If the element B is reciprocal, then it is a straight forward matter to show that the clockwise transfer matrix for B, B^-, is given by:

$$B^- = (B^+)_t^* \tag{3.4.8}$$

where the subscript t denotes the transpose of a matrix. Thus the clockwise propagation matrix, M^-, starting from point A, in figure 3.4.1.b, is given by:

$$\begin{aligned} M^- &= (M_o)^* B^- \\ &= (M_o)_t^* (B^+)_t^* \\ &= (B^+ M_o)_t^* \end{aligned} \tag{3.4.9}$$

since in our case $(M_o)^* = (M_o)_t^*$. We can easily see that in this case we must have $\lambda_n^+ = (\lambda_n^-)^*$, so that the resonance frequencies along the clockwise and counterclockwise

directions are identical. Thus if the intracavity element, B, is reciprocal, it does not create a separation between the clockwise and counterclockwise cavity resonance frequencies.

By contrast, if B is a nonreciprocal element, such as a Faraday cell in the presence of an axial magnetic field, then B^- is no longer equal to $(B^+)_t^*$ and as a result $\lambda_n^+ \neq (\lambda_n^-)^*$, representing a separation between the clockwise and counterclockwise resonance frequencies.

3.4.2. Observation of the Effects due to an Intracavity Birefringent Element

In this section we will present the behavior of a ring resonator with an intracavity birefringent element. The ring resonator is made from three mirrors defining a triangular cavity with a perimeter of 0.72 m, corresponding to a FSR of 420 MHz. One of the mirrors is mounted on a PZT, labeled PZT_c. The birefringent element is a $\lambda/2$ plate with antireflection coatings. The states of polarization of the two input beams, E^+ and E^-, can be controlled by polarization controllers PC^+ and PC^- respectively. Each of these controllers consists of a $\lambda/2$ and a $\lambda/4$ plate as shown in figure 4.3.2. The output intensities along the clockwise and counterclockwise directions of the cavity are monitored by photodetectors PD^- and PD^+ respectively.

Originally the fast axis of the intracavity $\lambda/2$ plate, B, is along the s axis. Here, the cavity has two eigen polarizations, s and p. In order to show the resonance lineshapes of the cavity we observe the output of the cavity along either clockwise or counterclockwise direction while applying a linear voltage sweep V_s to PZT_c. The voltage V_s can be expressed as an equivalent frequency by equating the voltage corresponding to one free spectral range of the ring cavity with 420 MHz. Figure 3.4.3 shows the output PD^+ as a function of V_s, when E^+ is p polarized, indicating a cavity resonance with a linewidth of 8 MHz. This lineshape corresponds to a finesse of approximately 50. Similarly Figure 3.4.4 shows the output of PD^+ as a function of V_s, when E^+ is s polarized, indicating a cavity resonance with a linewidth of 4 MHz. This lineshape corresponds to a finesse of 100.

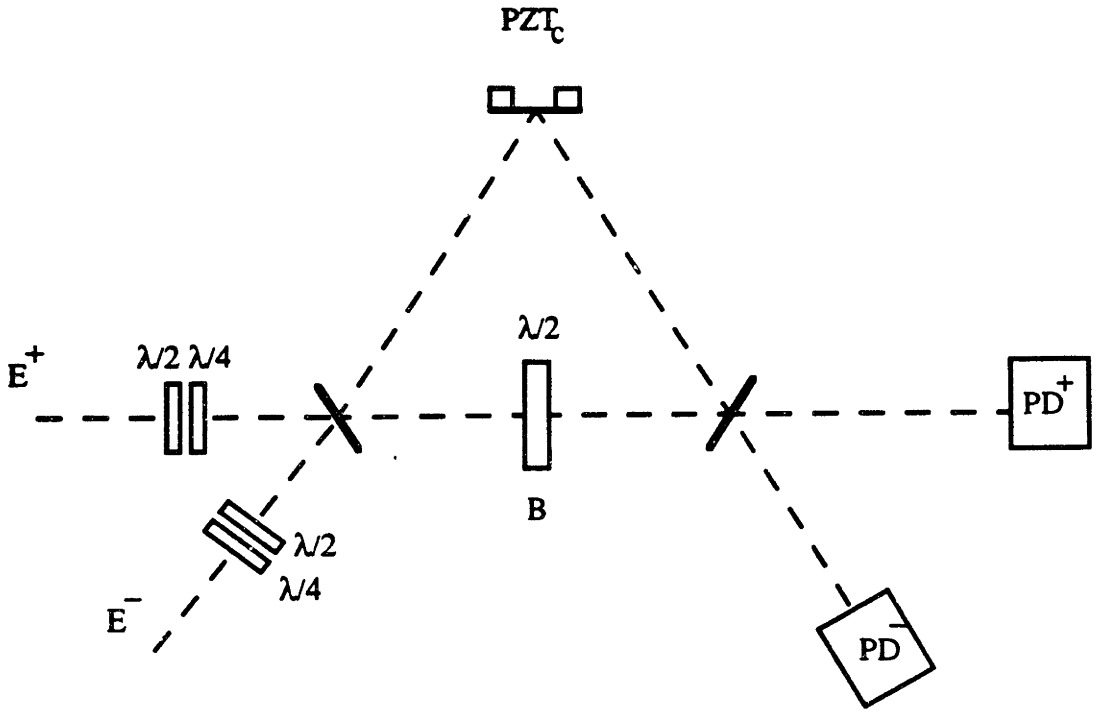

Figure 3.4.2. Schematic diagram for the setup used in evaluating the effects of an intracavity $\lambda/2$ plate

The s and p eigen polarizations of the cavity, in this case, have almost identical resonance frequencies. In order to observe the separation between the s and p resonances we set the polarization of E^+ to s and that of E^- to p. The top trace of Figure 3.4.5 shows the output of PD^- as a function of V_s, indicating the resonance due to p polarization, and the bottom trace of figure 3.4.5 shows the output of PD^+ as a function of V_s, indicating the resonance due to s polarization. This figure shows a separation of approximately 4 MHz between the centers of the s and p resonances.

We now rotate the element B by an angle θ_b, to observe its effect on the resonance frequencies and eigen polarizations of the cavity. Figures 3.4.6a through d show the output of PD^+ as a function of V_s, for a p polarized input beam. In figure 3.4.6a the fast axis of B is along s axis representing θ_b=0 the figure shows the cavity resonance lineshape associated

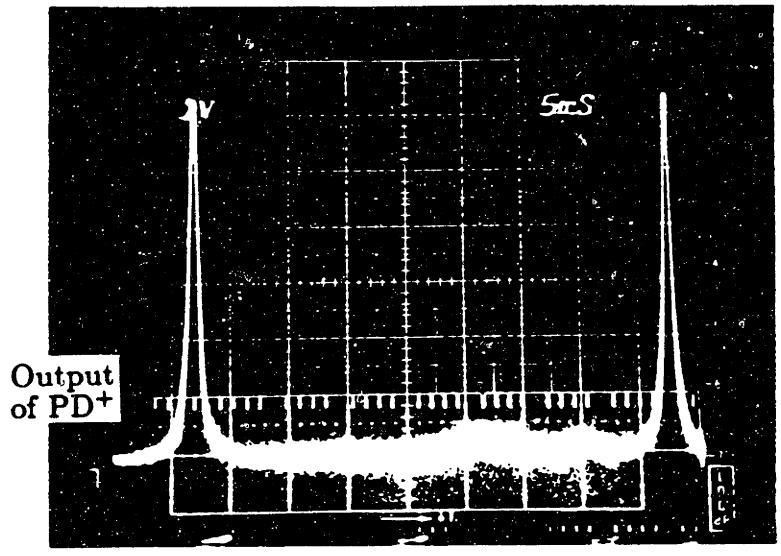

Figure 3.4.3. Output of PD^+ as a function of V_s for p polarized input when the fast axis of B is along s axis

with p polarization, as previously observed in figure 3.4.3. Figures 3.4.6b through f show the output of PD^+ as a function of V_s, when θ_b is varied from 15 to 75 degrees. These figures demonstrate simultaneous excitation of both eigen polarizations of the cavity for the p polarized input. Thus the cavity eigen polarizations are no longer purely s or p. Furthermore, as shown in figures 3.4.6b through d, the relative separation between the two eigen polarizations of the cavity changes as B is rotated. This indicates a change in the resonance frequencies of the cavity.

Now let us see if the rotation in B affects the clockwise resonance lineshapes differently from the counterclockwise resonance lineshapes. Figure 3.4.7b shows the output of PD^- (top trace) and that of PD^+ (bottom trace) as a function of V_s, when both E^+ and E^- are p polarized, and the fast axis of B is along the s axis, indicating no apparent shift between the clockwise and counterclockwise resonances. Figures 3.4.7a,c,d show the output of PD^- (top trace) and that of PD^+ (bottom trace) as a function of V_s, when the rotation angle of B is -1.5,1.5, and 3 degrees respectively. These figures indicate the excitation of both eigen

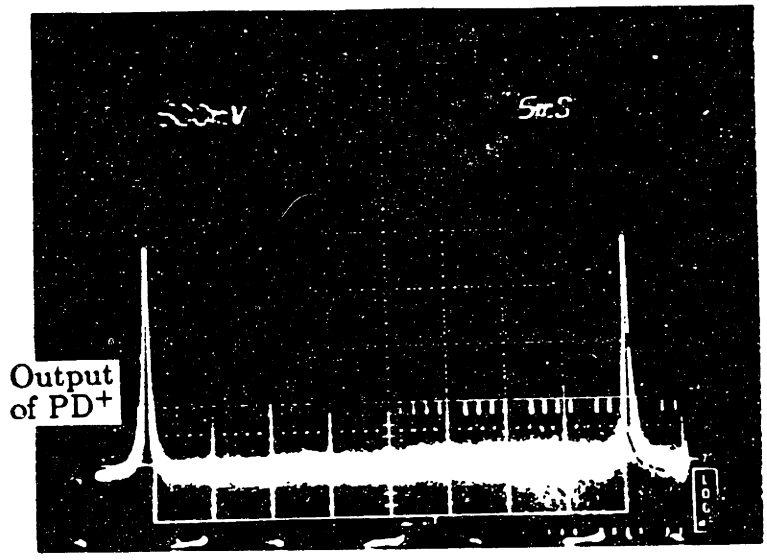

Figure 3.4.4. Output of PD^+ as a function of V_s for s polarized input when the fast axis of B is along s axis

polarizations of the cavity by the input beams. These figures further demonstrate that when both E^+ and E^- have the same state of polarization, then the mixture of the two cavity resonances for the clockwise direction is identical to that for the counterclockwise direction.

We will next demonstrate that the polarization of E^+ and E^- can be adjusted so that they excite only one eigen polarizations of the ring cavity. Figure 3.4.8a shows the output of PD^- (top trace) as well as that of PD^+ (bottom trace) as a function of V_s, when θ_b is -1.5°. Here, both E^+ and E^- are p polarized. The figure shows the excitation of both eigen polarizations of the cavity, as previously observed in figure 3.4.7a. Figure 3.4.8b shows the output of PD^- (top trace) and that of PD^+ (bottom trace) as a function of V_s, when the polarization of E^- is adjusted by PC^- and E^+ is still p polarized, clearly demonstrating the excitation of only one cavity eigen polarization along the clockwise direction. Figure 3.4.8c shows the output of PD^- (top trace) and that of PD^+ (bottom trace) as a function of V_s, when the state of polarization of E^+ is adjusted by PS^+, and that

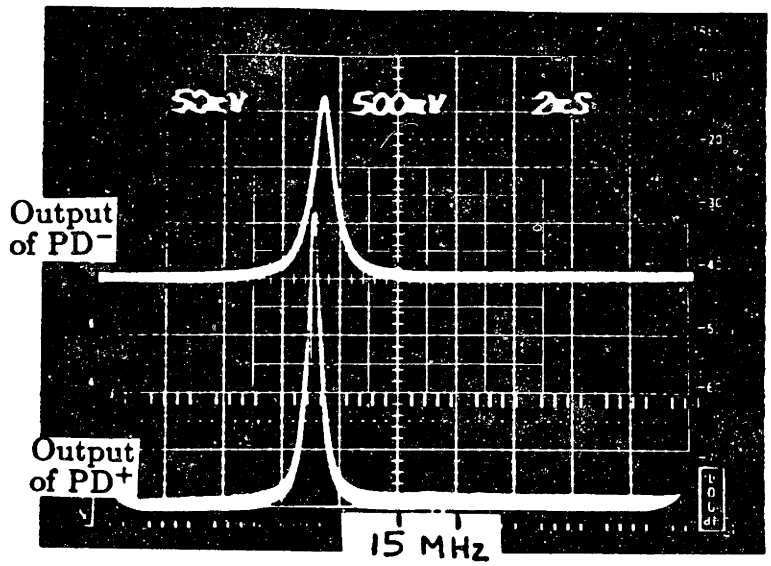

Figure 3.4.5. Output of PD^- (top trace) and that of PD^+ (bottom trace) as a function of V_s, when E^- is p polarized, E^+ is s polarized, and the fast axis of B is along s axis, indicating a 4 MHz separation between the p and s resonance linecenters.

of E^- is adjusted by PC^-. The figure clearly demonstrates the excitation of a single eigen polarization along both directions of the cavity. Figure 3.4.8d shows the outputs of PD^+ and PD^- as a function of V_s with an expanded scale, demonstrating that the clockwise and counterclockwise resonances are apparently symmetric, and there is no apparent separation between their centers.

We will now demonstrate the effect of a polarizer on the output of the cavity, while the polarizations of E^+ and E^- are both aligned with a cavity eigen polarization. Figure 3.4.9 shows the revised experimental setup. The setup now includes a polarizer, PL, placed on the output of the cavity along the counterclockwise direction. We choose $\theta_b = -1.5°$, and align the polarization of E^+ and E^- so that we have only one cavity eigen polarization as shown in figure 3.4.8c. Figure 3.4.10a shows the output of PD^- (top trace) and that of PD^+ (bottom trace) as a function of V_s, when the transmission axis of PL is along the s axis. The figure indicates an attenuation in the intensity of the output of PD^+ as compared

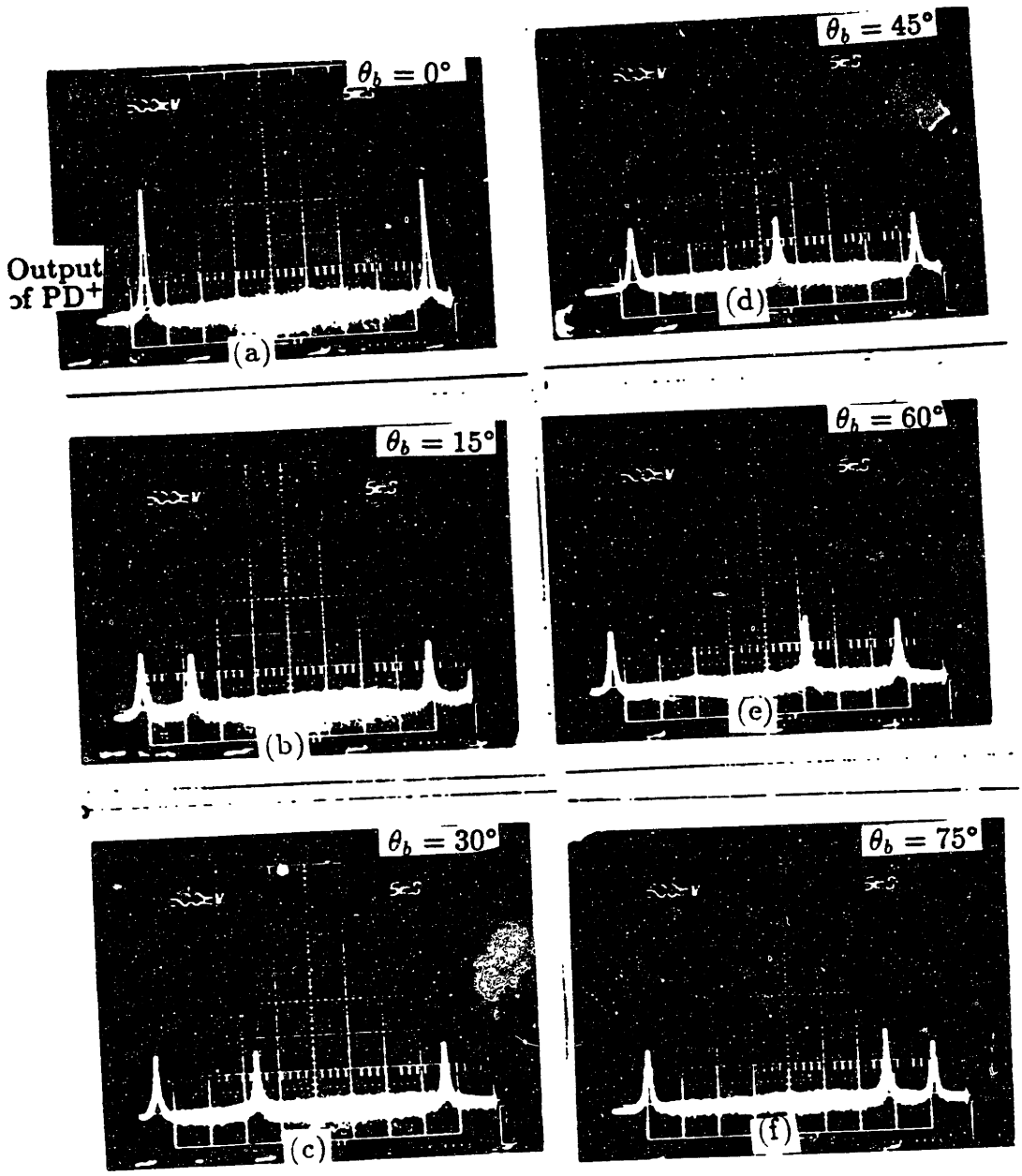

Figure 3.4.6. Output of PD^+ as a function of V_s when E^+ is p polarized and the rotation angle of B, θ_b, is varied from 0 to 75° with respect to s axis indicating excitation of both eigen polarization of the cavity by the p polarized light when $\theta_b \neq 0$

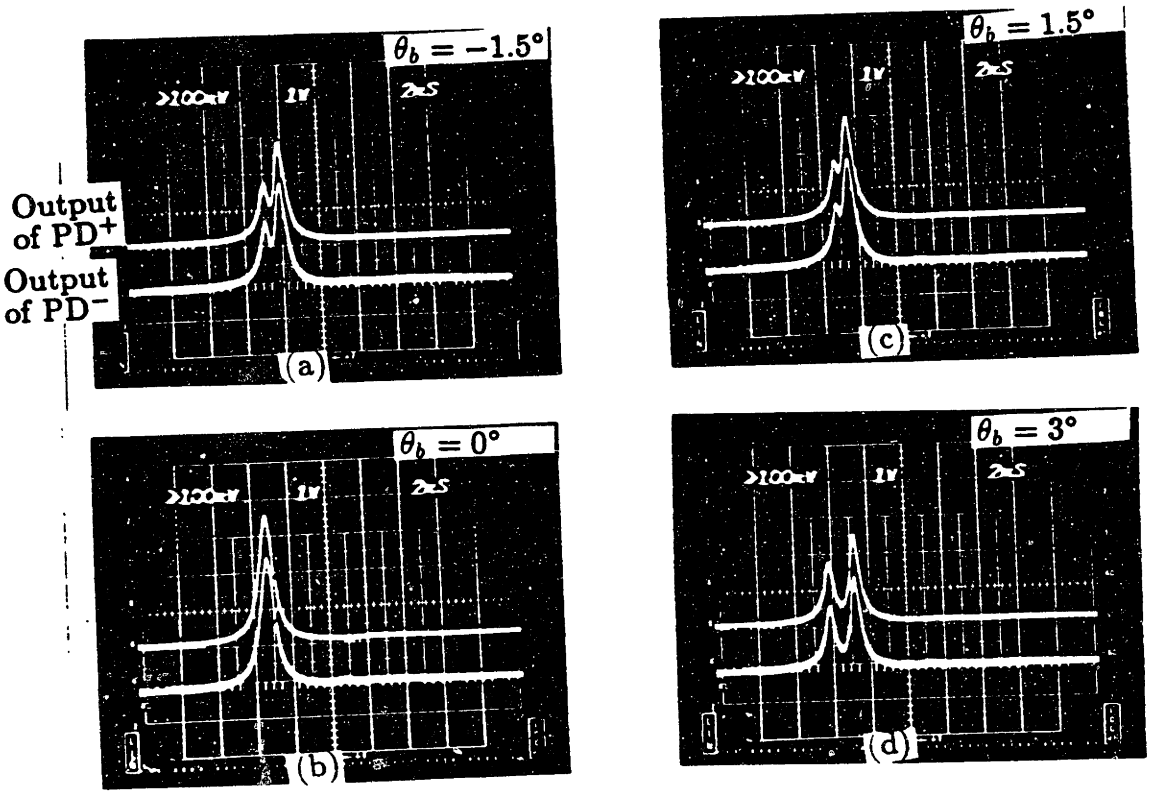

Figure 3.4.7. Output of PD^- (top trace) and that of PD^+ (bottom trace) as a function of V_s, when both E^+ and E^- are p polarized, for rotation angle of B, θ_b varying from -1.5° to 3 ° with respect to s indicating the same mixture of the two eigen polarization of the cavity along both clockwise and counterclockwise directions

with the output observed in figure 3.4.8c. Figure 3.4.10b shows the output of PD^- (top trace) as well the output of PD^- on an expanded scale (bottom trace) as a function of V_s indicating no distortion in the counterclockwise resonance due to the polarizer, and no apparent shift between the clockwise and counterclockwise resonances.

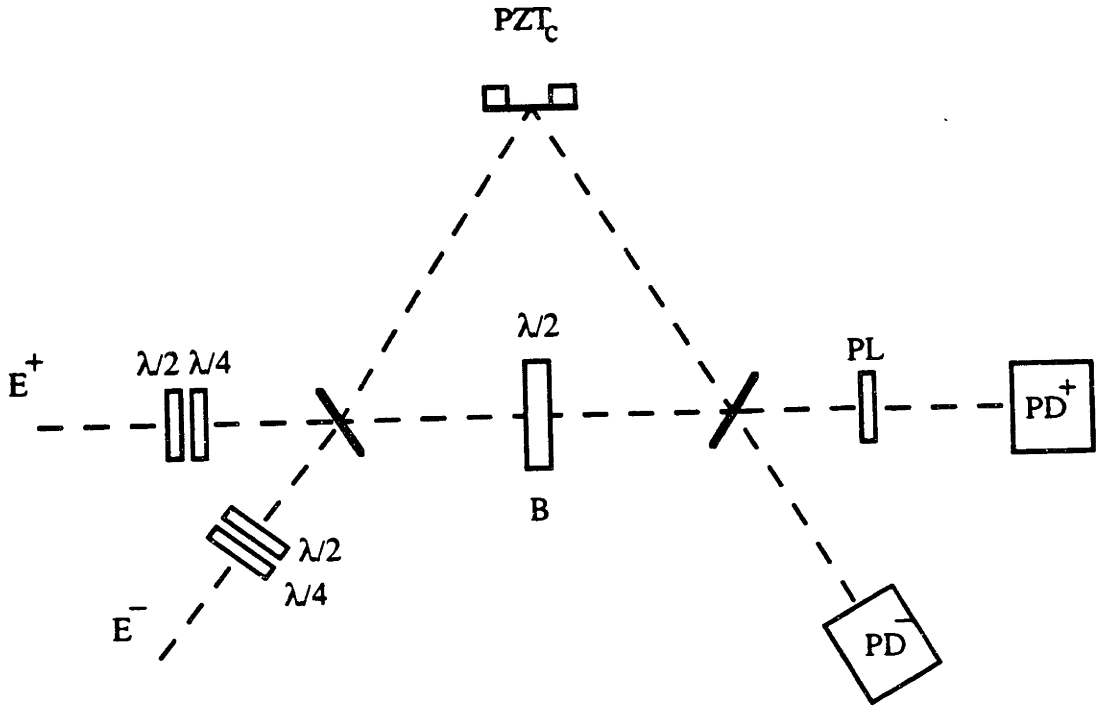

Figure 3.4.9. Revised schematic diagram for the setup with a polarizer on the counterclockwise output

Next, we demonstrate the effects of rotating PL, when the states of polarization of E^+ and E^- are not the same as a cavity eigen polarization We set $\theta_b = 6°$, with both E^+ and E^- p polarized. Figure 3.4.11a shows the output of PD^- (top trace) and that of PD^+ (bottom trace) as a function of V_s, when the transmission axis of PL is along the s axis, indicating a noticeable difference between the amplitude ratio of the two excited eigen polarizations along the clockwise and counterclockwise directions. This difference

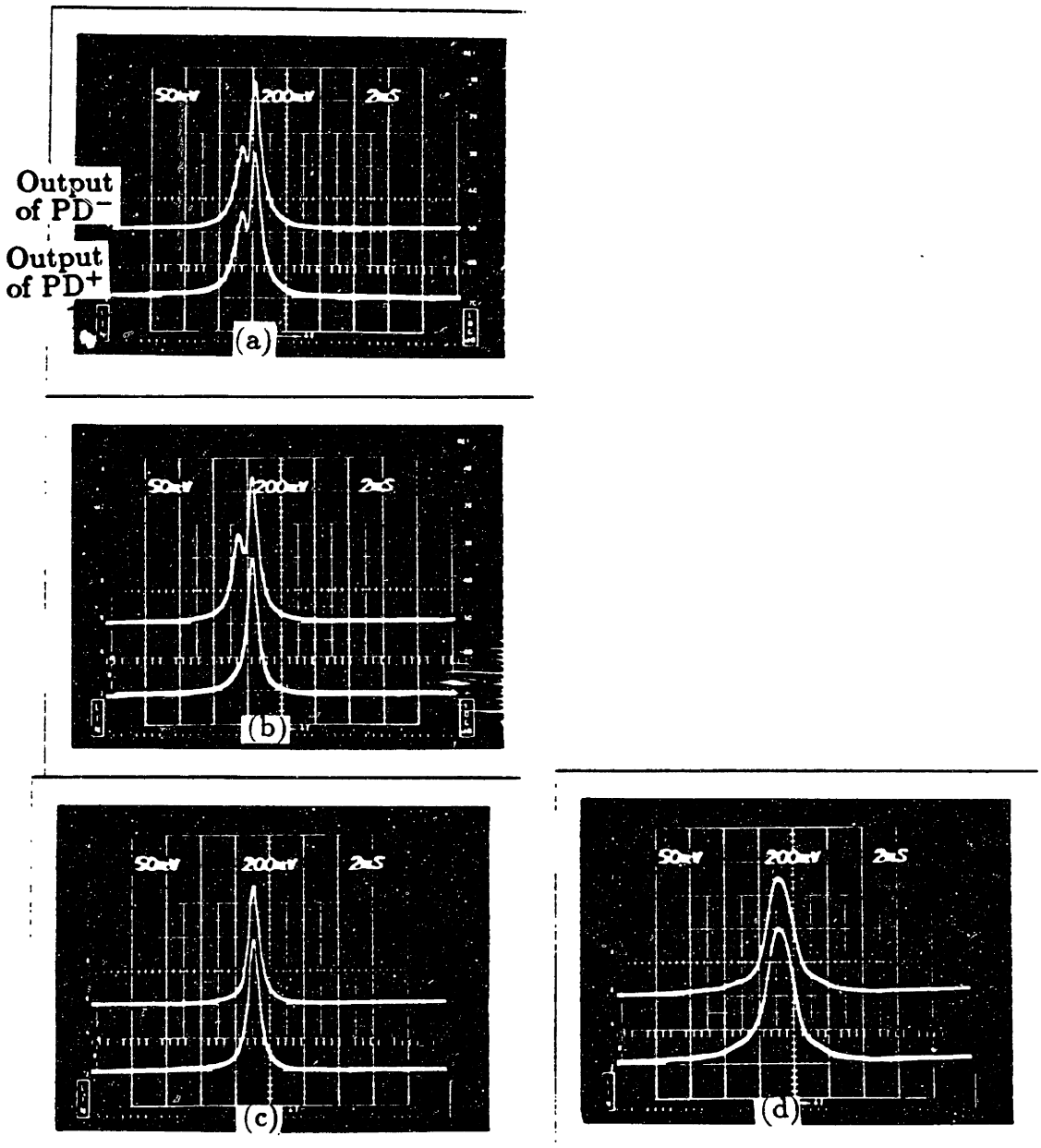

Figure 3.4.8. Output of PD^- top trace and that of PD^+ (bottom trace) as a function of V_S for $\theta_b = -1.5°$, when both E^+ and E^- are p polarized (b) only E^- is p polarized and the polarization of E^+ is adjusted to get only one eigen polarization (c) the polarizations of both E^+ and E^- are adjusted to excite only one eigen polarization (d) expanded scale version of (c).

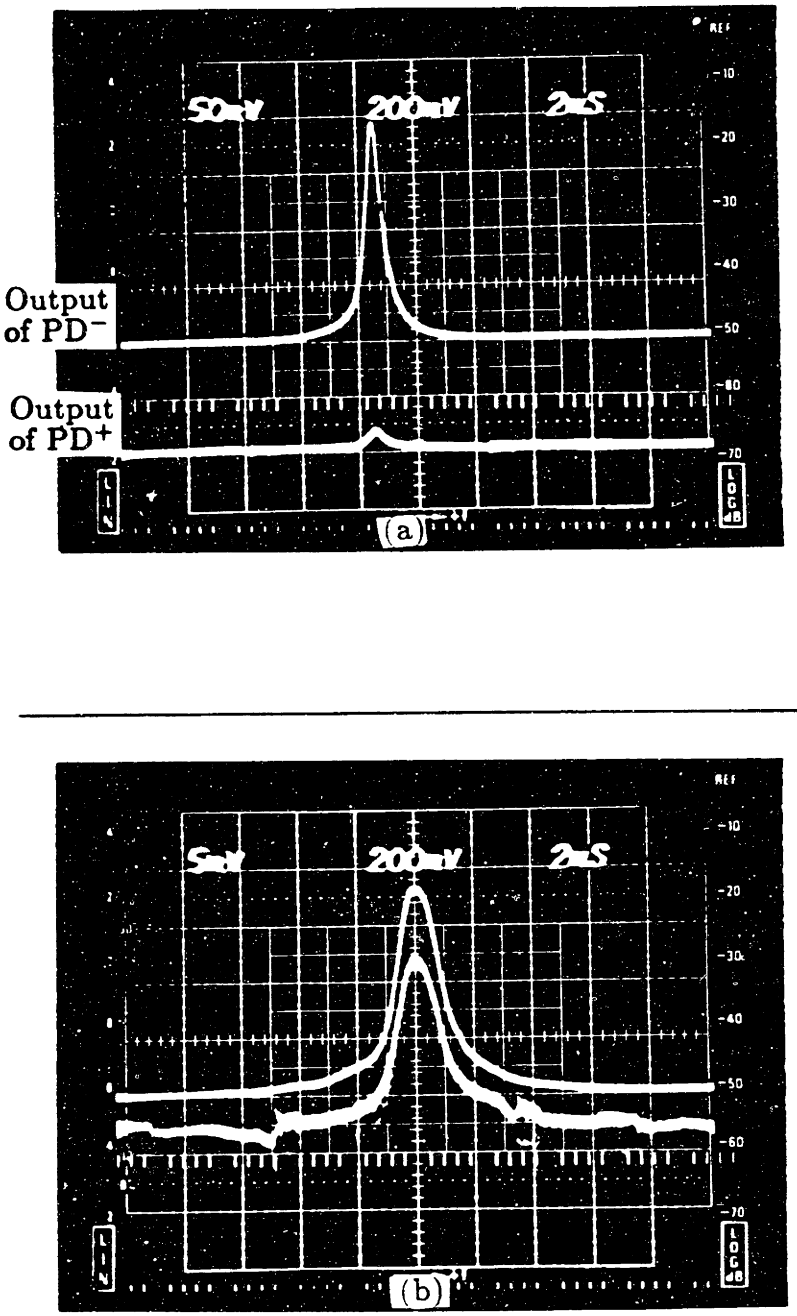

Figure 3.4.10. Output of PD^- (top trace) and that of PD^+ (bottom trace) for $\theta_b = -1.5°$, when the polarizations of E^+ and E^- are set along an eigen polarization of the cavity with (a) polarizer rotated so the transmission axis is along p axis. (b) same as before but the output of PD^+ has a magnified scale.

inevitably leads to an apparent separation between the clockwise and counterclockwise resonance frequencies via mode pulling.

Figures 3.4.11 b and c show the output of PD^- (top trace) and that of PD^+ (bottom trace) as a function of V_s, when PL is aligned along a 45° angle with respect to the s axis (in figure 3.4.11b) and along the p axis (in figure 3.4.11c). These figures indicate a variation in the ratio between the amplitudes of the two excited resonances as the polarizer is rotated, thus also indicating a variation in the separation between the clockwise and counterclockwise resonance frequencies as a function of the rotation angle of PL.

Thus, if the states of polarization of the input beams are not exactly aligned with an eigen polarization of the cavity, a polarizer, or any other optical element with a polarization sensitive transmission, on the output of the cavity an cause an apparent resonance shift between the clockwise and counterclockwise resonance frequencies.

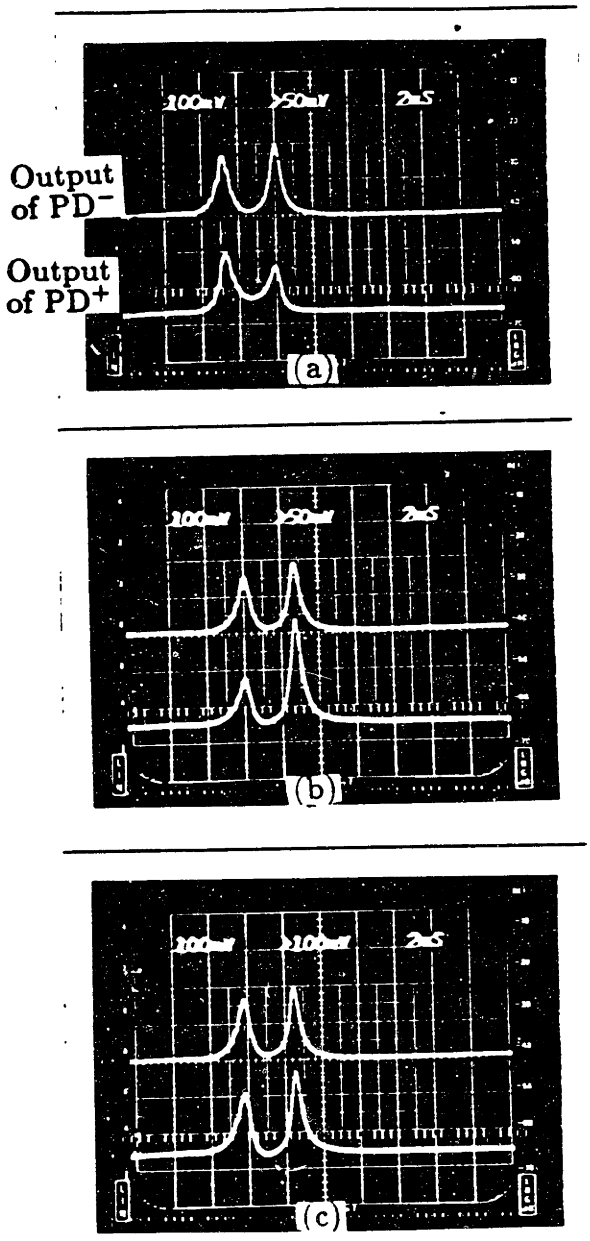

Figure 3.4.11. Output of PD^+ (top trace) and that of PD^- (bottom trace) as a function of V_s for $\theta_b = 6°$, when the transmission axis of PL is (a) along s axis (b) 45° with respect to s axis (c) along p axis.

CHAPTER 4

The Fiberoptic PRG

In this section we describe the behavior and major error sources of a passive fiber ring resonator gyroscope which uses a fiber ring resonator as the rotation sensing element. In contrast to the bulkoptic resonator, a fiber cavity can be made to have only one transverse mode by using a single mode fiber, and to have only one eigen polarization by using single polarization fiber.

4.1. The Experimental Setup

Figure 4.1.1 shows the experimental setup for the passive fiber ring resonator gyroscope. As shown in the figure, the fiber setup is very similar to the bulkoptic setup in figure 3.1.1 with a fiberoptic ring resonator replacing the bulkoptic cavity. The only difference is that the fiber resonator is operated in "reflection" as compared to the bulkoptic resonator which is operated in "transmission". Thus, in our fiber resonator we observe an intensity dip when the cavity is on resonance instead of an intensity peak associated with a resonator in transmission.

The laser used in the setup is a 2 mW He-Ne laser oscillating primarily at 1.15 μm. This wavelength is appropriate for our fiber cavity, which is designed for single mode operation around 1 μm. [In addition to the 1.15 μm output, the laser also oscillates at two other wavelengths, corresponding to two weak Ne lines, which can be easily separated by a diffraction grating.] The laser cavity is 35 cm long which corresponds to a FSR of 400 MHz. Since the bandwidth of the Ne gain curve at 1.15 μm is approximately 750 MHz, the laser can oscillate in one or at most two longitudinal modes of the laser cavity. As in the case of the He-Ne laser described in section 3.1, single frequency operation can be achieved by holding a longitudinal mode of the laser cavity at the center of the Ne gain curve.

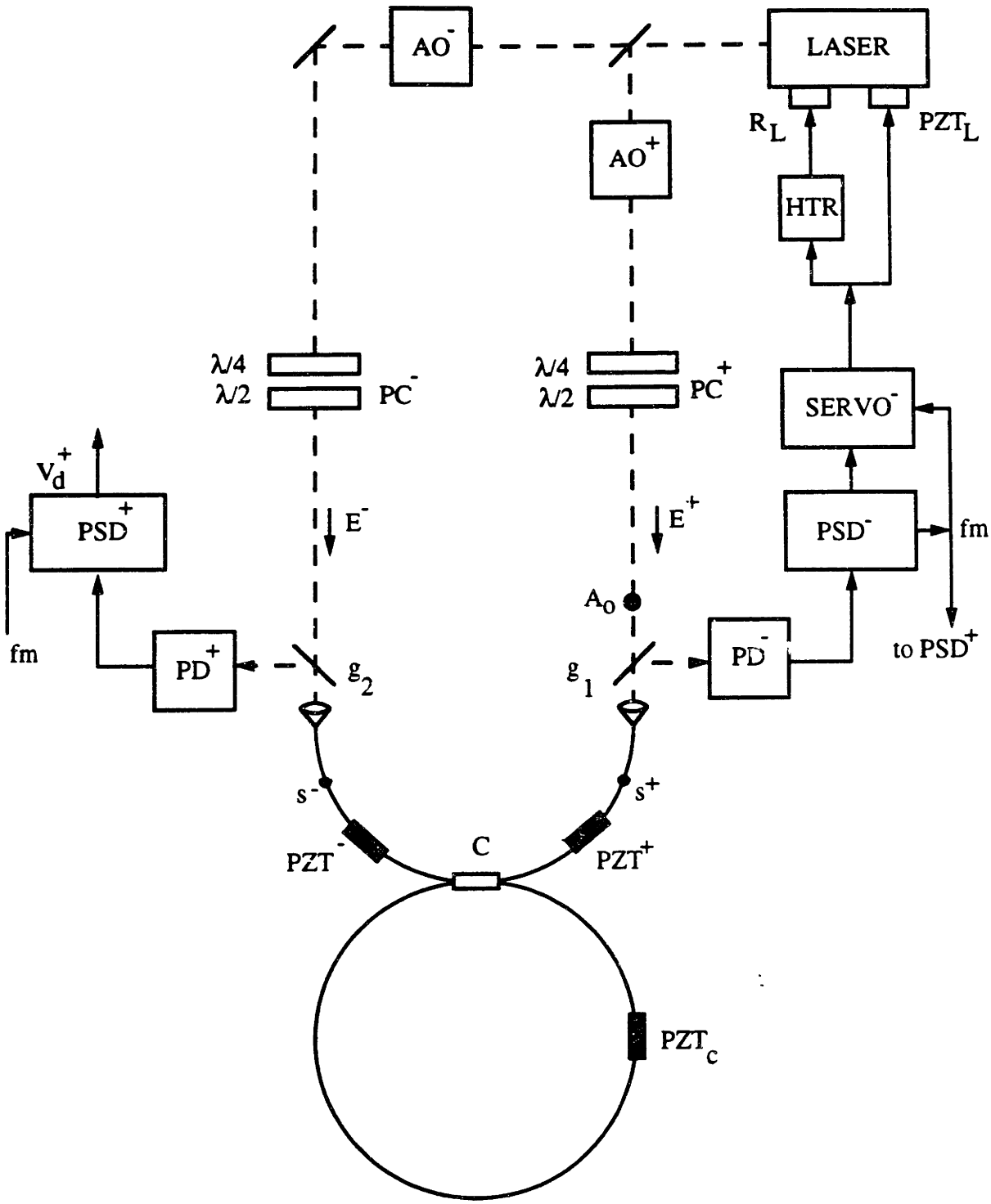

Figure 4.1.1. Schematic setup for the fiber PRG

Similar to the bulkoptic setup, the laser output is split into two beams and each beam is frequency shifted by a separate AO to yield the two beams E^+ and E^-. The AOs used

in the fiber setup are similar to the ones described in section 3.1, and operate at an AO drive frequency of 40 MHz, however, the AO crystals in the fiber setup have a special coating to reduce reflection at 1.15 μm.

After the AOs, E^+ and E^- are passed through polarization controlling elements PC^+ and PC^-, respectively, each consisting of a $\lambda/2$ and a $\lambda/4$ plate, which align the state of polarization of the input beams with an eigen polarization of the fiber cavity. E^+ and E^- are then launched into the fiber resonator arms. The ends of the two resonator arms are cut and polished at a 7° inclination so as to reduce the reflections at these ends, and there are two splices, s^+ and s^-, on the resonator arms, which reflect approximately 0.25% of the light intensity, and transmit 85% of the intensity.

E^+ and E^- then enter the fiber cavity through the coupler C, where E^+ is coupled into the counterclockwise direction of the cavity and E^- is coupled into the clockwise direction. A fraction of the output of the cavity along the clockwise direction is split off by a piece of glass, g_1, and directed to the photodetector PD^-. Similarly, a fraction of the counterclockwise output of the cavity is split off by the piece of glass g_2, and directed to photodetector PD^+. The photodetectors PD^+ and PD^- are identical to those described for the bulkoptic setup in section 3.3.1, except that they use Rofin Inc. model 7462 photodiodes which have a responsivity of 0.32 A/W at 1.15 μm, corresponding to a quantum efficiency of approximately 35%.

The fiber PRG setup has a primary loop, similar to that in the bulkoptic setup described in section 3.1, which holds the frequency of E^- at the center of a clockwise resonance by controlling the frequency of the laser via PZT_L. The components of the primary loop in the fiberoptic setup are identical to those described for the bulkoptic setup in section 3.1. The modulation frequency f_m, used in the fiber setup is 10 kHz.

The open loop output of the fiber PRG is V_4^+, obtained by demodulating the output of PD^+ via PSD^+, exactly as described for the bulkoptic setup in section 3.1. The expression

for V_d^+ in a fiber setup is also identical to that presented in equation 3.1.1 for the bulkoptic setup, i.e.:

$$V_d^+ = \kappa \Delta f_\Omega \tag{4.1.1}$$

where, as previously described, κ is the slope of the discriminant voltage, and Δf_Ω is the separation between the clockwise and counterclockwise resonance frequencies, that is proportional to the rotation rate Ω, as indicated by equation 1.3.4. Thus, in this section we have described the similarities and differences between the fiberoptic PRG setup and the bulkoptic PRG setup. In the next section, we will describe the fiberoptic resonator in more detail.

4.1.1. Parameters of the Fiberoptic Resonator

The fiber ring resonator is made of a continuous loop of a single mode non polarization preserving fiber and a polished evanescent wave coupler. The length of the resonator fiber is 25 m, which corresponds to a FSR of 7.7 MHz, and it is wrapped around a cylinder with a diameter of 7.5 cm. The optical perimeter of the resonator can be perturbed by stressing a segment of the resonator fiber via a piezoelectric transducer, PZT_c, as shown in figure 4.1.1.

Figure 4.1.2a shows the counterclockwise output of the cavity (for example), measured by PD^+, as a function of the laser frequency, when the state of polarization of E^+ is the same as one of the cavity eigen polarizations. The figure shows the dip at resonance previously described, and the 7.7 MHz free spectral range of the cavity. Figure 4.1.2b shows the output of the cavity when E^+ has an arbitrary state of polarization, demonstrating the two cavity eigen polarizations separated by 2.2 MHz.

The eigen polarization shown in figure 4.1.2a is expanded in figure 4.1.3, demonstrating an asymmetric lineshape[18,19] with a linewidth of approximately 30 kHz corresponding to a finesse of 250. The other eigen polarization of the cavity is also distorted and has the same linewidth. By adjusting the coupler C, linewidths as narrow as 20 kHz have been observed, corresponding to a finesse of 400, but the cavity resonance remains asymmetric. This resonance asymmetry of the fiber cavity in reflection is due to having a lossy coupler. We have included an explanation for this effect in appendix A.

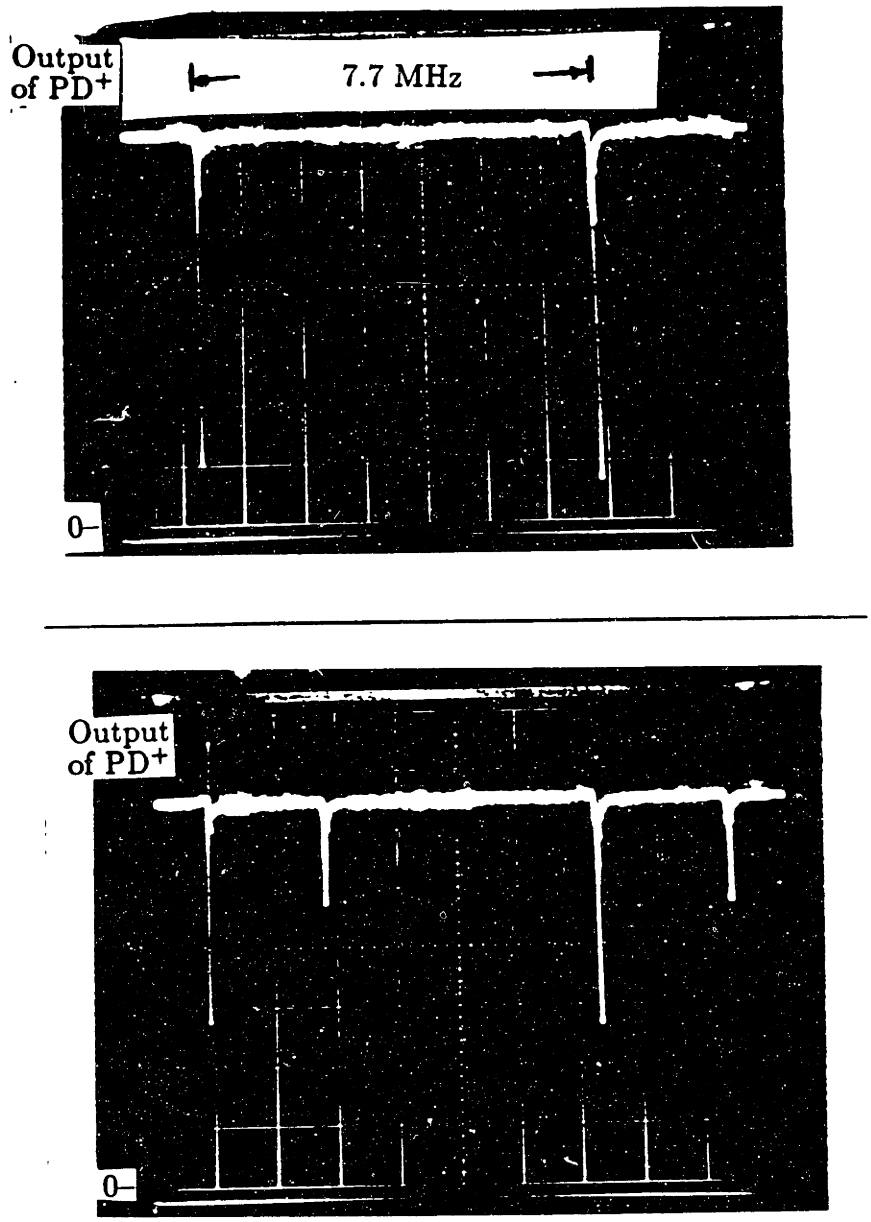

Figure 4.1.2. Output of PD^+ as a function of the laser frequency indicating (a) a single cavity eigen polarization (b) both cavity eigen polarizations

4.1.2. Preliminary Data on the Behavior of the Fiber PRG

In this section, we will present preliminary data on the open loop behavior of the fiber PRG. As mentioned previously, during the open loop operation of the fiber PRG, the primary loop holds the frequency of E^- at the center of a clockwise resonance. The

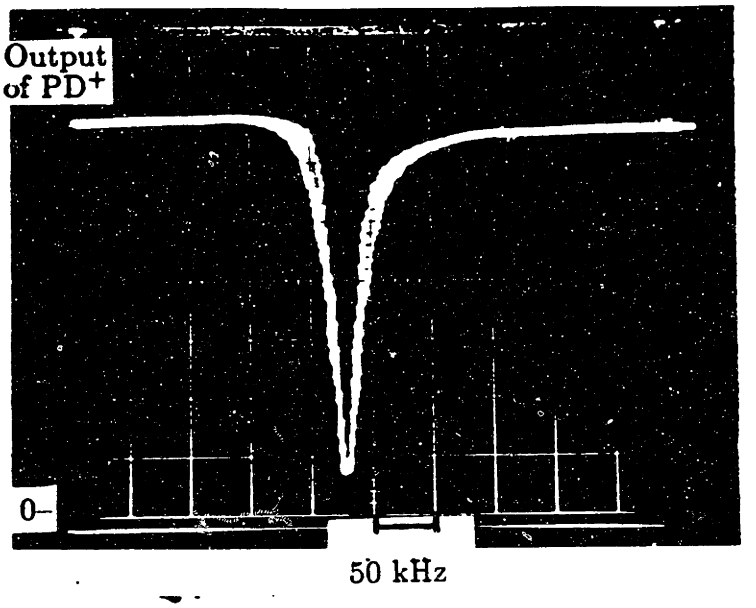

Figure 4.1.3. Output of PD^+ as a function of laser frequency indicating the resonance lineshape

operation of this primary loop is identical to that for a bulkoptic PRG described in section 3.1.2. Also mentioned previously, the open loop output of the fiber PRG is the output of PSD^+, i.e. V_d^+.

Figure 4.1.4 shows V_d^+ as a function of time, with a 100 ms 6 dB/octave filter, for a 1 Hz frequency difference between E^+ and E^-, indicating a sinusoidal variation with a peak to peak amplitude of ± 750 Hz. This sinusoidal variation is due to coherent backscattering and is analogous to that observed in figure 3.2.1b for the bulkoptic case. Backscattering issues in the fiber PRG are discussed in detail in section 4.2, and for now we can simply remove this oscillation by lowpass filtering.

In order to demonstrate the measurement of rotation by our fiber PRG, we use a rotatable platform, similar to that used in the bulkoptic setup and described in section 3.2.4, to rock the fiber cavity back and forth sinusoidally around an axis perpendicular to the plane of the resonator. Figure 4.1.5a shows the rotation angle of the platform, θ_p, as a function of time, indicating an amplitude of 5° and a period of 9 sec, which results in

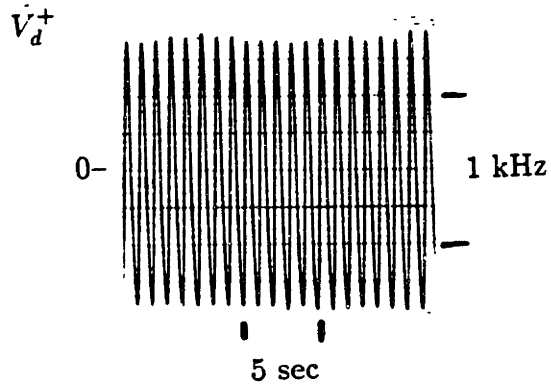

Figure 4.1.4. V_d^+ as a function of time with a 100 ms 6db/octave filter, when there is a 1 Hz frequency difference between E^+ and E^- indicating a coherent backscattering with amplitude of ±750 Hz

a sinusoidal variation in angular velocity with a peak of 3.5 deg/sec. In order to see the variations of V_d^+ due to rotation, we remove the sinusoidal oscillation of figure 4.1.4 by increasing the frequency difference between E^+ and E^- to 10 Hz, and observing V_d^+ with a 1 sec 6 dB/octave lowpass filter. Figure 4.1.5b shows the the variation of V_d^+ as a function of time in the presence of the applied rotation, indicating a 90° phase shift between V_d^+ and θ_p and a peak to peak V_d^+ variation of 5.2 kHz. The 90° phase shift between V_d^+ and θ_p has already been observed in our bulkoptic setup as shown in figures 3.2.10. The 5.2 kHz peak to peak variation of V_d^+ in figure 4.1.5b corresponds to a variation in angular velocity from −3.5 deg/sec to +3.5 deg/sec which gives a Sagnac scale factor of 750 Hz per deg/sec. From equation 1.3.4 we calculate the predicted value for this scale factor. In our case we have:

$$\begin{cases} A = 4.4 \times 10^{-3}\text{m}^2 \\ P = 0.23\text{m} \\ \lambda_o = 1.15\ \mu\text{m} \\ n = 1.48 \end{cases}$$

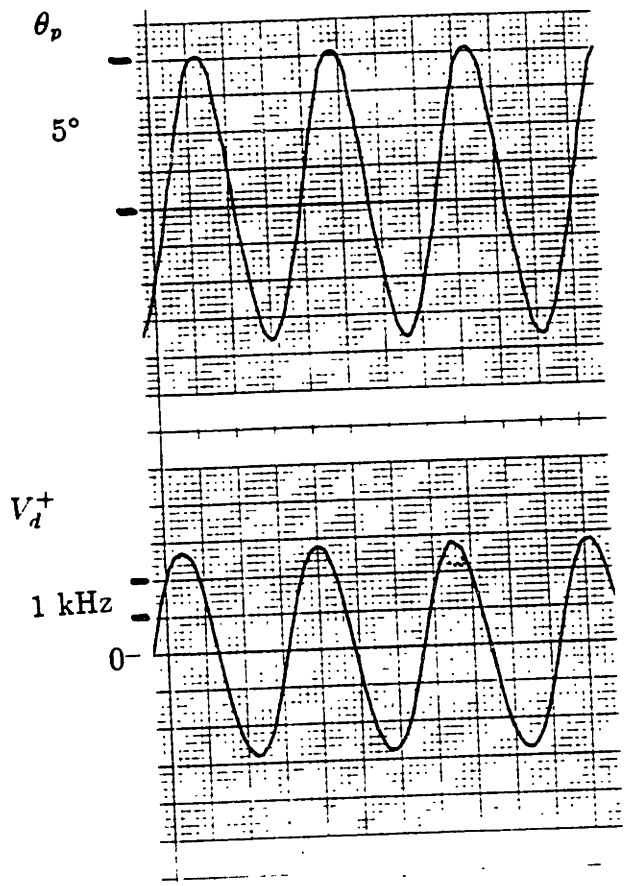

Figure 4.1.5. Demonstration of the operation of the gyroscope (a) the applied rotation angle of the platform as a function of time (b) corresponding variation in V_d^+ with a 1 sec 6db/octave filter and a 10 Hz frequency difference between E^+ and E^-

which gives a predicted scale factor of 750 Hz per degree/sec, and is in excellent agreement with the experimental observations.

In the next sections we will present the influence of backscattering, variations in the state of polarization of the input beams and the optical Kerr effect on the performance of the gyroscope.

4.2. Backscattering in Fiberoptic PRG

As discussed in section 3.2, backscattering of light in a ring resonator causes drifts. The backscattering inside a fiber ring resonator is due to Rayleigh scattering[20] in addition to numerous discrete scattering centers along the fiber, which in our case results in a larger overall scattering coefficient than that observed for the bulkoptic setup. In this section, we study the effects of backscattering on the open loop behavior of the fiber gyroscope.

4.2.1. Coherent Backscattering in a Fiber PRG

In section 3.2.1, we calculated and demonstrated the coherent backscattering error in our bulkoptic passive resonator gyroscope. The existence of coherent backscattering in our fiber PRG has already been demonstrated in figure 4.1.4, where we observed an oscillation of V_d^+ representing a peak to peak variation of 1.5 kHz.

We will now examine the variations in the amplitude of this coherent backscattering error as a function of the fiber resonator perturbations. We perturb the fiber resonator by applying a 500 V p-p saw-tooth voltage to PZT_c as shown in figure 4.2.1b, thereby stressing a segment of the cavity fiber. This causes approximately 8 MHz of variation in the resonance frequency of the cavity, and the primary loop changes the laser frequency to compensate for this variation. Similar to the conditions in figure 4.1.4, we observe the coherent backscattering, by setting a 1 Hz frequency difference between E^+ and E^- and passing V_d^+ through a 100 ms 6 dB/octave filter. Figure 4.2.1a shows V_d^+ as a function of time indicating a change in the peak to peak amplitude of the coherent backscattering error as a function of the voltage applied to PZT_c. As shown in the figure, the peak to peak amplitude of this error varies from 300 Hz to almost 2.3 kHz. Also, at several points in the figure, such as the one marked A, the coherent backscattering error becomes distorted. This distortion will be examined further in section 4.2.2.

We observe a variation in the magnitude of the coherent backscattering as a function of stressing the fiber cavity because the overall backscattering in our setup includes the

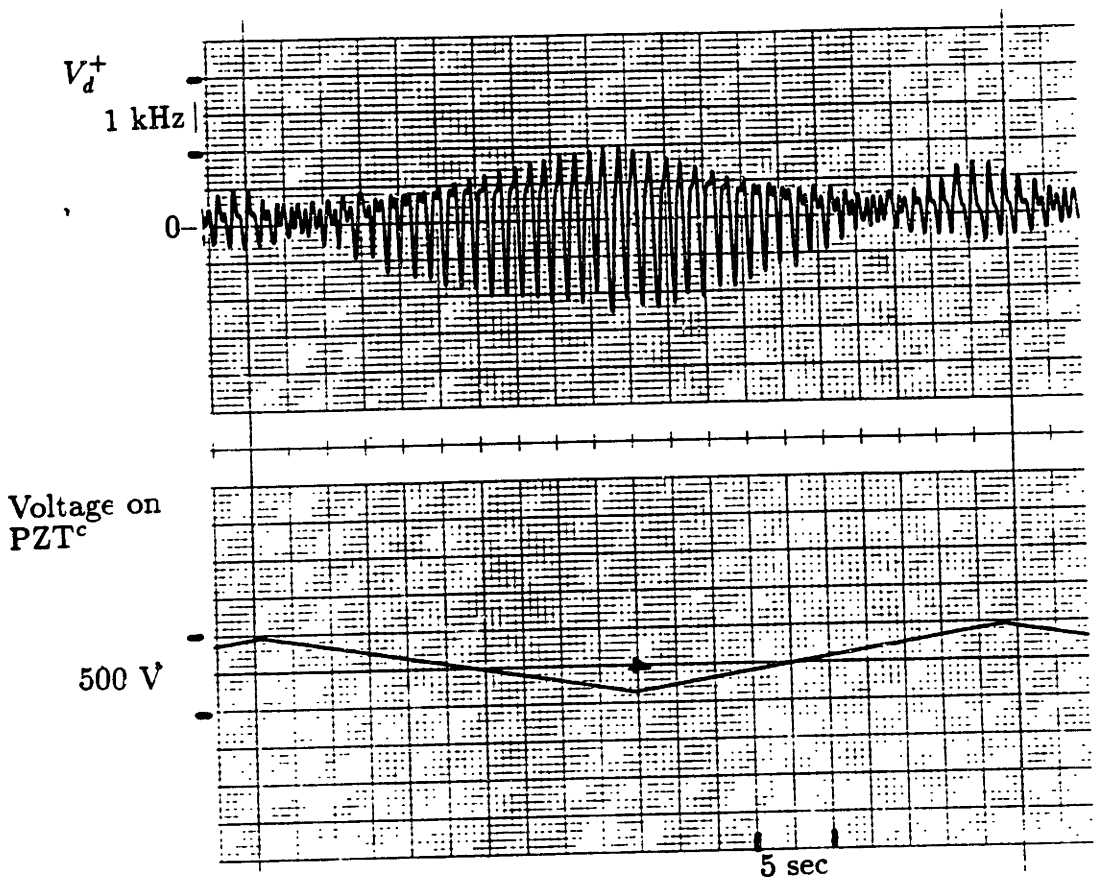

Figure 4.2.1. (a) V_d^+ as a function of time indicating oscillations due to coherent backscattering (b) voltage applied to PZT_c as a function of time

contribution of several scatterers, both inside and outside of the ring cavity. By stressing the cavity fiber, we vary the propagation phase between these scatterers and thus change the overall sum of their contribution to coherent backscattering.

As mentioned previously, in addition to the scatterers inside the ring cavity, we also

have strong scatterers outside the ring cavity, namely the two splices s^+ and s^-. These splices are located on the fiber resonator arms, as shown in figure 4.1.1, and, as mentioned in section 4.1, each of them reflects approximately 0.25% of the light intensity, and thus contributes to coherent backscattering as described in section 3.2.1b. Let us now examine the contribution of one of the splices, s^+, to the coherent backscattering error.

Figure 4.2.2b shows a 650 V p-p saw-tooth voltage applied to PZT^+, which stresses the fiber segment between s^+ and the coupler C. Figure 4.2.2a shows V_d^+, as a function of time indicating a change in the magnitude of the coherent backscattering error as the fiber arm is stressed. As shown in the figure, the magnitude of this error changes from 2.8 kHz to 5.0 kHz p-p. This change is due to external scattering only, since the scatterers inside the cavity are left unperturbed.

In summary, we have observed a maximum peak to peak magnitude of approximately 5 kHz for the coherent backscattering error, which is due to both internal and external scatterers. By using equation 3.2.7, which gives the amplitude of the backscattering error in terms of the internal scattering coefficient, we obtain a worst case estimate of 1.0×10^{-3} for the internal backscattering coefficient, which is three orders of magnitude larger than that observed for the bulkoptic case in section 3.2.1. In the next section we will demonstrate the elimination of the coherent backscattering error by a carrier suppression technique, similar to that described in section 3.2.2.

4.2.2. Elimination of Coherent Backscattering

As demonstrated in section 3.2.2, the coherent backscattering error in our bulkoptic resonator setup was removed by suppressed carrier phase modulation of E^+. To demonstrate the elimination of coherent backscattering error in the fiber setup, we also apply a suppressed carrier phase modulation by reflecting E^+ from a mirror, M_j, which is mounted on a sinusoidally vibrating piezoelectric transducer, as shown in figure 4.2.3. The frequency of this phase modulation or jitter is labeled f_j. In order to observe the change in coherent

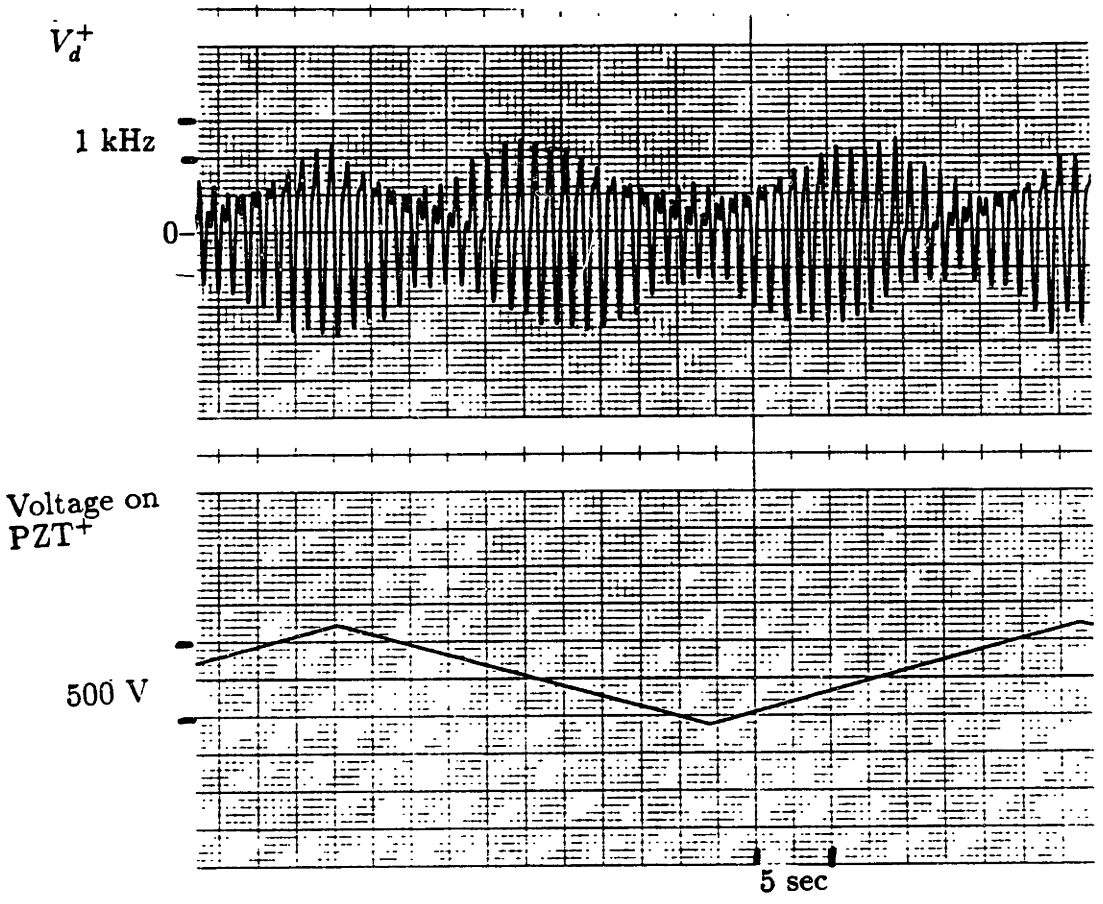

Figure 4.2.2. V_d^+ as a function of time indicating oscillations due to coherent backscattering (b) voltage applied to PZT^+ as a function of time

backscattering error due to this applied phase jitter, we set a 1 Hz frequency difference between E^+ and E^- and observe V_d^+ with a 100 ms 6 dB/octave filter.

Section *A* of figure 4.2.4 shows V_d^+ as a function of time, when there is no phase jitter, indicating a coherent backscattering error with a peak to peak amplitude of 2.7 kHz. In

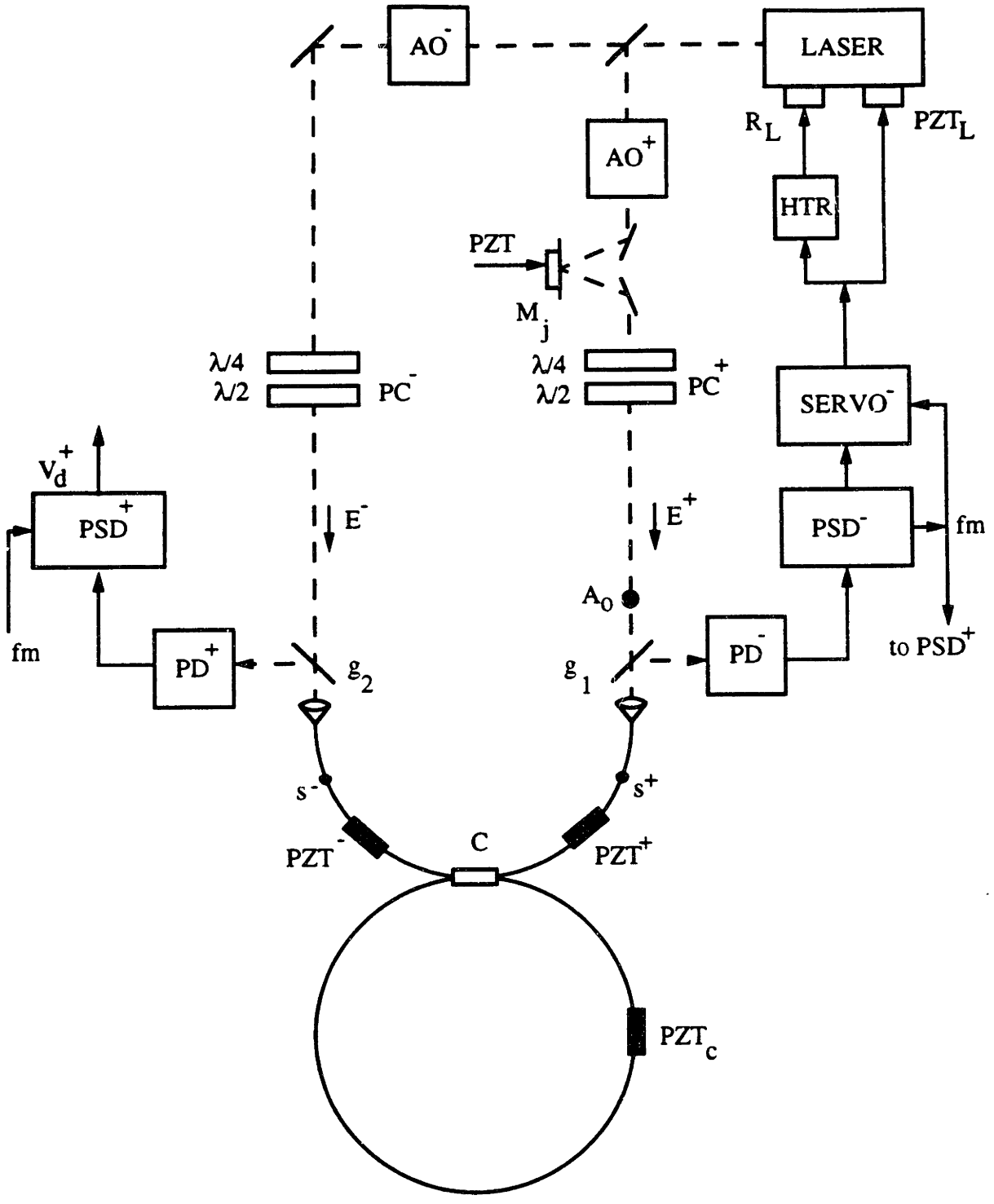

Figure 4.2.3. Revised schematic diagram with the phase modulating mirror M_j.

section B, a sinusoidal phase jitter with $f_j = 140$ Hz is applied to the setup, and its

amplitude is adjusted to eliminate the coherent backscattering error. This is analogous to the carrier suppression demonstrated for the bulkoptic PRG in figure 3.2.6a. In the fiber case, we also obtained a carrier suppression of approximately 5×10^{-3} which, similar to the bulkoptic case, is limited by the purity of the sinusoidal phase jitter.

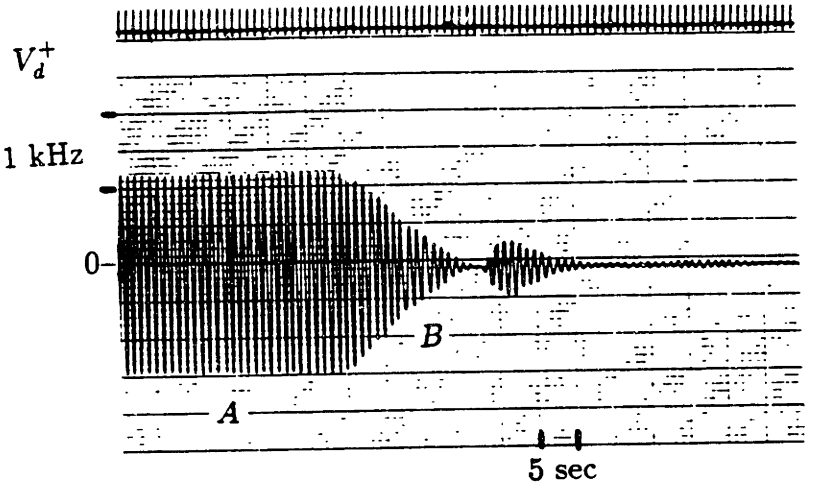

Figure 4.2.4. V_d^+ as a function of time for a 1 Hz frequency difference between E^+ and E^- in the presence of a phase jitter with $f_j = 140$ Hz when $\delta\phi_j$ was varied.

The suppression of coherent backscattering is not always as good as that represented in figure 4.2.4. For example, figure 4.2.5 shows the case where there is an incomplete suppression of the coherent backscattering. In section A of figure 4.2.5, we observe the coherent backscattering error with a peak to peak amplitude of 1.6 kHz in the absence of phase jitter. In section B, phase jitter at $f_j = 140$ Hz is applied to E^+, and we observe

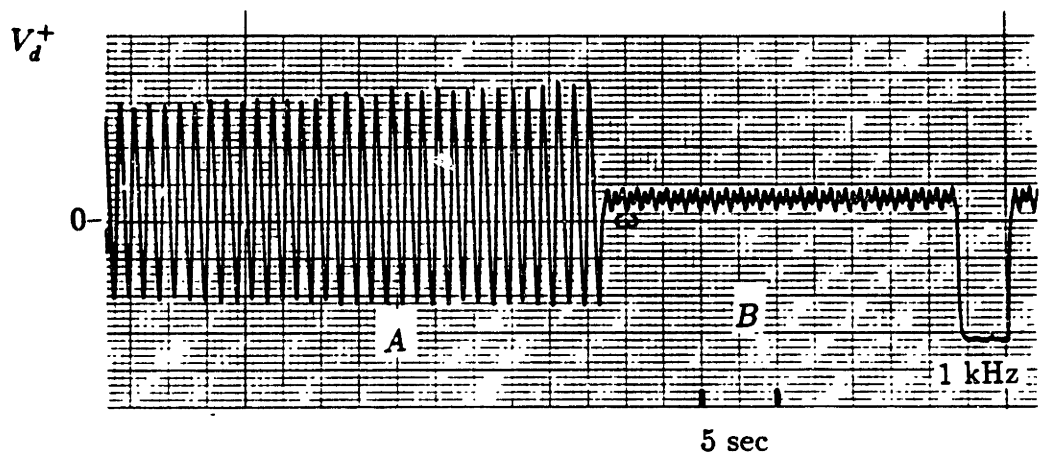

Figure 4.2.5. V_d^+ as a function of time for a 1 Hz frequency difference between E^+ and E^- (a) no phase jitter (b) phase jitter with $\delta\phi_j$ adjusted

that, although we have suppressed the 1 Hz oscillation due to coherent backscattering, we have a large unsuppressed oscillation at 2 Hz, with an equivalent amplitude of ± 75 Hz.

To understand this residual unsuppressed 2 Hz oscillation, we must consider the distortion of the coherent backscattering as demonstrated in region A of figure 4.2.1a. As observed in this region, the coherent backscattering is not a pure sinewave, but has second and higher harmonic components so that we can represent it as a sum of the harmonics of a pure sinewave. In this case, the coherent backscattering error, now labeled Δf_s, is, for example, given by:

$$\Delta f_s = a_1 \sin(\Delta\phi) + a_2 \sin(2\Delta\phi) + \cdots \tag{4.2.4}$$

where $\Delta\phi$ is the phase difference between E^+ and E^-, and a_1 and a_2 are the appropriate amplitude coefficients for $\sin(\Delta\phi)$ and $\sin(2\Delta\phi)$ respectively. Let us now add a sinusoidal

phase jitter to $\Delta\phi$, with an angular frequency of ω_j and a phase excursion of $\delta\phi_j$. With the addition of this phase jitter, the expression for Δf_s in equation 4.2.4 becomes:

$$\begin{aligned}\Delta f_s &= a_1 \sin\left(\Delta\phi + \delta\phi_j \sin(\omega_j t)\right) + a_2 \sin\left(2(\Delta\phi + \delta\phi_j \sin(\omega_j t))\right) + \cdots \\ &= a_1 \sin\left(\Delta\phi + \delta\phi_j \sin(\omega_j t)\right) + a_2 \sin\left(2\Delta\phi + 2\delta\phi_j \sin(\omega_j t)\right) + \cdots\end{aligned} \tag{4.2.5}$$

In section 3.2.2 we demonstrated that if $\delta\phi_j$ is set to 2.4 rad, we can suppress the first term in equation 4.2.5, which represents the fundamental component of the coherent backscattering error. However, at this point, the second term, with the coefficient a_2, has an equivalent phase excursion of $2\delta\phi_j$ =4.8 rad, and is therefore not completely suppressed. Thus we obtain only partial suppression of this second term.

This incomplete suppression of the coherent backscattering may be solved by adding additional carrier suppressed phase jitters at different frequencies so as to remove the residual backscattering effects. In order to demonstrate this, we set a 1 Hz frequency difference between E^+ and E^-, and observe V_d^+ with a 10 ms 6 dB/octave filter. In section A of figure 4.2.6, we observe a slightly distorted coherent backscattering error with a peak to peak magnitude of 2.6 kHz in the absence of phase jitter. In section B, a phase jitter at f_{j1} = 140 Hz is applied to E^+, and its amplitude is adjusted to suppress the coherent backscattering at 1 Hz. The residual backscattering in section B has a peak to peak amplitude of 250 Hz. In section C, the second phase jitter at f_{j2} = 90 Hz is applied to E^+, and its amplitude is adjusted to remove this residual backscattering error. The remaining fluctuations of V_d^+ are studied further in the following sections.

4.2.3. Intensity Backscattering and its Elimination

In our fiber setup, in addition to the coherent backscattering effects, we observe errors due to the intensity of the backscattered light [This intensity effect was negligibly small in our bulkoptic PRG]. To observe the intensity backscattering in the ring resonator, the outputs of PD^- and PD^+ are simultaneously recorded when E^+ is blocked at point A_o, shown in figure 4.1.1. The top trace of Figure 4.2.7 shows the output of PD^- as a function of the

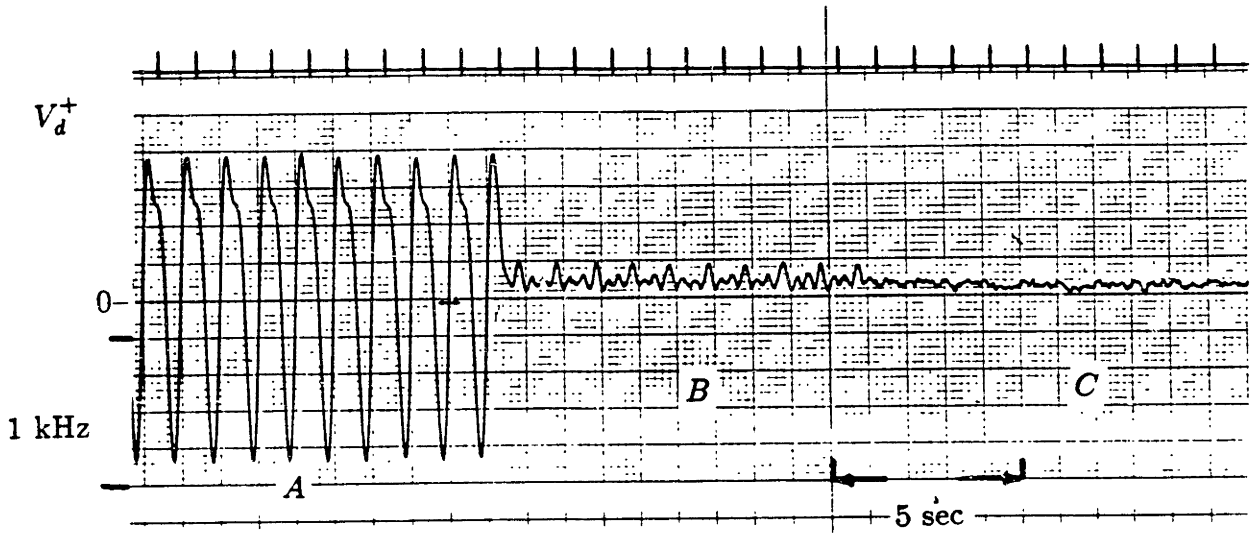

Figure 4.2.6 V_d^+ as a function of time for a 1 Hz frequency difference between E^+ and E^- (a) no phase jitter, (b) a single phase jitter at 140 Hz (c) two simultaneous phase jitters at 140 Hz and 90 Hz

laser frequency indicating the resonance dip for the clockwise direction. As can be seen, the output of PD^- when the cavity is not on resonance is 0.3 V, which corresponds to 20 μW of optical power. The bottom trace of figure 4.2.7 shows the output of PD^+ as a function of the laser frequency, which indicates the backscattered light intensity traveling in the counterclockwise direction of the cavity. The peak backscattered intensity in this case is 10 mV which corresponds to 0.7 μW of optical power. The intensity of the backscattered light is therefore 3.5% of the intensity of light in the forward direction, thus representing an intensity backscattering coefficient, α_i, of 3.5%. In our setup, the intensity backscattering ratio varies from 0 to 5% due to fluctuations of the intracavity backscattering.

The ratio of the peak backscattered electric field in figure 4.2.7 to the peak electric field of the beam in the forward direction is $\sqrt{\alpha_i}$ which is approximately 0.18. This ratio is

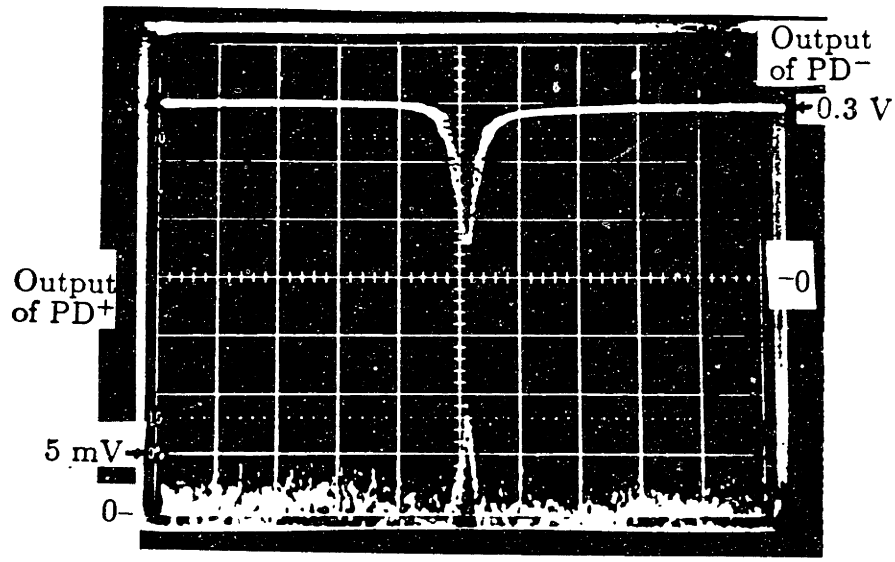

Figure 4.2.7. Output of PD^- as a function of laser frequency when E^+ is blocked (top) corresponding backscattering of E^- observed on PD^+ (bottom)

approximately 100 times larger than the worst case backscattering coefficient of 1.3×10^{-3}, obtained in section 4.2.1. The amplitude of the backscattered field is consistent with the expected resonant enhancement of backscattering inside the ring cavity by a factor of F/π, where F is the finesse of the resonator.

We shall now examine the effect of this backscattered field on the discriminant voltage. The bottom trace of figure 4.2.8 shows the backscattered intensity measured by PD^+, as a function of the laser frequency, for $\alpha_i = 3.5\%$. The top trace of figure 4.2.8 shows the demodulated backscattered intensity as a function of the laser frequency, indicating a small discriminant-like voltage, which corresponds to ± 500 Hz.

In order to demonstrate the drifts due to this demodulated intensity backscattering, we lock the frequency of E^- to the center of a clockwise resonance frequency, and observe the drift of V_d^+, while the beam E^+ is blocked. Figure 4.2.9b shows V_d^- with a 300 ms 12 dB/octave filter, as function of time, indicating V_d^- being held at zero Hz by the primary loop. By comparison, figure 4.2.9a shows V_d^+, on the same frequency scale as the previous

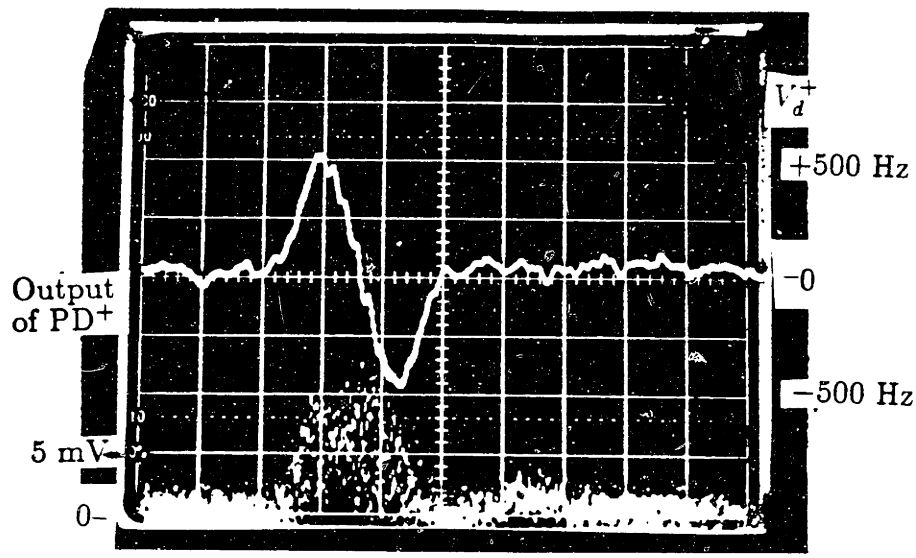

Figure 4.2.8. Backscattering of E^- measured by PD^+ as a function of the laser frequency (bottom) corresponding fluctuation in V_d^+ (top)

figure, indicating a drift of more than 160 Hz. Because of this drift of V_d^+, we must treat the intensity backscattering as an important error source in the gyroscope.

In order to eliminate the drifts due to intensity backscattering, we use two different modulation frequencies to generate the discriminants for the clockwise and counterclockwise directions, as shown in figure 4.2.10. For the clockwise discriminant, the RF drive of AO^- is FM modulated at a rate f_m^-. Similarly, for the counterclockwise discriminant, the drive to AO^+ is FM modulated at a rate of f_m^+. In this case, the intensity backscattering is not demodulated by the PSDs because it has a different modulation frequency.

In our setup, the separate modulation technique was implemented by FM modulating E^+ at $f_m^+ = 2$ kHz, and E^- at $f_m^- = 5$ kHz. We suppressed the coherent backscattering as described in section 4.2.3. Figure 4.2.11 shows V_d^+ and as a function of time for a filter time constant of 300 ms and 12 dB/octave, indicating a gyroscope offset of approximately -50 Hz. In section A of the figure, E^+ is blocked, and we can see that V_d^+ in this section is zero Hz, thus demonstrating the elimination of the intensity backscattering effect. In

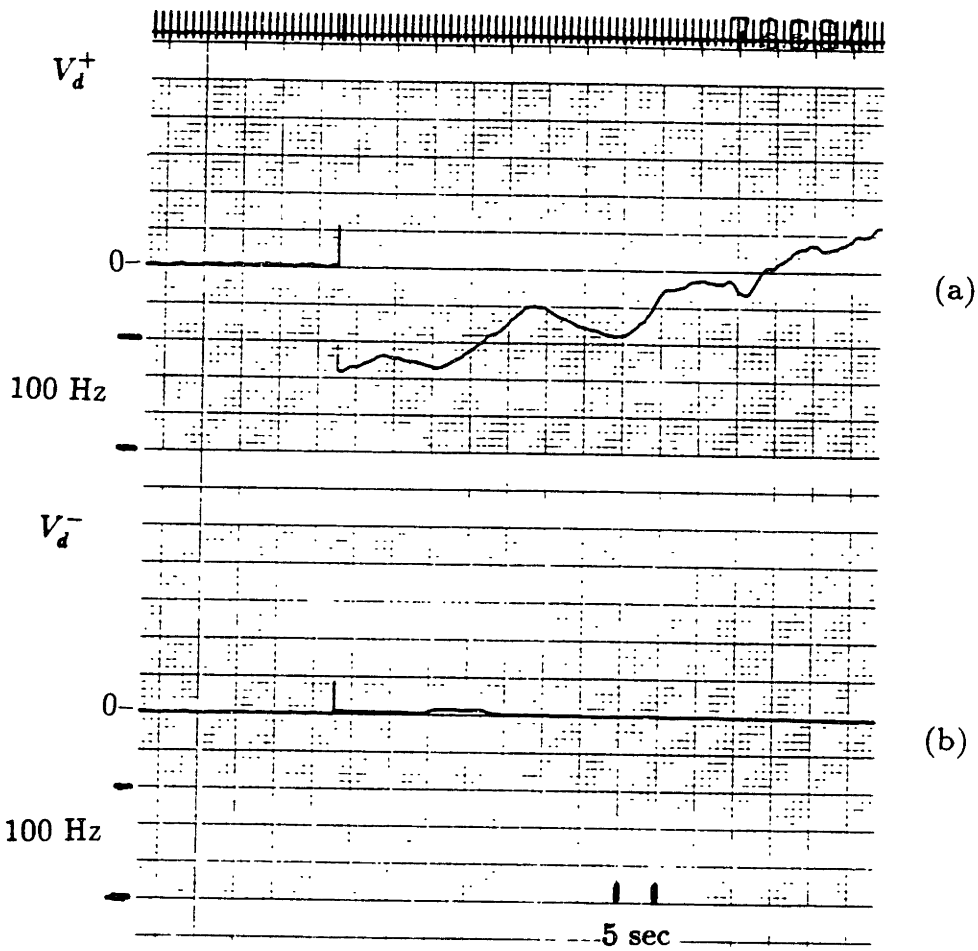

Figure 4.2.9. (a) variation of V_d^+ as a function of time due to backscattering (E^+ is blocked). (b) V_d^- is held at zero by the feedback loop

the next section we will discuss a possible source of the -50 Hz offset observed in figure 4.2.11.

When using separate modulation frequencies, one must be careful that the residual intensity modulation due to the separate frequency modulators is kept very small. In

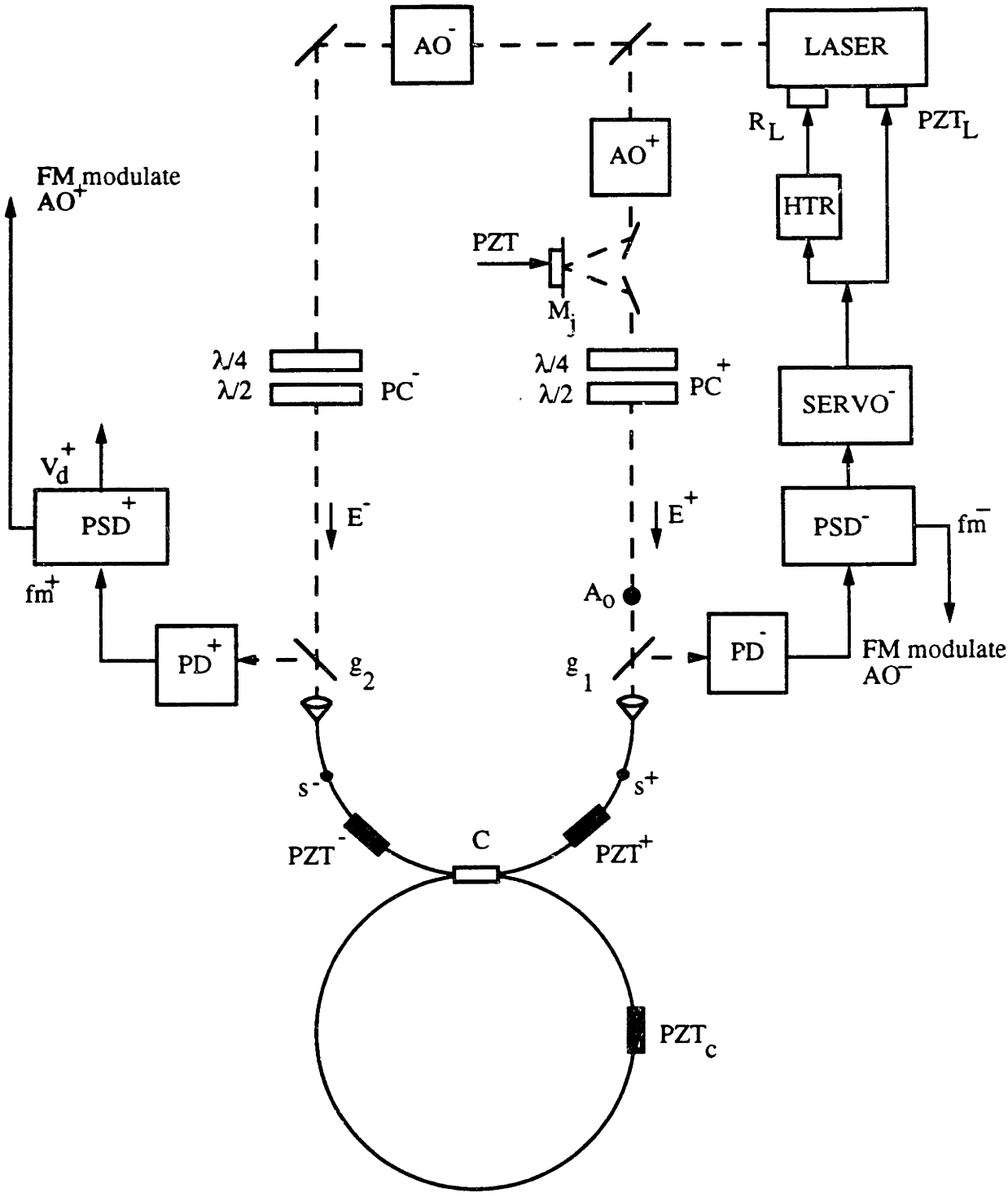

Figure 4.2.10 Revised schematic with separate modulation frequencies

our case these contributions were kept below 1 Hz. Also when using separate modulation frequencies, the gyroscope drifts become sensitive to the asymmetry of the resonance. This

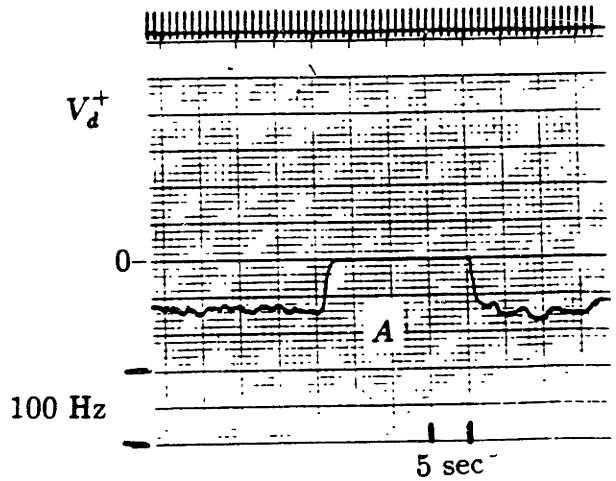

Figure 4.2.11 V_d^+ as a function of time for separate modulation scheme indicating a -50 Hz offset. In section A, E^+ is blocked.

is a very important consideration and is being studied by others in our laboratory.

4.2.4. Double Backscattering and its Elimination

In figure 4.2.11, we observed a -50 Hz offset while the coherent and intensity backscattering errors were both eliminated. In this section we demonstrate that this offset is partially due to double backscattering.

Double backscattering is the result of the back and forth reflection of light from two scattering centers in the setup. Let us consider the example in figure 4.2.12 which shows a simple diagram for double backscattering, where light E^+, is first scattered from s_1, generating the beam E_s^-, and E_s^- is then scattered from s_2, generating the double backscattered beam E_{ds}^+, which travels in the same direction as that of E^+. Analogous to the intensity backscattering described in the previous section, double backscattering can also cause drifts in the output of the gyroscope, and it can not be eliminated by the

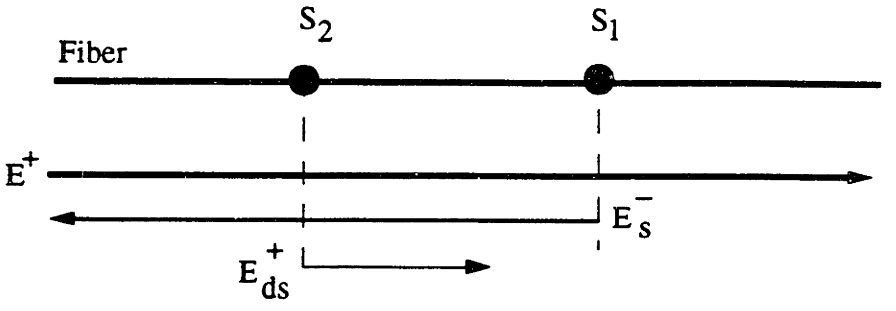

Figure 4.2.12 A simple illustration of double backscattering

separate modulation frequencies, used in the previous section, because it travels in the same direction as the original beam (E^+), and has the same modulation frequency, f_m^+.

We will now demonstrate double backscattering in our resonator by stressing a segment of the fiber between the splice s^+ and the coupler C using PZT$^+$ (see figure 4.1.1) and observing the corresponding variation in V_d^+. The coherent and intensity backscattering errors have both been eliminated as presented in the previous sections. Figure 4.2.13b shows a 400 V p-p saw-tooth voltage applied to PZT$^+$, and figure 4.2.13a shows the corresponding variation in V_d^+, indicating a bounded peak to peak fluctuation of 100 Hz due to double backscattering between s^+ and other scattering centers. As can be seen in the figure V_d^+ varies sinusoidally as the voltage of PZT$^+$ is swept linearly in a saw-tooth fashion. The figure indicates the case where the amplitude of the saw-tooth voltage is adjusted so that the variation of V_d^+ is a complete sinusoidal cycle. Thus, by increasing the frequency of the saw-tooth voltage we can average the contribution of double backscattering. This is

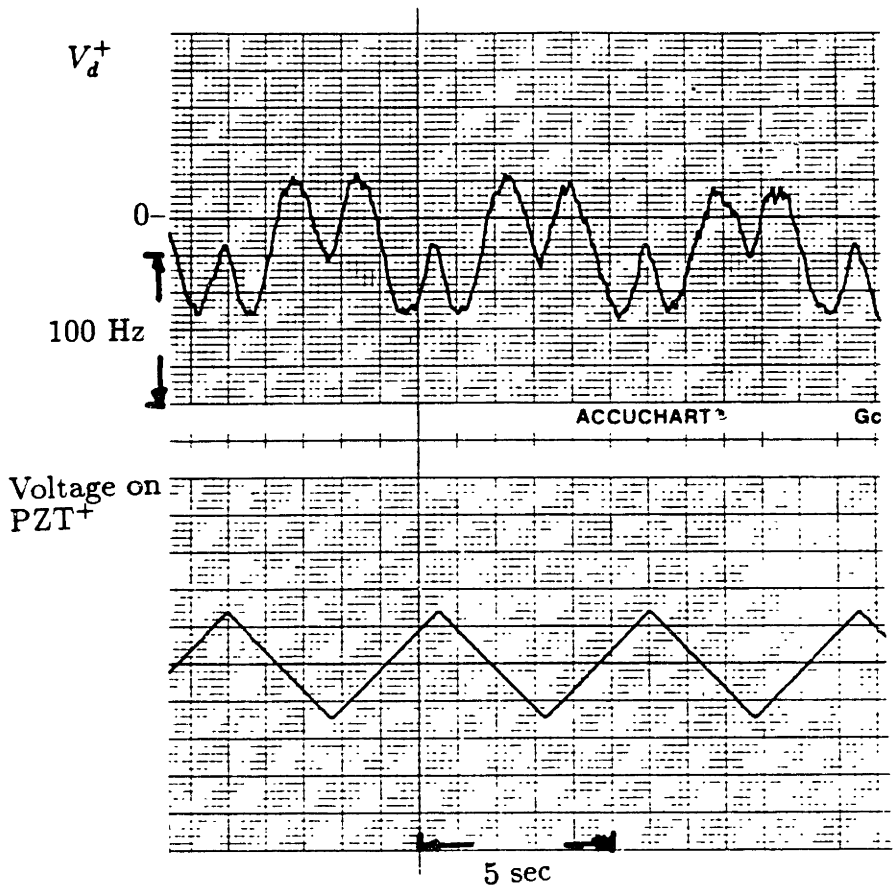

Figure 4.2.13 Fluctuation of V_d^+ as a function of time when both the coherent and incoherent backscattering effects have been removed and a saw-tooth voltage is applied to PZT^+ (b) the voltage applied to PZT^+

similar to the carrier suppressed phase modulation described earlier. We now demonstrate this method of averaging the double backscattering.

Figure 4.2.14 shows V_d^+ as a function of time, when the coherent and intensity backscattering effects have been removed as described in section 4.2.3 and 4.2.4 respectively. Initially V_d^+ is passed through a 100 ms 12 dB/octave filter. In section *A* of figure 4.2.14, a slow 0.18 Hz saw-tooth voltage applied to PZT^+ with the same amplitude as that in figure 4.2.13, which now results in a bounded 160 Hz variation in V_d^+. Similar to the

case in figure 4.2.13, the variations of V_d^+ represent complete sinusoial cycles, and could be averaged by increasing the frequency of the saw-tooth voltage. In section B, the frequency of this saw-tooth voltage is increased to 180 Hz and the fluctuation of V_d^+ shown in section A is filtered out. However, as indicated in this section of the figure, we still see a 50 Hz fluctuation of V_d^+. In section C a second 0.2 Hz saw-tooth voltage is applied to PZT^- which results in an additional 70 Hz of variation on V_d^+, due to double backscattering between s^- and the intracavity scatterers. In section D, the frequency of this saw-tooth voltage is increased to 200 Hz and then lowpass filtered to demonstrate the removal of the double backscattering errors between s^- and the intracavity scatterers. We also notice an increase in the noise. This noise is not present in section B and is due to the addition of our second saw-tooth voltage. In section E of figure 4.2.14, the time constant of the filter on PSD^+ is increased to 300 ms 12 dB/octave, and we can observe a variation in the gyroscope offset between 0 and 10 Hz. Although we have eliminated external double backscattering in this case, we have not removed double backscattering due to intracavity scatterers. Further studies on this topic is left for future work.

Figure 4.2.15a shows a sample run indicating an offset of 20 Hz. The step in the figure indicates a 100 Hz change in the frequency of E^+ and serves as a calibration for V_d^+. By comparison, figure 4.2.15b shows the case for a different longitudinal mode of the cavity indicating an offset of -20 Hz. Thus, inspite of the elimination of the coherent backscattering, intensity backscattering, and external double backscattering errors, we still see a variation from -20 hz to $+20$ Hz in the gyroscope offset as we select different longitudinal modes of the cavity. In addition to other sources of drift, examined in the next sections, the variations of V_d^+ may also be the result of having two separate modulation frequencies and an asymmetric resonance, as mentioned previously. The detailed evaluation of this error source shall be presented in a future work.

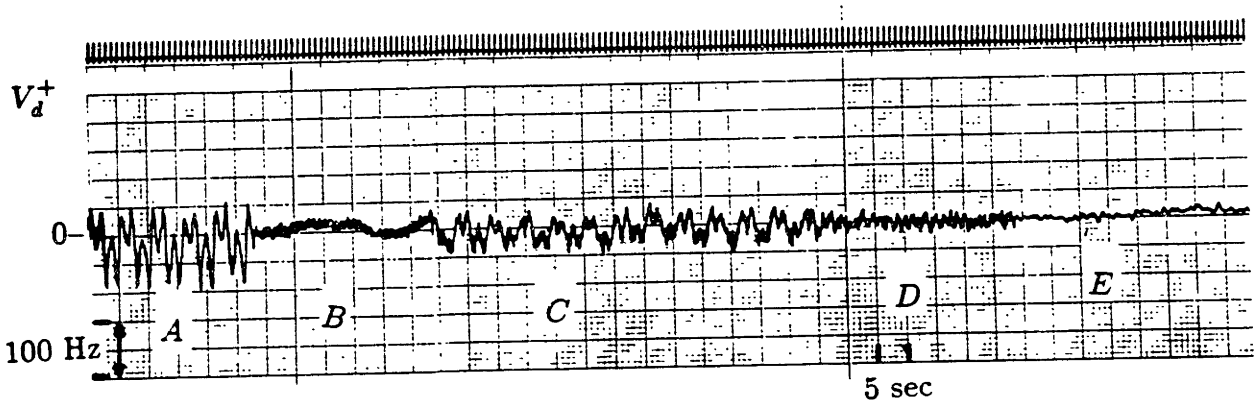

Figure 4.2.14 V_d^+ as a function of time with a 100 ms 6db/octave filter when (A) a 0.2 Hz saw-tooth voltage is applied to PZT^+ (B) frequency of this saw-tooth voltage is increased to 180 Hz (C) a 0.2 Hz saw-tooth voltage is applied to PZT^- (D) the frequency of this sawtooth voltage is increased to 150 Hz (E) filter time constant of V_d^+ is increased to 300 ms 6db/octave

4.3. Polarization-Induced Errors in a Fiber PRG

In section 3.4.2, we demonstrated that in the presence of an intracavity birefringent element, the cavity eigen polarizations are no longer along the *s* and *p* axes. This is directly applicable to a fiber resonator where the cavity fiber and the coupler are both birefringent elements, and as a result, the eigen polarizations of the fiber cavity are in general elliptical

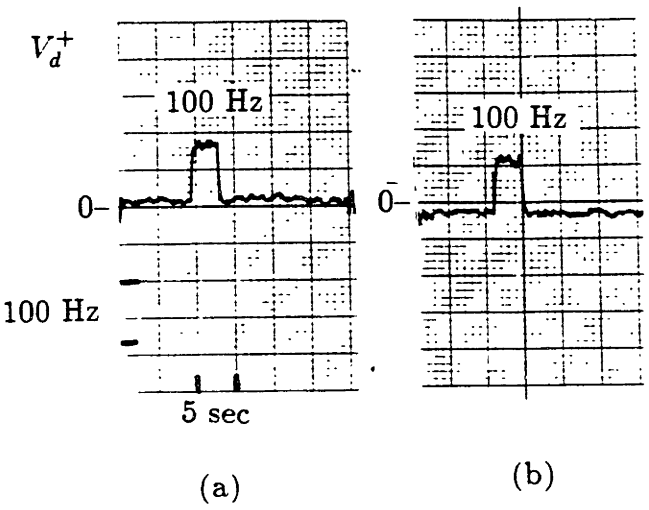

Figure 4.2.15 V_d^+ as a function of time (a) indicating a +20 Hz offset (b) indicating a −20 Hz offset for a different cavity longitudinal mode

states of polarization. However, based on the results of section 3.4 there is no apparent resonance shift between the clockwise and counterclockwise cavity resonances unless the states of polarization of the input beams are a mixture of the two eigen polarizations of the cavity, as shown in figure 3.4.11. Therefore, in our fiber setup we align the state of polarization of the input beams along an eigen polarization of the cavity by polarization controlling elements PC^+ and PC^- (shown in figure 4.1.1). Since the alignment between the state of polarization of the input beam and the eigen polarization of the cavity may drift with time, it is important to evaluate the drifts due to a variation in the state of polarization of the input[21].

4.3.1. Measurement of Polarization-Induced Offset

In this section, we will measure the variations in the open loop output of the gyroscope, V_d^+, as a function of the state of polarization of the input beams. At first, the states of polarization of both E^- and E^+ are aligned along one of the eigen polarizations of the cavity as shown in figure 4.1.2a. We then measure V_d^+ as a function of the rotation angles of the $\lambda/4$ and $\lambda/2$ plates in PC^+ and plot the results in figures 4.3.1(a) and (b). Figure 4.3.1a shows the variation in V_d^+ as a function of the rotation angle of the $\lambda/4$ plate. This figure indicates an approximately linear relationship with a slope of 5 Hz per degree of rotation of the $\lambda/4$ plate. Similarly, figure 4.3.1(b) shows the variation in V_d^+ as a function of the rotation angle of the $\lambda/2$ plate. The behavior here is different from the linear one in figure 4.3.1a. For negative rotation angles, we see an approximately linear dependence with a slope of 3 Hz per degree. However, for positive rotation angles up to 10°, the offset is practically constant. Because of the dependence of V_d^+ on the state of polarization of the input beams, careful attention must be paid to the polarization issues in our fiber ring resonator gyroscope. In the next two subsections we shall analyze two possible sources of polarization-induced perturbation of the cavity resonance frequency.

4.3.2. Offset due to Mode Pulling

In this section, we will estimate the change in the resonance frequency due to mode pulling between the eigen polarizations along a single direction of the cavity using the calculations presented in Appendix B. For the purpose of illustration, let us assume that the two eigen polarizations of our fiber cavity are linear states of polarization along the s and p axes, and that the polarization of the input beam E_1, is along the s axis. In order to simulate the conditions of figure 3.4.1a, we pass the input beam through a $\lambda/4$ plate and rotate the fast axis of this plate by an angle of $\theta_\circ$ with respect to the s axis. The output of this $\lambda/4$ plate is labeled E_t and is given by:

$$\begin{aligned} E_t &= E_1\left(j\sin^2(\theta_\circ) + \cos^2(\theta_\circ)\right)\hat{s} + E_1(1-j)\sin(\theta_\circ)\cos(\theta_\circ)\hat{p} \\ &\approx E_1(\hat{s} + (1-j)\sin(\theta_\circ)\hat{p}) \end{aligned} \tag{4.3.1}$$

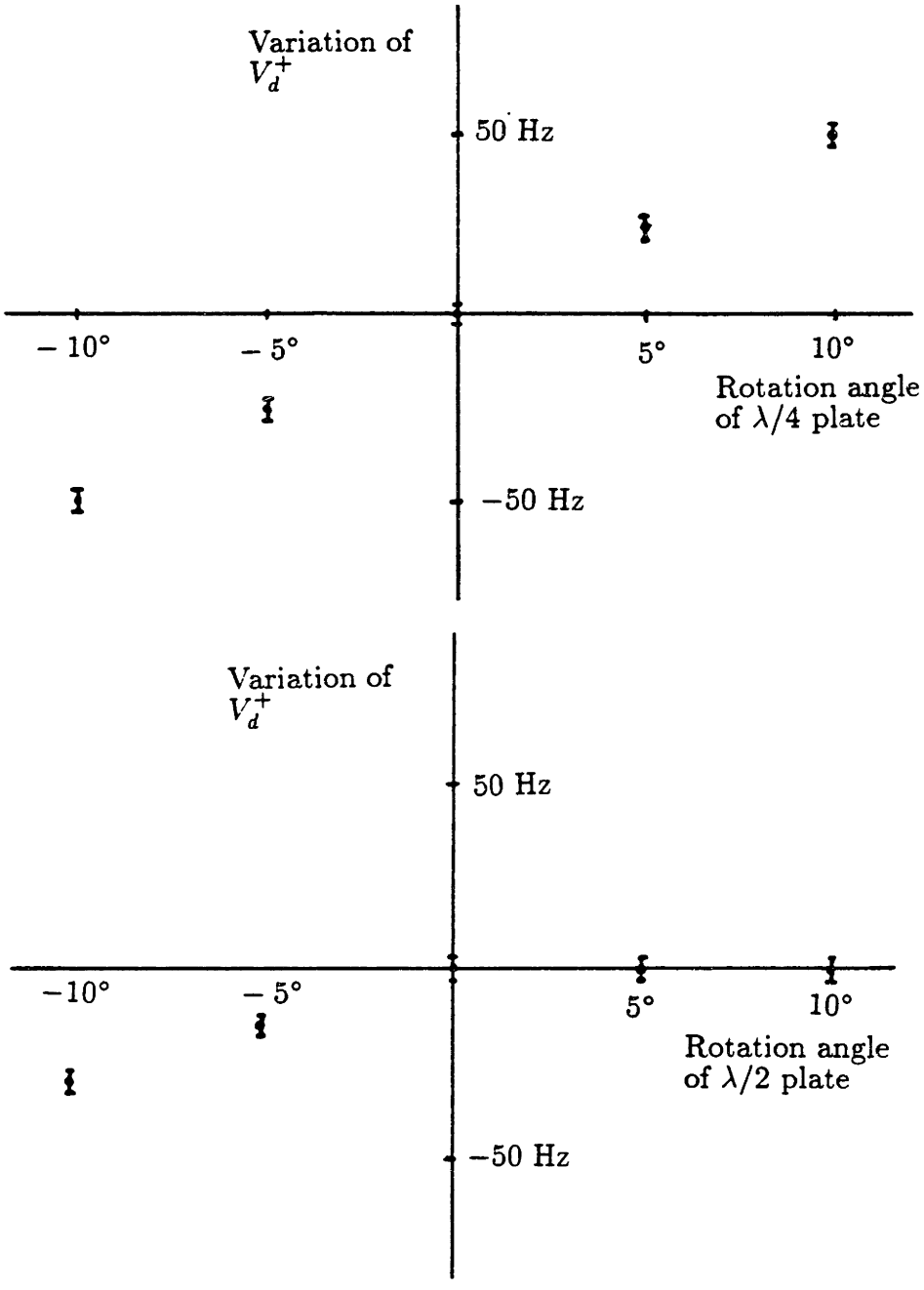

Figure 4.3.1. Variations of V_d^+ as a function of the rotation angles of the (a) $\lambda/4$ element and (b) $\lambda/2$ element in PC^+

The ratio between the amplitudes of the s and p components of E_i in equation 4.3.1 is

$\sqrt{2}\sin(\theta_o)$. E_i is now coupled into the cavity where it excites both s and p eigen polarizations of the cavity. The ratio between the peak electric fields of these two resonances is also $\sqrt{2}\sin(\theta_o)$. In this example, the two eigen polarizations of the cavity are orthogonal to each other and therefore there is no interference between them. Thus, the pull in the resonance at the s polarization, labeled Δf, is only due to the intensity of the p resonance and is given by equation B.5 in Appendix B:

$$\begin{aligned}\Delta f &= \frac{(\Gamma_1\Gamma_2)^2}{16f_o^3}(\sqrt{2}\sin(\theta_o))^2 \\ &= \frac{(\Gamma_1\Gamma_2)^2}{8f_o^3}\sin^2(\theta_o)\end{aligned} \tag{4.3.2}$$

where Γ_1 and Γ_2 are the FWHM linewidths of the two cavity eigen polarizations and f_o is the separation between the two resonances. For this example, we choose parameters equal to those measured for our fiber cavity:

$$\begin{cases}\Gamma_1 = \Gamma_2 = 30 \text{ kHz (see section 4.1.1)} \\ f_o = 2.2 \text{ MHz (see section 4.1.1)}\end{cases}$$

For $\theta_o = 1°$, we obtain $\Delta f = 2.3 \times 10^{-6}$ Hz which is six orders of magnitude smaller than the 5 Hz per degree shown in figure 4.3.1a. This pull is therefore insignificant.

We now calculate the pull, Δf, in the case which involves the interference between the two cavity eigen polarizations. We will use the example described above, but we now pass the output of the cavity through a polarizer with a transmission axis tilted 45° with respect to the s axis. In this case the two eigen polarizations of the cavity are projected onto the transmission axis of the polarizer, and the ratio between their peak electric fields is the same as before, i.e. $\sqrt{2}\sin(\theta_o)$. Now the major contribution to Δf is due to the interference between the two cavity eigen polarizations, and is given by equation B.6, i.e:

$$\begin{aligned}\Delta f &= \frac{\Gamma_2\Gamma_1}{4f_o}\sqrt{2}\sin(\theta_o) \\ &= \frac{\Gamma_2\Gamma_1}{2\sqrt{2}f_o}\sin(\theta_o)\end{aligned} \tag{4.3.3}$$

For $\theta_o = 1°$, $\Delta f = 2.3$ Hz. This value is still a factor of 2 less than the variation observed in figure 4.3.1a. It should be noted that this is an extreme case, and represents an upper bound on the perturbation in the resonance frequency due to mode pulling. Thus, to explain the errors in figure 4.3.1a, we need to consider another source of polarization-induced perturbation of the resonance frequency, which will be presented in the next section.

4.3.3. Offset due to Polarization-Induced Resonance Asymmetry

In this section, we will demonstrate and calculate a variation in the asymmetry of the resonance lineshape as a function of the polarization of the input light. This asymmetry shifts the cavity resonance frequency according to the calculations of Appendix A.

Figure 4.3.2 shows the setup we used in demonstrating the polarization-induced variation in the resonance asymmetry. As seen in the figure, light from the laser E_i, is coupled into the cavity in the clockwise direction only. The state of polarization of E_i can be adjusted prior to entering the resonator arm, by a polarization controller PC_i, which includes a $\lambda/2$ and a $\lambda/4$ plate. After exiting the resonator, the output beam E_o passes through another polarization controlling element, PC_o, as well as a polarizer PL, and is monitored by a photodetector PD.

Now let us demonstrate the variation in the symmetry of the resonance lineshape. At first, we align E_i along an eigen polarization of the cavity to establish this state of polarization. PC_o is then adjusted so as to align this cavity eigen polarization along an axis labeled s. We now perturb the state of polarization of E_i by using a random setting of PC_i. Figure 4.3.3a shows the cavity output E_o, monitored by PD, as a function of the laser frequency when the transmission axis of the polarizer is along s, showing a slightly asymmetric resonance line dip. Figure 4.3.3b shows E_o as a function of the laser frequency when the polarizer is rotated at a 45° angle with respect to s, clearly indicating a significant change in the asymmetry of the lineshape. This change in the asymmetry of the lineshape leads to a change in the resonance frequency of the cavity as shown in Appendix A.

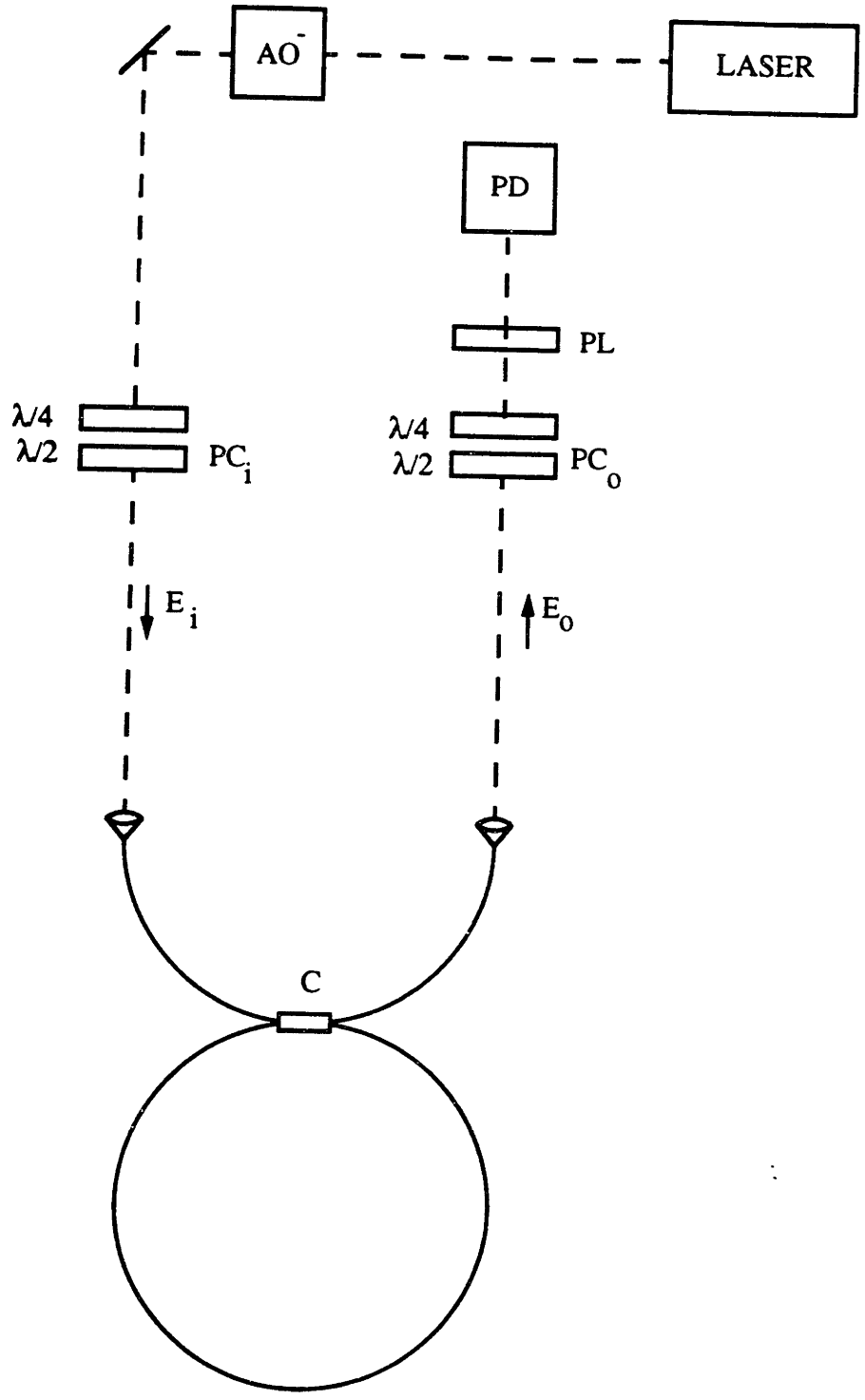

Figure 4.3.2. Schematic diagram for evaluating the effects of the polarization on the lineshape symmetry

In order to explain this polarization-dependent asymmetry, we must consider the

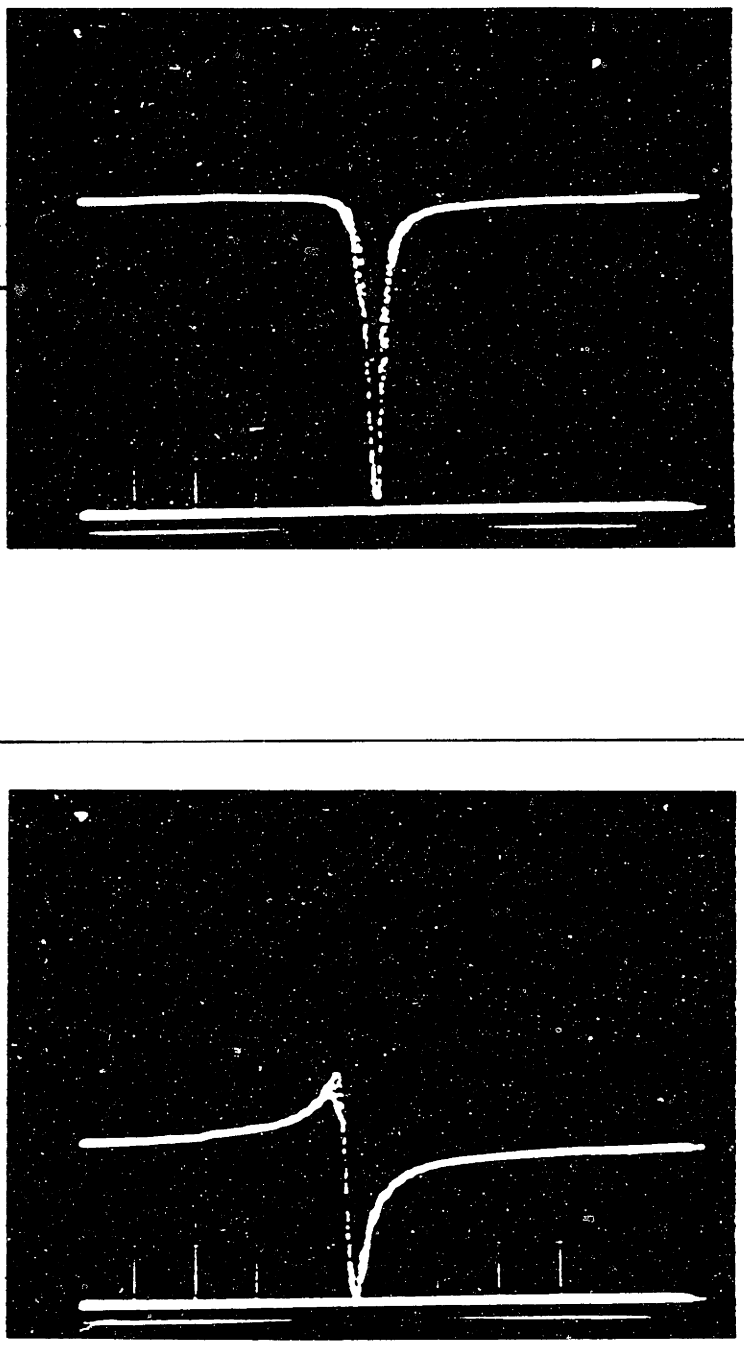

Figure 4.3.3. Output of PD as a function of laser frequency when the input is not aligned with an eigen polarization of the cavity when (a) the transmission axis of PL is along s axis (b) the transmission axis of PL is tilted 45° with respect to s axis

interaction between the two components of the output beam E_o, which are E_{ri} and E_c, as described in Appendix A. E_{ri} is the so-called primary reflection of E_i from the coupler C, and E_c is the field coupled out of the ring cavity by C.

Let us now consider an ideal fiber cavity with a lossless coupler. Similar to the case in section 4.3.2, the eigen polarizations of this cavity are along the s and p axes. Figure 4.3.4a shows both E_{ri} and the on-resonance E_c when E_{ri} is s polarized, indicating that the on-resonance E_c is equal and opposite to E_{ri}. In Appendix A. we defined ψ, as the phase between $-E_{ri}$ and the on-resonance E_c, and demonstrated that $\psi \neq 0$ leads to cavity asymmetry. In the ideal case shown in figure 4.3.4a, we have $\psi = 0$, which corresponds to a completely symmetric resonance line dip.

An arbitrary state of polarization of E_{ri} can be represented in terms of its components along s and p axes, i.e.:

$$E_{ri} = |E_{ri}|(a_1\hat{s} + a_2\hat{p}) \tag{4.3.4}$$

The corresponding on-resonance E_c is equal and opposite to the s component of E_{ri}, and is given by:

$$E_c = -a_1|E_{ri}| \tag{4.3.5}$$

which is graphically presented in figure 4.3.4b. The coefficient a_2 for the p component of E_{ri} is in general a complex number and can not be fully represented in this figure. Ordinarily, this p component of E_{ri} does not change the resonance symmetry because it can not interfere with E_c.

Let us now pass the cavity output through a polarizer. The transmission axis of this polarizer makes an angle of θ with respect to the s axis, as shown in figure 4.3.4c. The corresponding fields at the polarizer, E_c^P and E_{ri}^P, are given by:

$$\begin{aligned} E_c^P &= E_c \sin(\theta) = -a_1|E_{ri}|\sin(\theta) \\ E_{ri}^P &= |E_{ri}|\big(a_1 \sin(\theta) + a_2 \cos(\theta)\big) \end{aligned} \tag{4.3.6}$$

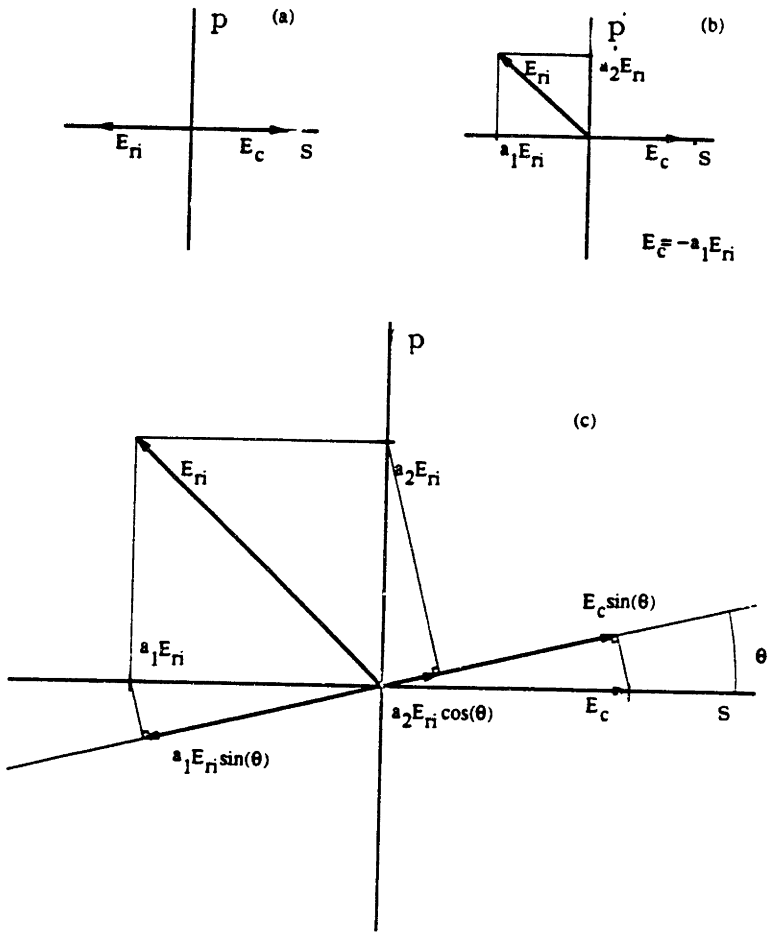

Figure 4.3.4. (a) polarization of E_{ri} is matched along an eigen polarization of the cavity (b) polarization of E_{ri} is not matched along an eigen polarization of the cavity (c) a polarizer is placed on the output beam where its transmission axis makes an angle θ with the vector associated with an eigen polarization of the cavity

Since a_2 is a complex number, it is obvious that E_c^P and E_{ri}^P are no longer exactly equal and opposite to each other and the phase ψ, defined previously in this section, is given by:

$$\psi = arg\left(1 + \frac{a_2}{a_1}\cot(\theta)\right) \neq 0 \tag{4.3.7}$$

Thus, ψ depends on both the initial state of polarization of E_i, which is represented by the ratio a_2/a_1, as well as on the polarizer rotation angle. This is consistent with the observations in figure 4.3.3a and 4.3.3b, where a change in the rotation angle of the polarizer caused a change in the resonance asymmetry, indicating a change in ψ.

Let us now compare this perturbation with the results of section 4.3.2. Similar to the case described in section 4.3.2, we assume s and p eigen polarizations for the cavity, and pass the cavity input beam through a $\lambda/4$ plate to simulate the conditions of figure 4.3.1a. We thus obtain a beam whose state of polarization is given by equation 4.3.1, resulting in $a_2/a_1 = (1-j)\sin(\theta_o)$. a_2 and a_1 are already defined in equation 4.3.4.

We now couple this beam into the fiber cavity, and pass the output through a polarizer which has its transmission axis tilted 45° with respect to the s axis. According to equation 4.3.7 we get $\psi = arg\left(1 + (1-j)\sin(\theta_o)\right) \approx arg\left(1 - j\sin(\theta_o)\right)$ when θ_o is small. This corresponds to $\psi \approx \sin(\theta_o)$ which results in a resonance frequency perturbation of $(\Gamma_1/2)\sin(\theta_o)$ (see Appendix A). For $\theta_o = 1°$ we obtain $\psi \approx 0.016$ which, according to calculations of Appendix A corresponds to a resonance shift of approximately 240 Hz. We can see that this pull is 2 orders of magnitude larger than the case obtained for mode pulling in section 3.4.2.

In general we may not have a polarizer in the output path but an optical element with a polarization sensitive transmission coefficient, which can cause a similar change in the asymmetry of the resonance. For example, in the gyroscope setup of figure 4.1.1, most of the optical components between the coupler and either photodetector, have a polarization sensitive loss, which can contribute to a change in the asymmetry if the input polarization is misaligned with respect to a cavity eigen polarization. Thus we can attribute the offset variations in figure 3.4.1a to a polarization dependent change in the resonance asymmetry.

This particular polarization problem can be solved if we use a fiber cavity in transmission, as shown in figure 4.3.5. In this case, we do not expect to observe any perturbation of the resonance symmetry due to the interference between E_{ri} and E_c because of the absence of E_{ri}.

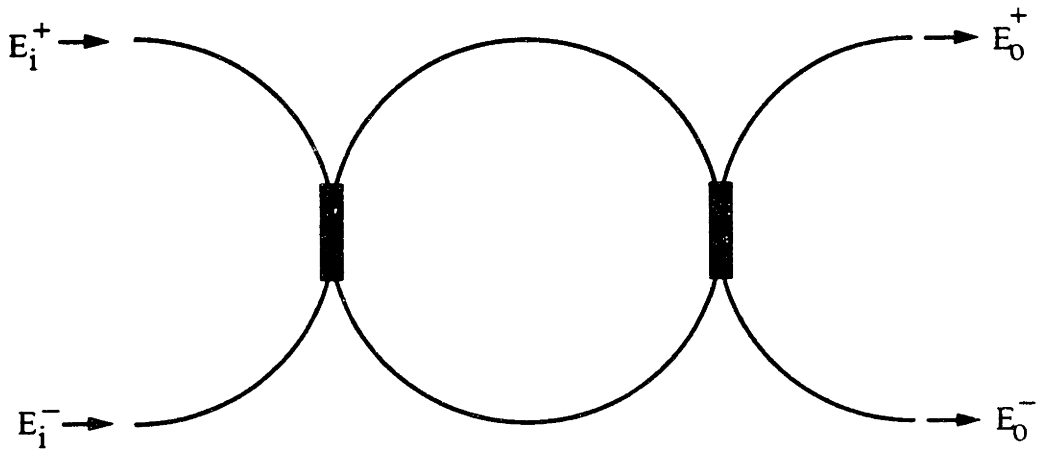

Figure 4.3.5. Illustration of a transmission fiber ring cavity

The state of polarization of the input beams in our setup do not drift significantly with

respect to a cavity eigen polarization. On occasions, we need to readjust the polarization of the input beams by less than 0.5° on either the $\lambda/2$ plate or the $\lambda/4$ plate in either PC^+ or PC^-. From figure 4.3.1a and b, this polarization drift corresponds to less than 2.5 Hz of variation in the offset. Therefore, although this drift is very important in general, it does not significantly contribute to the ±20 Hz of offset variation we observed in the end of section 4.2.4.

4.4. The Optical Kerr Effect in Fiberoptic PRG

Because of the small core diameter of single mode optical fibers, relatively moderate power levels can produce extremely large intensities. For example, in our case with the core diameter of 6 μm, a 1 mW beam has an intensity of 3.5 kW/cm^2. In the presence of such a large intensity, the optical nonlinearities of the fiber medium can no longer be ignored. One such nonlinearity, which can generate an offset in the gyroscope, is the change in the index of refraction of the fiber due to the intensity of light, the so called optical Kerr effect[22,23]. In this section we consider the optical Kerr effect in a fiber resonator and its influence on the gyroscope offset.

4.4.1. Derivation of the Optical Kerr Effect

We will now present the derivation of the optical Kerr effect[22]. The optical Kerr effect is a 3rd order nonlinear contribution to the polarization due to degenerate four-wave mixing inside an optical medium. The nonlinear component of the electric polarization, P^{NL}, is given by:

$$P_m^{NL} = \chi^{(3)}_{mjkl} E_j E_k E_l \tag{4.4.2}$$

where $\chi^{(3)}_{mjkl}$ is the 3rd order nonlinear susceptibility tensor, which in our case can be represented by a single scalar.

In the case of a single beam, propagating along $+z$ direction, we can represent the electric field E as:

$$E = E_1 e^{j(\omega t - kz)} \tag{4.4.2}$$

where k is the propagation wavenumber of the beam and ω is the optical angular frequency of the beam. In this case P^{NL}, which is proportional to E^3 will have components at ω and 3ω. The component of P^{NL} at ω is given by:

$$P^{NL}(\omega) = 3\chi^{(3)} E_1 E_1^* E_1 e^{j(\omega t - kz)} \tag{4.4.3}$$

This component of the nonlinear polarization is proportional to E, and can be modeled as a change in the index of refraction given by:

$$4\pi P^{NL}(\omega) = \Delta\epsilon E_1 e^{j(\omega t - kz)} = 2n\Delta n_1 E_1 e^{j(\omega t - kz)} \tag{4.4.4}$$

which in turn yields a simple expression for Δn_1 as a function of E_1, given by:

$$\Delta n_1 = \frac{6\pi}{n}\chi^{(3)} E_1 E_1^* \tag{4.4.5}$$

We can relate $E_1 E_1^*$ to the intensity of the beam I_1 which is given by:

$$I_1 = \frac{nc}{8\pi} E_1 E_1^* \tag{4.4.6}$$

so that Δn_1 can be expressed in terms of I_1 as:

$$\begin{aligned} \Delta n_1 &= \frac{48\pi^2 \chi^{(3)}}{n^2 c} I_1 \\ &= \beta_o I_1 \end{aligned} \tag{4.4.7}$$

where:

$$\beta_o = \frac{48\pi^2 \chi^{(3)}}{n^2 c} \tag{4.4.8}$$

As can be seen in equation 4.4.7, the change in the index of refraction is proportional to the intensity of the beam.

Let us now consider two counterpropagating beams E_1 and E_2. The total electric field is now given by:

$$E = E_1 e^{j(\omega_1 t - k_1 z)} + E_2 e^{j(\omega_2 t + k_2 z)} \tag{4.4.9}$$

The component of the polarization with the same time dependence as E_1 is given by:

$$P^{NL}(\omega_1) = 3\chi^{(3)}(E_1E_1^* + 2E_2E_2^*)E_1e^{j(\omega_1 t - jk_1 z)} \tag{4.4.10}$$

which is identical to the expression we had obtained for the single beam case except for the addition of $2E_2E_2^*$ to the terms inside the bracket. Following the same simplifications as above we obtain:

$$\Delta n_1 = \beta_o(I_1 + 2I_2) \tag{4.4.11}$$

where I_2 is the intensity of E_2. Thus equation 4.4.11 predicts a change in the index experienced by E_1 due to the intensity of E_2. It should be noted that the general derivations of these effects are valid even if E_1 were copropagating with respect to E_2.

Let us now consider the optical Kerr effect in a fiber ring resonator. For example, in the clockwise direction, the optical Kerr effect creates a change in the index of refraction by an amount, Δn^-, given by:

$$\Delta n^- = \beta_o(I_r^- + 2I_r^+) \tag{4.4.12}$$

where I_r^+ and I_r^- are the intensities of the intracavity beams traveling in the counter-clockwise and clockwise directions respectively. The clockwise resonance frequencies of the cavity are given by:

$$f_c^- = \frac{qc}{NPn^-} \tag{4.4.13}$$

where q is the longitudinal mode number of the resonance, P is the perimeter of the ring resonator, N is the number of turns of the resonator fiber, n is the index of refraction, and c is the speed of light. This expression is similar to equation 1.3.1, which was obtained for a bulkoptic resonator. The optical Kerr effect changes f_c^- by an amount Δf_k^-, given by:

$$\begin{aligned} \Delta f_k^- &= -\frac{qc}{NP(n^-)^2c}\Delta n^- \\ &= -\frac{qc}{NP(n^-)^2}\beta_o(I_r^- + 2I_r^+) \end{aligned} \tag{4.4.14}$$

The intracavity intensities, I_r^- and I_r^+ are enhanced by a resonant factor of F/π with respect to the intensities outside of the resonator. As mentioned previously, F is the finesse of the cavity. Thus, the intracavity intensities I_r^+ and I_r^- are given by:

$$\begin{aligned} I_r^- &= \frac{F}{\pi}\frac{W_i^-}{S} \\ I_r^+ &= \frac{F}{\pi}\frac{W_i^+}{S} \end{aligned} \tag{4.4.15}$$

where W_i^- and W_i^+ represent the optical power of the clockwise and counterclockwise beams outside the resonator respectively and S is the effective cross section area of the fiber. Thus, Δf_k^- is given by the direct substitution of equation 4.4.15 into equation 4.4.14, i.e.:

$$\begin{aligned} \Delta f_k^- &= -\frac{qcF\beta_o}{\pi n^2 NPS}(W_i^- + 2W_i^+) \\ &= -\frac{cF\beta_o}{\pi\lambda_o nS}(W_i^- + 2W_i^+) \end{aligned} \tag{4.4.16}$$

Here, we used $n^- \approx n$ where n is the unperturbed index of refraction of the medium, and we also used $q/nNP = 1/\lambda_o$, where λ_o is the free space wavelength of the light on resonance with the cavity.

There is a similar expression for the shift in the counterclockwise resonance frequency, labeled Δf_k^+, which is given by:

$$\Delta f_k^+ = -\frac{cF\beta_o}{\pi\lambda_o nS}(W_i^+ + 2W_i^-) \tag{4.4.17}$$

so that the overall separation between the clockwise and counterclockwise resonance frequencies due to the optical Kerr effect is given by:

$$\begin{aligned} \Delta f_c &= \Delta f_k^+ - \Delta f_k^- \\ &= \frac{cF\beta_o}{\pi\lambda_o nS}(W_i^+ - W_i^-) \\ &= \gamma_k(W_i^+ - W_i^-) \end{aligned} \tag{4.4.18}$$

where:

$$\gamma_k = \frac{cF\beta_o}{\pi\lambda_o nS} \tag{4.4.19}$$

As can be seen in equation 4.4.19, by reducing the power of the clockwise beam, i.e. W_i^-, we reduce Δf_c, and by reducing the power of the counterclockwise beam, W_i^+, beam we increase Δf_c. It should be noted that Δf_c is proportional to the difference between W_i^+ and W_i^-, and if we change the power along both directions by equal amounts, there is no corresponding change in Δf_c.

Let us now calculate γ_k. In fused quartz, $\chi^{(3)} \approx 5 \times 10^{-15}$ (esu)[22], which results in $\beta_o \approx 3.4 \times 10^{-16}$ cm^2/W. The effective fiber area S, is approximately the area of the fiber core, which in our case for a 6 μm core diameter is approximately 2.8×10^{-7} cm^2. The cavity finesse in our case is approximately 300, and the free space wavelength is 1.15×10^{-4} cm. Thus, we calculate $\gamma_k \approx 20$ Hz/μW. If we calculate β_o based on experimental observations of the optical Kerr effect in a fiber interferometer gyroscope[22], we obtain $\beta_o \approx 1.1 \times 10^{-16}$ cm^2/W, and $\gamma_k \approx 7$ Hz/μW. It should be noted that our estimates of β_o and the effective fiber cross-section area, S, are approximate, and this leads to an uncertainty in determining γ_k

4.4.2. Observation of the Optical Kerr Effect

As discussed in the previous section, any difference between the clockwise and counterclockwise beam intensities can create a separation between the clockwise and counterclockwise resonance frequencies. We will now demonstrate this in our setup.

Figure 4.4.1 shows the experimental setup used to evaluate the optical Kerr effect in a fiber ring resonator gyroscope. The setup shows the closed loop configuration for the fiber PRG. The closed loop operation of a PRG has already been described for the bulkoptic PRG in section 3.1.1, and will not be elaborated further. The closed loop output is the frequency of VCO$^+$ (shown in figure 4.4.1), labeled f_a^+, measured by a frequency counter, FC, as already described for the bulkoptic case in section 3.3. A neutral density filter,

NDF, could be inserted at any of the five points, A_1 through A_5, so that the intensities of E^+ and E^- can be attenuated in a controlled manner.

We eliminate the lockin behavior in the setup by separating the frequencies of E^+ and E^- by 1 FSR of the cavity [7.703 MHz in our case]. In this case E^- probes the q^{th} longitudinal mode of the cavity while E^+ probes the $q+1^{th}$ mode, and the beatnote between them does not cause a lockin behavior at zero rotation rate. We use separate modulation frequencies i.e. $f_m^- = 5$ kHz and $f_m^+ = 2$ kHz to eliminate the intensity backscattering as described in section 4.2.3. The double backscattering effects are eliminated as described in section 4.2.4.

Figure 4.4.2 shows the experimental data demonstrating the optical Kerr effect. The top trace of the figure represents the intensity associated with the clockwise resonance dip, which is obtained by demodulating the output of PD^- at $2f_m^-$ by PSD^{--} (shown in figure 4.4.1). Similarly, the middle trace represents the resonance dip for the counterclockwise resonance, which is obtained by demodulating the output of PD^+ at $2f_m^+$ by PSD^{++}. These measurements indicate the intensities of the beams coupled out of the cavity by the coupler C. The intensity scale in both traces is calibrated prior to the experiment to be 2 μW/division, and we measure the output of the cavity along either the clockwise or the counterclockwise direction to be approximately 17 μW. The bottom trace is the output of the frequency counter, FC, which measures f_a^+. The scale for the bottom trace is 25 Hz/division, and a positive variation of this trace corresponds to an increase in f_a^+. A variation in f_a^+ represents a change in the separation between the clockwise and counterclockwise resonance frequencies.

In section A of figure 4.4.2, the NDF in inserted at location A_1 (shown in figure 4.4.1) to attenuate E^- immediately before it falls on PD^-. The insertion of this NDF causes approximately 35% attenuation in the light intensity falling on PD^-, which in our case corresponds to a 6 μW drop in the optical power as measured by PSD^{--}. As seen in the bottom trace of the figure, there is no change in the output of FC indicating that

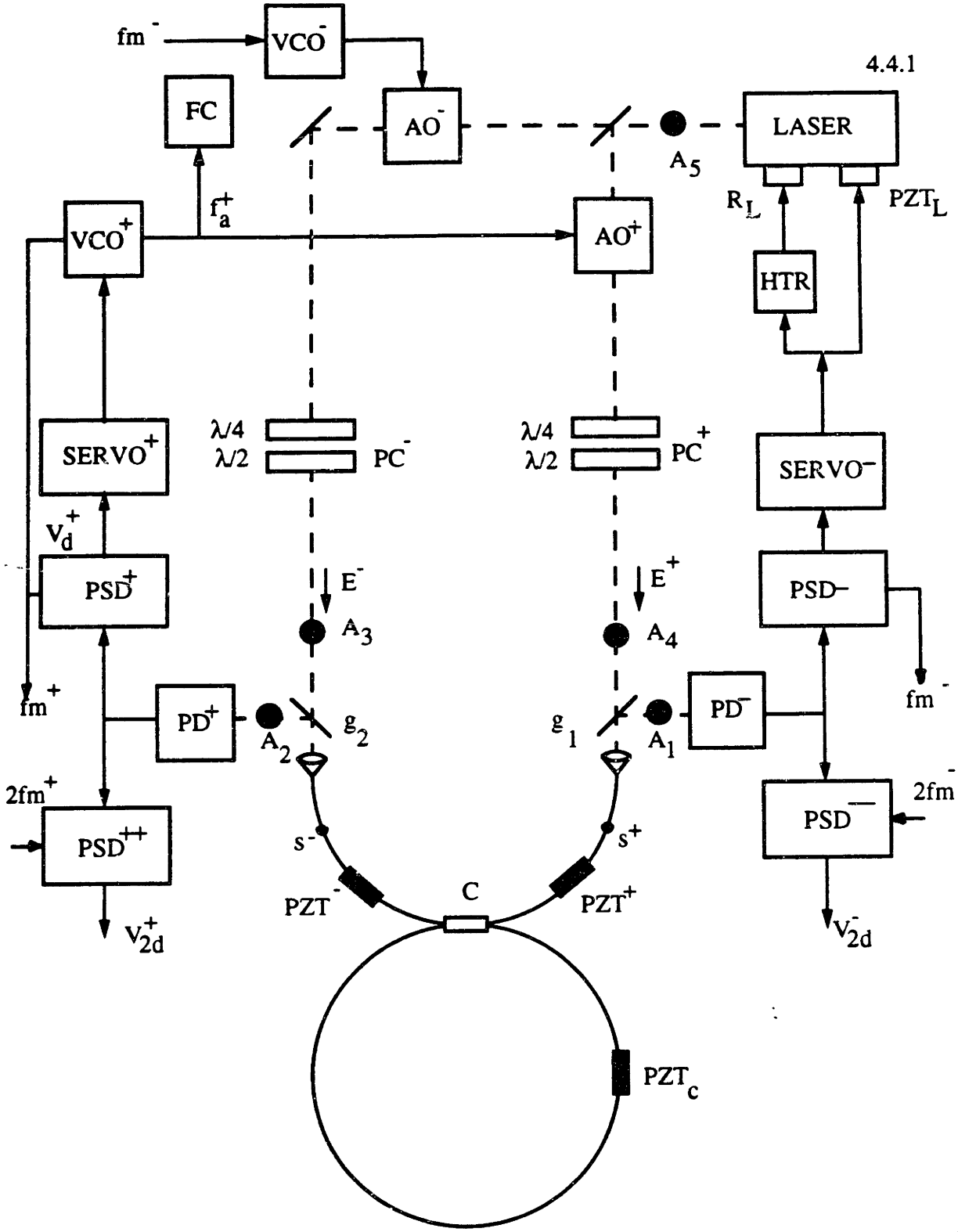

Figure 4.4.1. Schematic Diagram for the setup used in measuring the optical Kerr effect

the operation of the primary feedback loop is independent of the light intensity falling on

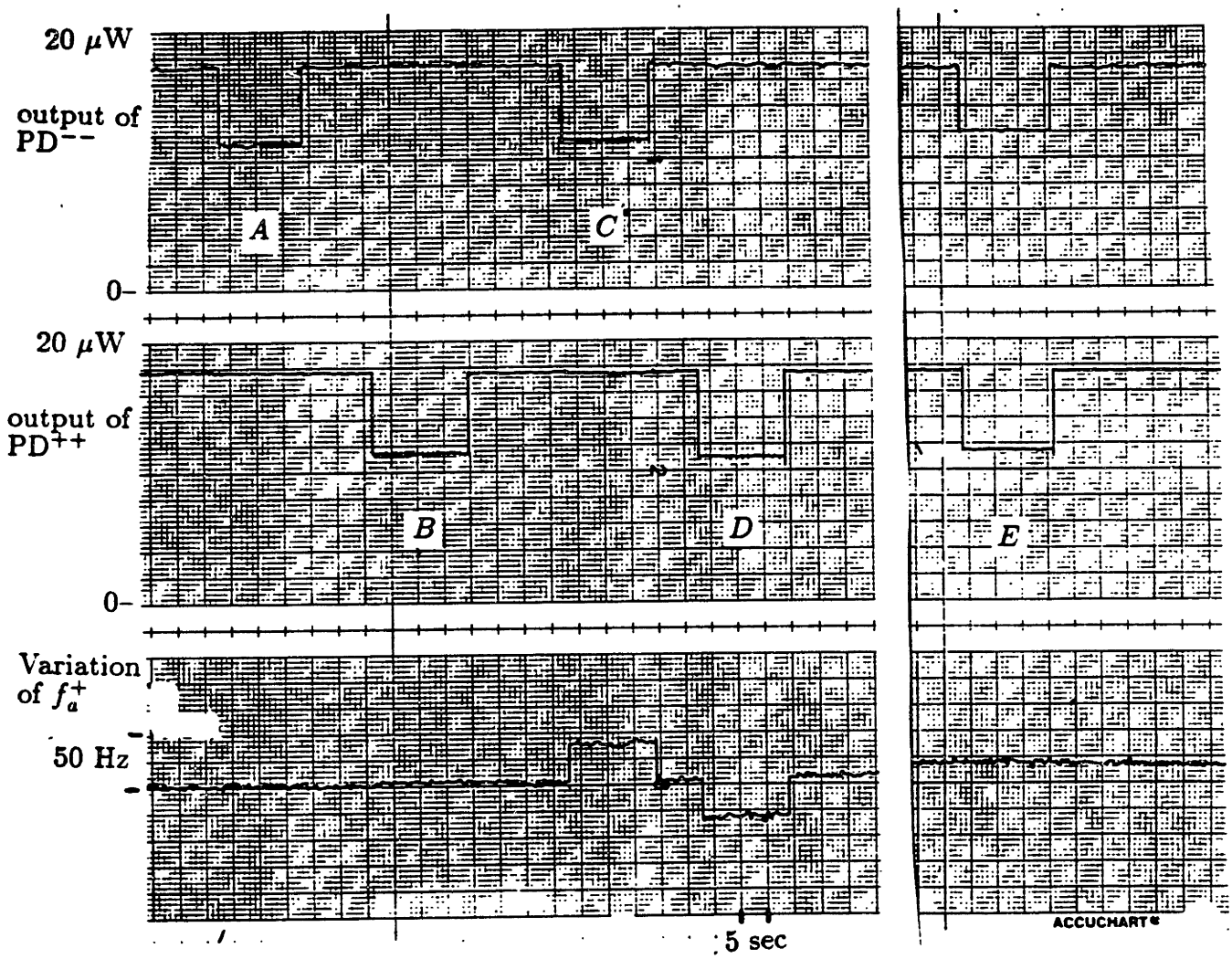

Figure 4.4.2. The variations in the f_a^+ (bottom trace) as a function of varying the intensities of the input beams (top two traces)

detector PD^-. Similarly, in section B of the figure, the NDF was placed at location A_2

to attenuate E^+ immediately before it falls on PD^+, resulting in a 35% reduction in the power falling on PD^+. The bottom trace of the figure shows no variation in the output of FC indicating that the operation of the secondary loop is also independent of the intensity of E^+.

In section C of figure 4.4.2, the NDF was inserted at A_3 to attenuate E^- before it is coupled into the resonator, corresponding to a 6μW drop in the intensity output as measured by PD^{--}. As can be seen in the bottom trace, this attenuation corresponded to an increase in the output of FC by approximately 40 Hz. This change is consistent with that predicted by the optical Kerr effect in equation 4.4.18. We measure an experimental value of 7 Hz/μW for γ_k, which is in good agreement with the theoretical predictions of section 4.4.1.

Similarly, in section marked D, the NDF is inserted in location A_4 to attenuate E^+ before it is coupled into the resonator, corresponding to a 6 μW drop in the cavity output intensity. As can be seen in the bottom trace of the figure the output of FC is reduced by 40 Hz. We can clearly see that when we reduce the beam power in the clockwise direction, f_a^+ decreases, where as when we reduce the power in the counterclockwise direction, f_a^+ increases. This is also in agreement with the predictions of equation 4.4.18.

Finally in section E, the NDF was inserted at point A_5 corresponding to a simultaneous reduction in both E^+ and E^- prior to entering the resonator, and as can be seen in the figure there is no corresponding change in f_a^+, proving that a change in f_a^+ is proportional to the difference between the intensities of E^+ and E^-, and when both these intensities are reduced by the same amount simultaneously, there is no net change in f_a^+.

Figure 4.4.3 shows a plot of changes in f_a^+ as a function of the variation of the counterclockwise beam power W_i^+. This figure indicates a linear change in f_a^+ as a function of W_i^+, with a proportionality constant of approximately 7 Hz/μW, which is consistent with the observations of figure 4.4.2, as well as with the theoretical predictions of section 4.4.1.

During the measurement of the $\pm$20 Hz offset drift at the end of section 4.2.4, we have tried to maintain equal intensities along clockwise and counterclockwise direction by

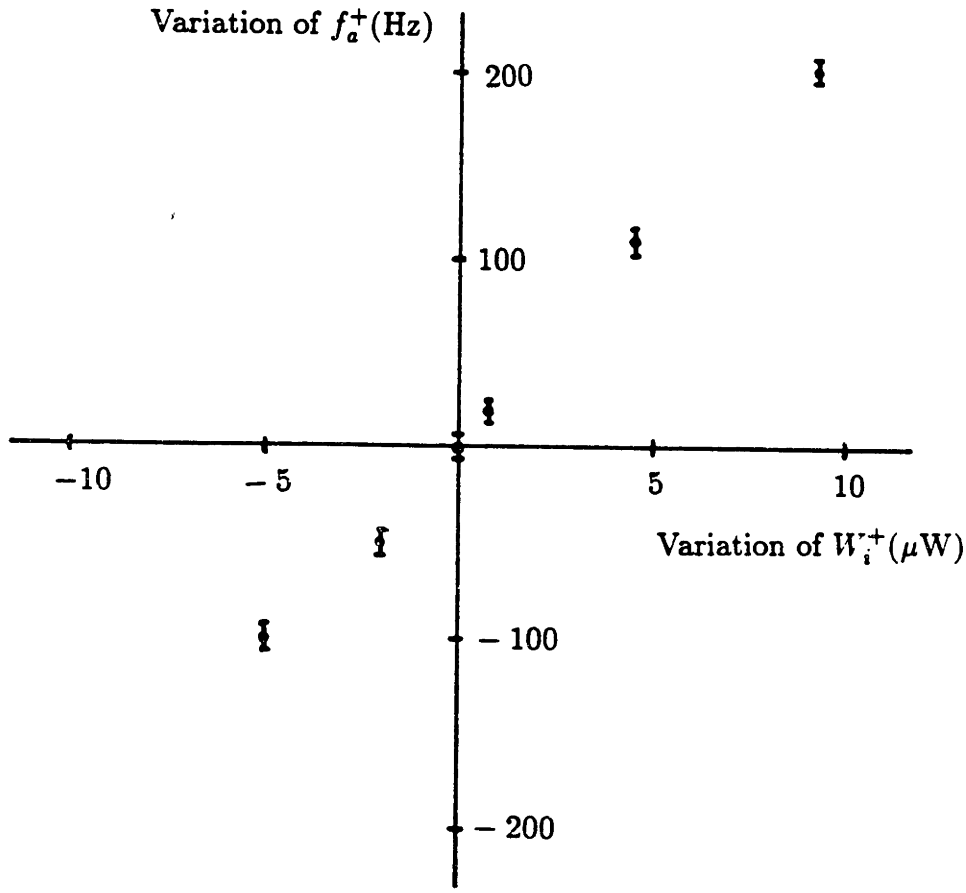

Figure 4.4.3. variation of f_a^+ as a function of the change in W_i^+

manual adjustment. However, during experimental runs, we have observed a 2% relative intensity fluctuation between the clockwise and counterclockwise directions. For a 20 μW input beam this corresponds to a difference of 0.4 μW between the clockwise and counterclockwise beam intensities. This change represents ±8 Hz of offset variation due to the optical Kerr effect, which, although significant, is small compared with the ±20 Hz offset variation observed in section 4.2.4. The existence of the optical Kerr effect, however, indicates that a precision gyroscope will need a feedback loop to keep the intensity of the clockwise beam equal to that of the counterclockwise beam.

4.5. Alternative Method for Measurement of Gyroscope bias

As mentioned in section 4.2.4, we have observed a ±20 Hz fluctuation in the gyroscope bias. In section 4.3.3, we attributed approximately ±3 Hz of fluctuation to the variation in the state of polarization, and in section 4.4.2 we attributed another ±3 Hz to the optical Kerr effect. Thus, there is still approximately ±14 Hz of fluctuation, which is not yet accounted for.

In this section, we present a measurement of the bias of the gyroscope in the absence of backscattering. As previously stated in section 4.2.3, in the presnence of separate modulation frequencies for clockwise and counterclockwise discriminants, the offset of the gyroscope now becomes sensitive to variations in the asymmetry of the resonance, as well as to variations in the applied modulation frequencies.

We will now explain the experimental procedure for our demonstration. We start by locking the frequency of beam E_1 to the center of a clockwise cavity resonance. Then we generate another beam E_2 with a frequency separation of 1 FSR, and launch this beam along the counterclockwise direction so it can probe the adjacent counterclockwise resonance mode for the cavity as shown in figure 4.5.1a. The drift in the discriminant voltage of E_2 is illustrated in figure 4.5.2 and it indicates the variation in the separation between the adjacent clockwise and counterclockwise resonances of the cavity. We now switch E_2 from the counterclockwise direction to the clockwise direction of the cavity, as shown in figure 4.5.1b. The drift in the discriminant now corresponds to the variation between the two adjacent clockwise resonances. As we switch E_2 from counterclockwise direction to the clockwise direction, we should observe an abrupt change or jump in the discriminant as indicated in figure 4.5.2b. This jump represents the separation between the clockwise and counterclockwise resonance frequencies of the same cavity longitudinal mode. A variation in the size of this jump, shown in figure 4.5.2c, would indicate a drift in the separation between the clockwise and counterclockwise resonance frequencies. In this

way, we can remove the effects of coherent and intensity backscattering, by using a single beam to separately probe the clockwise and the counterclockwise resonance.

Let us now consider the experimental setup used for this demonstration. Figure 4.5.3a shows the setup when the beam E_1 is coupled along the clockwise direction of the cavity and the beam E_2 is coupled along the counterclockwise direction of the cavity. Similar to the setup in figure 4.1.1, the frequency of E_1 is held at the center of a clockwise resonance frequency by a feedback loop. The discriminant voltage corresponding to E_2 is obtained by demodulating the output of PD^+ at f_2 by PSD_2, as shown in figure 4.5.3a. Block B prevents E_2 from coupling into the clockwise direction of the cavity. In Figure 4.5.3b, E_1 is left unperturbed but block B is now placed so as to allow a portion of E_2 to couple into the clockwise direction and prevent E_2 from coupling into the counterclockwise direction of the cavity. We also simultaneously switch the input of PSD_2 from PD^+ to PD^-, so it still generates the discriminant associated with E_2 which is now monitored by PD^-.

We now set $f_1 = 5$ kHz and $f_2 = 2$ kHz, and modulate the resonator arms to remove the double backscattering error due to splices as discussed in section 4.2.4. Figure 4.5.4a shows the output of the detector PD^+, indicating the switching of E_2 between clockwise and counterclockwise directions. A high level in this figure indicates the case where E_2 is traveling along the counterclockwise direction, and is thus picked up by PD^+, and a zero level indicates the case where E_2 is traveling along the clockwise direction and is detected only on PD^-. Figure 4.5.4b shows the output of PSD_2, which corresponds to the discriminant associated with E_2, as E_2 is being switched back and forth between the clockwise and the counterclockwise directions. It should be noted that as we switch E_2 from counterclockwise to clockwise direction, we simultaneously switch the input of PSD_2 from PD^+ to PD^- as indicated in figures 4.5.3.a and b. As shown in figure 4.5.4b, the output of PSD_2 exhibits a drift of about 100 Hz, which corresponds to a variation in the separation between the two adjacent cavity resonances. However, the important feature in the figure is the jump in this output as we switch E_2 between the clockwise and counterclockwise

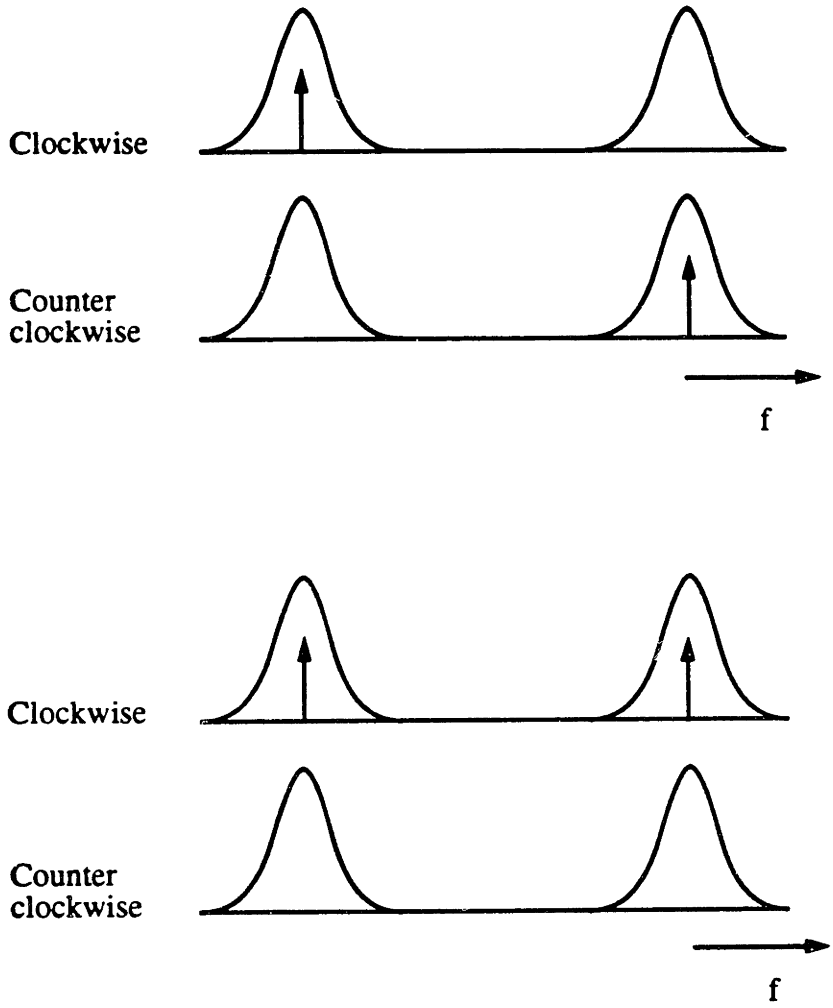

Figure 4.5.1. Procedure to setup an alternative measurement of the gyroscope bias (a) E_1 is coupled along the clockwise direction and E_2 is coupled along the counterclockwise direction (b) both E_1 and E_2 are coupled along the clockwise direction

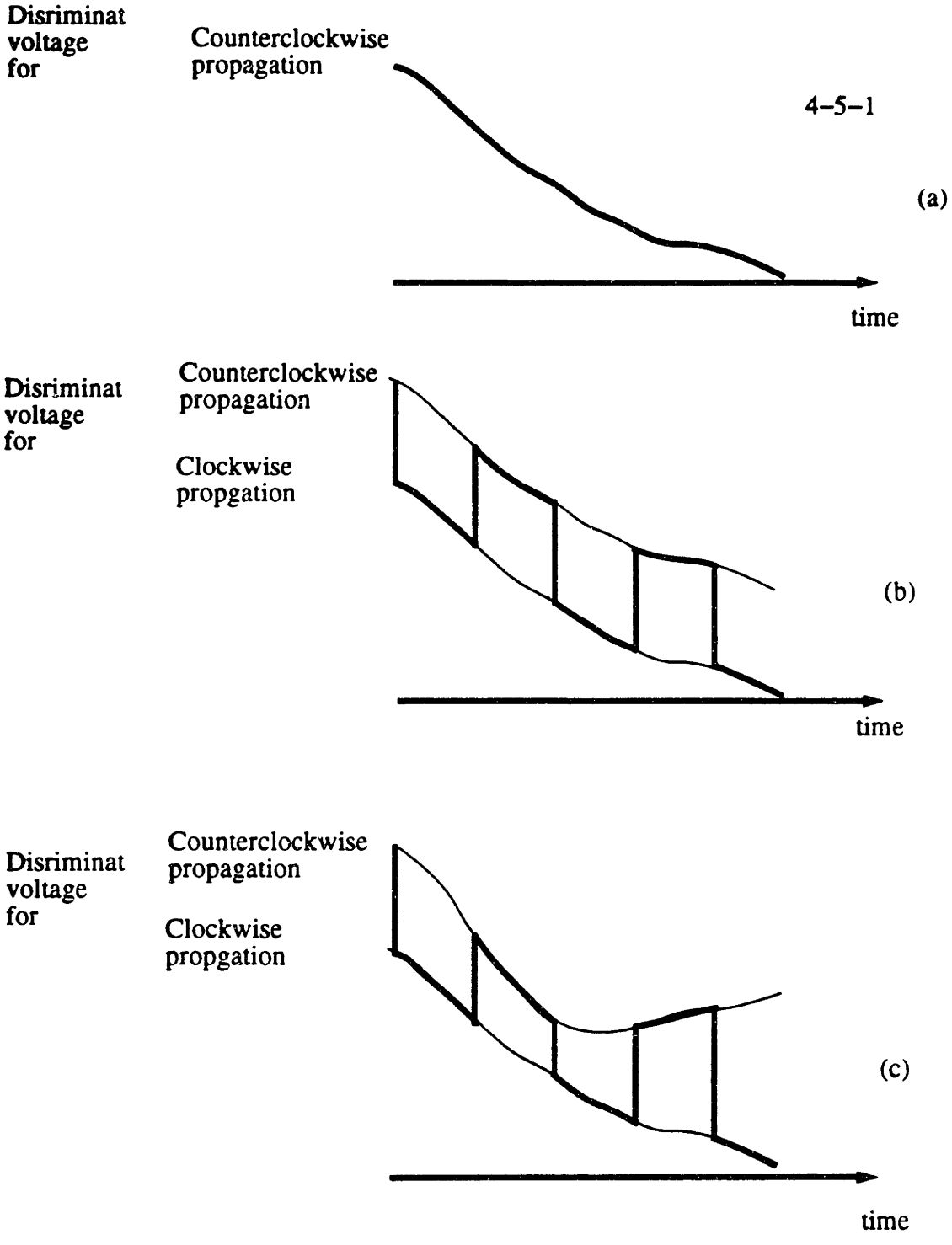

Figure 4.5.2. (a) Discriminant associated with E_2 indicating the drift between the resonance frequencies of the adjacent cavity longitudinal modes (b) this discriminant as E_2 is switched back and forth from counterclockwise direction to clockwise direction. The jump indicates a gyroscope offset (c) variation in the jump indicating an offset drift.

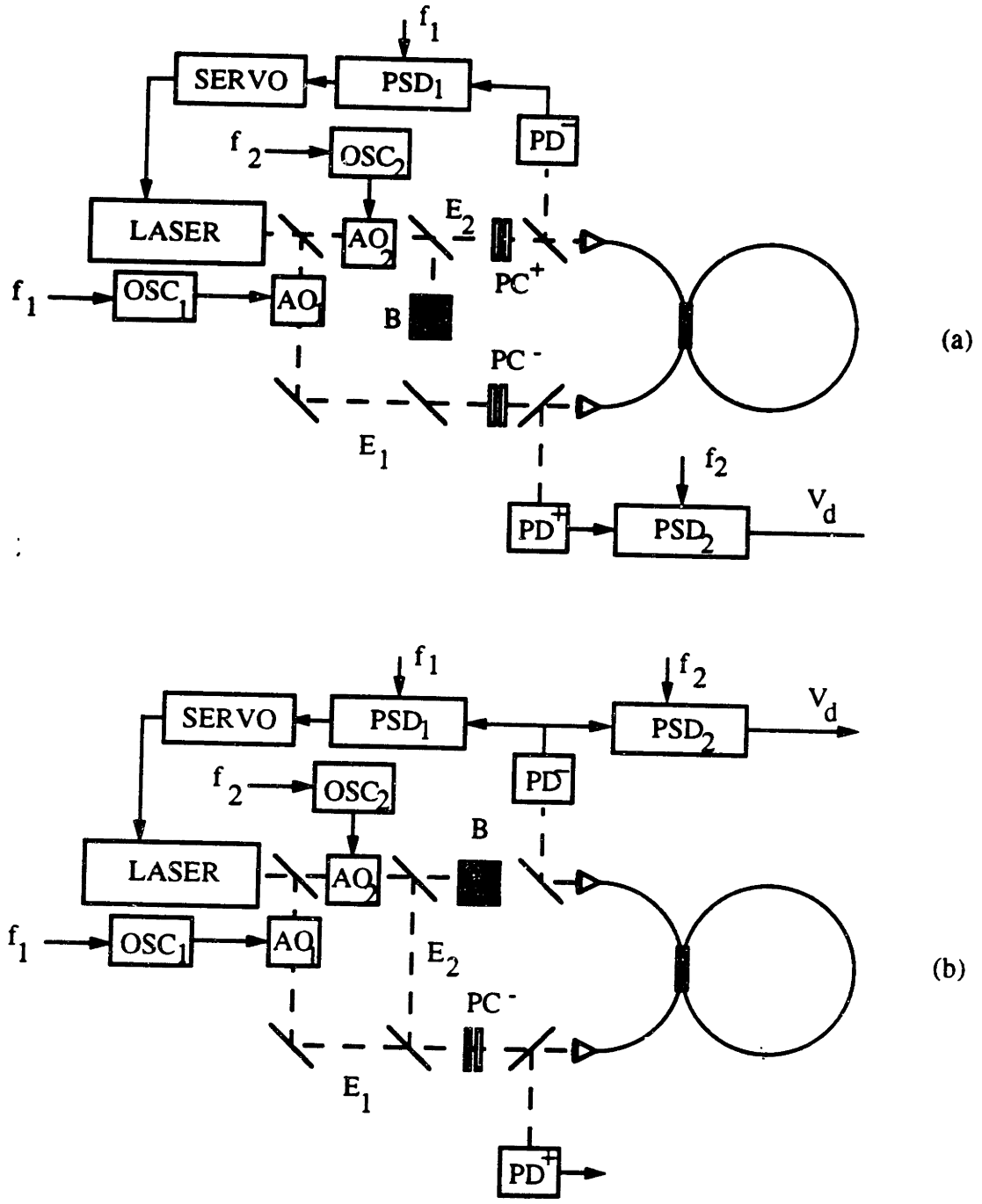

Figure 4.5.3. Experimental setup when (a) E_1 is along the clockwise direction and E_2 is along the counterclockwise direction (b) both E_1 and E_2 are along the clockwise direction

directions. One example of the jump is indicated in the area labeled A. As can be seen in

the figure. The magnitude of this jump is within the ±2.5 Hz noise of the PSD output.

These ±2.5 Hz fluctuations are consistent with the effects due to polarization drift and the Optical Kerr effect described in section sections 4.3 and 4.4. Thus, we have shown that without backscattering, there is no observable offset in our present setup.

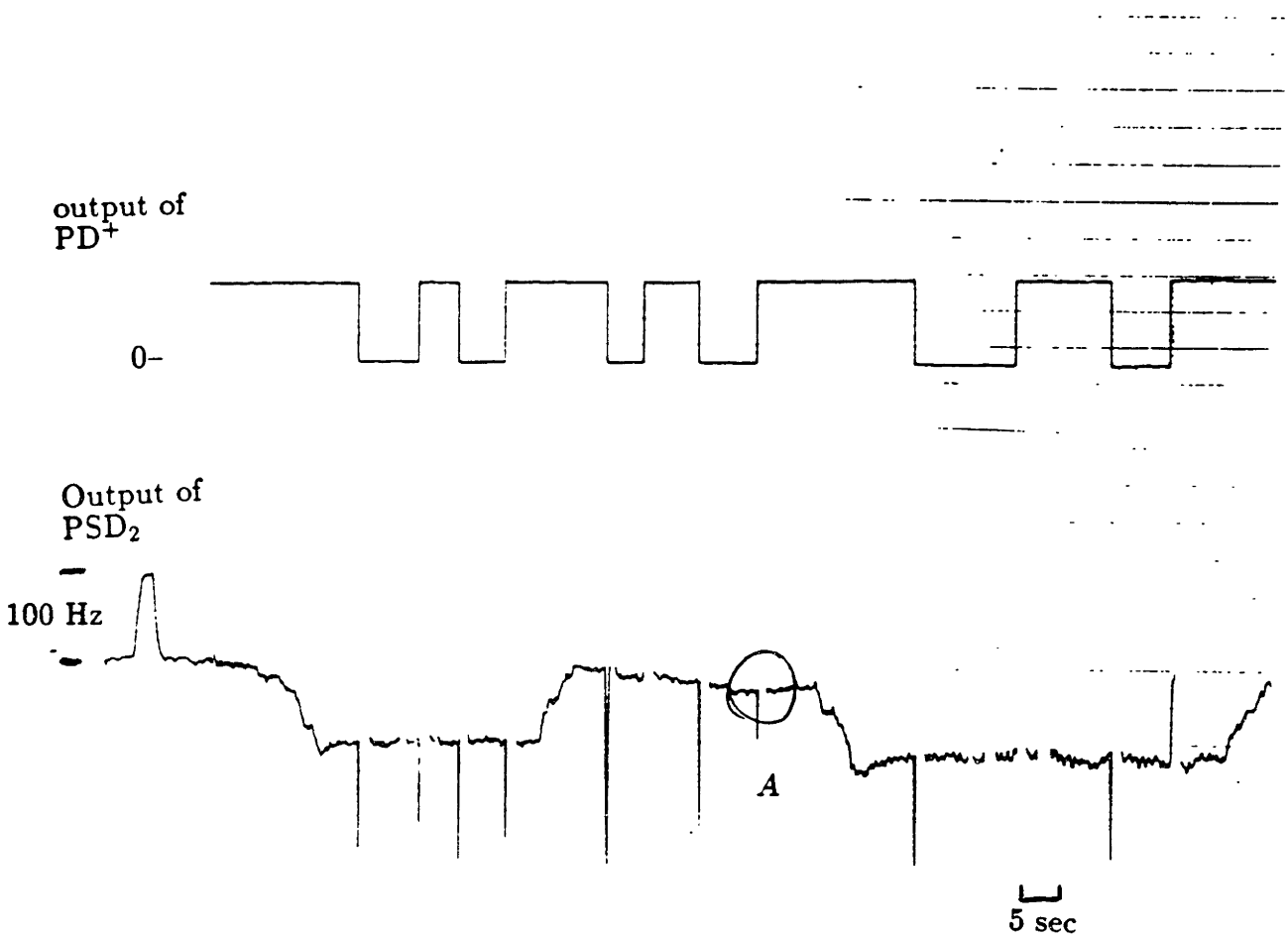

Figure 4.5.4. (a) output of PD^+ indicating whether E_2 is along the clockwise direction or along the counterclockwise direction (b) the discriminant associated with E_2 as it is switched back and forth from clockwise to counterclockwise direction

4.6 Additional Sources of Drift to be Studied

In this chapter we have demonstrated and evaluated sources of drift due to the backscattering of light, state of polarization of the input beams, and the optical Kerr effect in a fiberoptic PRG. We also demonstrated that the gyroscope offset in the absence of backscattering effects is less than 2.5 Hz (corresponding to 12.5 deg/hr).

Additional work on the drift sources in a fiber PRG is left for future studies. Possible sources of drift to be studied include, the evaluation of the change in the asymmetry of the cavity as a function of using separate modulation frequencies, the evaluation of drifts due to the quadrature component of the discriminant, and the change in the resonance asymmetry due to backscattering.

Additionally, in the future, by using a cavity in "transmission" we can reduce the resonance asymmetry shown in figure 4.1.3, in addition to reducing the polarization-induced errors described in section 4.3.3. It should be noted that, in order to remove the polarization-induced errors due to mode pulling, which are described in section 4.3.2, we need a single polarization cavity made from a single polarization fiber.

CHAPTER 5

Brillouin Fiber Ring Laser Gyroscope

As described in section 1.3, the main attraction of a ring laser gyroscope (RLG) is that the Sagnac resonance separation, Δf_Ω, is measured automatically by a clockwise and a counterclockwise laser generated inside the ring cavity. Although a fiberoptic PRG is relatively straight forward to implement, making a fiberoptic RLG is considerably more challenging.

The challenge in implementing a fiberoptic RLG is to find a suitable laser gain medium, which provides stable bidirectional lasing in a fiber ring cavity. Conventional solid-state gain media such as Nd-YAG[24] are not suitable for RLG applications because they are homogeneously broadened, thus preventing the simultaneous lasing along the clockwise and counterclockwise direction due to gain competition.

By comparison, a gain medium based on stimulated Brillouin scattering[25] (SBS) is directional[26,27,28,30] and therefore may support bidirectional lasing[29].

In this chapter we present the implementation of a fiberoptic RLG using SBS as the gain medium. After a brief description of the SBS process, we will demonstrate the operation of a simple SBS laser, as well as bidirectional lasing in a fiberoptic ring resonator. We will then use this setup to measure an applied angular velocity. We also demonstrate the lockin effect in a fiber RLG propose a method of eliminating this behavior. Finally, we show and analyze some drift data and demonstrate the optical Kerr effect in the Brillouin RLG.

5.1. Stimulated Brillouin Scattering (SBS)

Stimulated Brillouin scattering (SBS) is a third order nonlinear optical process, which can be used as the directional gain medium in a fiberoptic ring laser. Although the SBS process can be accurately described by a quantum mechanical treatment[31], it can also be understood using only classical mechanics. In this section, we will present the classical treatment of the SBS process in optical fibers.

5.1.1. A Physical Model for the SBS Process

In this section, we will describe the physical principles behind the SBS process. Let us consider an optical pump beam, E_p, which travels through the optical medium in the $+z$ direction, as shown in figure 5.1.1a, and is given by:

$$E_p = E_{p0} e^{j(k_p z - \omega_p t)} \tag{5.1.1}$$

where k_p is the amplitude of the k-vector associated with E_p and ω_p is the angular frequency of E_p. This wave can scatter from index perturbations due to thermal acoustic waves in the medium such as the one represented by A in figure 5.1.1b, which travel at the speed of sound, v, in the medium. The portion of E_p which is scattered in the forward direction experiences no frequency shift and is not of interest to us. The portion of E_p which is scattered in the backward direction, labeled E_b, is downshifted in frequency because of the doppler effect, as shown in figure 5.1.1c. Thus, E_b is given by:

$$E_b = E_{b0} e^{j(-k_b z + \omega_b t)} \tag{5.1.2}$$

where k_b is the amplitude of the k-vector associated with E_b and ω_b is the angular frequency of E_b. This angular frequency is given by$\omega_b = \omega_p(1 - \frac{2vn}{c})$ where n is the optical index of refraction of the medium. The frequency shift of E_b with respect to E_p, i.e. $\omega_p(2vn/c)$, is small compared to the absolute frequency of E_p.

The total electric field, E_T, which is now the sum of E_p and E_b, is given by:

$$E_T = E_{p0} e^{j(k_p z - \omega_p t)} + E_{b0} e^{j(-k_b z - \omega_b t)} \tag{5.1.3}$$

and the intensity, I_T, corresponding to this electric field, is given by:

$$I_T = \frac{nc}{8\pi}\left[|E_{p0}|^2 + |E_{b0}|^2 + 2Real\{E_{p0} E_{b0}^* e^{j\left((k_p + k_b)z - (\omega_p - \omega_b)t\right)}\}\right] \tag{5.1.4}$$

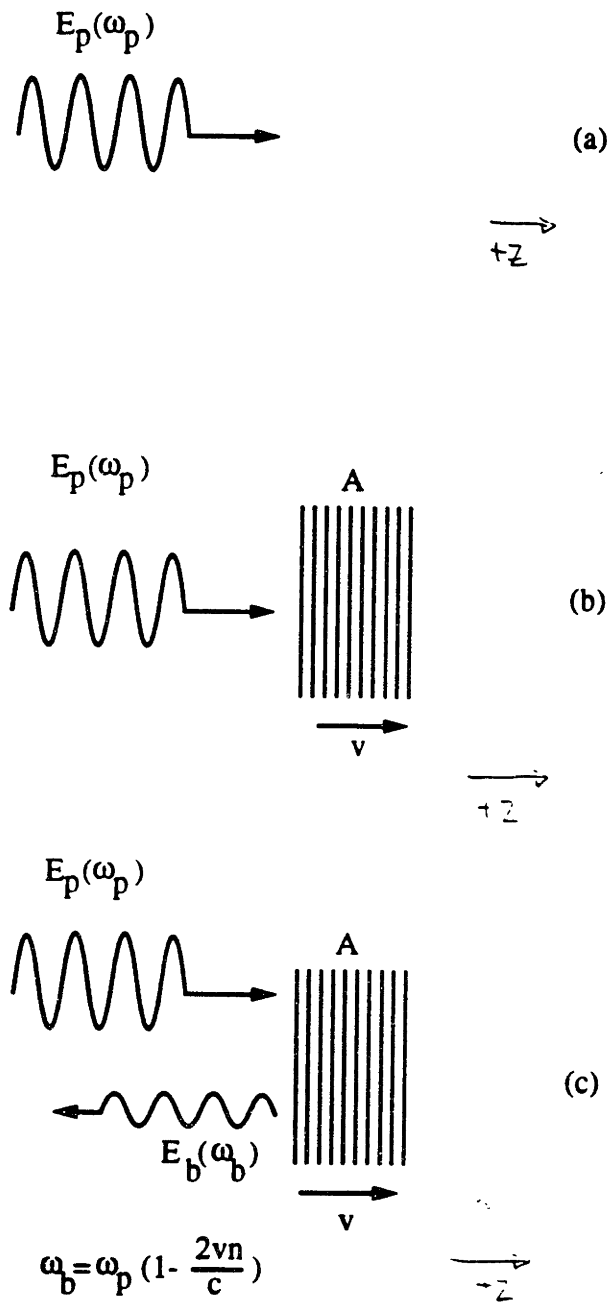

Figure 5.1.1. The SBS process (a) Propagation of a beam E_p in the medium (b) Interaction of E_p with an acoustic wave packet (c) $E-b$, generated by back-reflection of E_p from the wave packet

which corresponds to a partial intensity grating as a function of z with a peak to peak

amplitude of $2|E_p E_b^*|$, moving along the $+z$ direction with a velocity v_g, as shown in figure 5.1.2. The amplitude of the k-vector for this grating, k_g, is given by:

$$k_g = k_p + k_b \approx 2k_p \tag{5.1.5}$$

and the velocity of this grating is given by:

$$v_g = \frac{\omega_p - \omega_b}{k_g} = \frac{2vn\omega_p}{2ck_p} = v \tag{5.1.6}$$

which is equal to the velocity of sound in the fiber medium. This intensity grating is strongest if the thermal acoustic wave A satisfies the conditions:

$$\begin{aligned} k_a &= k_p + k_b \approx 2k_p \\ \omega_a &= \omega_p - \omega_b = \omega_p \frac{2v}{c} \end{aligned} \tag{5.1.7}$$

where k_a is the amplitude of the k-vector associated with the thermal acoustic wave, and ω_a is the angular frequency of this wave. The intensity grating thus formed amplifies this thermal acoustic wave by the elasto-optic coefficient of the material. Thus, both the acoustic wave and the Brillouin beam, E_b, gradually build up from thermal acoustic waves, similar to the amplification of spontaneous emission in a laser gain medium. In the next section a more rigorous derivation of the SBS process is presented.

5.1.2. Classical Derivation of the SBS Process

Now let us consider the classical derivation of SBS[32]. The acoustic and electromagnetic waves obey their respective wave equations in the medium, i.e.:

$$\begin{aligned} \nabla^2 E - \frac{n^2}{c^2}\frac{\partial^2 E}{\partial t^2} &= \frac{4\pi}{c^2}\frac{\partial^2}{\partial t^2} P^{NL} \\ v^2 \nabla^2 \rho - 2\Gamma_b \frac{\partial \rho}{\partial t} - \frac{\partial^2 \rho}{\partial t^2} &= \nabla^2 p^{EL} \end{aligned} \tag{5.1.8}$$

where E is the electric field inside the medium, ρ is the mass density of the medium, c is the free space speed of light, n is the optical index of refraction, and Γ_b is the halfwidth at half-maximum in angular frequency associated with the relaxation of the acoustic wave.

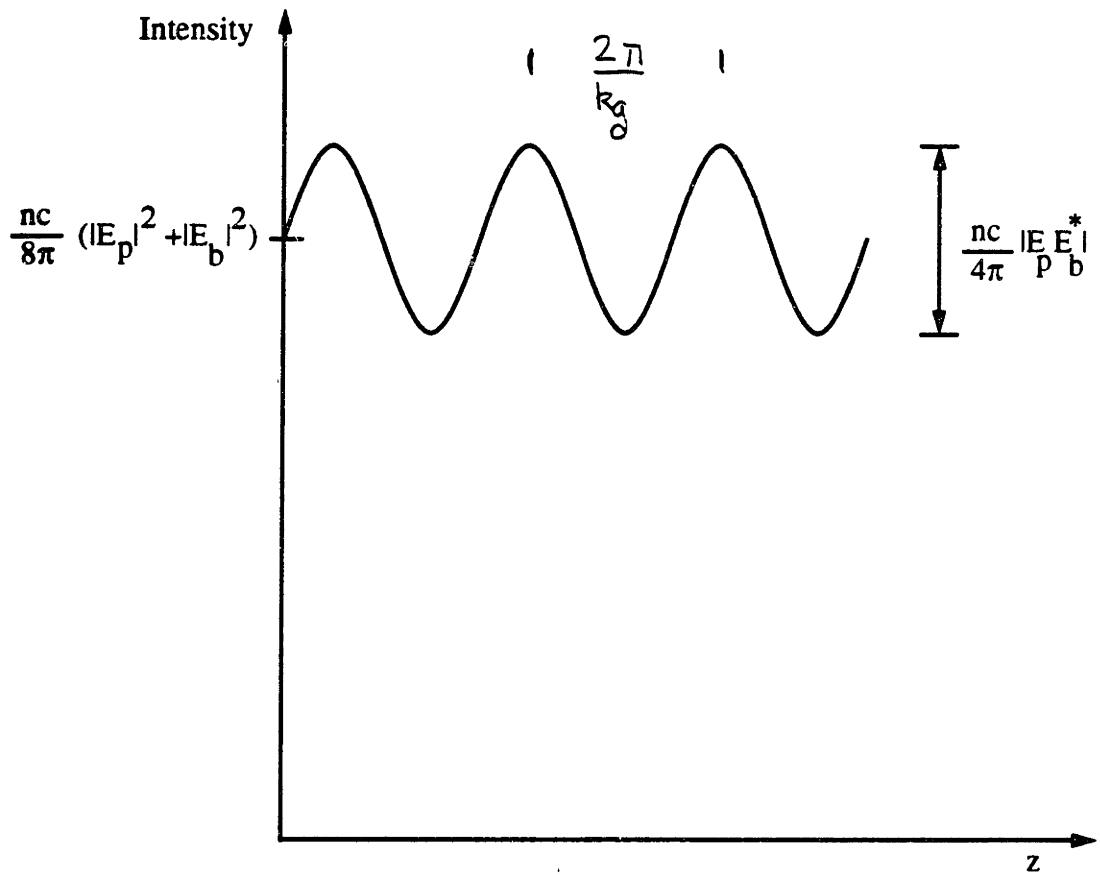

Figure 5.1.2. Sinusoidal variation in the intensity of light along the medium due to the interference between E_p and E_b

There are two coupling terms in equation 5.1.8: P^{NL}, which is the nonlinear polarization caused by the variations in ρ, and p^{EL}, which is the electrostrictive pressure in the material resulting from the energy density associated with E.

The nonlinear polarization term P^{NL} is expressed as the change in the polarization

ϵE due to the variation in the density of the medium, ρ, and is given by:

$$\begin{aligned} P^{NL} &= \frac{1}{4\pi}\rho\frac{\partial}{\partial\rho}(\epsilon E) \\ &= \frac{1}{4\pi}\frac{\partial\epsilon}{\partial\rho}E\rho \end{aligned} \tag{5.1.9}$$

This term couples the variation in density caused by the acoustic wave to the electromagnetic wave equation.

The electrostrictive pressure, p^{EL}, corresponds to the build up of internal mechanical stress inside the medium in response to the energy density of light, $\epsilon E^2/8\pi$, and is given by:

$$\begin{aligned} p^{EL} &= \frac{1}{8\pi}\rho_\circ\frac{\partial}{\partial\rho}(\epsilon E^2) \\ &= \frac{1}{8\pi}\rho_\circ\frac{\partial\epsilon}{\partial\rho}E^2 \end{aligned} \tag{5.1.10}$$

where $\rho_\circ$ is the average mass density of the medium.

We can now represent the electric field as the sum of the complex field for the pump beam, E_p, and that for the backscattered Brillouin beam, E_b. The acoustic wave is represented as a complex scalar ρ_a. These waves are given by:

$$\begin{cases} E_p = E_{p0}e^{j(k_p z-\omega_p t)} \\ E_b = E_{b0}e^{j(-k_b z-\omega_b t)} \\ \rho_a = Ae^{j(k_a z-\omega_a t)} \end{cases} \tag{5.1.11}$$

where E_{p0}, E_{b0}, and A are the complex amplitudes of E_p, E_b, and ρ_a respectively. k_p, k_b, and k_a are the amplitudes of the k-vectors associated with these waves, and ω_p, ω_b and ω_a are the angular frequencies associated with these waves. The electromagnetic and acoustic wave equations can now be rewritten for E_p, E_b, and ρ_a as:

$$\begin{aligned} \nabla^2 E_p + \frac{n^2\omega_p^2}{c^2}E_p &= -\frac{4\pi\omega_p^2}{c^2}P^{NL}(\omega_p) \\ \nabla^2 E_b + \frac{n^2\omega_b^2}{c^2}E_p &= -\frac{4\pi\omega_b^2}{c^2}P^{NL}(\omega_b) \\ v^2\nabla^2\rho_a + 2\Gamma_b\omega_a\rho_a + \omega_a^2\rho_a &= \nabla^2 p^{EL}(\omega_a) \end{aligned} \tag{5.1.12}$$

where $p^{EL}(\omega_a)$, $P^{NL}(\omega_p)$ and $P^{NL}(\omega_b)$ are given by:

$$\begin{aligned} P^{NL}(\omega_p) &= \frac{1}{4\pi}\frac{\partial \epsilon}{\partial \rho} E_{b0} A e^{j(-k_b+k_a)z-j\omega_p t} \\ P^{NL}(\omega_b) &= \frac{1}{4\pi}\frac{\partial \epsilon}{\partial \rho} E_{p0} A^* e^{j(k_p-k_a)z-j\omega_b t} \\ p^{EL}(\omega_a) &= \frac{1}{8\pi}\rho_\circ \frac{\partial \epsilon}{\partial \rho} E_{p0} E_{b0}^* e^{j(k_p+k_b)z-j\omega_a t} \end{aligned} \tag{5.1.13}$$

The complex nonlinear polarization term $P^{NL}(\omega_b)$ depends on the amplitude of the acoustic wave A, which is calculated from the acoustic wave equation. The following relationships are used to simplify the acoustic wave equation:

$$\begin{cases} \nabla^2 A e^{jk_a z} = (jk_a + \partial/\partial z)^2 A e^{jk_a z} \approx (-k_a^2 + 2jk_a \partial/\partial z) A e^{jk_a z} \\ \nabla^2 p^{EL}(\omega_a) \approx -k_a^2 p^{EL}(\omega_a) \\ \omega_a = v k_a \end{cases} \tag{5.1.14}$$

The simplified acoustic wave equation is given by:

$$\begin{aligned} 2jk_a v^2 \frac{\partial A}{\partial z} + 2jv\Gamma_b k_a A &= -k_a^2 p^{EL}(\omega_a) e^{-j(k_a z-\omega_a t)} \\ &= -\frac{k_a^2}{8\pi}\rho_\circ \frac{\partial \epsilon}{\partial \rho} E_{p0} E_{b0}^* e^{j(k_p+k_b-k_a)z} \\ &= -\frac{k_a^2}{8\pi}\rho_\circ \frac{\partial \epsilon}{\partial \rho} E_{p0} E_{b0}^* e^{j\Delta k z} \end{aligned} \tag{5.1.15}$$

where $\Delta k = k_p + k_b - k_a$.

In order to solve for A from the above equation we use the fact that the primary z-dependence in the above equation is due to term $e^{j\Delta k z}$, and make the simplifying assumption of $A = A_\circ e^{j\Delta k z}$, to arrive at:

$$A = \frac{k_a \rho_\circ}{16\pi v}\frac{\partial \epsilon}{\partial \rho}\frac{1}{v\Delta k - j\Gamma_b} E_{p0} E_{b0}^* e^{j\Delta k z} \tag{5.1.16}$$

which results in an expression for the nonlinear polarization, $P^{NL}(\omega_b)$, given by:

$$\begin{aligned} P^{NL}(\omega_b) &= \frac{k_a \rho_\circ}{64\pi^2 v}\frac{\partial \epsilon}{\partial \rho}^2 \frac{1}{v\Delta k + j\Gamma_b} E_{p0} E_{p0}^* E_{b0} e^{j(-k_b z-\omega_b t)} \\ &= \chi^{(3)}(\omega_b) E_{p0} E_{p0}^* E_b \end{aligned} \tag{5.1.17}$$

where the third order nonlinear susceptibility $\chi^{(3)}(\omega_b)$ is given by:

$$\chi^{(3)}(\omega_b) = \frac{k_a \rho_o}{64\pi^2 v}(\frac{\partial \epsilon}{\partial \rho})^2 \frac{1}{v\Delta k + j\Gamma_b} \tag{5.1.18}$$

$v\Delta k$ in equation 5.1.18 can be replaced by $\Delta\omega_b$, which represents the difference between ω_b and $\omega_p(1 - 2vn/c)$. Thus, $\chi^{(3)}$ is given by:

$$\chi^{(3)}(\omega_b) = \frac{k_a \rho_o}{64\pi^2 v}(\frac{\partial \epsilon}{\partial \rho})^2 \frac{1}{\Delta\omega_b + j\Gamma_b} \tag{5.1.19}$$

Using a similar treatment for the electromagnetic wave equation for E_b we arrive at:

$$\begin{aligned} \frac{\partial E_b}{\partial z} &= -\frac{2\pi j k_b}{n^2} P^{NL}(\omega_b) \\ &= -\frac{2\pi j k_b}{n^2} \chi^{(3)}(\omega_b) E_{p0} E_{p0}^* E_b \end{aligned} \tag{5.1.20}$$

The gain coefficient, g, for the intensity of E_b is given in terms of $\chi^{(3)}(\omega_b)$ to be:

$$\begin{aligned} g &= \frac{4\pi k_b}{n^2} Im\{\chi^{(3)}(\omega_b) E_{p0} E_{p0}^*\} \\ &= -\frac{k_a k_b}{16\pi n^2 v} \rho_o (\frac{\partial \epsilon}{\partial \rho})^2 \frac{\Gamma_b}{\Delta\omega_b^2 + \Gamma_b^2} E_{p0} E_{p0}^* \end{aligned} \tag{5.1.21}$$

where the maximum gain, g_o, is reached when $\Delta\omega_b = 0$, and is given by:

$$g_o = \frac{k_a k_b}{16\pi n^2 v \Gamma_b} \rho_o (\frac{\partial \epsilon}{\partial \rho})^2 E_{p0} E_{p0}^* \tag{5.1.22}$$

We now make the following substitutions:

$$\begin{cases} k_b = 2\pi n/\lambda_o \\ k_a = 4\pi n/\lambda_o \\ \rho_o(\partial\epsilon/\partial\rho) = \delta_e \\ E_{p0} E_{p0}^* = (8\pi/nc) I_p \\ \Gamma_b = \pi\Delta\nu \end{cases}$$

where λ_o is the wavelength of the pump beam E_p, δ_e is the electrostriction coefficient for the material, c is the free space speed of light, $\Delta\nu$ is the full width half maximum bandwidth of the acoustic excitation, and I_p is the intensity of the pump beam.

$$\begin{aligned} g_o &= \frac{4\pi\delta_e^2}{\lambda_o^2 ncv\rho_o\Delta\nu} I_p \\ &= \gamma_b I_p \end{aligned} \tag{5.1.23}$$

where:

$$\gamma_b = \frac{4\pi\delta_e^2}{\lambda_o^2 ncv\rho_o\Delta\nu} \tag{5.1.24}$$

which predicts that the gain g, associated with the SBS process, is linearly proportional to the intensity of the pump beam, I_p, with a proportionality constant of γ_b. γ_b, in turn, is proportional to the square of the electrostriction coefficient, i.e. δ_e^2, which determines the coupling between the acoustic and electromagnetic waves.

5.2. The SBS Ring Laser

As described in the previous section, the SBS process can be used as the gain medium of a fiber ring laser. In this chapter, we demonstrate the operation of such a fiber ring laser. We measure the SBS laser power output as a function of the pump power input, and determine the minimum (threshold) pump power required for the operation of our Brillouin laser. We then compare this pump threshold power with theoretical predictions. We also demonstrate a secondary Brillouin laser oscillation for very strong pump powers.

5.2.1. Observation of Brillouin Lasing

Figure 5.2.1 shows a SBS fiber ring laser setup, which lases in the counterclockwise direction of the fiber ring cavity. As shown in the figure, the SBS laser pump beam, E_p^-, is originally generated by a single frequency He-Ne laser operating at 1.15 μm, and subsequently coupled into the fiber cavity along the clockwise direction. The polarization controlling element PC^-, which consists of a $\lambda/2$ and a $\lambda/4$ wave plate, aligns the polarization of E_p^- with an eigen polarization of the cavity for maximum intracavity pump intensity. The photodetector, PD^-, monitors E_p^- when it emerges from the resonator. The frequency of E_p^- is locked to the center of a clockwise cavity resonance by a feedback loop, similar to the case described for a fiberoptic PRG in section 4.1.1.

In order to demonstrate the operation of the SBS laser, we monitor the beam traveling along the direction opposite to that of E_p^-, by a scanning Fabry-Perot spectrum analyzer,

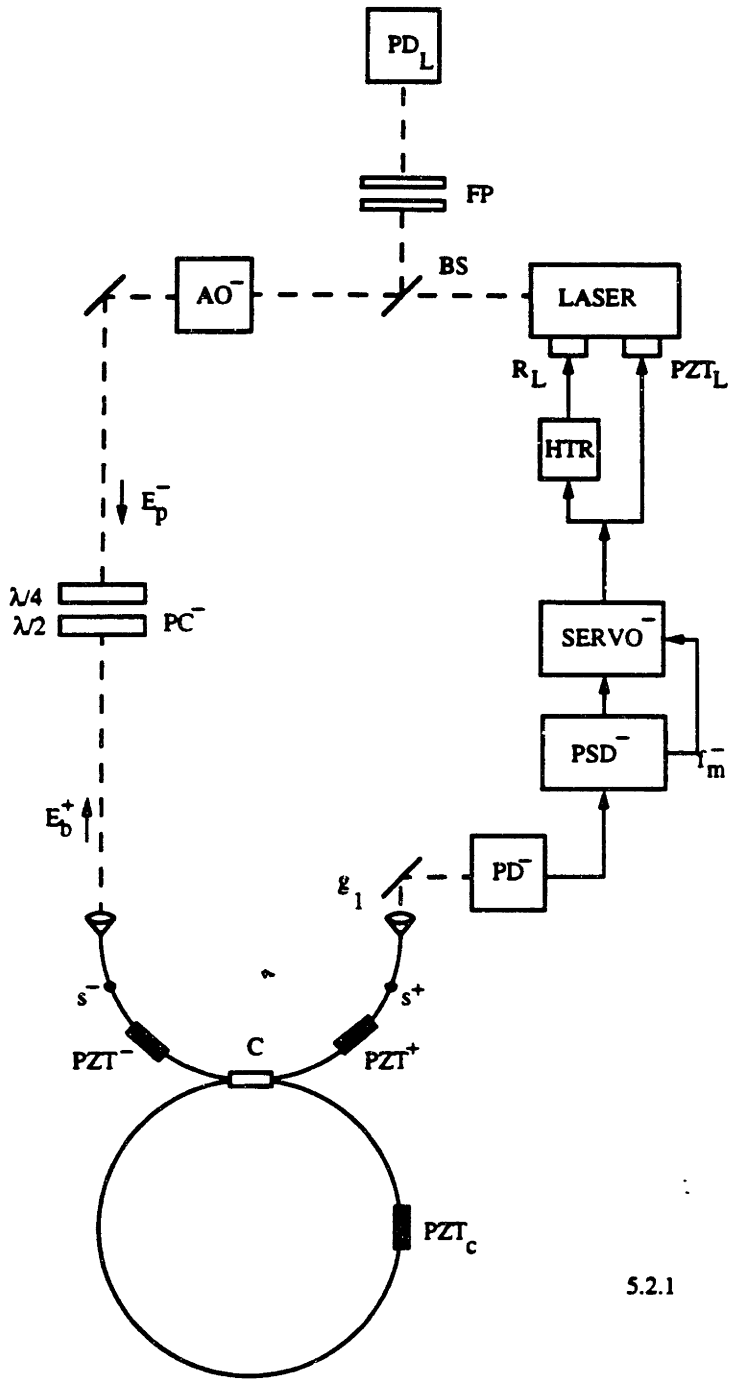

Figure 5.2.1. Experimental setup to observe SBS lasing, with output E_b^+, along the counterclockwise direction of the cavity

FP, as shown in figure 5.2.1. This analyzer has a free spectral range of 70 GHz and a

linewidth of 2 GHz. Figure 5.2.2a shows the output of the scanned spectrum analyzer, when the intensity of E_p^- is 40 μW. In this case the Brillouin gain is not large enough for SBS lasing. The peaks shown in figure 5.2.2a, are due to the backscattering of E_p^-, as described in section 4.2.1. The separation between these peaks in figure 5.2.2a shows the 70 GHz free spectral range of the Fabry-Perot spectrum analyzer. By contrast, figure 5.2.2b, shows the analyzer output when the intensity of E_p^- is increased to 100 μW, corresponding to the case where there is enough gain for the SBS laser to operate. In this case, in addition to the small backscattering peak of the previous figure, we also observe a strong peak due to SBS lasing, which is shifted by 15 GHz with respect to the pump beam. This 15 GHz frequency shift is consistent with the predictions of equation 5.1.2. Thus we have demonstrated the operation of an SBS ring laser. In the next section we will discuss the pump threshold power and conversion efficiency for this laser.

5.2.2. Threshold and Lasing Efficiency of the Brillouin Laser

Figure 5.2.3 shows the counterclockwise Brillouin laser output power, W_b^+, as a function of the clockwise pump intensity, W_p^-, indicating a pump threshold power of 60 μW. The maximum conversion efficiency of this Brillouin laser, i.e. $\Delta W_b^+ / \Delta W_p^-$, is approximately 30%.

To calculate the Brillouin threshold we must first calculate the cavity loss, which is the attenuation in the intensity of the intracavity beam, I_r after one round trip. For a high finesse cavity the loss is given by:

$$\text{cavity loss} = \frac{\Delta I_r}{I_r} \approx \frac{2\pi}{F} \tag{5.2.1}$$

where F is the finesse of the resonator. The round trip amplification in I_r due to the SBS process, which is labeled G, is given by:

$$\begin{aligned} G &= \gamma_b I_{rp} N P \\ &= \frac{\gamma_b W_p F N P}{\pi S} \end{aligned} \tag{5.2.2}$$

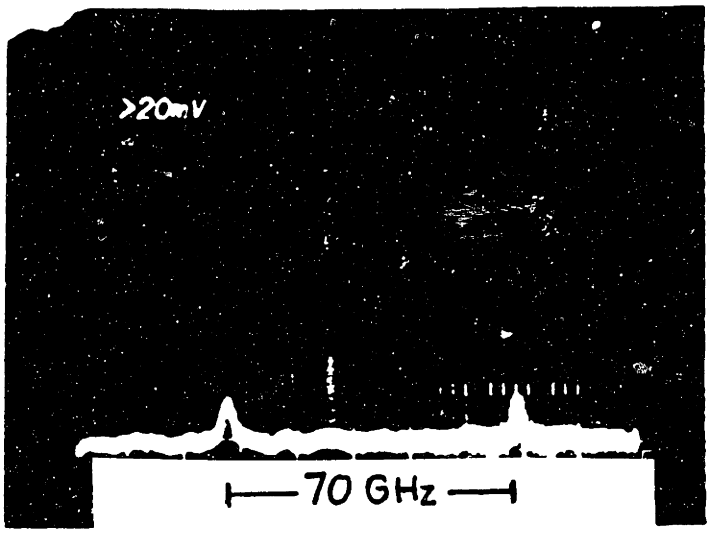

(a)

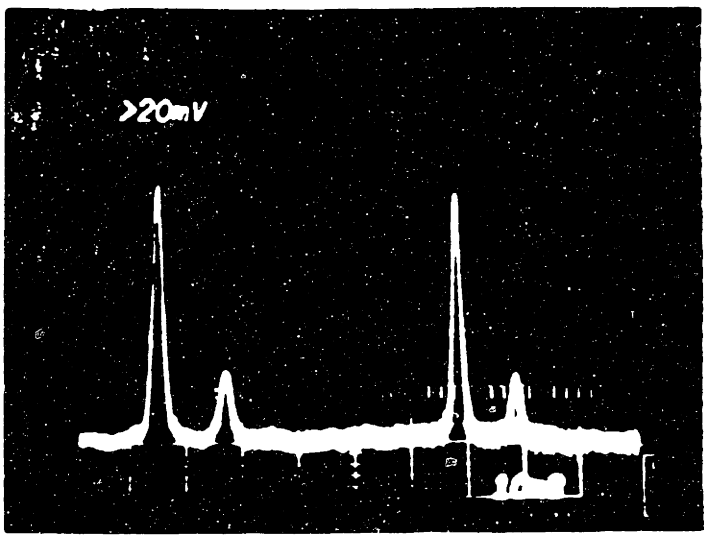

(b)

Figure 5.2.2. output of the linear FP analyzer monitored by PL as a function of the scan voltage of the analyzer indicating (a) a small backscattering of pump beam (b) pump backscattering together with the SBS laser output.

where γ_b is the Brillouin gain constant defined in equation 5.1.24, I_{rp} is the intracavity

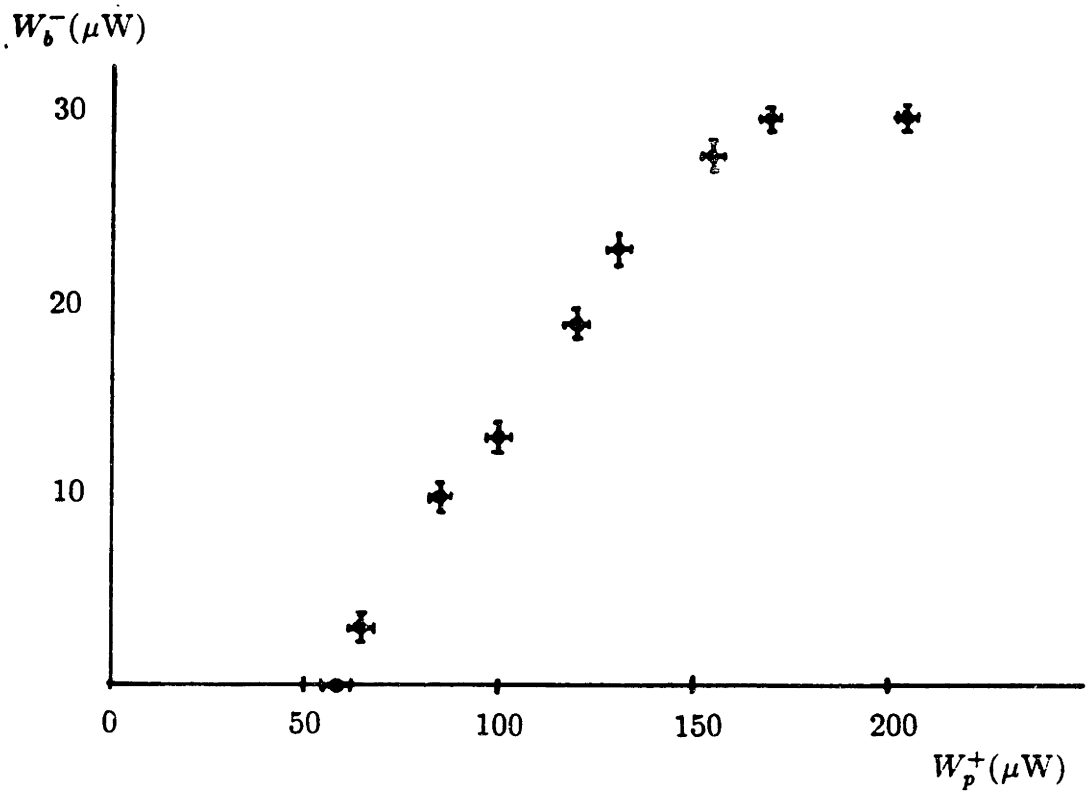

Figure 5.2.3. SBS laser power output, W_b^-, as a function of pump power input W_p^+, indicating a 60μW pump threshold for SBS lasing and a conversion efficiency of 30%

pump intensity, W_p is the pump power coupled into the resonator, P is the perimeter of the fiber resonator, N is the number of turns of the resonator fiber and S is the equivalent fiber cross section area. It should be noted that the Brillouin gain depends on the finesse of the resonator, because the intracavity light is a factor of F/π more intense than the

light outside of the resonator. The threshold power W_p^{th} is obtained by setting, G = cavity loss, which yields:

$$W_p^{th} = \frac{2\pi^2 S}{\gamma_b NPF^2} \tag{5.2.3}$$

As expected, W_p^{th} is inversely proportional to the perimeter of the resonator. However, W_p^{th} is also inversely proportional to the square of finesse because both G and cavity loss depend on the finesse as shown in equation 5.2.1 and 5.2.2.

In order to numerically evaluate W_p^{th}, we first need to calculate γ_b, which is represented by equation 5.1.24. In our case we have:

$$\begin{cases} \delta_e = \rho_o(\delta\epsilon/\delta\rho) = 0.3 \\ \lambda_o = 1.15 \times 10^{-4}\ \mu\text{m} \\ n = 1.48 \\ c = 3 \times 10^{10}\ \text{cm/sec} \\ v = 5.9 \times 10^{5}\ \text{cm/sec} \\ \rho_o = 2.2\ \text{g/cm}^3 \\ \Delta\nu_B \approx 30\ \text{MHz}\ [33] \end{cases}$$

resulting in $\gamma_b = 5.5 \times 10^{-10}$ cm/W. For $F = 300$, $NP = 2500$ cm, and $S = 2.8 \times 10^{-7}$ cm^2, the pump threshold power is calculated to be approximately 40 μW. This is in reasonable agreement with our observed threshold of 60 μW. We have observed the a threshold intensity as low as 30 μW when the finesse of the resonator is increased to approximately 400. This is also consistent with the predictions of equation 5.2.3.

5.2.3. Secondary Brillouin Lasing

As shown in figure 5.2.3 the intensity of the Brillouin beam E_b^+ increases with the pump intensity. If E_b^+ is strong enough, it can act as the pump for a secondary Brillouin laser E_{bb}^-. This beam is counterpropagating with respect to the primary Brillouin beam E_b^+, and is therefore along the same direction as that of the original pump beam E_p^-.

In order to observe the secondary Brillouin lasing, the optical power of E_p^- is increased to 250 μW, i.e. approximately 4 times the Brillouin lasing threshold. As described in the previous section. we observe the spectrum of light traveling in the direction opposite to

that of E_p^- by a scanning Fabry-Perot analyzer with a FSR of 70 GHz whose output is monitored by a photodetector PD_1 as shown in figure 5.2.4. Figure 5.2.5a shows the output of PD_1 as a function of the scanning voltage of the Fabry-Perot analyzer, where the small peak A, is due to the backscattering of E_p^- and the larger peak B, is due to the primary Brillouin beam E_b^+. We now observe the spectrum of the light traveling in the same direction as that of E_p^- by splitting off some of this light using the piece of glass g_2. This light is then passed through a Fabry-Perot analyzer similar to that used in figure 5.2.5a, and monitored by a photodetector PD_2 as shown in figure 5.2.4. Figure 5.2.5b shows the output of PD_2 as a function of the laser frequency, where the off-scale peak A is due to E_p^-. The peak B which is 15 GHz from E_p^-, is due to the backscattering of E_b^+. Finally, the peak C which is 30 GHz from E_p^-, is due to secondary Brillouin laser E_{bb}^-, which, as expected, travels in the same direction as E_p^-.

The secondary Brillouin lasing in our cavity starts at a pump power greater than 200 μW. More over, we have also observed a third order Brillouin laser as we increased the pump power further. In general, the higher order Brillouins interfere with the operation of the gyroscope and must be avoided.

5.3. The Brillouin Ring Laser Gyroscope (BRLG)

In this section we describe the operation of a fiberoptic ring laser gyroscope (RLG) based on SBS. Figure 5.3.1 shows the experimental setup for the fiber Brillouin ring laser gyroscope (BRLG). Similar to the passive resonator gyroscope of section 4.1.1, light from a single frequency He-Ne laser is split by a beam splitter BS into two beams, E_p^+ and E_p^-, which are then shifted in frequency by AO modulators, AO^+ and AO^- respectively, and coupled into the fiber ring resonator. The beam E_p^+ is coupled along the counterclockwise direction of the resonator, where it pumps a Brillouin laser along the clockwise direction of the cavity. This Brillouin laser has an output beam E_b^-. Similarly, the beam E_p^- is coupled along the clockwise direction of the cavity, where it excites a Brillouin laser along the

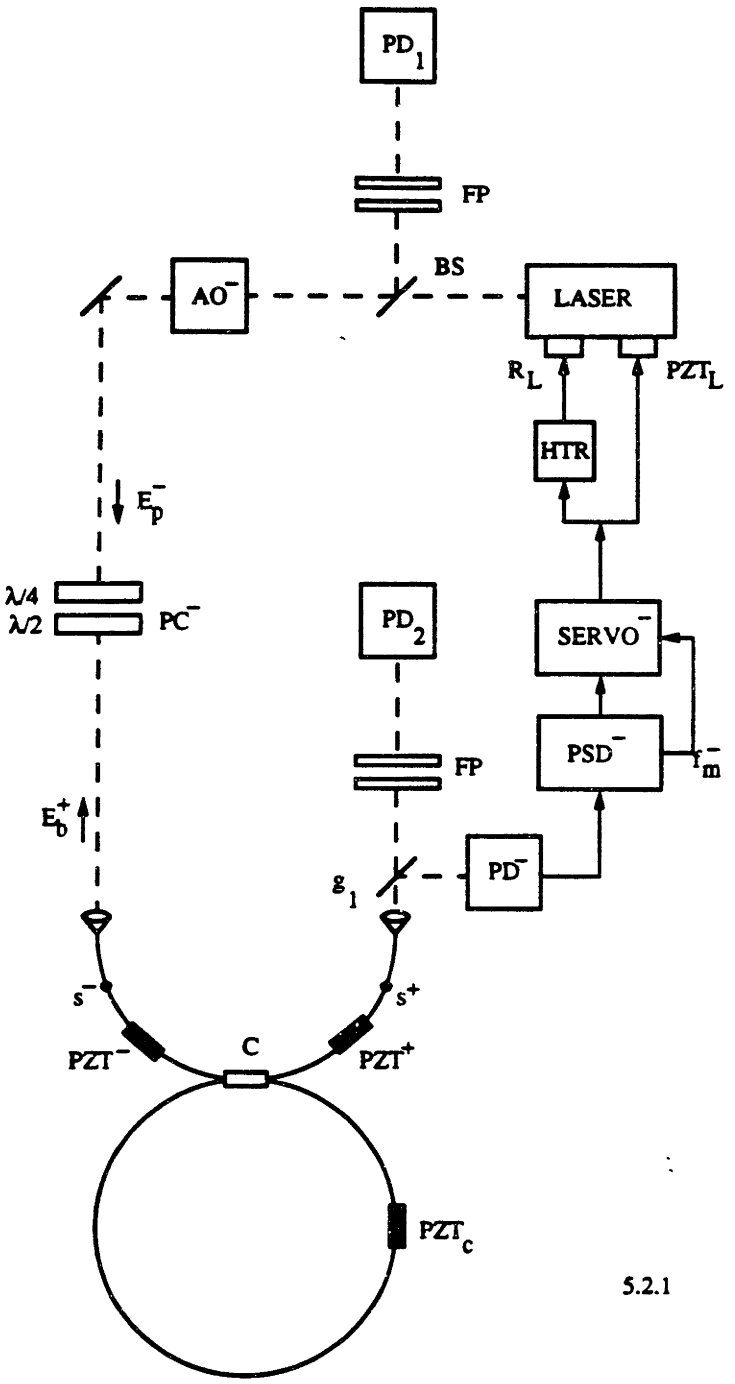

Figure 5.2.4. Schematic diagram of the setup used in observing secondary Brillouin lasing

counterclockwise direction of the cavity. This Brillouin laser has an output beam E_b^+. The

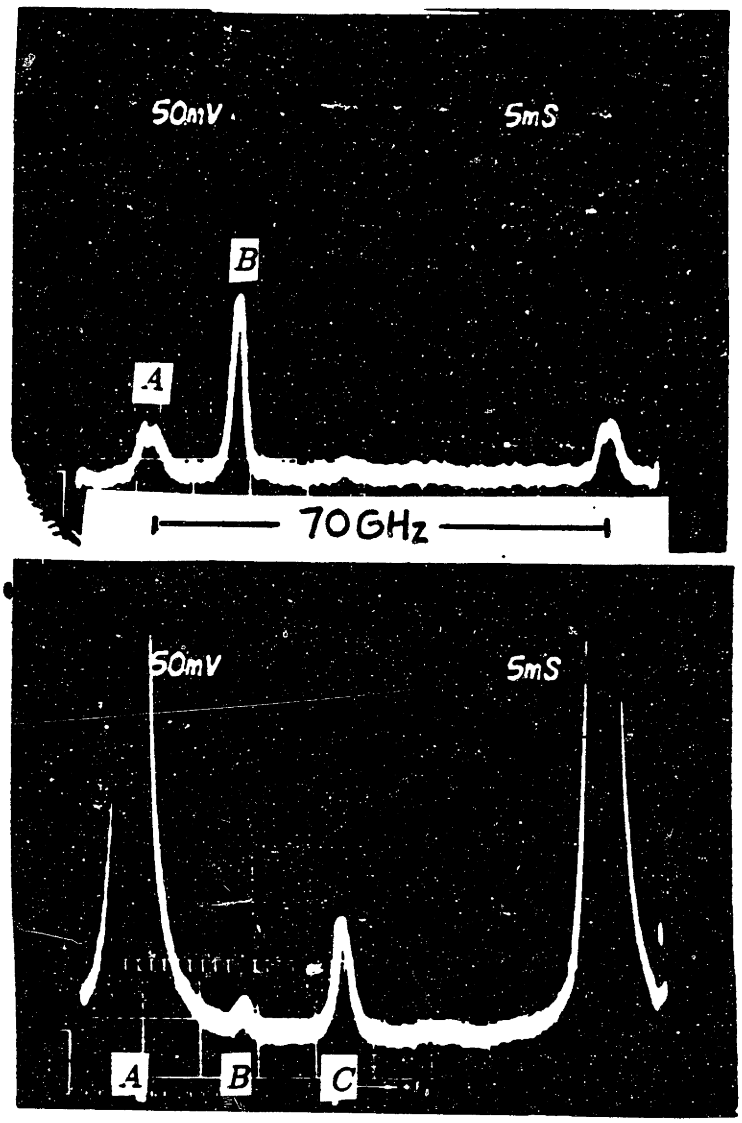

Figure 5.2.5. (a) Spectrum of the beams traveling along the counterclockwise direction of the cavity indicating a small backscattering of the pump E_p^- (A) and the SBS laser output E_b^+ (B) (b) Spectrum of the beams traveling along the clockwise direction of the cavity indicating the pump beam E_p (A), the backscattering of the original SBS beam E_B^+ (B), and the secondary Brillouin beam E_{bb}^- (C)

two Brillouin laser outputs, E_b^+ and E_b^-, together with residual pump intensities due to E_p^+ and E_p^- are combined into one beam, E_o, by the beam splitter BS. The Fabry-Perot interferometer, FP, mentioned in section 5.2.1, is adjusted to pass the Brillouin components of E_o and block the residual pump intensities. The beatnote between the two Brillouin beams is then monitored either by a low frequency detector, PD_L, which is sensitive to frequency components from 0-50 kHz, or by a high frequency detector, PD_H, which is sensitive to frequency components from 1-200 MHz.

As mentioned in section 5.2.1, a feedback loop holds the the frequency of E_p^- at the center of a clockwise cavity resonance. The frequency of E_p^+ is then manually adjusted to be at the center of a clockwise resonance.

5.3.1. Bidirectional Lasing in the BRLG

In section 5.2.1, we demonstrated unidirectional Brillouin lasing along the counterclockwise direction of our fiber ring cavity. In this section we demonstrate stable and simultaneous lasing of a clockwise and a counterclockwise Brillouin laser.

In order to show the simultaneous presence of both E_b^+ and E_b^-, we monitor the beatnote between these two beams by either PD_H or PD_L. We separate the frequencies of E_b^+ and E_b^- by 11 FSR of the cavity, i.e. 84.7 MHz, to force the Brillouin lasers to also use two cavity modes separated by 11 FSRs. Figure 5.3.2 shows the spectrum of the beatnote between E_b^+ and E_b^- obtained by feeding the output of PD_H to a spectrum analyzer. The frequency of the beatnote on PD_H is measured by a digital frequency counter to be approximately 169.4 MHz, which is due to the additional frequency shifting of E_b^+ and E_b^- by the AO modulators. The measured width of the Brillouin beatnote in figure 5.3.2 is 30 Hz. Although limited by the resolution of our spectrum analyzer, figure 5.3.2 demonstrates simultaneous and stable lasing of both the clockwise and counterclockwise Brillouin lasers.

To obtain a more accurate measurement of the width of the Brillouin beatnote, the output of PD_H was electronically mixed down to approximately 40 Hz using a stable

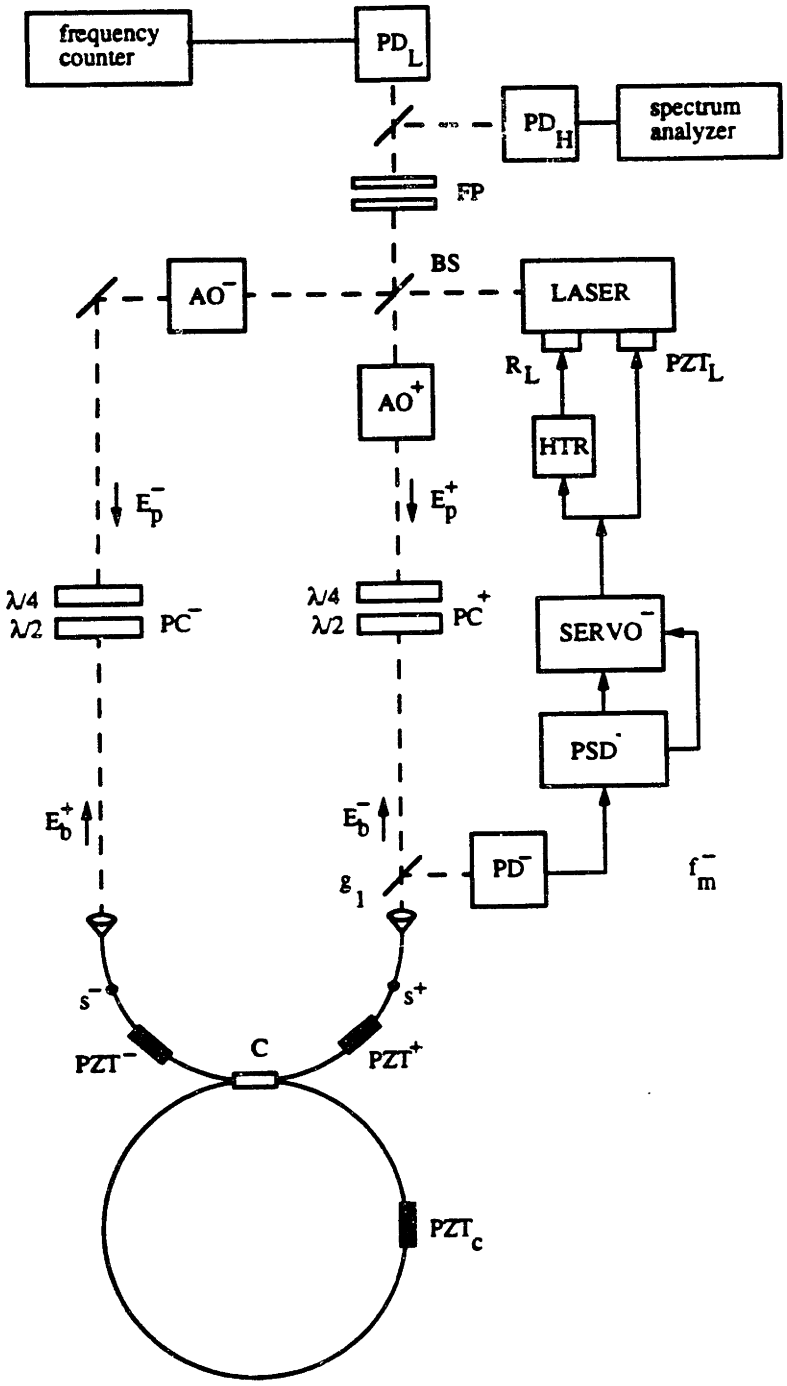

Figure 5.3.1. Experimental setup for the fiber BRLG

reference frequency generated by a high precision frequency synthesizer. The spectral width of our reference signal has been previously measured to be less than 0.1 Hz. Figure

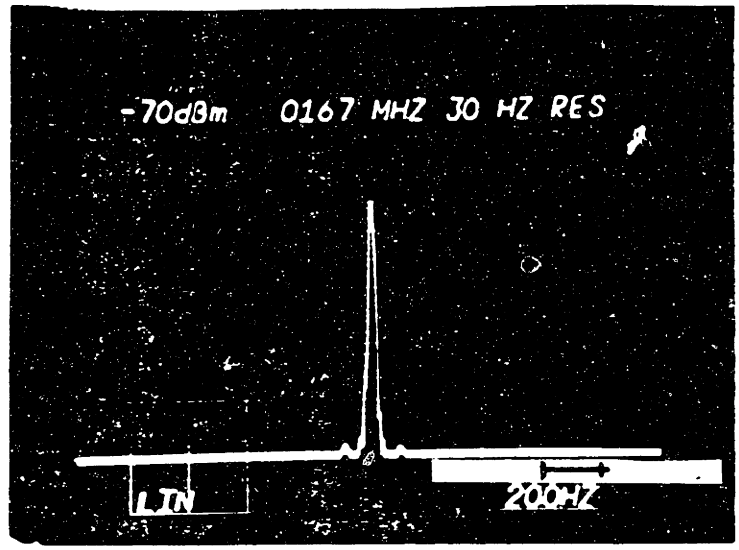

Figure 5.3.2. Output of the PD_H observed on a spectrum analyzer indicating an instrument limited measurement of the spectral width of the beat between the two Brillouin lasers E_b^+ and E_b^- for $\Delta q = 11$ operation

5.3.3 shows the spectrum of the down-mixed output of PD_H measured by an FFT spectrum analyzer, indicating a 41 Hz signal frequency with a spectral width of 2 Hz, due to slow drifts in the frequencies of E_b^+ and E_b^-.

The narrow spectral width of the beatnote between E_b^+ and E_b^- indicates that there is no mode competition behavior between the two Brillouin lasers. Thus, the SBS process is a suitable gain medium for a fiber RLG.

5.3.2. Measurement of Rotation by the BRLG

In the previous section we demonstrated stable SBS lasing along the clockwise and counterclockwise directions of our fiber cavity. In this section, we will demonstrate the operation of a Brillouin fiberoptic RLG by measuring the frequency difference between E_b^+ and E_b^- when a rotation rate is applied to the fiber ring resonator.

In this case, we allow both E_b^+ and E_b^- to use the same longitudinal mode of the fiber cavity (i.e. $\Delta q = 0$), by setting the frequency of E_p^+ equal to that of E_p^-. Figure 5.3.4a

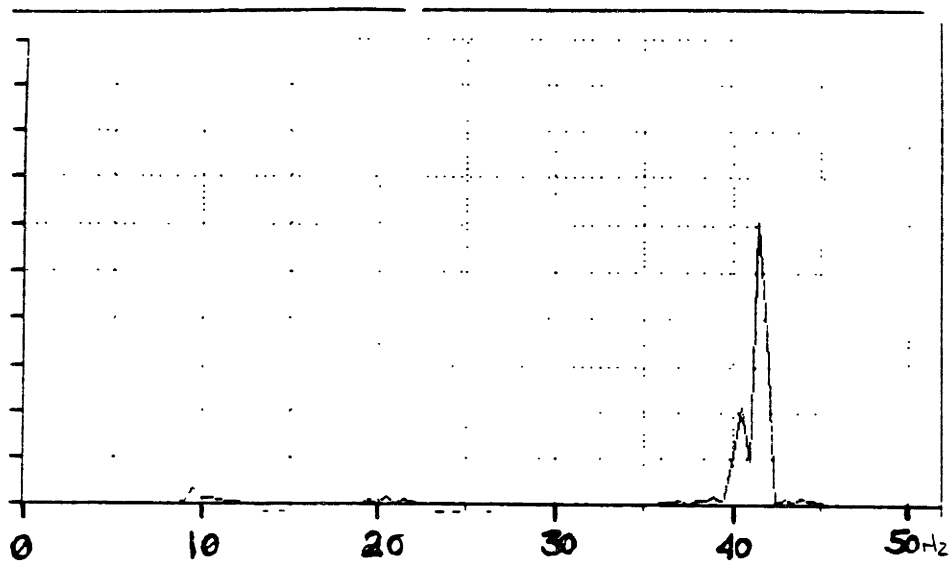

Figure 5.3.3. Observation of the beat between E_b^+ and E_b^- measured by a digital FFT spectrum analyzer

shows the output of PD_L as a function of time, when a rotation rate of approximately 4 deg/sec is applied to the fiber cavity, indicating a 3 kHz beatnote between E_b^+ and E_b^-. The frequency of this beatnote is consistent with the Sagnac scale factor of approximately 750 Hz per deg/sec, already measured when the fiber cavity was used as a passive resonator gyroscope in section 4.1.2.

Similarly, figure 5.3.4b shows the output of PD_L as a function of time when the rotation rate is reduced to 2.3 deg/sec, indicating a 1.7 kHz frequency difference between E_b^+ and E_b^-, which is also consistent with the Sagnac scale factor of approximately 750 Hz per deg/sec.

Thus, we have demonstrated the basic operation of the BRLG. In the next sections, we now examine some of the problems which interfere with the operation of this gyroscope.

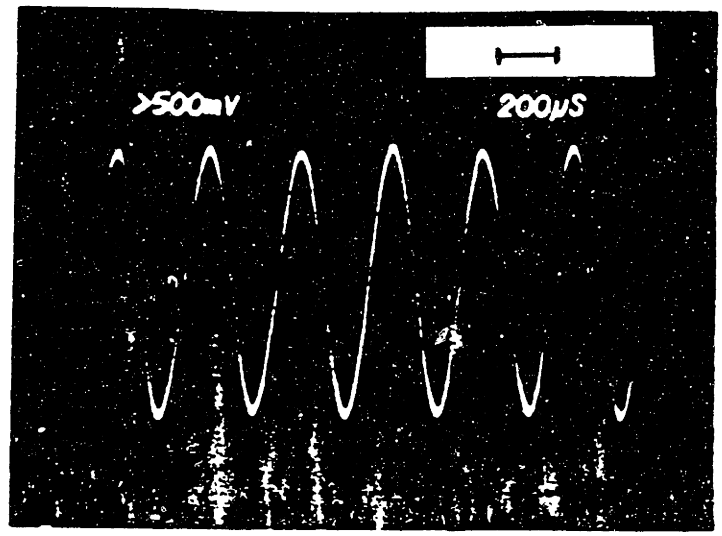

(a)

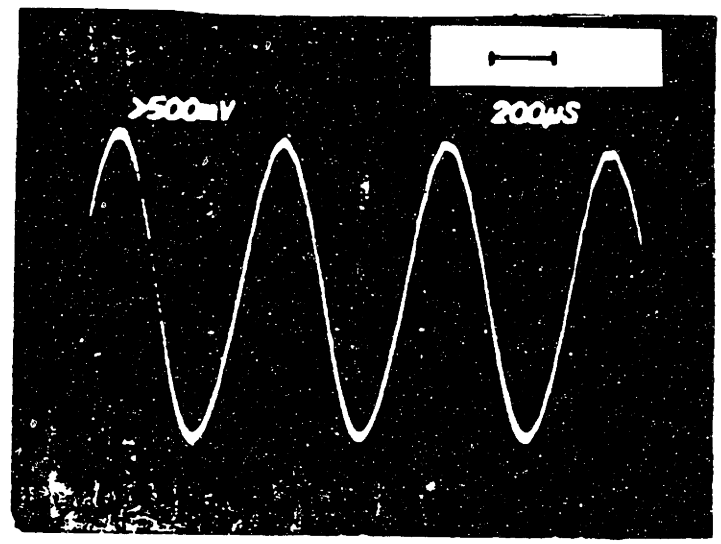

(b)

Figure 5.3.4. The beat between E_b^+ and E_b^- for $\Delta q = 0$ operation when (a) a rotation rate of 4 deg/sec is applied indicating a 3 kHz beat-frequency (b) a rotation rate of 2.3 deg/sec is applied indicating a 1.7 kHz beat-frequency

5.3.3. Lockin Behavior in the BRLG

In this section, the lockin behavior in a BRLG is demonstrated, which is similar to that observed for closed loop passive gyroscope in section 3.3. The Brillouin lockin behavior corresponds to a frequency locking of the two Brillouin lasers, E_b^+ and E_b^-, when the magnitude of the applied rotation is smaller than a threshold value, Ω_T. As described in section 3.3, the lockin threshold is determined by the backscattering coefficients of the ring resonator.

We observe the lockin behavior when we study the frequency of the beatnote between E_b^+ and E_b^-, labeled Δf_b, as a function of the angular velocity applied to the fiber cavity. As previously described in section 4.1.2, the cavity is mounted on a rotatable platform and rocked sinusoidally around the axis perpendicular to the plane of the fiber cavity. The rotation angle of this platform, θ_p, is shown in figure 5.3.5a. θ_p has a peak to peak amplitude of $\pm 5°$ and a period of 11.5 sec. The applied angular velocity is equal to $\partial\theta_p/\partial t$, which in our case also varies sinusoidally with time, but is 90° out of phase with respect to θ_p, and has a peak amplitude of 2.7 deg/sec.

We now measure Δf_b, the frequency of the beatnote between E^+ and E^-, by feeding the output of PD_L to a digital frequency counter. Figure 5.3.5b shows Δf_b as a function of time for the applied rotation, θ_p, shown in figure 5.3.5a. The variation of Δf_b as a function of time resembles a rectified sinewave, because the frequency counter cannot distinguish between frequencies due to positive and negative rotation rates. The peak value of Δf_b measured by the counter in figure 5.3.5b is approximately 2 kHz, and occurs when $\theta_p = 0$ (Ω =2.7 deg/sec), which is consistent with our Sagnac scale factor of 750 Hz per deg/sec. The lockin behavior is apparent in figure 5.3.5b, as for example in the region labeled A. The lockin region of figure 5.3.5b corresponds to a lockin threshold (Ω_T) of approximately 0.33 deg/sec.

Let us now examine the Brillouin beatnote, when the rotation rate is near the lockin threshold in figure 5.3.5b. Figure 5.3.6a shows the output of PD_L as a function of time

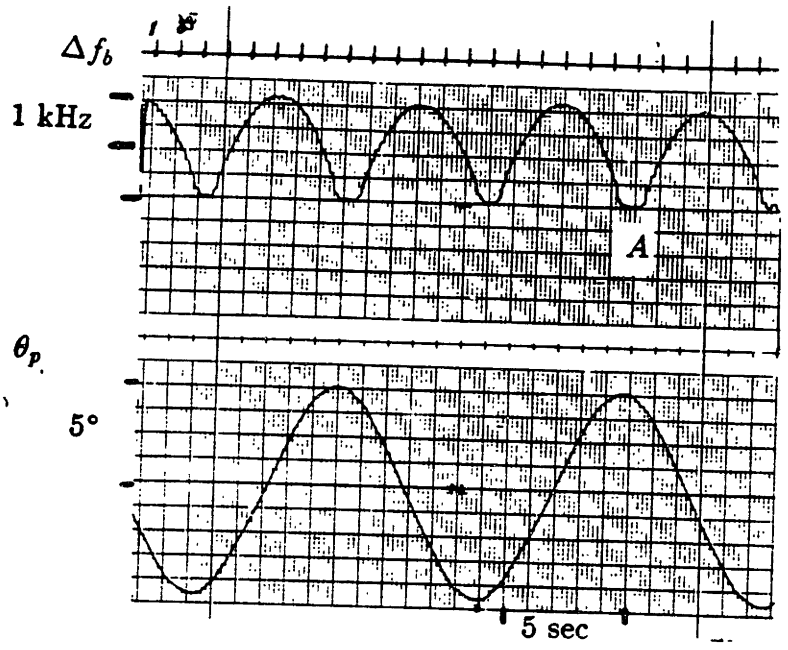

Figure 5.3.5. Variation in Δf_b as a function of time when a rotation rate is applied to the setup (a) the angle of the rotation platform, θ_p, as a function of time (b) the corresponding Δf_b indicating the lockin zone A

when the applied rotation rate is approximately 0.8 deg/sec. The beatnote between E_b^+ and E_b^- is not a pure sinewave, but is distorted due to the coupling of the two Brillouin lasers. This distortion is similar to that predicted for the passive resonator lockin shown in figure 3.3.2. The separation between the successive peaks of the beatnote in figure 5.3.6a is 1.8 ms, indicating an average frequency of approximately 550 Hz, which is consistent with the prediction of section 3.3, i.e. $\Delta f = (4A/n\lambda_o P)\sqrt{\Omega^2 - \Omega_T^2}$. Figure 5.3.6b shows the beatnote when the rotation is 0.53 deg/sec, further demonstrating the distortion in

the beatnote as Ω approaches the lockin threshold. The separation between the peaks of the beatnote is 3 ms, indicating an average frequency of 330 Hz, which is again consistent with the predictions section 3.3.

In order to observe the lockin zone better, we apply a 5 kHz bias to Δf_b by setting the drive frequency of AO^+ to be 5 kHz larger than that of AO^-. Since E_b^+ travels through AO^- and E_b^- travels through AO^-, a difference between the drive frequencies of AO^+ and AO^- appears as an additional shift between the frequencies of E_b^+ and E_b^- at detector PD_L. Figure 5.3.7b shows the Brillouin beat-frequency, Δf_b, measured by a frequency counter as a function time, with a 5 kHz bias, for an applied rotation θ_p, shown in figure 5.3.7a. In this case, we can clearly see the sinusoidal-like variation in Δf_b as a function of time, which is 90° out of phase with respect to θ_p, and has a peak to peak amplitude of ± 2 kHz. The lockin zone is very clearly demonstrated in figure 5.3.7b in region A. Also seen in figure 5.3.7b, the maxima of Δf_b in region B are 2.1 kHz above zero (lockin), where as the minima in region C are only 2 kHz below zero, thus indicating a gyroscope offset of approximately 50 Hz. A more accurate measurement of the offset requires the elimination of the lockin behavior.

We will now examine whether a drift in the offset of the primary loop results in a gyroscope offset. In this case, we apply a 5 kHz frequency bias to Δf_b via the AO modulators as described previously. Figure 5.3.8a shows Δf_b as a function of time for the applied sinusoidal rotation angle, θ_p, shown in figure 5.3.8b. As shown in the figure, Δf_b varies sinusoidally as a function of time with a peak to peak amplitude of ± 2 kHz. We can also see the lockin behavior in this figure as previously described. Figure 5.3.8c shows the output of PSD^-, i.e. V_d^-, as a function of time, which represents the bias of the primary loop. In the section labeled A, we applied a ± 2 kHz bias to the primary loop using the potentiometer R_b shown in figure 3.1.3, which shifts the frequencies of both E_p^- and E_p^+ with respect to a cavity resonance. As shown in figure 5.3.8a, the application of this bias does not affect Δf_b, and therefore the operation of a Brillouin RLG does not require a high precision feedback loop, and can be achieved using a simpler and less accurate loop.

The precise evaluation of the offset errors in our ring laser gyroscope involves the removal of the lockin zone by mechanical or optical dithering, and is left for future work.

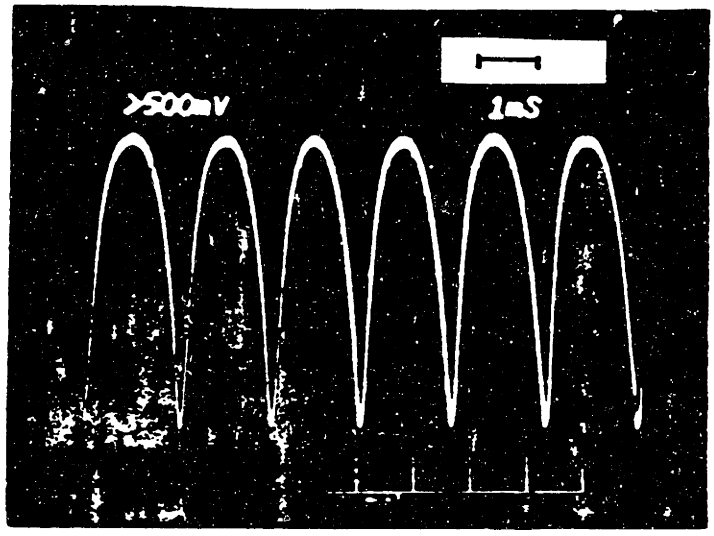

(a)

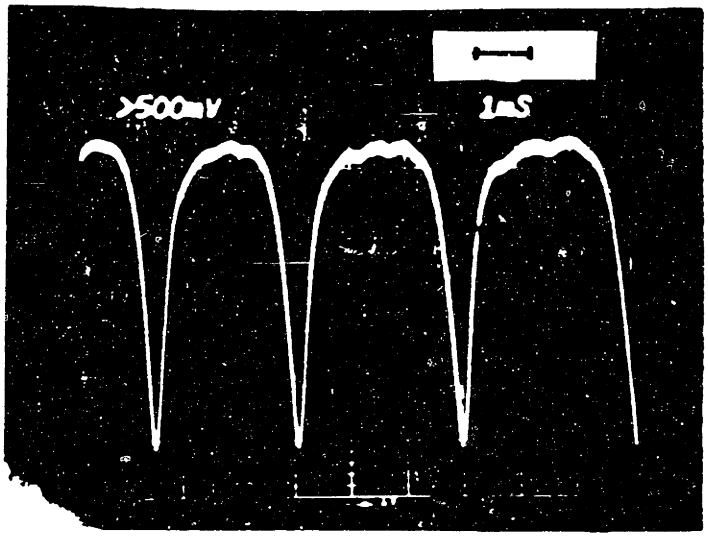

(b)

Figure 5.3.6. The beatnote between E_b^- and E_b^+ observed when (a) a rotation rate of 0.8 deg/sec indicating a distorted beatnote with an average frequency of 550 Hz (b) a rotation rate of 0.53 deg/sec is applied indicating a more severly distorted beat note as Γ approaches the lockin threshold

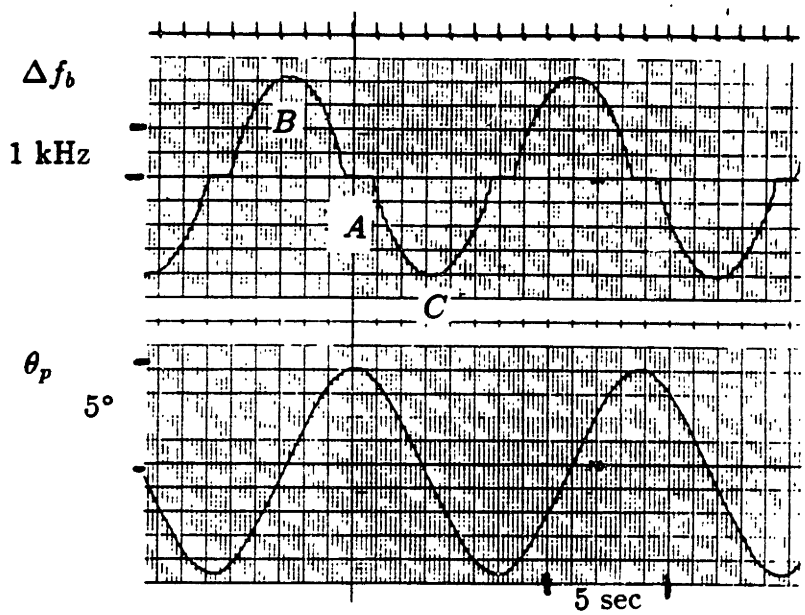

Figure 5.3.7. Observation of lockin in Brillouin RLG (a) Δf_b as a function of time with a 5 kHz bias indicating the lockin zone A(b) θ_p as a function of time

5.3.4. Multi-Mode Lasing in the BRLG

Although both Brillouin lasers in our setup are single-frequency most of the time, occasionally we observe simultaneous lasing in two adjacent longitudinal modes of the cavity[34,35], which disrupts the operation of the gyroscope.

In order to demonstrate this occasional multi-mode behavior we use the setup in figure 5.3.9, which represents a modified version of the original BRLG setup. Initially we have two counterpropagating Brillouin lasers at the same longitudinal mode of the cavity,

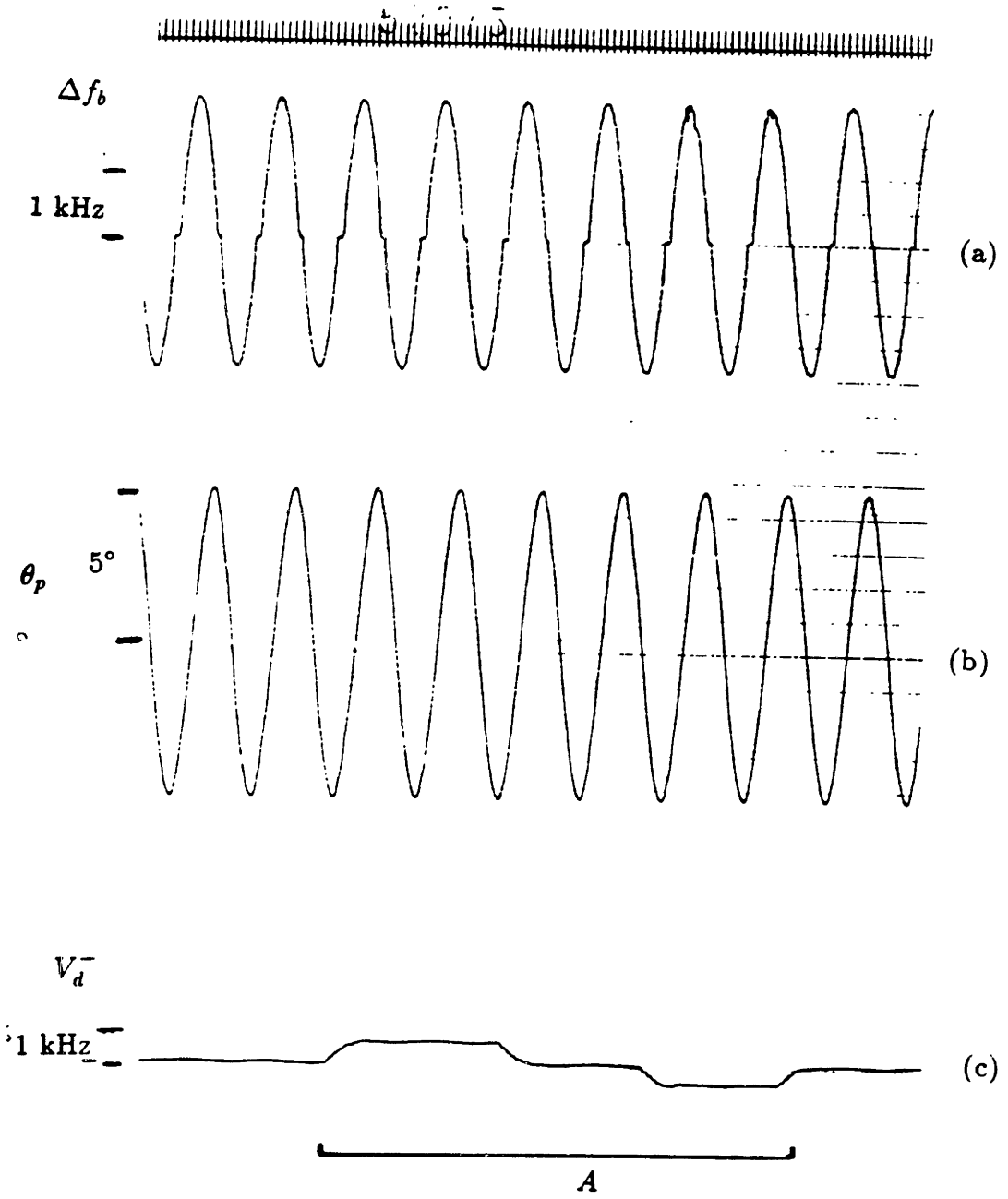

Figure 5.3.8. Independence of Δf_b from variations in the offset of the primary loop (a) Δf_b as a function of time (b) θ_p as a function of time (c) V_d^- as a function of time indicating the offset of the primary loop, where in region A we perturbed this offset by approximately ± 1 kHz.

E_b^+ and E_b^-. The beatnote between these two beams indicates the rotation rate, and is monitored by the low frequency detector, PD_L. The output of PD_L is fed into a frequency counter, which measures Δf_b. This output is also given to an AC voltmeter, $ACVM_1$, which measures the amplitude of this beatnote. In the presence of an additional Brillouin oscillation in an adjacent cavity, mode we will observe a beatnote due to the interference between this field and the original laser fields E_b^+ and E_b^-. This beatnote is approximately 7.70 MHz, which corresponds to 1 FSR of the fiber cavity, and is monitored by the high frequency detector, PD_H. To detect this high frequency beatnote, we mix the output of PD_H with a reference oscillator at 7.69 MHz to produce a signal at 10 kHz, and then feed this signal into a second AC voltmeter $ACVM_2$.

We now apply a sinusoidal rotation θ_p with a peak to peak angle of $\pm 5°$ and a period of 11.5 sec to the setup as described in section 5.3.2, and shown in figure 5.3.10b. Figure 5.3.10a shows Δf_b as a function of time, measured by the frequency counter indicating a sinusoidal variation as described previously in section 5.3.2. Figure 5.3.10d shows the output of $ACVM_1$, indicating the amplitude of the beat between E_b^- and E_b^+ as a function of time. Figure 5.3.10c shows the output of $ACVM_2$, which indicates the occasional presence of a third laser oscillation 7.7 MHz away from E_b^+ and E_b^- at points such as the ones marked A and B in the figure. This multi-mode behavior clearly interferes with the operation of the gyroscope as indicated in the figure 5.3.10a. This multi-mode behavior in the Brillouin laser may be attributed to spontaneous mode lockin already observed by others[35].

This behavior can be avoided by using a cavity with a larger free spectral range, so that the adjacent cavity modes will not be able to lase. For example, a cavity with a total length of 4m has a FSR of 30 MHz. Thus, in our case, the adjacent modes of the cavity will be separated by the width of the Brillouin gain medium and will not have sufficient gain to lase.

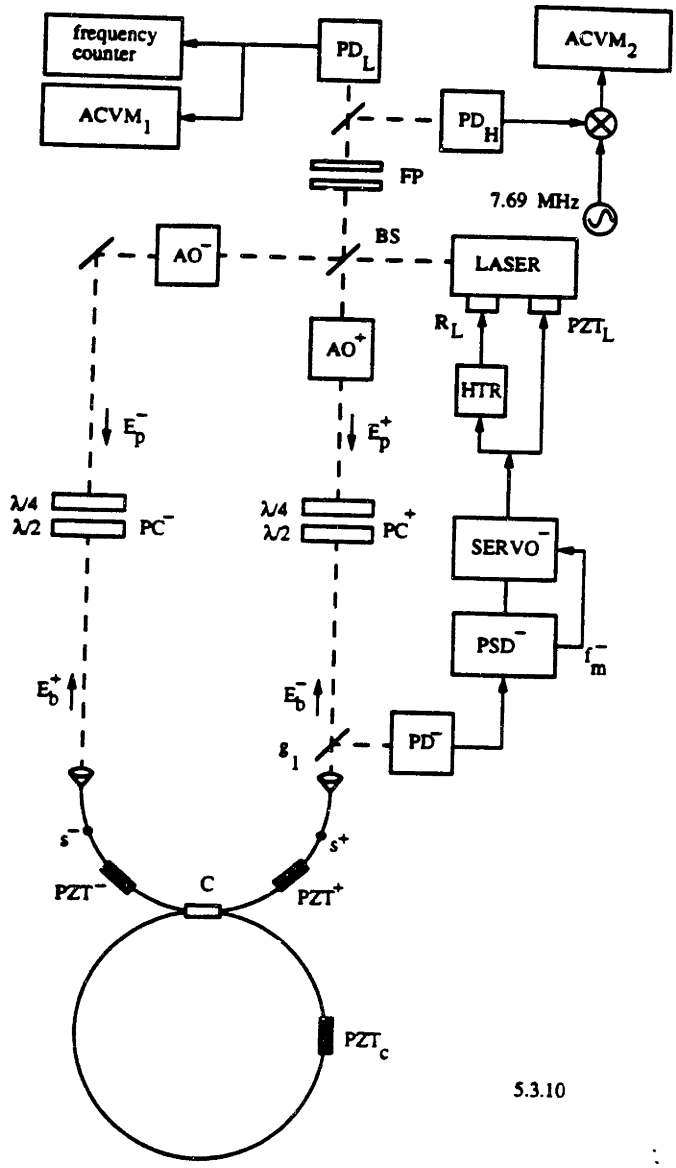

Figure 5.3.9. The schematic setup used in observing the multi-mode Brillouin lasing in BRLG

5.4. Evaluation of a Method for Eliminating the Lockin Behavior in the BRLG

As demonstrated in section 5.3.3, the BRLG exhibits lockin behavior similar to that observed in bulkoptic RLG. Although, the lockin behavior in an RLG can be eliminated

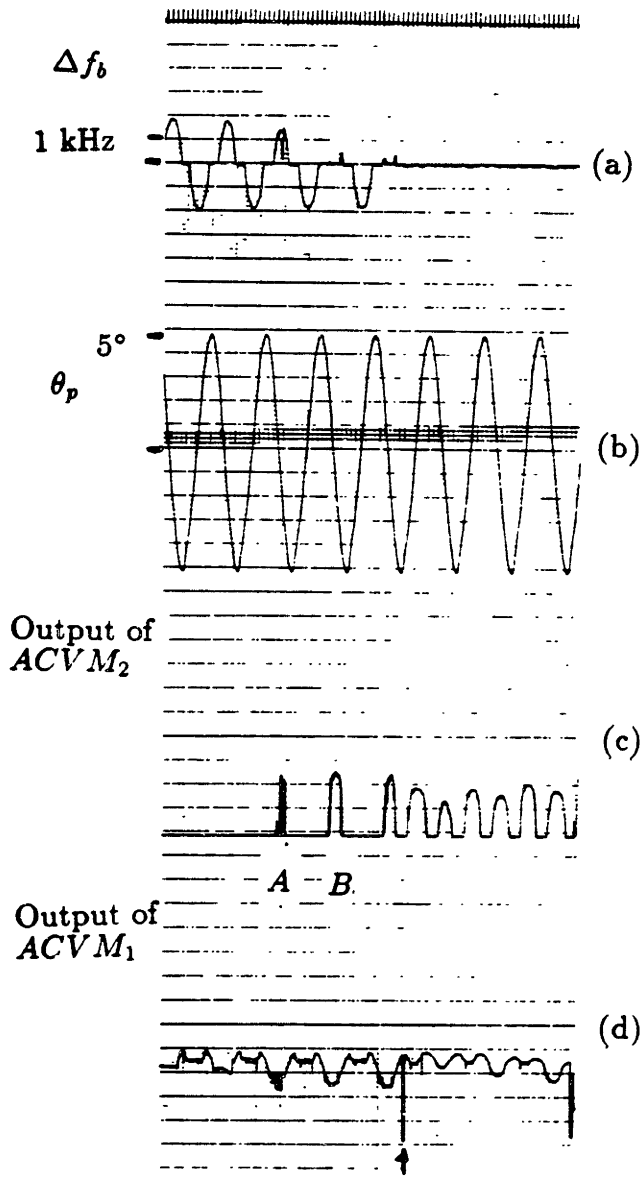

Figure 5.3.10. Observation of multi-mode lasing (a) Δf_b as a function of time (b) θ_p as a function of time (c) output of $ACVM_2$ as a function of time indicating a 7.7 MHz beatnote between E_b^+ and E_b^- (b) output of $ACVM_1$ as a function of time indicating the amplitude of the beatnote between E_b^+ and E_b^-.

by a dithering technique, which is commonly used in bulkoptic RLG, an alternative way of eliminating the lockin behavior is to force the clockwise ring laser to use a different cavity longitudinal mode than that used by the counterclockwise ring laser, i.e. to have $\Delta q \neq 0$. We do this by separating the frequencies of the clockwise and counterclockwise pump beams by an integer multiple of the cavity FSR, as, for example, demonstrated in section 5.3.1. In this section we will demonstrate the removal of lockin behavior in $\Delta q \neq 0$ operation, and evaluate the sources of frequency drift in this configuration.

5.4.1. Elimination of Lockin Behavior in the BRLG

In this section we will demonstrate the elimination of lockin behavior by forcing the clockwise Brillouin laser to use a cavity mode 11 free spectral ranges away from that used by the clockwise laser, i.e. $\Delta q = 11$, by setting a 84.7 MHz frequency difference between the two pump beams E_p^+ and E_p^- via the two AO modulators AO^+ and AO^-. The beatnote between the Brillouin laser outputs, E_b^+ and E_b^-, is monitored by PD_H, and the frequency of this beatnote, labeled Δf_b, is measured by a digital frequency counter.

Figure 5.4.1a shows the output of the digital frequency counter, indicating the variation of Δf_b as a function of time, recorded simultaneously with the rotation angle of the platform, θ_p, shown in figure 5.4.1b. The figure shows the elimination of the lockin behavior observed previously in figure 5.3.7 for $\Delta q = 0$. The figure also shows the expected 90° phase shift between the variations of Δf_b and θ_p.

Figures 5.4.2 shows Δf_b for a period of 3 minutes when the platform is at rest. The time scale of the figure is 2 sec/mm. As shown in the figure, Δf_b drifts by approximately 300 Hz during this run. Although we have demonstrated the elimination of the lockin behavior, we have also observed drifts in Δf_b as shown in figure 5.4.2, which would potentially make this configuration useless as a precision sensor. In the next two sections we will discuss some of the sources for the drift in Δf_b for this configuration.

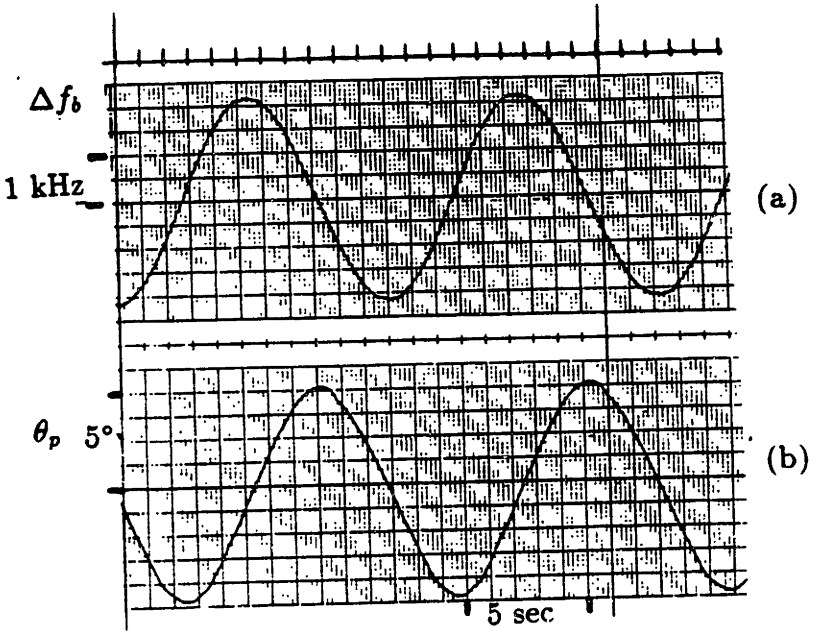

Figure 5.4.1. $\Delta q = 11$ operation of the BRLG, demonstration of the elimination of lockin behavior (a) Δf_b as a function of time (b) platform rotation angle as a function of time

5.4.2. Frequency Errors due to External Double Backscattering

The double backscattering errors in a Brillouin RLG are similar to those observed for the fiber PRG in section 4.2.4. As in the case of the PRG, these errors are due to backscattering from an external splice s^+ or s^-, and another scatterer. Thus, in order to observe these errors in a Brillouin RLG, we use PZT^+ and PZT^- to stress fiber segments between the splices, s^+ and s^-, and the coupler C.

In order to observe the frequency error due to double backscattering associated with

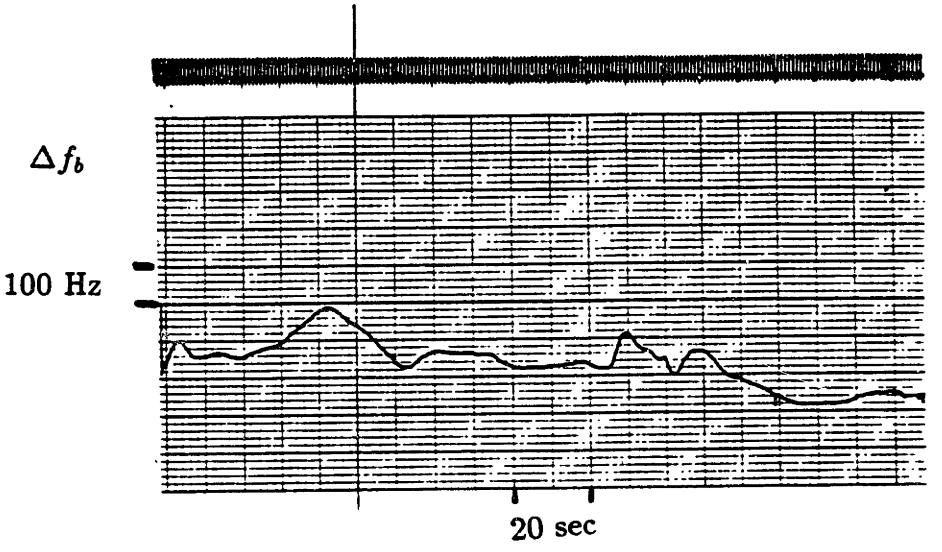

Figure 5.4.2. Δf_b as a function of time indicating a 300 Hz drift

s^-, we apply 200 V p-p 0.2 Hz voltage applied to PZT^- as shown in figure 4.5.3c, and observe the corresponding variation in Δf_b. Figure 5.4.3a shows a 150 Hz variation in Δf_b as a function of the voltage applied to PZT^-. this error varies sinusoidally with the applied PZT voltage, similar to the double backscattering error in a fiber PRG. We adjust the amplitude of the saw-tooth voltage on PZT^- so the variation of Δf_b corresponds to a complete sinusoidal cycle. We then increase the frequency of the saw-tooth voltage to 100 Hz, thereby averaging this error.

Similarly, we can observe the error due to double backscattering between PZT^+ and

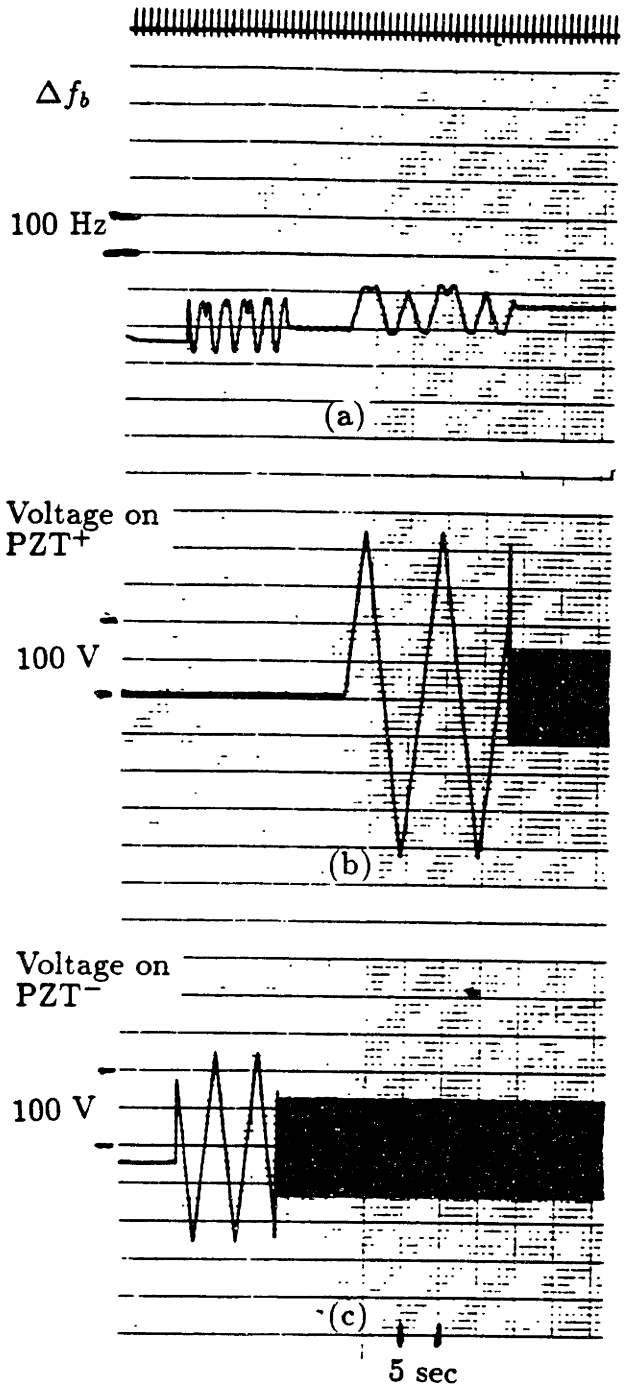

Figure 5.4.3. Demonstration of the variations in the SBS beat-frequency in $\Delta q = 12$ operation due to external optical feedback (a) the SBS beat-frequency as a function of time (b) Voltage applied to PZT^+ as a function of time (c) voltage applied to PZT^- as a function of time.

the other scatterers by applying a 400 V p-p 0.1 Hz saw-tooth voltage to PZT^+ as shown in figure 5.4.3b. We now observe a 120 Hz p-p variation in Δf_b which is also removed by increasing the frequency of the saw-tooth voltage to 50 Hz and thus averaging this error. Figure 5.4.4. shows the drift in Δf_b as a function of time when these double backscattering errors have been eliminated, indicating a 400 Hz drift over 7 minutes. In the next section we will consider another source of drift which is responsible for this variation.

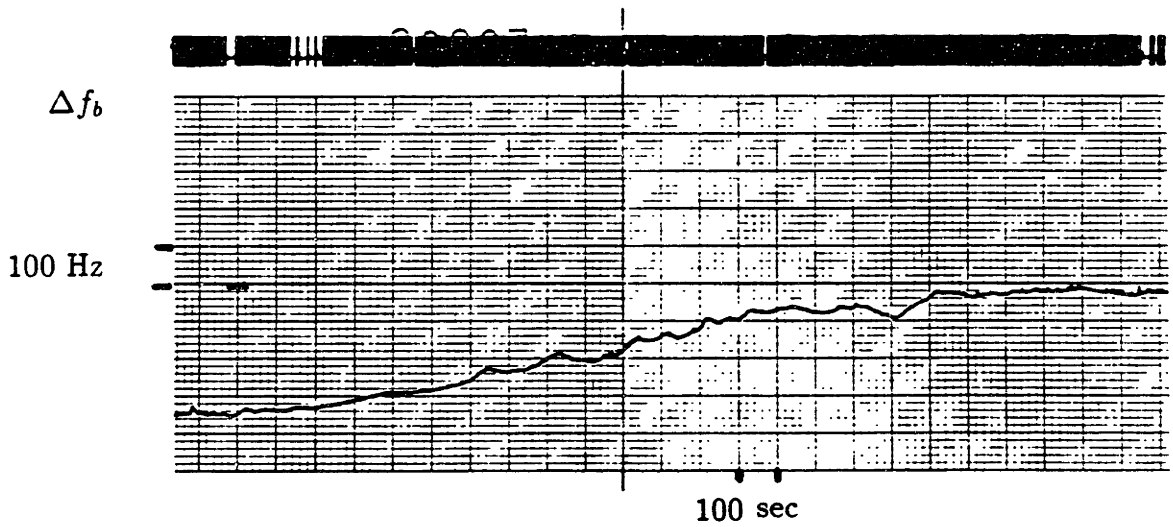

Figure 5.4.4. Drift of Δf_b as a function of time when the external double backscattering errors have been removed

5.4.3. Errors due to Brillouin Dispersion Pulls

In our setup, even though the external scattering effects have been washed out as described in section 5.4.2, Δf_b varies as we select different longitudinal modes of the cavity. To

illustrate this variation, Δf_b is observed for $\Delta q = 11$ operation, while the frequency of E_p^- is locked to the center of several successive longitudinal modes of the cavity. Figure 5.4.5 shows Δf_b as a function of selecting different longitudinal modes of the cavity, indicating a 400 Hz variation in Δf_b. In a similar way, figure 5.4.6 shows Δf_b for $\Delta q = 2$ operation, as a function of selecting different longitudinal modes of the cavity, indicating a 2 kHz fluctuation in Δf_b.

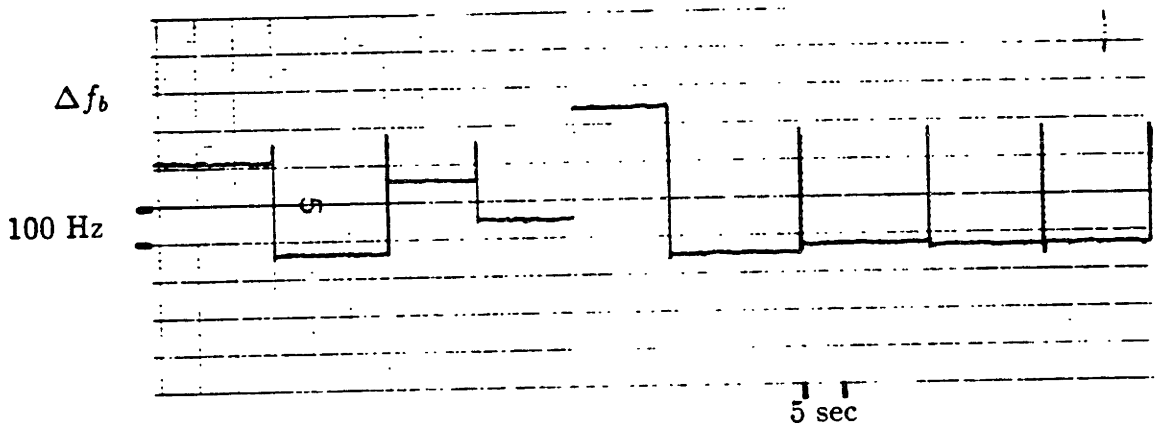

Figure 5.4.5. Demonstration of a 400 Hz variation of Δf_b for $\Delta q = 11$ operation, as the frequency of E_p^- is locked to successive longitudinal modes of the cavity.

These fluctuations are consistent with the errors due to phase dispersion of the Brillouin gain medium. In order to illustrate the Brillouin dispersion pull, let us consider figure 5.4.7a, which shows the frequency domain representation of the counterclockwise

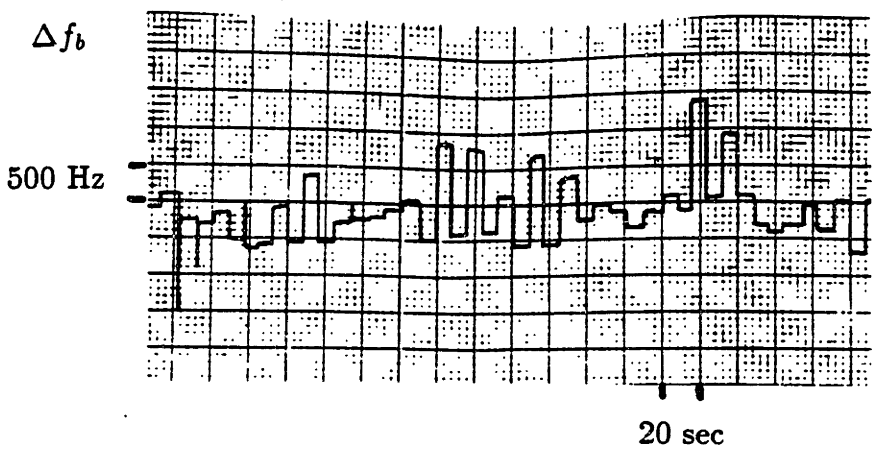

Figure 5.4.6. Demonstration of a 2 kHz variations of Δf_b for $\Delta q = 2$ operation, as the frequency of E_p^- is locked to successive longitudinal modes of the cavity.

pump beam E_p^+ which generates the clockwise Brillouin gain B^-, together with the clockwise pump beam E_p^- which generates the counterclockwise Brillouin gain medium B^+. The figure, also indicates the clockwise Brillouin laser E_b^-, and the counterclockwise Brillouin laser E_b^+. Ideally B^+ and B^- do not affect each other. However, in the presence of backscattering a fraction α_i^- of the intensity of E_p^+ will spill along the direction of E_p^-, as shown in figure 5.4.7b. This backscattered beam will generate another Brillouin gain medium B_r^+, which perturbs the frequency of E_b^+. Similarly a fraction α_i^+ of intensity of E_p^- scatters along E_p^+, as shown in figure 5.4.7c, which will ultimately pulls the frequency of E_b^-.

Let us now calculate the perturbation in the frequency of E_b^- due to the Brillouin gain medium B_r^-, which is caused by the backscattering of E_p^-. The backscattered intensity

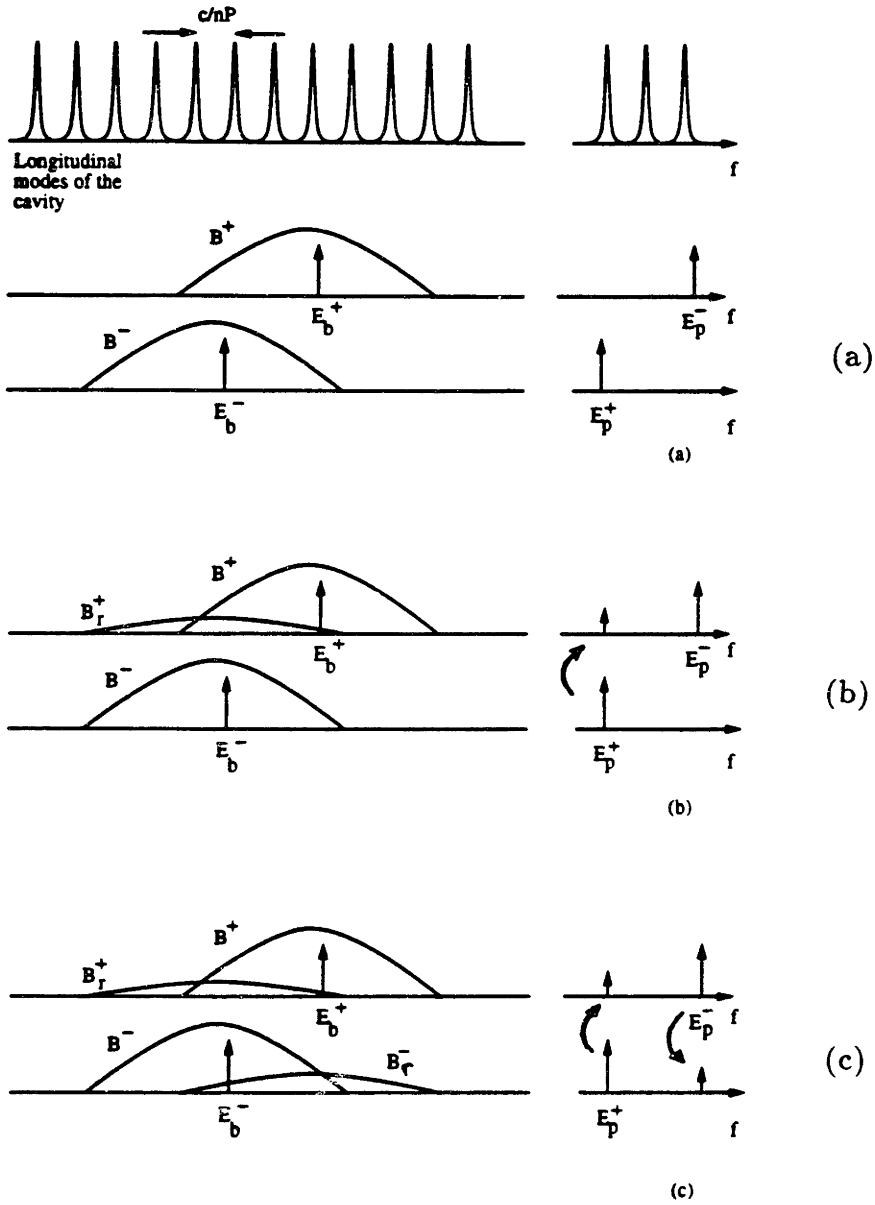

Figure 5.4.7. Illustration of the effect due to SBS dispersion pull (a) optical frequency spectrum of the pump and Brillouin beams along clockwise and counterclockwise directions (b) The additional counterclockwise Brillouin gain medium B_r^+ due to the intensity of the scattered counterclockwise pump beam E_p^+. (c) The two additional Brillouin gain media B_r^+ and B_r^- due to the backscattering of the pump beams E_p^+ and E_p^-.

responsible for B_r^- is equal to $\alpha_i^+ I_{rp}^-$, where I_{rp}^- is the intracavity intensity along the clockwise direction.

We can calculate the perturbation in the index of refraction from the expressions for $\chi^{(3)}$ given in section 5.1.2. By using equations 5.1.19, 5.1.22, and 5.1.23 we arrive at:

$$\Delta n^- = \alpha_i^+ \frac{\lambda_o n \Delta\nu \gamma_b I_{rp}^-}{4\pi} \frac{\Delta f}{\Delta f^2 + (\Delta\nu/2)^2} \tag{5.4.1}$$

As described in section 5.2.2, when the Brillouin laser is active, we have

$$\gamma_b I_{rp} P \approx \frac{2\pi}{F} \tag{5.4.2}$$

where P is the perimeter of the resonator and F is the finesse of the resonator. Therefore the expression for Δn^- can be further reduced to:

$$\Delta n = \alpha_i^+ \frac{\lambda_o n \Delta\nu}{2FP} \frac{\Delta f}{\Delta f^2 + (\Delta\nu/2)^2} \tag{5.4.3}$$

The frequency of E_b^- is perturbed by an amount Δf_d given by:

$$\begin{aligned} \Delta f_d &\approx -f_o \frac{\Delta n}{n} \\ &\approx -\alpha_i^+ \frac{c\Delta\nu}{2FP} \frac{\Delta f}{\Delta f^2 + (\Delta\nu/2)^2} \end{aligned} \tag{5.4.4}$$

In our case for $\Delta f = 84.7$ MHz, corresponding to $\Delta q = 11$ operation, we obtain $\Delta f_d = \alpha_i^+ \times 7.0$ kHz.

In section 4.2.3, it was mentioned that the intensity backscattering coefficient in our ring resonator fluctuated from zero to maximum of approximately 5%. Based on these numbers, the largest fluctuation on Δf_b results when the backscattering coefficient, for both E_p^+ and E_p^- are 5%. This means that for $\Delta q = 11$ we predict a maximum shift of 350 Hz for the frequency of E_b^- and similarly a maximum shift of 350 Hz for the frequency of E_b^+. This results results in a total of 700 Hz change in Δf_b, which is a factor of 2 larger than the variations we observed in figure 5.4.5. Thus, this effect explains the mode to mode variation in the gyroscope offset.

As we have demonstrated, $\Delta q \neq 0$ operation exhibits large drifts in Δf_b, and thus cannot be used as a precision rotation sensor. In order to implement a precision sensor, we must use $\Delta q = 0$ and remove the lockin zone by a dithering technique.

5.5. The Optical Kerr Effect in BRLG

In section 4.4, we derived and demonstrated the optical Kerr effect in a PRG. As described in section 4.4.1, the optical Kerr effect creates a separation between the clockwise and counterclockwise resonance frequencies of the cavity when the intensities of E^+ and E^- are not equal. In this section we will demonstrate the Kerr effect in a BRLG.

5.5.1. Derivation of the Optical Kerr Effect in BRLG

Unlike the PRG, in which we had only two intracavity beams, in a BRLG, we have four beams inside the ring cavity, two pump beams E_p^+ and E_p^-, and two Brillouin beams E_b^+ and E_b^-. Thus, we would like to determine the changes in the index of refraction of the cavity experienced by the Brillouin beams due to the intensity of all four beams.

We now calculate the perturbation in the index experienced by E_b^+, and E_b^-, i.e. Δn^+ and Δn^- respectively. Following a derivation similar to that presented in section 4.4.2, we obtain expressions for Δn^+ and Δn^- given by:

$$\begin{aligned} \Delta n^+ &= \beta_\circ(I_b^+ + 2(I_p^+ + I_p^- + I_b^-)) \\ \Delta n^- &= \beta_\circ(I_b^- + 2(I_p^+ + I_p^- + I_b^+)) \end{aligned} \tag{5.5.1}$$

We can see that the contributions to the index change due to the pump beams are identical for clockwise and counterclockwise directions. Thus the pump intensities will not affect the frequency separation, Δf_c, given by:

$$\begin{aligned} \Delta f_c &= \Delta f_b^+ - \Delta f_b^- \\ &= \gamma_k(W_b^+ - W_b^-) \end{aligned} \tag{5.5.2}$$

Δf_b^- and Δf_b^+ are the frequency shifts in E_b^- and E_b^+ respectively, due to optical Kerr effect, W_b^- and W_b^+ are the power levels associated with E_b^- and E_b^+ respectively, and γ_k is the optical Kerr scale factor evaluated in section 4.4.2 to be approximately 7 Hz/μW.

Thus, the Kerr effect is independent of the intensity of the pump beams and only depends on the difference between the intensities of the two Brillouin lasers.

5.5.2. Measurement of the Optical Kerr Effect in BRLG

Figure 5.5.1 shows the setup used in demonstrating the optical Kerr effect in a BRLG. In this demonstration, we chose $\Delta q = 11$ in order to avoid the lockin behavior, and placed a neutral density filter NDF at points A_1, A_2, A_3 in the setup. Placing the NDF at A_1 attenuates E_p^- thus reducing the intensity associated with E_b^+. Placing the NDF at A_2 attenuates E_p^+ thus reducing the intensity associated with E_b^-. Finally by placing the NDF at point A_3 we can simultaneously attenuate both E_p^+ and E_p^- thus reducing the intensities of both E_b^+ and E_b^-.

Because the pump and Brillouin beams are in general mixed together, we calibrated the drop in the intensity of E_b^+ while E_p^+ was blocked. We placed the NDF at point A_1 and measured a 5 μW drop in the power of E_b^+. Similarly, while blocking E_p^-, we inserted the NDF at the point A_2 and measured a 5 μW drop in the power of E_b^-. Finally we inserted the NDF at the point A_3 and measured a drop of 5μW in both E_b^- and E_b^+.

Figure 5.5.2b shows Δf_b as a function of time, measured by the frequency counter, recorded simultaneously with the amplitude of the Brillouin beatnote beatnote shown in figure 5.5.2a. In section A of figure 5.5.2b, the NDF is inserted at point A_1 attenuating E_p^-, thereby reducing W_b^+ by 5 μW. As shown figure 5.5.2b, this drop results in a 35 Hz increase in the frequency of the beatnote. Similarly we inserted the NDF at the point A_2, reducing W_b^- by 5 μW. We now observed a 35 Hz decrease in Δf_b. Finally, we inserted the NDF at the point A_3 and observed that although both Brillouin beams are attenuated, we see no change in the beat-frequency. The 7 Hz/μW Kerr scale factor is consistent with that observed for the passive case in section 3.4.1.

Thus the Kerr effect is a significant error source in a BRLG, and must be eliminated by making sure the intensities of the two Brillouin beams are equal. We can use a feedback loop to set these two intensities equal to each other. Further work on this topic is left for future investigation.

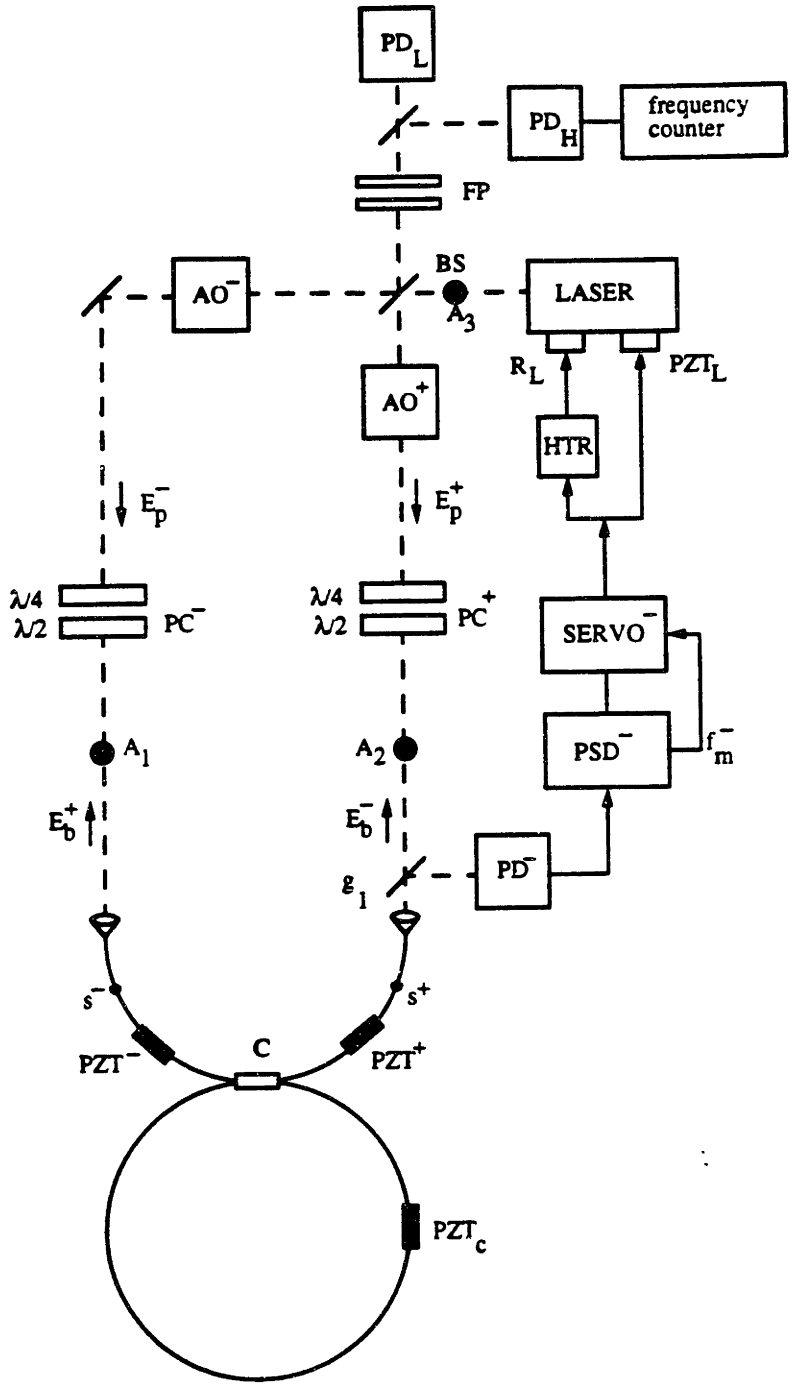

Figure 5.5.1. Schematic diagram for evaluating the optical Kerr effect in BRLG

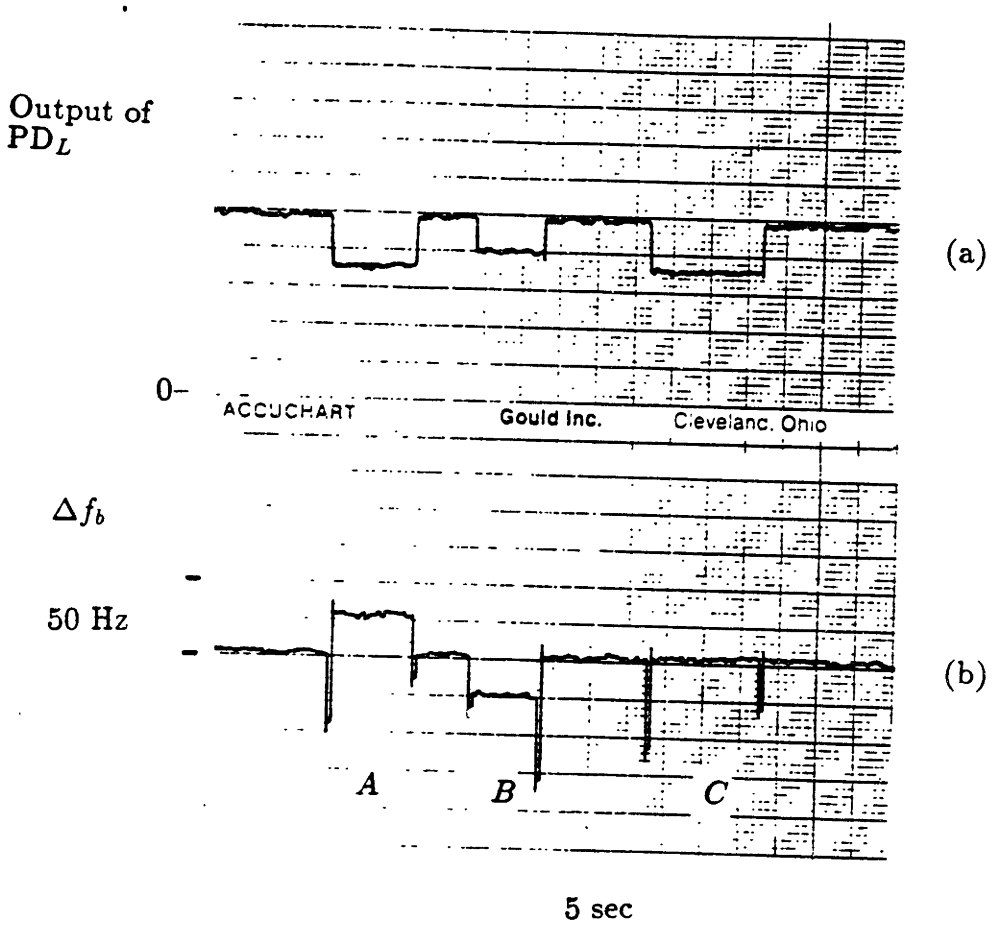

Figure 5.5.2. Demonstration of the optical Kerr effect in BRLG (a) the amplitude of the beatnote observed by PD_H (b) Δf_b when the neutral density filter (NDF) is inserted the point A_1 (section A) corresponding to an attenuation of the counter clockwise Brillouin beam power W_b^+, at point A_2 (section B) corresponding to an attenuation of the clockwise Brillouin beam power W_b^-, and at point A_3 (section C) corresponding to an attenuation of both W_p^+ and W_p^-.

CHAPTER 6

Summary and Suggestions for Future Work

The objective of this thesis was to study the behavior and error sources of ring resonator gyroscopes. We studied a bulkoptic passive ring resonator gyroscope (PRG), a fiberoptic PRG and a fiberoptic ring laser gyroscope using stimulated Brillouin scattering as the gain medium.

First, we studied the bulkoptic resonator and demonstrated that the dominant error source was due to coherent backscattering. We also observed an abrupt offset change of 20 deg/hr, when the frequencies of the two input beams were swept past each other. The size of this jump did not depend on either the size of the coherent backscattering, or the input beam intensities. Both the backscattering effects and the offset jump were eliminated by phase modulating one of the beams with the carrier suppressed. We also demonstrated the lockin behavior for closed loop operation of this gyroscope, related this effect to the coherent backscattering, and eliminated it by the same carrier suppressed phase modulation mentioned above.

We evaluated the rms noise of the bulkoptic gyroscope as a function of integration time, τ. For $\tau = 10$ ms, the rms noise was approximately 0.17 deg/hr, which was very close to the shot noise limit, (for 2μW on the detectors) but for longer values of τ, the noise became larger than the shot noise. For example, for $\tau = 1$ sec the rms noise was 0.35 deg/hr which was twice the predicted shot noise limit, and for $\tau = 100$ sec, the rms noise was 0.01 deg/hr, i.e., 7 times larger than the shot noise limit.

In order to explain the increase in the rms gyro noise relative to shot noise for long averaging times, we evaluated three possible sources of drift. The first source was the influence of a change in the plane of polarization of the input beams. This resulted in a bias variation of 0.01 deg/hr for every degree of variation in the plane of polarization of the input beam. In our setup, the plane of polarization of the input beams could be maintained to within 0.1°, which corresponded to a total output drift of less than

0.001 deg/hr. Therefore, the variation in the input polarization does not explain the observed drifts. The second source was the effect of the drift in the spatial alignment of the input beams, which resulted in less than 0.05 deg/hr for every 2 arc minutes of spatial misalignment. In our setup, the beam alignments were maintained to within 2 arc seconds, which corresponded to an offset error of less than 0.001 deg/hr. Again, this could not explain the observed drifts. The third source was the effect of the rate of change in the relative phase between the two input beams, which generates an input frequency difference. We measured this phase variation to be less than $\pi/2$ radians during 300 sec, and this corresponded to a gyroscope output drift of less than 0.0008 deg/hr in our case. Thus, the input phase variation in our setup does not explain the observed drifts. Other sources of drift that should be investigated include: the fluctuation in the discriminant slope due to backscattering; the incomplete suppression of the 20 deg/hr offset jump; and the errors due to Fresnel drag in the gas filled optical resonator.

In our fiberoptic ring resonator gyroscope, although we had the advantage of a single transverse mode resonator, we also had a severely asymmetric resonance and a 6 kHz p-p coherent backscattering error, 30 times larger than that observed for the bulkoptic case. To eliminate the backscattering, we again used a carrier-suppressed phase modulation technique similar to the bulkoptic case. However, due to the observed distortions in the coherent backscattering, we had to use multiple carrier-suppressed phase modulations to totally eliminate the coherent backscattering errors. In addition to coherent backscattering, we also experienced intensity backscattering errors as large as 200 Hz, which we eliminated by using different modulation frequencies to generate the clockwise and the counterclockwise discriminants. [These intensity backscattering errors were insignificant in the bulkoptic case]. Finally, we observed an external double backscattering error due to the interference between the backreflection from the splices on the resonator arms and the backscattering from the intracavity scatterers, which was as large as 180 Hz p-p. We eliminated this error by carrier-suppressed phase modulation of the input arms, and observed a gyro bias variation from 0 to 10 Hz. In addition to this, by selecting different

longitudinal modes of the fiber cavity, we observed a variation of approximately ±20 Hz (corresponding to ±100 deg/hr). In order to investigate the backscattering-dependence of this variation, we devised a special technique to determine the gyro offset in the absence of coherent and intensity backscattering. Using this technique, we measured a gyro offset of less than ±2.5 Hz (±12.5 deg/hr), demonstrating that the previously observed ±20 Hz variation is due to backscattering effects. One explanation of this variation is the influence of internal backscattering in the case where separate modulation frequencies are used in the presence of an asymmetric cavity resonance, and this should be studied further.

In addition to studying the backscattering-induced drifts, we also examined several other sources of gyro drift in the fiber PRG. First, we examined the dependence of the gyro offset on the state of polarization of the input beams. We observed approximately 5 Hz of offset change (25 deg/hr) for every degree of rotation of a $\lambda/4$ plate in one of the input beams. We attributed this primarily to a variation in the asymmetry of our resonance due to a change in the state of polarization of the input. We also observed 7 Hz (35 deg/hr) of offset variation for every micro-Watt of power difference between the clockwise and the counterclockwise beams, which was attributed to the optical Kerr effect.

To reduce the polarization-induced drift, we can use a single polarization fiber cavity, and to reduce the asymmetry of the resonance lineshape, we can use a fiber cavity in "transmission". Finally, to eliminate the drifts due to the optical Kerr effect, a feedback loop is required to keep the intensities of the two beams equal at all times.

In chapter 5, we demonstrated the first implementation of a fiberoptic ring laser gyroscope using stimulated Brillouin scattering as the gain medium. With this device, we demonstrated the measurement of rotation by applying a rotation rate of 4 deg/sec, and observing a pure beatnote of 3 kHz corresponding to a scale factor of 750 Hz per degree/sec. We also observed the lockin behavior which is due to coherent backscattering, as in the case of the passive resonator gyroscope, which can be eliminated using either a mechanical or an optical dither.

We also demonstrated another method of eliminating the lockin effect in the Brillouin ring laser gyroscope by forcing the two Brillouin lasers to use different longitudinal modes of the cavity. However, by doing so, we introduced large drifts of approximately 400 Hz (for $\Delta q = 11$) caused by the dispersion of the Brillouin gain medium associated with backscattering. Thus, this method of eliminating the lockin behavior is not too suitable for a precision gyroscope.

Finally, we measured the optical Kerr effect in the Brillouin ring laser gyro which was 7 Hz (35 deg/hr) of output variation for every micro-Watt of power difference between the clockwise and the counterclockwise Brillouin lasers, consistent with our measurements in the passive case. Therefore, as in the passive case, a feedback loop is required to maintain equal intensities between the two Brillouin lasers. Although, the precise measurement of gyroscope offset and drift requires the complete elimination of the lockin behavior, nevertheless we were able to estimate this bias to be less than ± 25 Hz for $\Delta q = 0$. Therefore, the Brillouin fiber ring laser gyroscope is worth further investigation.

APPENDIX A. Calculation of Resonance Asymmetry

In order to describe our asymmetric resonance lineshape, let us consider the case of a simple Fabry-Perot resonator, which is made of 2 identical mirrors M_1 and M_2 separated by a distance d, as shown in figure A.1. Light outside of the resonator is reflected from M_1 with a coefficient r, and transmitted through it with a coefficient t. Similarly, light inside the resonator is reflected from M_1 with a coefficient r' and transmitted through M_1 with a coefficient t'. The transmission and reflection coefficients of M_2 are identical to those of M_1.

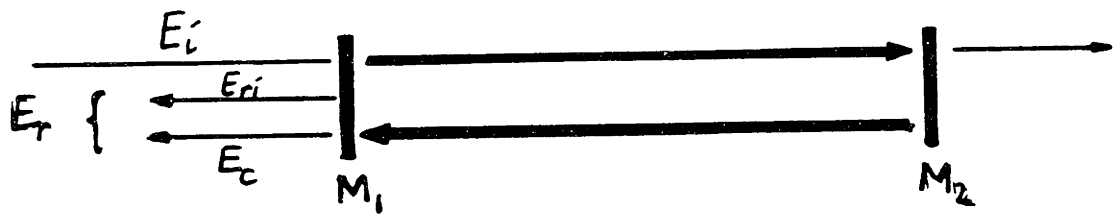

Figure A.1 Illustration of an simple resonator in reflection

Let us now have an input field of $E_i = E_o e^{j\omega t}$ incident on the mirror M_1. ω is the optical angular frequency of E_i and is given by $2\pi f$ where f is the optical frequency of E_i.

If the mirrors M_1 and M_2 are lossless, the reflected field E_r is given by[36]:

$$\begin{aligned} E_r &= E_o e^{j\omega t} r + E_o e^{j\omega t} r' \frac{tt' e^{j\delta}}{1 - r'^2 e^{j\delta}} \\ &= E_{ri} + E_c \end{aligned} \tag{A.1}$$

where:

$$\delta = 2\frac{n\omega}{c} d = \frac{\omega}{FSR} = 2\pi \frac{f}{FSR} \tag{A.2}$$

where FSR is the free spectral range of the resonator and is equal to the quantity $c/(2nd)$. The field E_{ri} is referred to as the primary reflection of E_i and the field E_c is the cavity output. For lossless mirrors, we have $r = -r'$ and $tt' = 1 - r'^2$ which results in:

$$E_r = E_o e^{j\omega t} r' (-1 + \frac{(1 - r'^2) e^{j\delta}}{1 - r'^2 e^{j\delta}}) \tag{A.3}$$

Figure A.2a and A.2b show the amplitude and phase of E_c as a function of δ for $r'^2 = 0.99$, indicating a symmetric cavity resonance. Figure A.2c shows the amplitude of E_r as a function of δ, also indicating a perfectly symmetric resonance lineshape. The reason behind the symmetry of E_r is that since symmetric points of E_c, such as the ones labeled A and A' in figure A.2a, have an equal and opposite phase with respect to E_{ri}, so that when we add E_{ri} and E_c these points will give exactly equal amplitudes, thus resulting in a symmetric E_r.

Now consider a small loss for mirror M_1. This loss will mean that there is a small phase difference of ψ between r and $-r'$ so that $r = -r' e^{j\psi}$. Thus equation A.3 is now given by:

$$E_r = E_o e^{j\omega t} r' (-e^{j\psi} + \frac{(1 - r'^2) e^{j\delta}}{1 - r'^2 e^{j\delta}}) \tag{A.4}$$

Figure A.3a and A3.b show the amplitude and phase of E_c as a function of δ, identical to that shown in figures A.2a and A.2b. By comparison, figure A.3c shows the amplitude of E_r as a function of δ indicating an asymmetric resonance. The reason behind this asymmetry is quite simple. As can be seen in figure A.3 symmetric points of E_c such as the ones labeled A and A' no longer have an equal and opposite phase with respect to

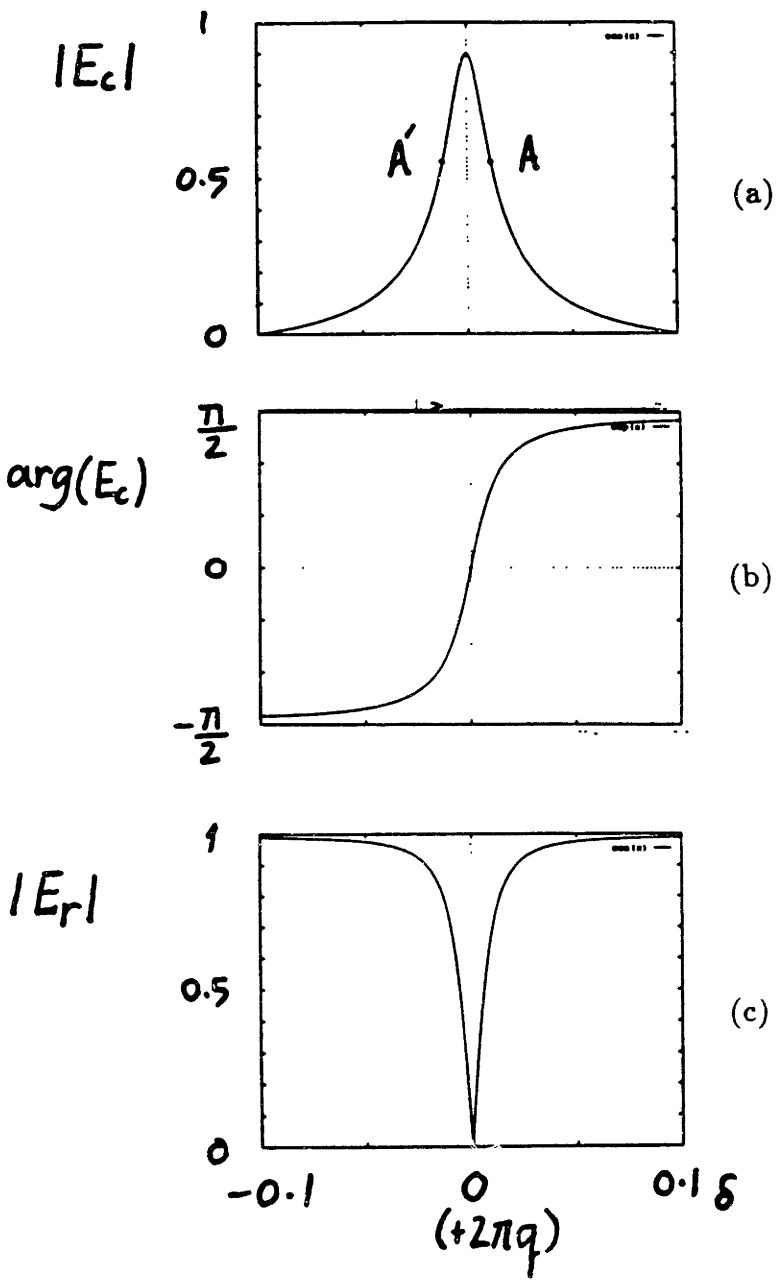

Figure A.2 Lossless mirrors: (a) Amplitude of E_c as a function of δ (b) phase of E_c as a function of δ(c) amplitude of E_r as a function of δ

E_{ri} because of ψ. Therefore, when we add E_{ri} and E_c, these points yield different values

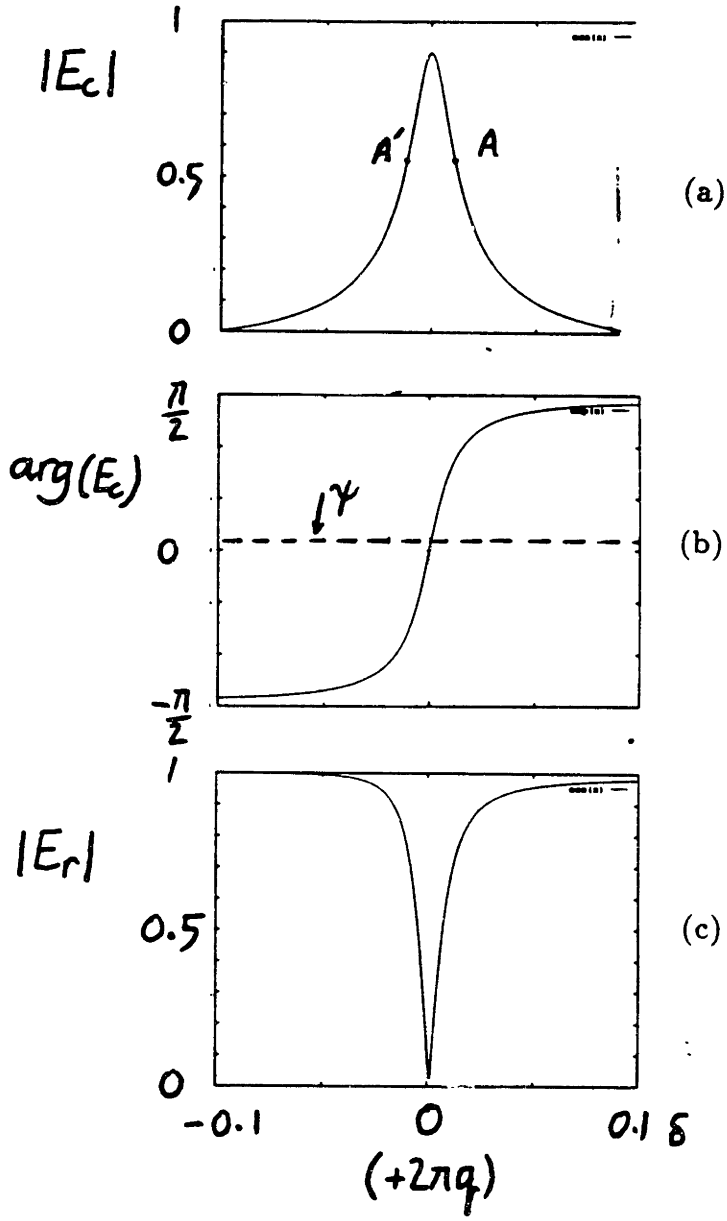

Figure A.3 Lossy mirrors: (a) Amplitude of E_c as a function of δ (b) phase of E_c as a function of δ(c) amplitude of E_r as a function of δ for $\psi = 0.1$

resulting in an asymmetric E_r.

The shift in the resonance frequency associated with E_r due to ψ is obtained by calculating the solution to the equation:

$$\frac{\partial}{\partial \delta}|E_r|^2 = 0 \tag{A.5}$$

δ_r is the solution to the equation A.9 and is given by:

$$\begin{aligned}\sin(\delta_r) &\approx -(1-R)\frac{2\cos(\psi) - 1 - \sqrt{(2\cos(\psi)-1)^2 + 4\sin^2(\psi)}}{2\sin(\psi)} \\ &\approx (1-R)\psi\end{aligned} \tag{A.6}$$

where $R = r'^2$. It should be noted that the results of equation A.6 are only valid for small values of ψ. Thus form equation A.6., δ_r is given by:

$$\delta_r = 2\pi q + (1-R)\psi$$

The resonance frequency of the cavity, f_r, is obtained by using the definition of δ from equation A.2, to give:

$$\begin{aligned}f_r &= \frac{1}{2\pi}\delta_r FSR \\ &\approx \frac{qc}{2nd} + (\frac{1-R}{2\pi}\psi)FSR \\ &\approx \frac{qc}{2nd} + \frac{1}{2}(\frac{1-R}{\pi}FSR)\psi \\ &\approx \frac{qc}{2nd} + \frac{1}{2}\Gamma_c\psi\end{aligned}$$

where Γ_c is the FWHM of the cavity resonance and when $1-R \approx 0$, $\Gamma_c \approx FSR(1-R)/\pi$. The quantity $qc/(2nd)$ is the resonance frequency of the cavity for the lossless case. The perturbation in the resonance frequency of the cavity due to lossy mirrors is therefore given by $(\Gamma_c/2)\psi$. This asymmetry calculations is equally applicable in the case of our fiber resonator.

APPENDIX B. Calculation of Resonance Frequency Pull due to the Interaction of two Resonance Lineshapes

In this appendix, we calculate the shift in a cavity resonance Λ_1, due to the influence of a second cavity resonance, Λ_2, separated by a frequency of f_o as shown in figure B.1.

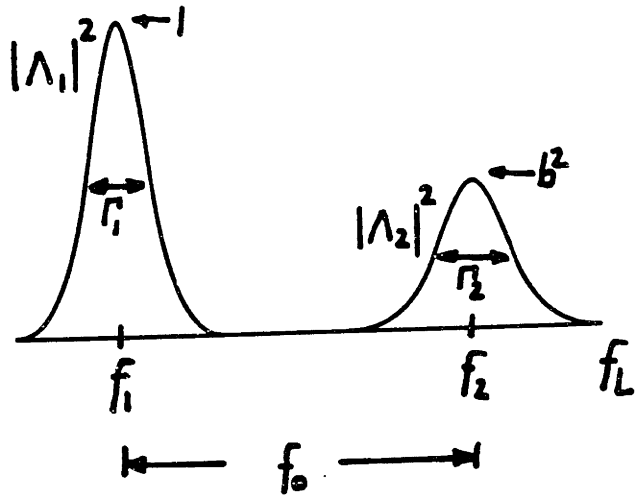

Figure B.1 Illustration of the intensities associated with the two resonance lineshapes Λ_1 and Λ_2 as a function of frequency f_L

Λ_1 and Λ_2 represent the ratio of the E field of the resonator output beam to the E field of the input beam. The input beam has a frequency of f_L. Λ_1 has a resonance frequency

of f_1 and Λ_2 has a resonance frequency of f_2. Although these cavity resonances are in general Airey functions, we can approximate them by Lorenzian lineshapes, given by:

$$\begin{aligned}\Lambda_1(f_L) &= \frac{j\Gamma_1/2}{(f_L - f_1) + j\Gamma_1/2} \\ \Lambda_2(f_L) &= b\frac{j\Gamma_2/2}{(f_L - f_2) + j\Gamma_2/2}\end{aligned} \tag{B.1}$$

where f_L is the frequency of the input light, Γ_1 and Γ_2 represent the FWHM of the intensity associated with Λ_1 and Λ_2 respectively. b is ratio of the peak field of Λ_1 to that of Λ_2.

Using the substitution $f = f_L - f_1$ we can represent Λ_1 and Λ_2 as:

$$\begin{aligned}\Lambda_1(f) &= \frac{j\Gamma_1/2}{f + j\Gamma_1/2} \\ \Lambda_2(f) &= b\frac{j\Gamma_2/2}{(f - f_o) + j\Gamma_2/2}\end{aligned} \tag{B.2}$$

We now add Λ_1 and Λ_2 and calculate the total intensity, I, given by:

$$\begin{aligned}I &= |\Lambda_1(f) + \Lambda_2(f)|^2 \\ &= |\Lambda_1(f)|^2 + |\Lambda_2(f)|^2 + 2Real(\Lambda_1(f)\Lambda_2(f)^*) \\ &= \frac{\Gamma_1^2/4}{f^2 + \Gamma_1^2/4} + b^2\frac{\Gamma_2^2/4}{(f - f_o)^2 + \Gamma_2^2/4} + \\ &\quad 2b\ Real\{\frac{\Gamma_1\Gamma_2/4}{f^2 - f(2f_o + j(\Gamma_1/2 - \Gamma_2/4)) + \Gamma_1\Gamma_2/4 - j\Gamma_1 f_o)}\}\end{aligned} \tag{B.3}$$

We now calculate the resonance frequency of $\Lambda_1(f)$ by finding the solution to $\partial I/\partial f = 0$, which gives:

$$\frac{\partial I}{\partial f} \approx -\frac{8f}{\Gamma_1^2} + b^2\frac{\Gamma_2^2}{2f_o^3} - b\frac{2\Gamma_2}{\Gamma_1 f_o} = 0$$

which yields:

$$\Delta f = b^2\frac{\Gamma_2^2\Gamma_1^2}{16f_o^3} - b\frac{4\Gamma_2}{\Gamma_1 f_o} \tag{B.4}$$

The first term on the right handside of equation B.3 is the contribution due to the addition of the intensities of Λ_1 and Λ_2. This term results in a resonance pull given by:

$$\Delta f = \frac{b^2\Gamma_1^2\Gamma_2^2}{16f_o^3} \tag{B.5}$$

which is proportional to b^2 and varies with $1/f_o^3$. The second term on the right handside of equation B.4 is due to the interference between Λ_1 and Λ_2. This term results in a resonance pull proportional to:

$$\Delta f = -\frac{b\Gamma_1\Gamma_2}{4f_o} \qquad (B.6)$$

which is proportional to b and varies with $1/f_o$

References

1. E.J.Post, Rev. Mod. Physics 39, 475 (1967)
2. M.P.Hangan, M.O.Scully, and K. Just, Phys. Lett 77A, 88 (1980).
3. M.O.Scully in Proceedings of the Fifith International Conference on Laser Spectroscope, H. Walther and K. Rothe Editros, Springer Verlag Berlin, (1979)
4. D.H. Ekhardt, Proc. Soc. Photo-Opt. Instrum. Eng. 157, 172, (1978)
5. W.R.Carrington and R. Fredricks, Lear Siegler, Inc. Grand Rapids, Michigan 49508, Final Rep. to U.S. Office of Naval Research N00014-73-C-0377, Nov. 1973
6. V.Vali and L.W. Shorthill, Appl. Opt. 15, 1099 (1976)
7. A.H.Rosenthal, J.Opt.Soc.Am. 52,1143 (1962)
8. S.Ezekiel and R.Balsamo, Appl. Phys. Lett. 30, 478 (1977)
9. R.E.Meyer, S.Ezekiel, D.W.Stowe, V.J.Tekippe Optics Letters 8 644 (1983)
10. W.M. Macek and D.T.M.Davis, Jr., Appl. Phys. Lett. 2, 67 (1963)
11. F.Aronowitz, Laser Applications Vol.1., edited by Monte Ross,Academic Press (1971), pp. 133-200.
12. S.Ezekiel, J.A.Cole, J.Harrison, G.Sanders, Proc. Soc. Photo-opt Instrum Eng. 157, 68 (1978)
13. G.A. Sanders, M.G.Prentiss, S.Ezekiel, Optics Letters 11, 569 (1981)
14. G.A.Sanders, PhD. Thesis, MIT, 1983
15. M.Hereld, and D.Anderson, SPIE publication 487 pp.33-38 (1984)
16. T.J.Hutchings and D.C.Stjern Proc. IEEE Nat. Aero and Electrical Conference. p.549 (1978)
17. F.Zarinetchi and S.Ezekiel, Opt. Letters, 11, p.401 (1986)
18. R.C.Youngquist, L.F.Stokes, H.J.Shaw IEEE Jouranl of Q.E. 19, 1888 (1983)
19. M.Takahashi, S.Tai, K.Kyuma, Journal of Lightwave Tech. 8, 811 (1990)
20. K.Iwatsuki, K.Hotate, and M. Higashiguchi, Applied Optics 23, 3916 (1984)

21. K.Iwatsuki, K.Hotate, and M.Higashiguchi, Applied Optics 25, 2606 (1986)
22. S.Ezekiel, J.L.Davis, R.W.Hellwarth, Optics Letters 7, 457 (1982)
23. K.Iwatsuki, K.Hotate, and M. Higashiguchi, Journal of Lightwave Tech. 6, 645 (1986)
24. A. Yariv, Introduction to Optical Electronics, Holt, Reinhard and Winston Inc. (1971)
25. E.P. Ippen, in Laser Applications to Optics and Spectroscopy, S.F. Jacobs, M.Sargent III, J.F. Scott and M.O. Scully, eds, Addison-Wesley (1975), p.213.
26. K.O. Hill, B.S. Kawasaki, and D.C. Johnson, Appl. Phys Lett. 28, 608 (1976)
27. L.F. Stokes, M.Chodorow and H.J.Shaw Opt. Letters 7, 509 (1982)
28. P. Bayvel and I.P Giles, Opt. Letters 14, 581 (1989)
29. P.J.Thomas, H.M.van Driel, and G.I.A. Stegeman, Appl. opt. 19, 1906 (1980)
30. D.R. Ponikvar and S.Ezekiel, Opt. Letters 6, 398 (1981).
31. R.H. Pantell and H.E. Puthoff, Fundamentals of Quantum Electronics, John Wiley & Sons (1969)
32 Y.R. Shen, The Principles of Nonlinear Optics, J.Wiley & Sons (1984)
33. N. Shibata, R.G. Waarts, R.P.Braun Optics Letters 12, 269 (1987)
34. S.P. Smith, F.Zarinetchi, and S.Ezekiel, Opt. Letters 16, p.393(1991)
35. I. Bar-Joseph, A.Dienes, A.A.Friesem, E.Lichtman, R.G.Waarts and H.H. Yaffe, Optics Communications, 59, p.296 (1986)
36. E. Hecht and A. Zajac, Optics, Addison-Wesley (1979)